

**NASA CONTRACTOR
REPORT**



NASA CR-1

c.1

LOAN COPY AVAILABLE
AND FOR
KIRTLAND, NEW EX

0099823



TECH LIBRARY KAFB, NM

NASA CR-757

ANALYTICAL STUDY OF IMPACT EFFECTS AS APPLIED TO THE METEOROID HAZARD

by R. L. Bjork, K. N. Kreyenhagen, and M. H. Wagner

Prepared by

SHOCK HYDRODYNAMICS, INC.

Sherman Oaks, Calif.

for





ANALYTICAL STUDY OF IMPACT EFFECTS AS
APPLIED TO THE METEOROID HAZARD

By R. L. Bjork, K. N. Kreyenhagen,
and M. H. Wagner

Distribution of this report is provided in the interest of
information exchange. Responsibility for the contents
resides in the author or organization that prepared it.

Prepared under Contract No. NASw-805 by
SHOCK HYDRODYNAMICS, INC.
Sherman Oaks, Calif.

for

NATIONAL AERONAUTICS AND SPACE ADMINISTRATION

CONTENTS

Abstract	v
Section 1 INTRODUCTION AND SUMMARY	1
Approach 1, Conclusions Regarding Meteoroid Perforation Hazard 2	
Section 2 ANALYTICAL TECHNIQUES FOR PREDICTION OF IMPACT EFFECTS	7
Principal Phases of Hypervelocity Impact 7, Phase I - Shock System Formation and Detachment 7, Phase II - Cratering Flow 10, Numerical Technique for Analysis of Impact Problems 10, Hydrodynamic Model 10, Particle-In-Cell (PIC) Code 11, Termination of Crater Growth 14, Dynamic Pressure-Target Strength Criteria 14, Target Heating and Melting Effects 19, Perforation of Finite Targets 27, Elastic-Plastic Considerations 28, Oblique Incidence 28, The Equation of State of Aluminum 29	
Section 3 DESCRIPTION OF CURRENT NUMERICAL SOLUTIONS	31
Selection of Cases 31, Target Materials 31, Impact Velocities 31, Meteoroid Densities 32, Use of Prior Calculations 32, Numerical Results 32, Initial Conditions 33, Penetration Predictions 33, Energy and Momentum Partitions 33, Discussion and Interpretation of Important Features 36, Penetration vs Density and Velocity 36, Interpolation to Intermediate Conditions 38, Distribution of Energy in Cratering 40, Effects of Shock-Induced Residual Temperature on Cratering 41, Target Strength 41, Target Melting 41, Projectile Vaporization and Blowoff 44, Vortex Flow 45, Comparisons with Other Work 46, Other Hydrodynamical Computations 47, The Fit of Herrmann and Jones 49	
Section 4 METEOROID ENVIRONMENT	51
Meteoroid Densities 52, Photographic Observations 52, Radar Observations 52, Conclusions Regarding Densities 53, Meteoroid Flux as a Function of Mass 53, Photographic Meteors 53, Radio Meteors 55, Rocket and Satellite Sounding Board Data 56, Direct Measurements of Penetrating Flux 58, Summary of Mass Flux Data 61	

CONTENTS (Con't)

Section 5	CONCLUSIONS REGARDING PERFORATING FLUX	65
Appendix A	ANALYTICAL FORMULATION OF AN EQUATION OF STATE FOR ALUMINUM	69
	Zero Degree Isotherm 71, Nuclear Thermal Contribu- tion to Pressure and Energy 72, Electronic Thermal Contribution to Pressure and Energy 75, Equation of State for Hydrodynamic Code Calculations 75, Calculation of Hugoniot, Adiabats and Release Temperatures 79, Analytical Fit to Electronic Thermal Contribution 88	
Appendix B	USE OF SPECIFIC INTERNAL ENERGY AND DYNAMIC PRESSURE PROFILES FOR PENETRATION PREDICTIONS	97
	Specific Internal Energy Profiles vs Depth 99, Dynamic Pressure and Residual Strength vs Depth 107	
Appendix C	DESCRIPTIONS OF NUMERICAL SOLUTIONS OF IMPACT CASES 8051-8058, INCLUDING PLOTS OF MASS POSITIONS, AND VELOCITY AND PRESSURE FIELDS	115
	Types of Plots 115, Scale 115, Grid Changing 116, Energy and Momentum Partitioning 116	
Appendix D	REVIEW OF OTHER THEORETICAL TREATMENTS	175
	Late Stage Equivalence 175, Comments on Identical Flow Fields 176, One Dimensional Late Stage Equivalence 180	
References	183

ABSTRACT

A two-dimensional hydrodynamic code is used to predict effects of impacts at 20 and 72 km/sec by porous and solid materials simulating meteoroids upon aluminum and steel plates. A target strength criterion, incorporating effects of thermal degradation due to residual heating, is used to terminate crater growth in these hydrodynamic analyses.

Available data regarding the meteoroid flux are reviewed and interpreted in the light of results of the impact analyses, and a consistent meteoroid mass flux is obtained.

Using this environment and the impact effect predictions, penetrating fluxes are obtained as functions of thickness for aluminum and steel. A square meter area of 0.032-in. aluminum is found to have a 0.9 probability of surviving without penetration for one year in a near-earth orbit.

SECTION 1

INTRODUCTION AND SUMMARY

1.1 Approach

This is the final report of an analytical investigation of the meteoroid impact hazard to space vehicles. The study is based upon detailed numerical analyses of several impact cases which are representative of possible meteoroid-spacecraft encounters, and upon an evaluation of available meteoroid environment data.

In the analyses of impacts, a hydrodynamic model was assumed, and the phenomena were examined using the two-dimensional particle-in-cell (PIC) code. Hypervelocity impact effects and the numerical techniques are described in Section 2 of this report. Penetration predictions are obtained from the hydrodynamic analyses using the criterion that crater formation is arrested at the maximum depth where the dynamic pressure in the cratering flow field is equivalent to the local target strength. Effects of residual target temperatures upon material strengths are incorporated in the technique for predicting penetration.

The eight impacts examined during the program were:

- a. Porous aluminum ($\rho = 0.44$, simulating porous, stony meteoroids) into aluminum and iron targets at 20 and 72 km/sec.
- b. Aluminum ($\rho = 2.7$, simulating solid, stony meteoroids) into iron targets at 20 and 72 km/sec.
- c. Iron ($\rho = 7.86$, simulating high density meteoroids) into aluminum targets at 20 and 72 km/sec.

Results of prior hydrodynamic analyses for impacts of aluminum into aluminum and iron into iron at 5.5, 20 and 72 km/sec were also used in this investigation. All of these impact results are summarized and discussed in Section 3, and curves showing penetration as a function of impact velocity and projectile density are given there.

The simulation of stony meteoroid material by aluminum in these calculations is consistent with the measured similarities of shock Hugoniot properties of aluminum with some important classes of rock, and permitted utilization of the more extensive data which are available to describe the properties of aluminum under extreme pressures. It was necessary, however, to revise the aluminum equation of state to more accurately describe shocked porous material.

Data from experiments which have been conducted to establish the characteristics of the meteoroid environment are reviewed in Section 4. These data include radar and photographic observations, rocket and satellite sounding board momentum measurements, and perforating flux observations from Explorer XVI and XXIII, and from Pegasus I, II, and III. Results of the numerical analyses of impact phenomena were used for more specific interpretations of some of these data, and to obtain a consistent meteoroid mass flux curve.

The impact effect results and the environmental data are combined in Section 5 to give the predicted meteoroid penetrating flux.

Much of the detailed information generated during the program is contained in four appendices. The revised equation of state for aluminum is described in Appendix A. Appendix B contains the specific derivation of the crater predictions for each impact case. Detailed results of the numerical solutions are given in series of plots in Appendix C. Appendix D is a review of numerical treatments of hypervelocity impact phenomena.

1.2 Conclusions Regarding Meteoroid Perforation Hazard

Figure 1-1 summarizes the conclusions of this study regarding the flux of meteoroids capable of perforating aluminum and steel plates of various thicknesses. In this figure the average number of perforations per square meter per second is shown as a function of plate thickness. As an example of the use of these curves, it is seen that a square meter aluminum plate of 1 mm thickness experiences a perforative flux of about 2×10^{-9} per second. Thus on the average, it would be perforated once every 5×10^8 seconds, or about every 16 years.

The penetrating flux data are shown in different form in Figures 1-2 and 1-3. Here the thicknesses of aluminum or steel necessary to provide various probabilities of remaining unperforated are presented. The curves are parameterized on $P(0)$, which represents the probability of no perforation occurring, computed from the data of Figure 1-1 on the basis of Poisson statistics. In these figures the near Earth flux has been used, with Earth-shielding taken into account. To obtain the corresponding probabilities for a vehicle far from Earth in an omnidirectional flux, each curve in Figures 1-2 and 1-3 should be lowered by $\log_{10} 2 \sim 0.3$. Of course this treatment assumes that the meteoroid environment does not depend on distance from Earth.

As examples of the use of Figures 1-2 and 1-3, a square meter area of .031-in. aluminum skin would have a probability of about 0.9 of surviving 1 year in a near-Earth orbit. A steel skin of the same areal density has a thickness of .011-in., and the corresponding probability of survival would be about $1/e$, or 0.37. Such a steel skin would have a 0.9 chance of surviving without perforation for only one month.

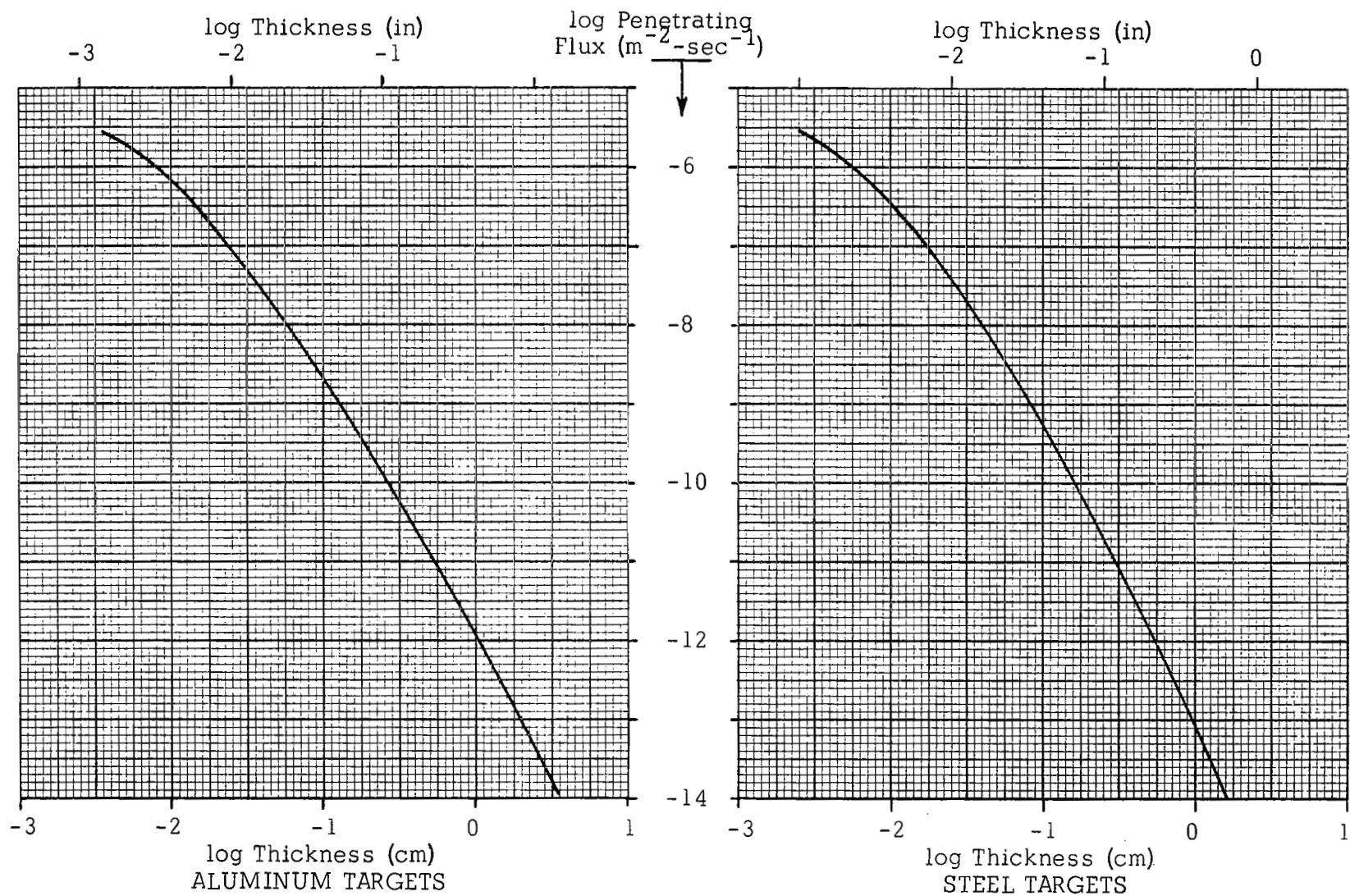


Figure 1-1: PENETRATING FLUX NEAR EARTH

Figure 1-2
LOGARITHMIC PLOT OF PROBABILITIES OF
SURVIVAL OF ALUMINUM TARGETS
IN METEOROID ENVIRONMENT NEAR EARTH

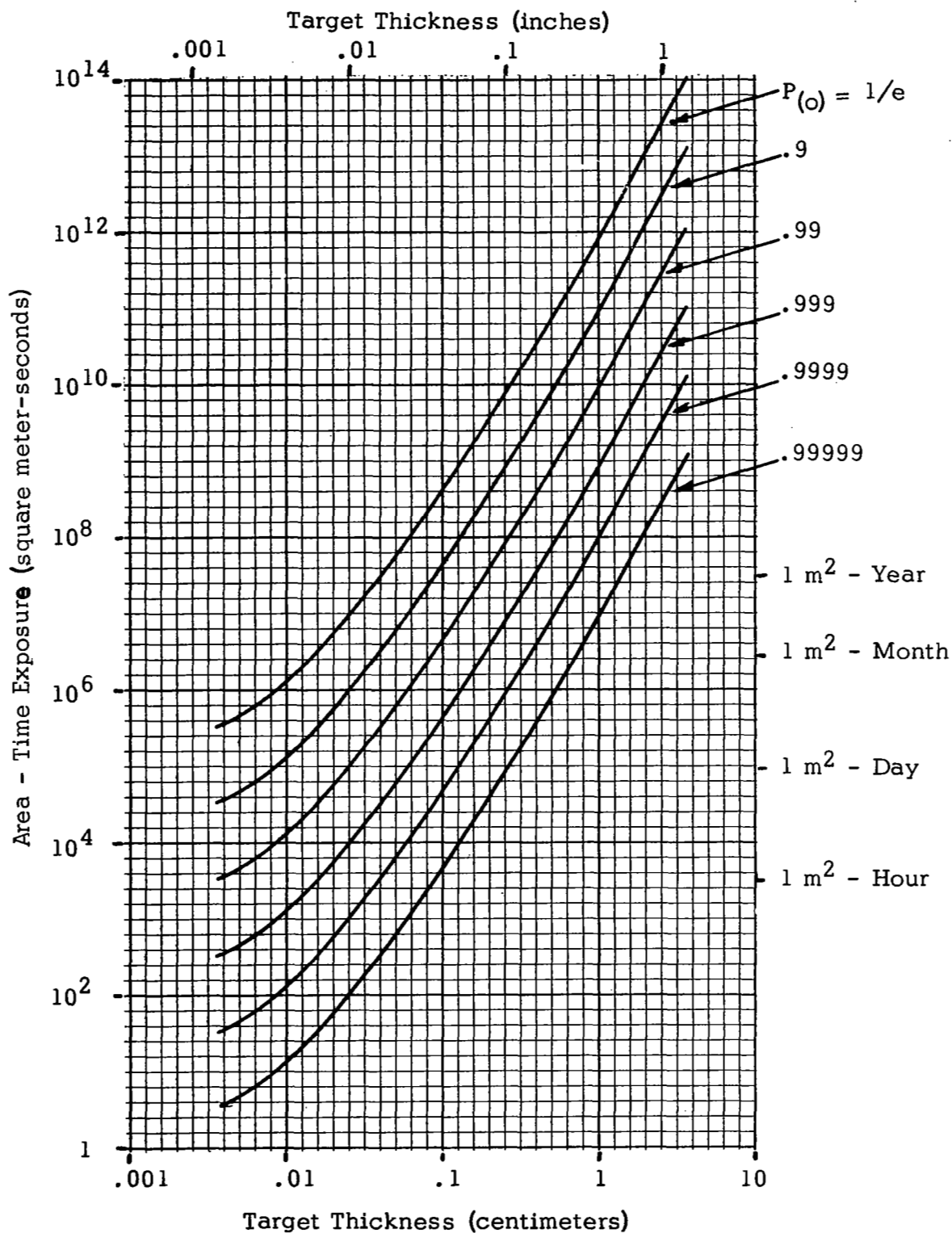
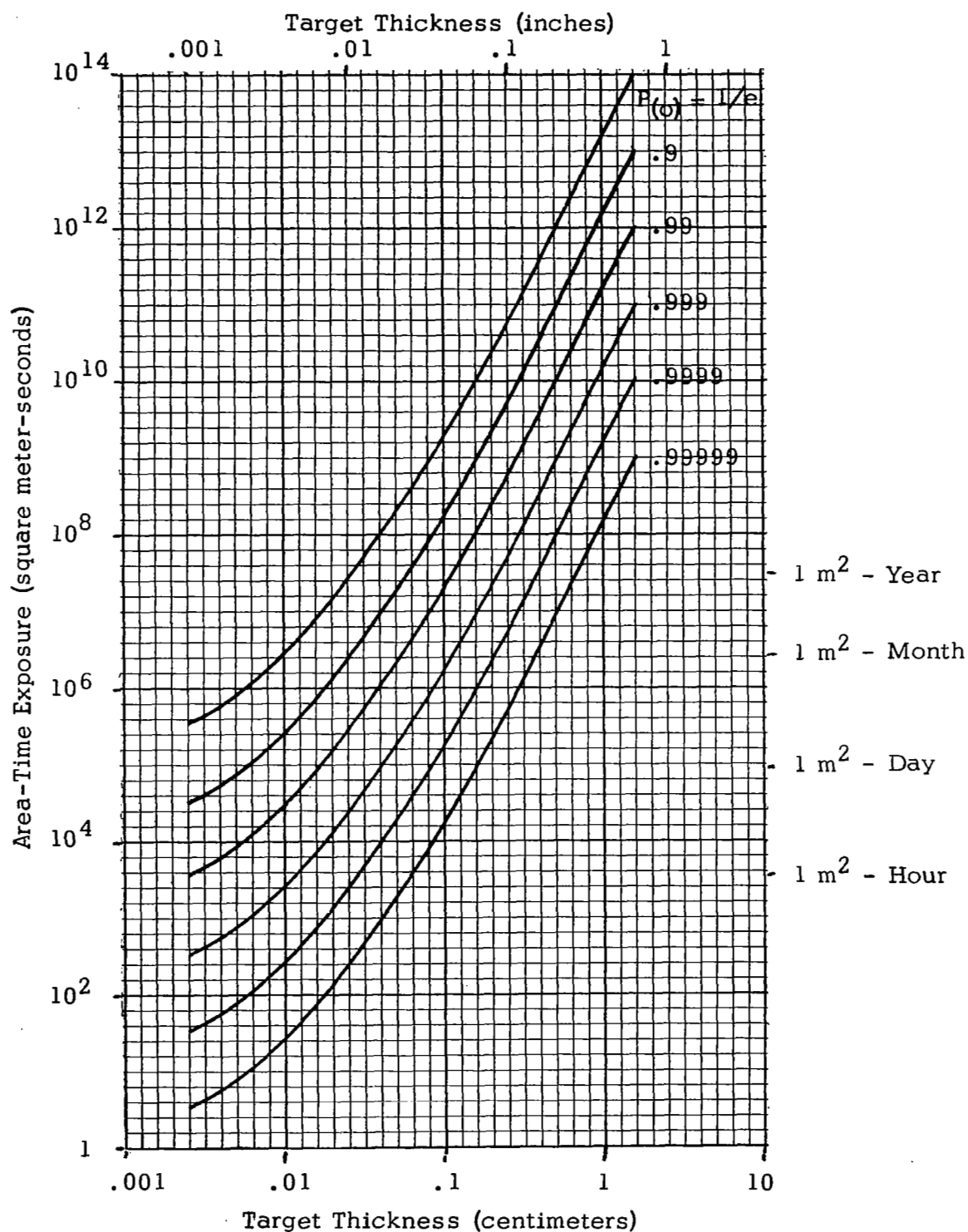


Figure 1-3
LOGARITHMIC PLOT OF PROBABILITIES OF
SURVIVAL OF STEEL TARGETS
IN METEOROID ENVIRONMENT NEAR EARTH



From the standpoint of spacecraft designs, the larger meteoroids (10^{-6} gm), and correspondingly lower flux levels are the more significant portions of these curves. Direct measurement of penetrating flux for thicker targets (i.e., larger meteoroids) is difficult because of the low frequency of encounter by a detector of manageable dimensions. Measurements of the frequency of these larger meteoroids has therefore come from radar and photographic observations, over large areas of the sky, of the ionized and luminous trails left by meteoroids entering the atmosphere.

Those observations do not directly measure the penetrating flux, but instead provide the flux as a function of photographic magnitude or as a function of ionized particles per unit trail length. In addition, radar and photographic observations specify the velocity of the meteor as a function of altitude. Analysis of the data has suggested that the primary particle breaks up almost immediately upon entering the atmosphere and that the observed effects are created by a group of fragments rather than by a single particle. As a result, it becomes difficult to compute the initial velocity of the primary particle and to deduce its mass and density. The literature on this difficult subject is reviewed and the best current approximations of the flux as a function of mass and density are identified.

The range of target thicknesses which will be perforated by a specified mass are then determined through use of the penetration predictions obtained from the calculations in this study, adjusted for effects of oblique incidence as well as to account for the difference between penetration of a semi-infinite target versus marginal perforation of a finite target.

The higher flux levels in these curves, corresponding to smaller meteoroids, are based upon direct observations of the penetrating flux by five satellites: Explorer XVI and XXIII, and Pegasus I, II, and III. These experiments measured the rates of perforation of specific thicknesses of metals. Neglecting effects of variations in the flux with time, the penetrating flux as a function of thickness determined by these experiments is considered to be quite accurate.

The penetrating fluxes presented in Figure 1-1 for thicknesses smaller than .01 cm are based on the perforation experiments (pressurized cells) carried on Explorer XVI and XXIII. Other computations of the mass flux have been conducted based on satellite sounding board experiments. These results slightly overlap at the low end of the thickness range considered here. However, the present interpretation of the sounding board experiments predicts penetration rates substantially higher than those measured by the pressurized cell experiments. The pressurized cell result is used here since we believe it places an unambiguous upper limit on the perforation rate of a given thickness.

SECTION 2

ANALYTICAL TECHNIQUES FOR PREDICTION OF IMPACT EFFECTS

2.1 Principal Phases of Hypervelocity Impact

The processes involved in impacts in the meteoroid velocity range can be divided into two phases. The first phase lasts from impact until the target shock "breaks away" from the immediate impact zone. This initial interaction is relatively short, and is characterized by extreme pressures in the target and projectile materials. In the second phase, there are two essentially separate flow fields in the target. One of these is the isolated target shock which has previously broken away from the impact zone. It is comprised of material which is suddenly accelerated by the shock's passage, and is then decelerated to rest by the pressure gradient appearing behind the shock. (The term "isolated shock" thus refers to a pulse which is headed by a shock, and in the strictest sense is a misnomer. However, the usage of this term is common.) The other flow field is termed the "cratering flow". It consists of target material near the point of impact which continues to flow, by virtue of its inertia, to ultimately form the crater. This cratering flow is a relatively long duration process, characterized by low stress levels and large plastic deformation.

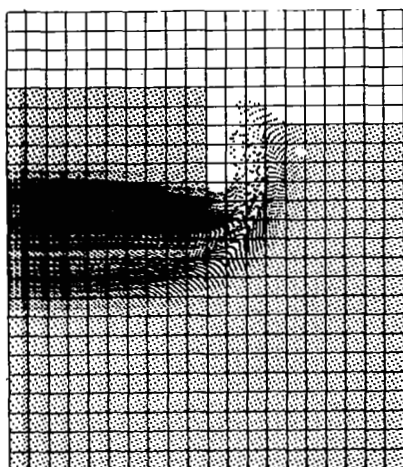
2.1.1 Phase I - Shock System Formation and Detachment

When a hypervelocity projectile strikes a target, shock waves propagate from the interface both into the target and back into the projectile. These diverging shocks form an expanding high pressure region, embracing material from the target and the projectile.

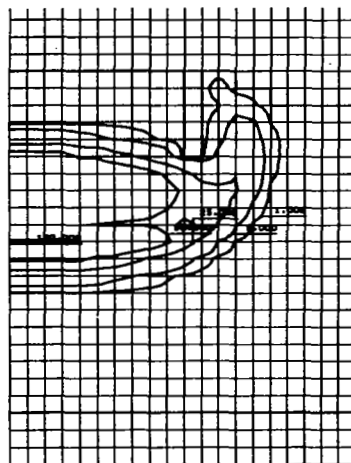
Figure 2-1 contains a series of mass disposition and pressure contour plots illustrating the development of the shock system. These plots are from a numerical solution performed during this study for the impact of an aluminum cylinder at 20 km/sec into a semi-infinite iron target. (The y-axis of each plot is the axis of the axisymmetric problem.)

Plots 2-1(a) to (d) show the initial response of the target and projectile. The central portion of the flow (near the axis) is one-dimensional in the early stages. As the high pressure region interacts with the lateral free surface of the projectile and with the adjacent target surface, some pressure relaxation occurs due to rarefaction waves which propagate into the pressurized material. High pressures persist even after these lateral rarefactions reach the axis, supported by the continued flow of projectile mass into the target.

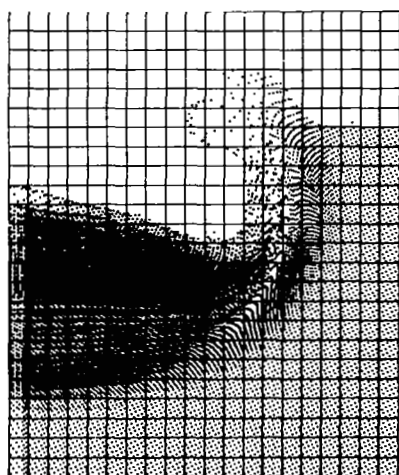
When the shock wave reaches the rear surface of the projectile, this flow is greatly reduced by a rarefaction which emanates from the rear surface and propagates into the shocked region. Plots 2-1(c) and (d) show this process starting. The pressure gradient in the rarefaction causes upward acceleration of the rear elements of the projectile.



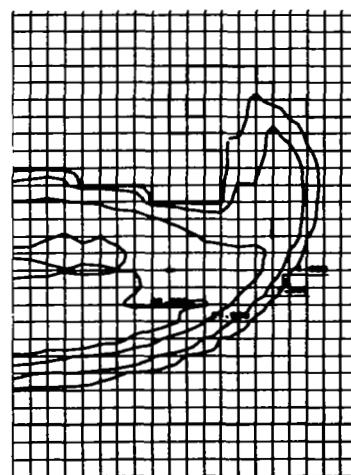
(a) Mass Positions
at $t = 1.2 \mu\text{sec}$



(b) Pressure Field
at $t = 1.2 \mu\text{sec}$

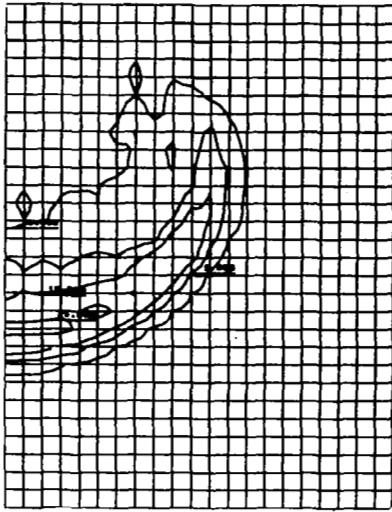


(c) Mass Positions
at $t = 1.8 \mu\text{sec}$

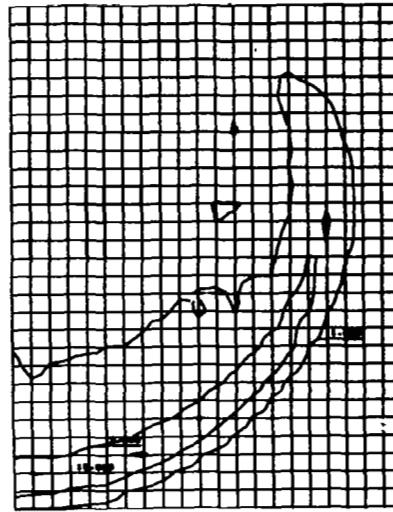


(d) Pressure Field
at $t = 1.8 \mu\text{sec}$

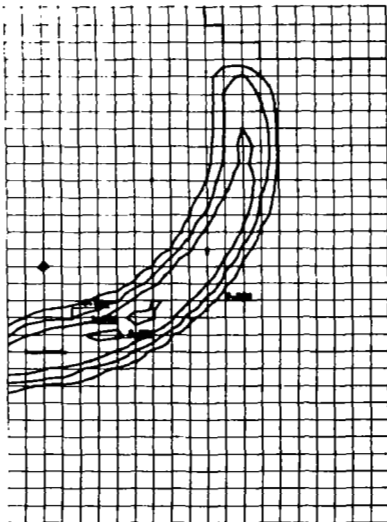
FIGURE 2-1
FORMATION AND DETACHMENT
OF SHOCK SYSTEM
Aluminum into Iron at 72 km/sec
(Case 8056)



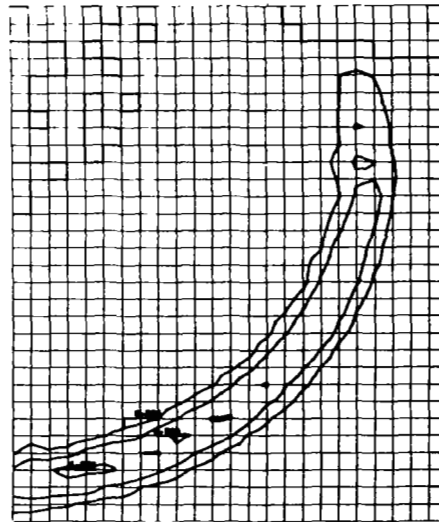
(e) Pressure Field
at $t = 4.1 \mu\text{sec}$



(f) Pressure Field
at $t = 9.0 \mu\text{sec}$



(g) Pressure Field
at $t = 22.0 \mu\text{sec}$



(h) Pressure Field
at $t = 42.8 \mu\text{sec}$

FIGURE 2-1 (Con't)
FORMATION AND DETACHMENT
OF SHOCK SYSTEM
Aluminum into Iron at 72 km/sec
(Case 8056)

Subsequently, the pressure drops relatively quickly throughout the projectile and in the target material behind the shock wave. Plots 2-1(d) through (f) illustrate the rarefaction overtaking the shock, and reducing the pressure and compression behind the shock to essentially zero. In plot (f) this process is nearly complete, and the shock wave which continues to propagate into the target in plots (g) and (h) is separated or detached from the impact zone. Once this separation occurs, the isolated shock propagating into the target does not further influence the crater formation in a direct way. It does, however, exert an indirect effect by leaving the material in a heated or melted condition.

2.1.2 Phase II - Cratering Flow

The target and projectile material which is left behind in the impact region after breakaway of the isolated shock, retains a small but highly important part of the velocity which was imparted to it during Phase I. It is the inertia of this remaining material which is responsible for the final stages of crater formation.

Most of the momentum and kinetic energy of the impacting projectile ultimately resides in the ejecta and in the isolated shock. The kinetic energy which is available for cratering flow is the difference between two quantities, namely the initial projectile kinetic energy minus the energy carried away by the isolated shock and ejecta. Hence, the cratering flow, and thus the final crater dimensions, are quite sensitive to the mechanics of the energy partition. This feature of impact phenomena may be a major element in the observed variability of experimental data.

2.2 Numerical Technique for Analysis of Impact Problems

All but a small portion of the meteor impact velocity spectrum is inaccessible to experimental investigations. Even in the accessible velocity range, it is impractical to perform impact experiments with porous, low density projectiles simulating meteoroids. It is therefore necessary to utilize analytical techniques in the assessment of meteoroid impact effects. One can place a high degree of confidence in predictions made on the basis of analytical computations if it can be shown that the analysis includes consideration of all the important physical phenomena occurring at velocities in excess of experimental capabilities, and if the computational model exhibits agreement with experiments in the velocity range wherein tests can be conducted.

2.2.1 Hydrodynamic Model

Since the stresses produced in the projectile and impacted target material in the initial stages of hypervelocity impact greatly exceed the material strength, a hydrodynamic model can appropriately be adapted for analysis of the phenomena involved. Such a model was initially proposed and used as a basis for development of a two-dimensional numerical technique for analyses of impacts by Bjork (1959, 1959a), and has subsequently been the basis for the two-dimensional analyses by Walsh (1963) and Riney (1963).

The state of stress in any medium is precisely specified by the components of the stress tensor. With few exceptions the stress tensor is symmetrical, so that it may be diagonalized. Thus, the state of stress may be described by giving the three principal components of this stress tensor, and the corresponding principal directions. Let us assign the name, "stress space", to the cartesian three space in which a component of the principal stress tensor is plotted along each axis. The theory of plasticity specifies that only a certain region of stress space, centered about (1, 1, 1) line, is accessible to a medium. In the case of media obeying the von Mises yield criterion, the accessible region consists of a cylinder whose radius is $\sqrt{2/3}Y$, where Y is the yield stress in simple tension. For materials obeying the Tresca yield criterion, it consists of a hexagonal cylinder whose greatest distance from the (1, 1, 1) line is again $\sqrt{2/3}Y$.

For large stresses, the accessible region has lateral dimensions small compared with the stress, so that its plot resembles a line rather than a cylinder. In the hydrodynamic approximation, the accessible region is assumed to be the (1, 1, 1) line itself, so that the three principal stress components are all equal. It is clear that the approximation is best when the stresses are large compared with Y. For most materials Y is on the order of a few kilobars, so that the approximation becomes good at pressures as low as 50 kilobars. It will be demonstrated that in certain hypervelocity impacts, the crater is formed in material which has been pre-conditioned by a shock, and therefore left in a heated state. If the material is heated, Y is decreased, which reinforces the validity of the hydrodynamic approximation. The diminution of Y due to heating is a characteristic of hypervelocity impact, and should, where practical, be taken into account in the analyses of such impacts.

A great deal of experimental information relative to the equation of state of solids has been accumulated by measuring shocks which are generated in material samples. These data have been satisfactorily interpreted on a hydrodynamic model in which thermal conductivity and viscosity are neglected. That the neglect of thermal conductivity is a valid approximation can be demonstrated by order of magnitude arguments. Neglecting viscosity is justified from the widths of the shock structure observed, since the rise time of a typical shock in a solid is on the order of 10^{-7} seconds.

2.2.2 Particle-In-Cell (PIC) Code

Despite the assumption of a hydrodynamic stress tensor, two and three-dimensional impact problems remain far too complex for analysis by closed form techniques. Numerical techniques are therefore needed for analysis of practical impact problems.

Stringent requirements must be imposed on a numerical program to be used for these analyses. Among these are the following:

a) Ability to treat flows in which large distortions of the material occur. This is critical in studying the early stages of hypervelocity impact. Purely Lagrangian formulations are therefore unsuitable, unless an unusually high degree of spatial resolution is possible - a condition which is not economically feasible under normal circumstances.

b) Ability to accommodate different materials in a given problem, such as a projectile and target of dissimilar materials or multilayer targets. This means that there must be no spurious diffusion of mass across material interfaces. Ordinary Eulerian formulations are defective in this regard, in that continuous diffusion of mass occurs, not only across material boundaries, but also into the vacuum across exposed surfaces.

c) Provision for optimum resolution in all phases of a problem. The active region in hypervelocity impact is initially small, but the phenomena occurring in this small region are often very important to the subsequent response. Thus details in the initially small region must be well-resolved to provide accuracy in later stages. Therefore the program must have the capability to enlarge the "field of view" from a small, highly-resolved active zone at the beginning to a larger field as more material is engulfed by the shock systems.

The PIC code employed for the solutions in this study was developed specifically to treat hydrodynamic behavior of solids. Applications to analysis of impact problems are found in Bjork (1959a, 1961b), Olshaker and Bjork (1962), Kreyenhagen, Bjork and Brooks (1965), and Bjork and Rosenblatt (1965). Brode and Bjork (1960) describes an application to nuclear cratering. Complete documentation of the code is provided in Bjork, Brooks and Papetti (1963).

In PIC, the motion of target and projectile are assumed to be governed by the compressible hydrodynamic equations, which may be written in terms of Eulerian variables as follows:

$$\rho \frac{\partial u^i}{\partial t} + \rho u^j u^i_{,j} + g^{ij} P_{,j} = 0 \quad (2-1)$$

$$\frac{\partial \rho}{\partial t} + u^i \rho_{,i} + \rho u^i_{,i} = 0 \quad (2-2)$$

$$\rho \frac{\partial e}{\partial t} + \rho u^i e_{,i} + P u^i_{,i} = 0 \quad (2-3)$$

$$P = P(\rho, e) \quad (2-4)$$

where the variables are

u^i = particle velocity

P = pressure

e = specific internal energy

ρ = density

t = time

g^{ij} = metric tensor

The comma notation is used to denote covariant differentiation, and the Einstein summation convention is employed. The independent variables are the space variables and time.

PIC overcomes the difficulties mentioned earlier by treating mass points moving through an Eulerian mesh. Integration is carried out with respect to time, starting with the initial conditions and imposing the appropriate boundary conditions. The advance over Δt is carried out in two steps. In the first step, the transport terms in Eq. (2-1) to (2-3) are neglected and the integration is performed by solving the difference analog of the resulting differential equations. In the second step, the transport terms are accounted for by noting which masses changed cells in the first step.

To get the new mass of the cells affected, one merely sums the masses now present in each cell. This accounts for the mass transport term in Eq. (2-2). A mass which changes cells is assumed to carry with it an increment of internal energy equal to the product of the mass in question and the specific internal energy transport term in Eq. (2-3).

A mass, in changing cells, also brings with it an increment of momentum given by the product of the mass and the velocity of the cell which it left. This increment of momentum is added to the cell entered by the mass, and that cell is given a new velocity equal to the new momentum divided by the new mass. Thus, the momentum transport term in Eq. (2-3) is taken into account. The process described conserves mass, internal energy, and momentum. However, it is possible to show that kinetic energy is always lost in this repartitioning process unless the velocities of the two cells involved are equal. This loss is accounted for by arbitrarily adding the loss in kinetic energy of the two cells to the internal energy of the entered cell. Thus, total energy is conserved but a small fraction of the kinetic energy is converted into internal energy in the process. This conversion may be shown to smear shock fronts in a manner similar to an artificial Landshoff type viscosity of the problem. The magnitude of the artificial viscosity introduced by the kinetic energy conversion is ideal in the sense that it spreads the shock jumps over about three mesh spaces.

The PIC numerical technique, involving two space dimensions and the time dimension, has been tested in numerous ways against both analytical one dimensional solutions, and also against spherically symmetrical one dimensional code solutions. These tests indicated that the method provides correct values of the jumps in pressure, density, and velocity across a shock, and also the correct shock velocities. This means that the entropy change across the shock is given correctly and thus the final state is correctly placed on the Hugoniot.

The problem shown in Figure 2-1 is typical of those which have been investigated with this hydrodynamic model. These problems have an axis of symmetry so that only two space variables are required to describe the process. It is necessary to use a projectile having cylindrical symmetry which has a velocity normal to a cylindrically-symmetric target.

2.2.3 Termination of Crater Growth

The phenomena occurring in the late stages of impact, particularly in the region of cratering flow, involve complex interactions between the characteristics of the material flow and the material properties. Since the upper target elements have higher velocities than those which are deeper into the target, a high degree of shearing distortion is produced. There exist no reported numerical calculations in which the entire cratering flow process is carried to completion. Indeed, a purely hydrodynamic analysis of this flow would be inappropriate, inasmuch as the cratering flow in the second phase of an impact occurs at a low pressure level, of the order of a few kilobars.

2.2.3.1 Dynamic Pressure-Target Strength Criteria

In this current research, as in a prior study (Bjork 1959), the approach used has been to carry out the hydrodynamic calculations until the isolated shock is clearly detached from the cratering flow region, and then to deduce the ultimate crater dimensions from the characteristics of the cratering flow at that point. Specifically, the deepest surface in the cratering flow region on which the dynamic pressure is equal to the yield stress of the material is taken to be the final crater depth. The results obtained are insensitive to the time chosen, since the dynamic pressure field in the cratering flow region is fairly stable over a long duration. A second region of high dynamic pressures will be found deeper in the target in the isolated shock. In the absence of severe shearing distortion, however, these dynamic pressures do not influence the crater formation.

Justification for the use of the dynamic pressure criteria for predicting crater depths is based upon consideration of the distortional processes occurring in the cratering flow. The hydrodynamic solutions which specify the cratering flow field just after breakaway of the isolated shock reveal that subsequent cratering flow will be in the incompressible regime. The thermodynamic pressure is very low because free surfaces are close by and there has been sufficient time for their presence to be felt in the medium. In addition, the dynamic pressure, $\frac{1}{2} \rho u_i u_i$, is on the order of a few kilobars. Although Bernoulli's law is not strictly applicable to this flow, the dynamic pressure provides a reasonable estimate of the highest pressures which could be produced in the flow (i.e., by suddenly stopping the flow). Thus maximum pressures on the order of only a few kilobars can arise, and the material compression will be on the order of 1% or less.

At the outset of the final cratering flow, a partial crater has been formed by the physical processes during the initial phase of the impact. Since the subsequent cratering flow is essentially incompressible, further crater growth must occur by plastic flow, in which only distortion of material elements occurs, with no volume change. More precisely, the deformation rate tensor is deviatoric. Knowledge of the initial cratering flow field together with the characteristics deduced above permits one to estimate the final crater dimensions.

For this purpose it is first assumed that the target material is elastic-plastic and follows the yield criterion of von Mises, namely

$$s_{ij} s_{ij} \leq 2/3 Y^2 \quad (2-5)$$

where Y is the yield stress in simple tension. Plastic strain in general tends to raise the yield stress, but at the high strain rates present in the process under consideration, the distortional strain energy raises the temperature and opposes this tendency. The combination of the two effects is represented to a first approximation by the linear relation

$$Y = Y_0 + ke \quad (2-6)$$

where Y_0 is the yield stress under normal conditions, e is the internal energy per unit volume, and k is a dimensionless constant.

Assume next that the deformation rate tensor varies slowly enough so that the stress keeps pace with it. Together with equation (2-5), this leads to the relation

$$s_{ij} = \frac{\sqrt{\frac{2}{3}} Y}{\sqrt{d_{mn} d_{mn}}} d_{ij} \quad (2-7)$$

where s_{ij} is the stress deviator, and d_{ij} is the deformation rate tensor (which the above physical arguments have shown to be deviatoric.)

Finally, elastic distortions are assumed negligible in comparison with the large plastic flows, so that the total strain is plastic, and its increment in time dt is given by

$$d\epsilon_{ij}^P = d_{ij} dt. \quad (2-8)$$

We may now use Eq. (2-7) and (2-8) to specify the energy dissipated by plastic work during dt :

$$de = s_{ij} d\epsilon_{ij}^P = Y \sqrt{\frac{2}{3} d_{ij} d_{ij}} dt. \quad (2-9)$$

By virtue of Eq. (2-8) this may be written as

$$de = Y d\bar{\epsilon}_P \quad (2-10)$$

where $d\bar{\epsilon}_P$, the increment of generalized plastic strain, is defined as

$$d\bar{\epsilon}_P = \sqrt{\frac{2}{3} d\epsilon_{ij}^P d\epsilon_{ij}^P} \quad (2-11)$$

Using the strain-dependent yield stress of Eq. (2-6), the energy per unit volume absorbed as plastic work by an element suffering generalized plastic-strain $\bar{\epsilon}_p$ is given by the solution of Eq. (2-10),

$$\bar{\epsilon}_p = \frac{1}{k} \ln \left(1 + \frac{ke}{Y_0} \right). \quad (2-12)$$

If one evaluates the constant, k , in Eq. (2-6) by assuming a linear decrease in yield stress from Y_0 to 0 over the energy increment e_m , (where e_m is the energy required to bring the material to the incipient melting condition), one obtains $k = -Y_0/e_m$. Eq. (2-12) then becomes

$$\bar{\epsilon}_p = - \frac{e_m}{Y_0} \ln \left(1 - \frac{e}{e_m} \right) \quad (2-13)$$

It is noteworthy that the generalized plastic strain becomes infinite when $e = e_m$. This reflects the physical fact that there is an upper bound on the energy which the element can absorb due to plastic work. Deformations which carry the element to the melting point destroy its ability to resist shear stress, and thus its ability to absorb plastic work.

However, another physical consideration even further limits the ability to absorb plastic work. It has been found in other studies conducted by the authors that material failure is closely correlated with the generalized plastic strain. For 2024-T3 aluminum, the critical value, $\bar{\epsilon}_p^*$, has been determined to be 0.30. When this value is attained, the material loses its ability to resist shear stress, which implies inability to absorb additional plastic work. Equation (2-13) shows that this implies that failure will occur when

$$e = e_m \left[1 - \exp \left\{ - \frac{Y_0 \bar{\epsilon}_p^*}{e_m} \right\} \right] \quad (2-14)$$

When $\frac{Y_0 \bar{\epsilon}_p^*}{e_m} \ll 1$, as it is for the target materials considered in the present study, Eq. (2-14) is well approximated by

$$e \cong Y_0 \bar{\epsilon}_p^*. \quad (2-15)$$

Now the kinetic energy per unit volume in the cratering flow is $1/2 \rho u_i u_i$, or precisely the dynamic pressure. When an element is finally brought to rest, its kinetic energy has been entirely dissipated. Part of the kinetic energy has gone into plastic work on the element itself, and part has been communicated to adjacent elements. The exact partition depends on the details of the flow, being governed specifically by the equations:

$$- \frac{d}{dt} \int_V \frac{1}{2} \rho u_i u_i dV = - \int_V (\sigma^{ij} u_i)_{,j} dV + \int_V \sigma^{ij} d_{ij} dV \quad (2-16)$$

where V is the volume of the element. The left hand side represents the rate at which the element loses kinetic energy and the terms on the right represent respectively the rate at which energy is communicated to external elements and the rate of plastic work on the element itself. Typically, the two integrals on the right are of the same order, so that the energy going into plastic work is about half of the initial kinetic energy. This approximately cancels the nominal values for the factor $\bar{\epsilon}_p^*$ appearing in Eq. (2-15), so that the final estimate of the conditions required to induce failure can be based on the equation

$$\frac{1}{2} \rho u_i u_i^i = Y_0 \quad (2-17)$$

The deepest surface in the cratering flow region on which the dynamic pressure is equal to the ultimate strength of the material can thus be taken to be the final crater depth.

It is recognized that this interpretation represents an oversimplification of the complex physical interactions between material in motion and adjacent quasi-static material. The dynamic pressure criteria, however, represents at least a first approximation of material strength effects in cratering, and this criterion can readily be used in hydrodynamic solutions.* We find that the crater predictions obtained with this criterion are insensitive to the exact strength properties chosen, inasmuch as the dynamic pressure gradients are quite steep near the periphery of the cratering flow field.

Figure 2-2 is a representative dynamic pressure field, showing 1.5, 3.0, and 4.5 kilobar dynamic pressure contours at $t = 84.8 \mu\text{sec}$ after impact of a porous aluminum projectile into iron at 72 km/sec. Note the two major regions of high dynamic pressure. In the isolated shock (extending at $t = 84.8 \mu\text{sec}$ from depths of about 42 to 56 cm), the dynamic pressure remains high due to the particle velocities associated with the extreme pressures. As can be seen in Figure 2-2, the leading surface of this shock is nearly hemispherical, and it produces a uniform divergence of material as the wave propagates further into the target. Shearing distortion is small, and the isolated shock wave has no effect on the cratering at this late time.

The second region of high dynamic pressures in Figure 2-2 is in the cratering flow, extending from depths of about 16 to 30 cm. Whereas the isolated shock is propagating deeper into the target, the location of the cratering flow region is stable. The high dynamic pressure in this region is due to kinetic energy of the convecting material. It is in this region of high shear distortion that the final crater is formed. To predict the crater depth, the maximum depth in the cratering flow field where the dynamic pressure corresponds to the material strength is determined. Using a nominal strength criteria of 4.5 kilobars ($\sim 65,000$ psi) for structural steels, the predicted crater dimensions in this impact will correspond with the 4.5 kb contour. A heavy dashed curve

*Footnote: See Section 2.2.5 for comments regarding a rigorous elastic-plastic numerical technique which has recently been developed.

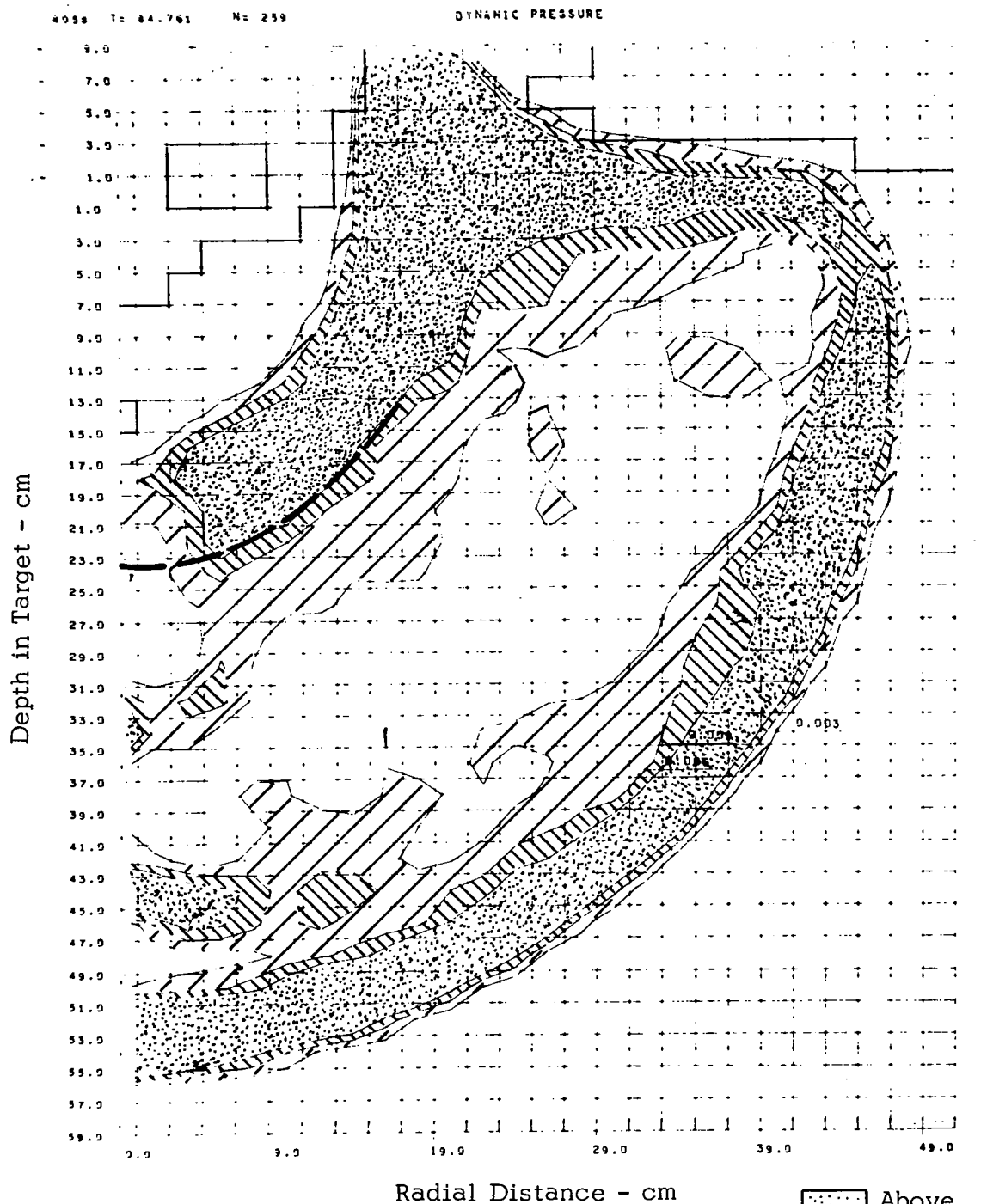


FIGURE 2-2
DYNAMIC PRESSURE CONTOURS
(1.5, 3.0, 4.5 KB) AT 84.8 μ SEC
Case 8058 - Porous Aluminum
vs Iron at 72 km/sec

has been superimposed on the plot at this level. (Near the axis of symmetry, the numerical solution at late times produced somewhat distorted contours over a limited region. The reality of these boundary effects has not been fully evaluated, but in any event they are ignored in cratering predictions because the region involved is quite small.)

Figure 2-3 shows the dynamic pressure and the compression ratio (ρ/ρ_0) plotted as functions of depth in the target at $t = 103 \mu\text{sec}$ after the impact of porous aluminum projectile into aluminum at 72 km/sec. This plot is made at an offset distance of 10 cm from the axis to avoid minor oscillations which occur near the axis. The two major regions of high dynamic pressure are again evident in the isolated shock and in the cratering flow.

Using a nominal value of material strength for aluminum alloys of 2 kb ($\sim 29,000$ psi) would lead to a prediction of about 42 cm for the crater depth, since that is the depth to which dynamic pressures greater than 2 kb extend in the cratering flow field.

As noted, the analysis of the dynamic pressure field is made after the cratering flow reaches a relatively stable maximum extent. Figure 2-4 gives a comparison of plots of dynamic pressure at $t = 122 \mu\text{sec}$ and $t = 141 \mu\text{sec}$ to illustrate this stability. To the right in these plots, the target shock is seen to move progressively to greater depths. The high dynamic pressure in the cratering flow, however, remains centered at about 34 cm. With increasing time, the dynamic pressure levels in this region are seen to drop, and the depths which are experiencing a given level of dynamic pressure recede.

In Figure 2-4, a smaller "secondary" shock is apparent between the isolated shock and the cratering flow region. This shock propagates with sonic velocity behind the primary shock. Secondary shocks of this type can always be distinguished from the cratering flow region, since the shocks propagate at speeds close to sonic, whereas the cratering flow region is stable. Between the secondary shock and the cratering flow, an expanding, relatively quiescent region is observed. Experimental evidence for such an intermediate region is seen in impacts on relatively thick targets, where the isolated shock produces spallation and/or bulging of the rear surface, while nevertheless being separated from the front surface crater by a thickness of solid, competent material.

2.2.3.2 Target Heating and Melting Effects

In the preceding illustrations of the termination of crater growth, a fixed nominal value of material strength was assumed. In the current program, a technique was implemented that specifically incorporates the effects of shock heating upon the material properties.

Irreversible work leaves the target material through which the target shock has propagated in a heated state. If the peak shock pressure experienced by a target element is sufficiently high (about 650 kb in aluminum or 1.8 mb in iron) at least a portion of the material will be left in a melted state. The effects of such heating will be to reduce the target strength in the cratering flow region. Where melting occurs, the strength drops to zero.

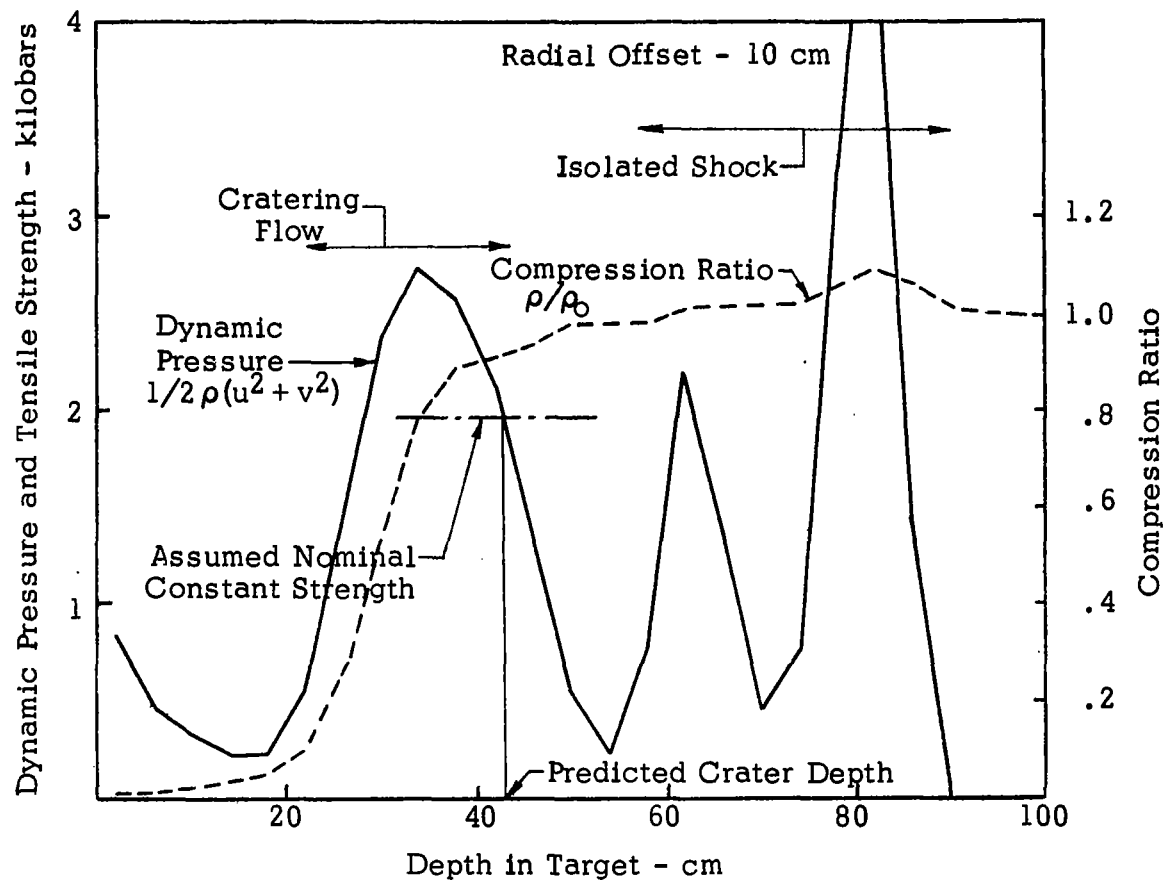


FIGURE 2-3
 USE OF DYNAMIC PRESSURE PROFILE
 FOR PREDICTION OF CRATER DEPTH,
 ASSUMING CONSTANT TARGET STRENGTH OF 2KB
 Case 8052 - Porous Aluminum ($\rho = 0.44$)
 vs Aluminum at 72 km/sec
 at $t = 103.2$ Microseconds

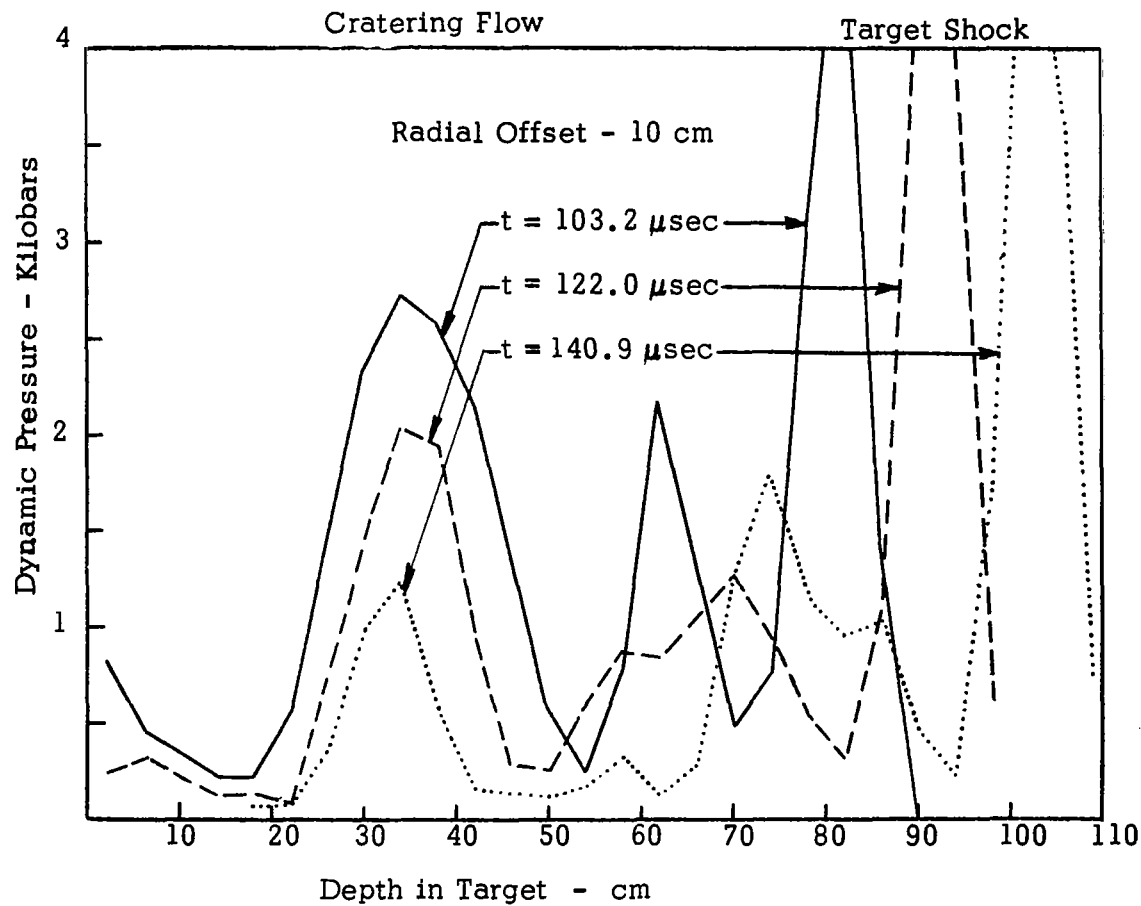


FIGURE 2-4
DYNAMIC PRESSURE PROFILES AT THREE SUCCESSIVE TIMES

Case 8052 - Porous Aluminum ($\rho = 0.44$) vs Aluminum
at 72 km/sec.

Since the penetration predictions in this study are based upon comparing the dynamic pressure with the target material strength, it is important to determine the extent to which target heating influences the predictions, and to include these effects if they are significant. Such an analysis requires detailed consideration of the dynamic pressure and temperature profiles, as well as the variations in target strength with temperature.

a. Residual Temperatures - To determine the residual temperature profiles after passage of a strong shock, it is not sufficient to consider only the peak pressures to which the target elements have been subjected. One must also determine the spatial displacement of these elements which is induced by the shock. To illustrate, consider a target element at a certain depth which is acted upon by a shock. The initial interaction raises the element to a high pressure, temperature, and density, and imparts a particle velocity to it, causing the element to be displaced deeper into the target. As the pressure decays behind the shock, the velocity of the element is decelerated, and it simultaneously undergoes isentropic expansion. This process continues until the element attains essentially zero pressure and its temperature becomes the release temperature which is characteristic of the peak shock pressure.

In this process the element has moved from its initial position, the amount of the displacement depending on both the peak pressure and the duration of the high pressure. Outside of the cratering flow region, the displacements are relatively small, and have only a minor effect upon the residual temperature fields. In the cratering flow, the target elements not only are subjected to higher peak pressures which cause greater displacements, but they retain a sensible velocity even after the pressure drops and the release temperature has been attained. This difference in residual velocities forms one basis for defining the cratering flow region. After dropping to small pressures, elements in the cratering flow retain their individual release temperatures, but move with the flow such that the energy and temperature fields continue to change.

Figure 2-5 shows the specific internal energy profile as a function of depth at 103 μ sec after impact of a porous aluminum projectile into aluminum at 72 km/sec (Case 8052). This profile reflects the combined effects of shock heating and the convection, or displacement, of the target elements occurring during passage of the shock wave. The specific internal energy in the isolated shock appears to the right in Figure 2-5. Of course the latter energies are not of the release state, but rather are representative of elements in the process of expanding from the initial state in the shock. The release energies of these elements will be small, as can be seen in Figure 2-6, which plots the specific internal energy profile vs depth for the same impact problem at 141 μ sec after impact. At 103 μ sec (Figure 2-5), the elements between depths of 78 and 90 cm are in the isolated shock and consequently have high energies. At 141 μ sec (Figure 2-6), these same elements (between 78 and 90) have attained the release state and have only small energies. Since the shock pressure is relatively low at this depth in the target, only a minor displacement of the particles is induced, which has an insignificant effect on the energy profile.

Specific internal energies can be directly converted into temperatures by use of the values in Tables B-1 and B-2 in Appendix B. Temperature values obtained by this means are flagged at the appropriate energy levels in Figures 2-5 and 2-6. The magnitude of the change in residual temperature fields which

can be attributed to the displacement of the heated elements is seen by noting the depths at which melting occurs. The deepest point in the target for Case 8052 which is reached by the 650 kb shock pressure required to melt aluminum is about 31 cm. Melted particles initially at this depth, however, are displaced to a depth of 37 cm by the shock pulse. Residual melting will therefore extend to a depth of 37 cm.

b. Residual Strength - By combining data showing residual temperature in the target as a function of depth with the target material strength as a function of temperature, one can estimate the residual strength at various depths in the target. This information can be directly incorporated into the material strength criteria described in Section 2.2.3. The process is illustrated in Figure 2-7, in which the residual temperature profile is superimposed on the dynamic pressure plot for Case 8052. Using the relationship of strength with temperature for 2024-T3 aluminum which is given in Table B-1 in Appendix B, the residual strength in the target as a function of depth is also superimposed on the dynamic pressure profile. The predicted crater depth is taken as the depth for which the local strength is equivalent to the dynamic pressure (i.e., where the residual strength and dynamic pressure profiles cross), at a depth of 42.8 cm.

The importance of temperature softening is evident from the observation that the local strength at the predicted crater depth was less than 60% of the nominal room temperature strength in the target material. For all of the impacts considered in this program, the residual temperature gradients were relatively steep in the regions near the crater depths. The temperature dependence of strength has therefore been included in the cratering predictions. In this program, we used the properties for 2024-T3 aluminum and Type 301 full-hard stainless steel, as given in Tables B-1 and B-2, to represent structural alloys of aluminum and steel respectively. Predictions for other alloys can be obtained by substituting the strength vs temperature characteristics for these alloys in the above tabulations. The properties used are from essentially static tests. Properties under dynamic loading would, of course, be preferable, but these were not available for high temperature conditions.

c. Target Melting - In some impacts, the temperature gradient (and hence strength gradient) in the target is very steep, so that the melted region encompasses nearly all of the predicted crater volume. In such cases, the melting phenomena may be considered to essentially dominate the crater formation, and the melted depth becomes a good approximation of the crater depth. In an earlier study (Bjork 1963) melting was found to dominate crater formation in aluminum-aluminum and iron-iron impacts at 72 km/sec.

In the current research, the technique described above, by which the temperature dependence of strength is included in the cratering predictions, automatically incorporates the effect of melting. The difference between the strength-determined crater depths and the maximum depths at which residual melting occurs is a good indication of the influence of melting upon the crater formation. Where the melted region extends close to the ultimate crater depth, the surface of the crater will be formed through high temperature, very ductile flow of the materials. Thus even in relatively brittle targets, the crater surface in melt-dominated cases will be smooth, more in the nature of craters in 1100 aluminum alloys.

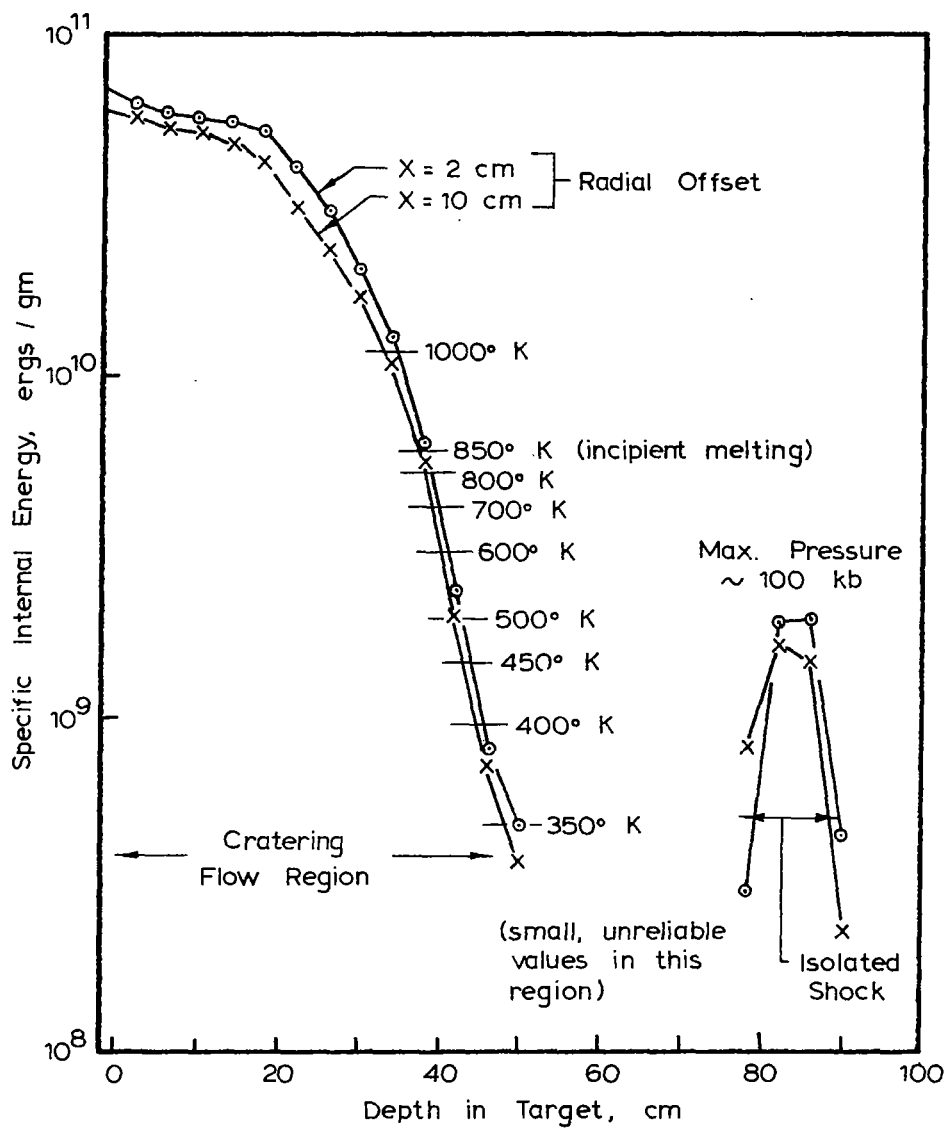


FIGURE 2-5
 SPECIFIC INTERNAL ENERGY PROFILES
 103.2 MICROSECONDS AFTER IMPACT
 CASE 8052 - POROUS ALUMINUM ($\rho = 0.44$)
 VS. ALUMINUM AT 72 KM/SEC

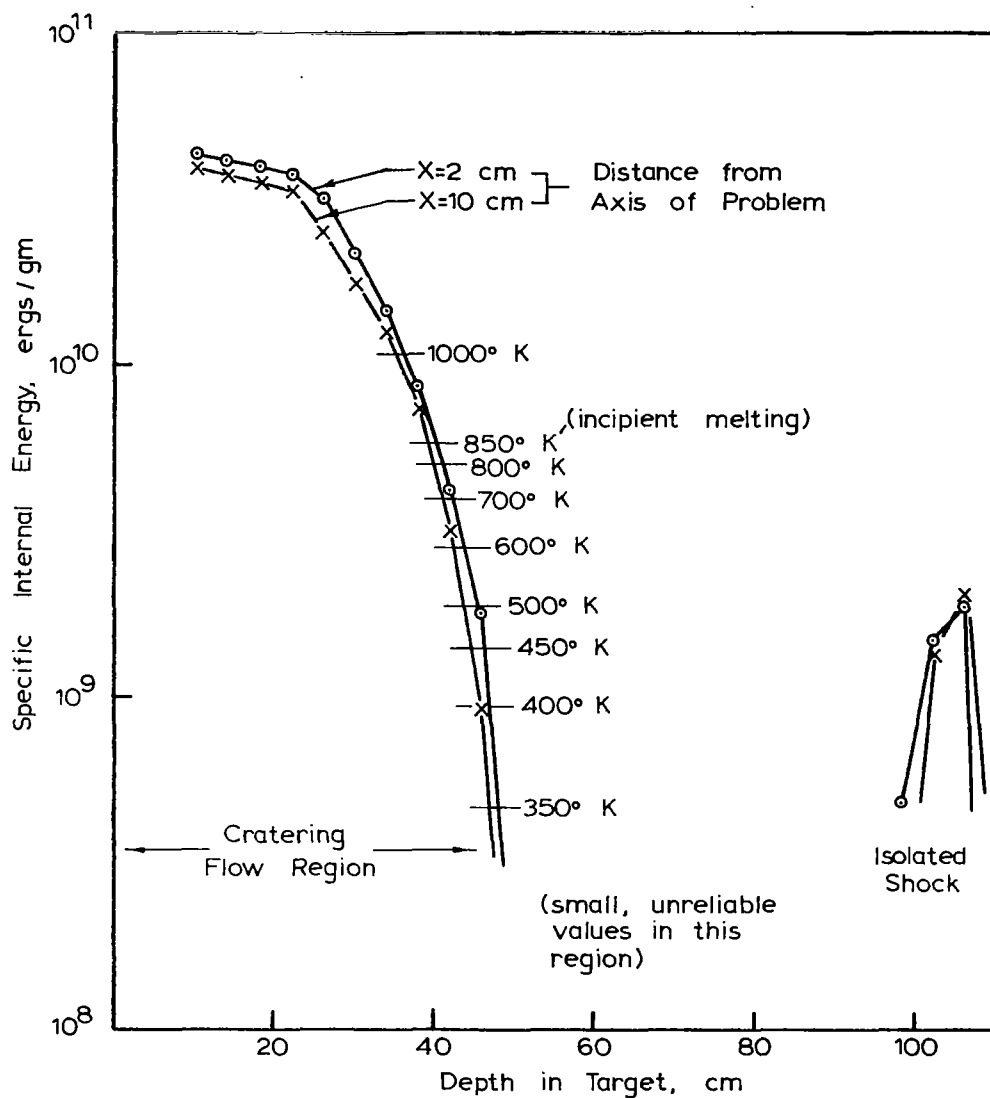


FIGURE 2-6
 SPECIFIC INTERNAL ENERGY PROFILES
 140.9 MICROSECONDS AFTER IMPACT
 CASE 8052 - POROUS ALUMINUM ($\rho = 0.44$)
 VS. ALUMINUM AT 72 KM / SEC

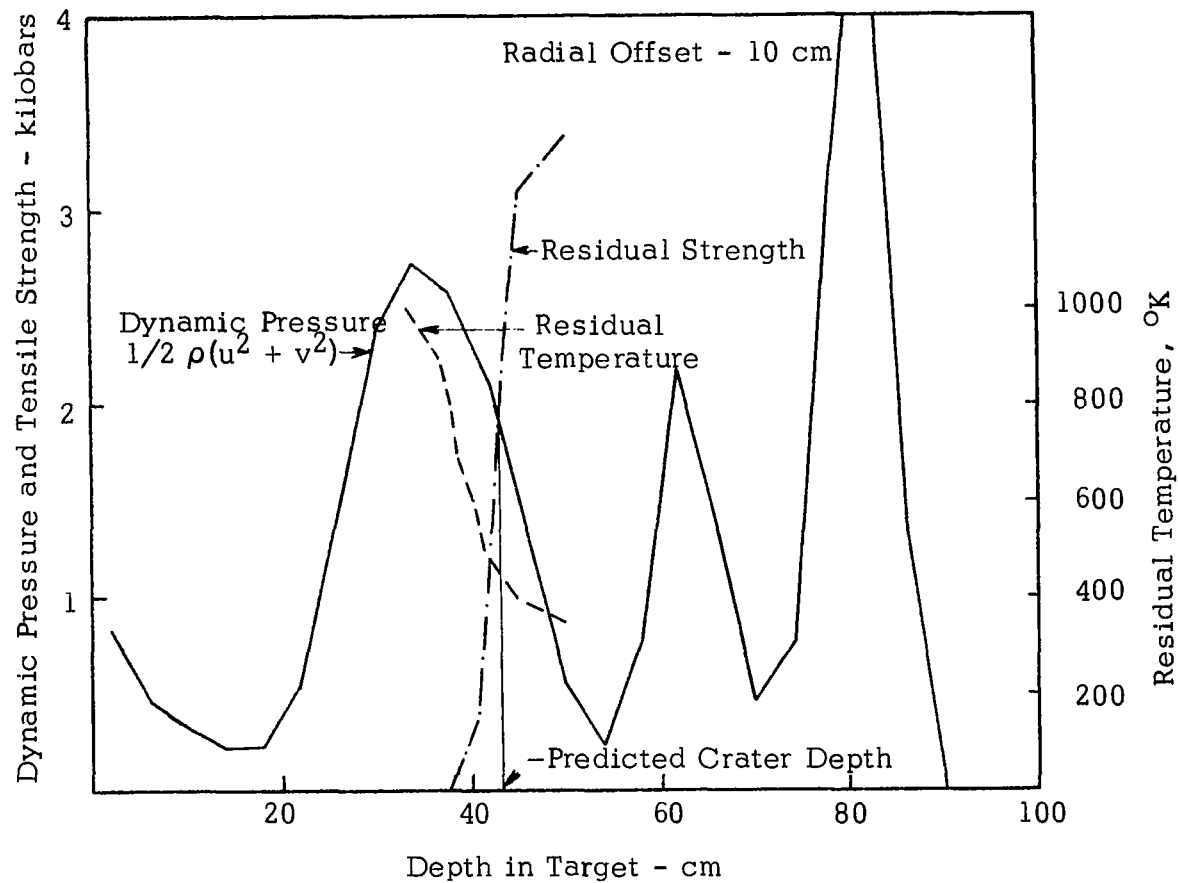


FIGURE 2-7
 MODIFIED TECHNIQUE FOR CRATER DEPTH PREDICTIONS
 INCORPORATING THERMAL DEGRADATION
 OF TARGET STRENGTH
 Case 8052 - Porous Aluminum ($\rho = 0.44$)
 vs Aluminum at 72 km/sec
 at $t = 103.2$ Microseconds

2.2.4 Perforation of Finite Targets

The above discussions have been primarily concerned with cratering produced by impacts into semi-infinite targets. A relationship between such cratering and the perforation of finite targets is necessary in order to assess the hazards of meteoroid impacts to a space vehicle.

Marginal perforation of a finite target is a case which is pertinent to this study. Such perforation does not occur due to direct growth of the primary crater. Rather, the threshold occurs when relatively severe material damage at the rear surface of the target merges with the crater expansion from the front. Thus, the hole which forms is a combination of a truncated crater on the front surface with a spall layer on the rear surface.

In a finite target near the ballistic limit, the target shock interacts with the rear free surface before it completely disengages from the cratering flow. In addition to the free surfaces at the front of the target and in the projectile, this provides another source of rarefactions which propagate into the interaction region. Thus the pressure in the interaction zone drops more rapidly in a finite target than in a semi-infinite target. The lateral cratering flow is arrested more quickly, resulting in a crater of smaller diameter. However, the downward cratering flow is less impeded so that the crater is deeper.

Damage to the rear surface of the target is caused by interactions of the incident target shock with the rarefaction wave. These interactions produce a strong net tension within the target, which will cause spallation or scabbing to occur if the material failure criterion is exceeded. The stress level for onset of such spallation, as well as the characteristics of the spall, are determined by the material properties. Generally, a ductile material will form a relatively smooth scab layer which will adhere to the parent material around its periphery. If the impulse absorbed during formation of the spall is sufficiently high, the scab may either petal open, or it may break off around its periphery, forming a high velocity fragment. Such spalling may or may not be accompanied by complete perforation of the target. If a significant thickness of target remains between the bottom of the crater and the spall zone, perforation does not occur. Otherwise, the downward cratering flow persists, general collapse in the region results, and an opening is produced.

In brittle materials, the spall which forms is more likely to quickly fracture around its periphery away from the target, and collapse of the material between the spall zone and the crater bottom tends to be more catastrophic.

The stresses which cause spallation and subsequent fracture and perforation under conditions of marginal perforation are usually assumed to be comparable to the ultimate strength of the material. The hydrodynamic model is therefore not applicable to an analysis of these processes. Clearly, a suitable plastic-elastic model, coupled with experimentally determined fracture criteria, is needed for such analyses. For this purpose, a numerical technique which rigorously treats material deformation and flow on a plastic-elastic model has recently been developed under another NASA contract.

For purposes of the current study of the meteoroid hazard, we have chosen to apply a factor of 1.4 to the crater depths calculated for semi-infinite targets to establish the thickness of a finite target which will be marginally perforated. As more accurate perforation criteria are obtained from the plastic-elastic solutions mentioned above, it will be readily possible to refine the perforation probabilities which are given in this report.

2.2.5 Elastic-Plastic Considerations

As has been emphasized in the preceding sections, the cratering flow phase of the impact process occurs at relatively low stress levels, so that the lateral extent of the accessible region in stress space (as discussed in Section 2.2.1) may be comparable with the stress itself. Hence the material strength may be expected to make significant contributions to the cratering flow.

Under these circumstances, the hydrodynamic model is no longer a valid representation of the processes involved. The computation of the final stages of crater formation is based on dynamic pressure, which represents an approximation of the true physical process. Justification for this approximation is found in the agreement which has been obtained between the crater predictions obtained from the code solutions and experiments which have been conducted for similar impacts.

Notwithstanding the apparent adequacy of the hydrodynamic code for limited analysis of cratering flow, it is evident that an elastic-plastic model is needed to rigorously describe the final response of the target, especially in the computation of marginal perforation of metallic sheets and plates by high speed particles. The development and utilization of a numerical technique based upon such a model was not a part of this current study. However, we have recently developed, under another NASA contract, a comprehensive numerical technique which will permit detailed analysis of the hydrodynamic, plastic, and elastic phenomena in impacts against homogeneous targets. This technique contains the capability of treating yield stress as a function of the material state, including temperature. It is clear that this is necessary in view of the preconditioning by the isolated shock of the material in which the cratering flow occurs. Since this flow occurs at low pressure levels, the material parameters must be determined by experiments in the same stress regime that the flow takes place.

2.2.6 Oblique Incidence

For a vehicle in a uniform, omnidirectional meteoroid flux, a meteoroid velocity vector has an equal probability of coming from any direction. This gives rise to a distribution of impact angles on the surface of a randomly-oriented or tumbling vehicle wherein the probability of an impact occurring at an angle with the surface greater than θ is equal to $\cos \theta$. The average, and also the most probable angle, is thus 45° .

Existing hydrodynamic codes are limited to analysis of problems which can be described in two space dimensions. These include three dimensional cases where the geometry has an axis of symmetry, such as the normal impact of a symmetrical, oriented projectile on a planar or symmetrical target.

Oblique incidence impacts cannot be described in two dimensions, and are therefore not amenable to rigorous analysis by existing codes. Approximate solutions of oblique impact problems have been obtained by Kreyenhagen, Bjork and Brooks (1965) by assuming a planar geometry (i.e., impact of a sphere is simulated by an infinitely long rod impacting on its side). While this technique gives solutions which are qualitatively similar to experimental observations, they cannot be used for quantitative penetration predictions.

For this study, the simplifying assumption has been made that the effect of oblique incidence is primarily to increase the effective thickness of the target to be penetrated - a reasonable approximation at all but the most severe obliquities. At the average angle of obliquity of 45° , the target thickness is effectively increased by a factor of 1.4. This factor, when divided into the penetration predictions obtained from the numerical analyses of normal impacts, results in cancellation of the adjustment constant used to convert penetration depths in semi-infinite targets into the threshold thickness for perforation of finite targets.

A three-dimensional numerical program is currently under development which will remove the necessity for estimating or approximating significant effects operating in oblique incidence impacts.

2.3 The Equation of State of Aluminum

For hydrodynamic solutions, material characteristics are completely specified by their equations of state. The equation of state for aluminum was used to simulate a typical stony meteoroid material both in the solid and porous states. This substitution is consistent with the similarities of measured Hugoniot of aluminum and some important types of rocks, and permitted us to make use of the very considerable experimental and theoretical data which exists for aluminum.

Existing formulations of the aluminum equation of state had been derived with emphasis on the Hugoniot of aluminum centered at normal density. Thus it was quite inaccurate for states far from the normal Hugoniot which may be achieved in the case of porous aluminum impacts. It was therefore necessary to revise the aluminum equation of state to include the important information derived by Russian experiments involving the shocking of porous aluminum samples. The details of the revision are presented in Appendix A. The resulting equation of state represents one of the most complete specifications currently available for any material.

SECTION 3

DESCRIPTION OF CURRENT NUMERICAL SOLUTIONS

3.1 Selection of Cases

Using the two-dimensional numerical techniques described in the prior section, eight representative meteoroid impact cases were analyzed. These cases are summarized in Table 3-1. Selection of the conditions for these cases was based upon the considerations outlined in the following paragraphs.

TABLE 3-1: IMPACT CONDITIONS FOR HYDRODYNAMICS CALCULATIONS

Numerals in parentheses refer to case numbers. Cases 8051-8058 were analyzed during this program. Cases 9-14 were previously analyzed and published in Bjork (1959). Cases 11 and 14 were subsequently revised to include melting effects in Bjork (1963) and Bjork and Olshaker (1965).

<div style="text-align: center;"> <div>Projectile</div> <div>Target</div> </div>	Aluminum (simulating solid stony meteoroids)	Iron (simulating high density meteoroids)	Porous Aluminum, $\rho=0.44$ (simulating porous stony meteoroids)
Aluminum	5.5 km/sec (9) 20 km/sec (10) 72 km/sec (11)	20 km/sec (8053) 72 km/sec (8054)	20 km/sec (8051) 72 km/sec (8052)
Iron (steel)	20 km/sec (8055) 72 km/sec (8056)	5.5 km/sec (12) 20 km/sec (13) 72 km/sec (14)	20 km/sec (8057) 72 km/sec (8058)

3.1.1 Target Materials

The objective of this program was to evaluate the perforative hazard posed to space vehicles by meteoroids. 2024-T3 aluminum and type 301 stainless steel, two commonly used materials, were therefore selected for the study. The results can readily be converted to other aluminum or steel alloys.

3.1.2 Impact Velocities

Geocentric velocities of meteoroids in the vicinity of the earth range between 11 and 72 km/sec. The velocity with which a meteoroid strikes a vehicle is the vector difference between the geocentric velocities of the meteoroid and of the vehicle. Knowledge regarding the distribution of meteoroid velocities within this range is very tenuous at present, but most meteors are believed to have velocities at the low end of the scale, near 20 km/sec. This velocity was therefore chosen as one to be considered in the study. 72 km/sec is near the

high end of the possible velocity range, and was chosen in order to assess whether new types of impact response occur at high velocities. Velocities up to 9 or 10 km/sec are accessible in the laboratory. Interpolation should provide sufficiently accurate data in the velocity range between 10 and 20 km/sec.

3.1.3 Meteoroid Densities

Three meteoroid densities, 0.44, 2.7 and 7.86 gm/cm³ were considered. When these densities were selected early in the program, 0.44 gm/cm³ represented the best estimate given by meteor astronomers for the density of porous, cometary meteors (Whipple, 1963). Recent estimates, as discussed in Section 4.1, suggest that 0.26 gm/cm³ is a more pertinent value. Fortunately, it is felt that extrapolation of the present results from 0.44 to 0.26 gm/cm³ can be conducted with reasonable accuracy. The density of 2.7 was chosen as characteristic of the solid, stony meteorite finds. The density of 7.86 is that of iron, intended to be representative of postulated asteroidal meteoroids. (Recent data, also outlined in Section 4, indicate that asteroidal meteoroids occur only rarely, and are hence not likely to constitute a significant hazard.)

3.1.4 Use of Prior Calculations

Table 3-1 includes six prior calculations which have been conducted, using the hydrodynamic model, to analyze impacts at 5.5, 20, and 72 km/sec (Bjork 1959 and 1963). To the maximum extent possible, pertinent aspects of these results have been incorporated into this investigation in order to provide information over the wide range of material densities and velocities which are involved in the meteoroid hazard problem.

The technique used in obtaining cratering predictions in the earlier calculations differed from the current method, in that the effects of residual target temperature upon strength were not considered (except in the extreme case of melting). Incorporation of temperature effects in the earlier calculations would increase the cratering predictions for those cases where significant thermal degradation of target strength occurs in the region just under the predicted crater depth. The original predictions are nonetheless considered to be useful in this meteoroid hazard investigation.

No other prior calculations of crater dimensions in this velocity range have been published. In Appendix D, the hydrodynamic computations conducted by Walsh (1965) and Riney (1965) are discussed. These investigators stopped short of using the computations to predict crater dimensions. Rather, they predict the rate at which penetration varies with velocity. The assumptions which are inherent in these relationships, and the necessary normalization of the relationships with experimental points are discussed in Appendix D.

3.2 Numerical Results

Appendix C contains detailed plots of the numerical calculations, including sequences showing the development of mass positions and velocity and pressure fields for each impact case. Appendix B contains the dynamic pressure profiles and specific internal energy profiles at late times for each problem, and shows how each cratering penetration prediction was obtained.

Table 3-2 summarizes important aspects of the computational results obtained from the eight current impact analyses. Results of the six earlier calculations are also included. (Energy and momentum partitions were not made in the earlier cases, so these data are not available for inclusions in the Table.)

3.2.1 Initial Conditions

Physical dimensions used in this table are those of the gram-centimeter-microsecond system. Lines 1-5 specify the impact conditions. Lines 6-11 tabulate the initial conditions which exist in the one-dimensional shocked portions of the projectile and target immediately after impact. Pressure and particle velocity are the same in both the projectile and target regions engulfed by this state, but where the projectile and target are of dissimilar materials (Cases 8051 - 8058), they undergo different compressions (ρ/ρ_0) and contain different specific internal energies. The initial density, ρ_0 , used to determine compression is that of the parent material. Thus in the case of porous aluminum projectiles, ρ_0 is taken to be 2.7 gm/cm^3 , even though the bulk density is 0.44 gm/cm^3 .

3.2.2 Penetration Predictions

Lines 12 and 13 concern the penetration predictions, as obtained from the hydrodynamic solutions by application of the dynamic pressure = material strength criterion to the late stage cratering flow region. Application of this criterion, and the subsequent derivation of penetration predictions are shown in detail for each impact case in the current study in the figures in Appendix B.

Line 12 tabulates the dimensionless quantity P/d , or penetration divided by the projectile's diameter. 10 cm x 10 cm cylinders were used in all problems, but the numerical results scale with linear dimensions.

Line 13 shows the penetrations normalized to the cube root of projectile mass ($P/m^{1/3}$). Line 14 is the approximate volumetric efficiency of the impacts, (crater volume per unit incident kinetic energy) assuming hemispherical craters. This is not exact, inasmuch as some departure from the hemispherical shape occurs, especially in impacts between materials of different densities. However, the hemispherical assumption is sufficient for nominal comparisons.

Lines 15 and 16 contain data regarding the extent of residual melting in the cratering. These data are discussed in Section 3.3.3.2.

3.2.3 Energy and Momentum Partitions

Lines 17-27 show the energy and momentum partitions, normalized by dividing the pertinent values by the energy or momentum of the incident projectiles. The partition is made into three regions. Region I encompasses the isolated shock. Region II contains the material involved in the cratering flow, plus the portion of the ejecta material which remains below the original surface of the target. Region III is that portion of the material which is above the

TABLE 3-2: SUMMARY OF RESULTS OF IMPACT CALCULATIONS

IMPACT CONDITIONS ↓	Impact Case No. →	Current Calculations			
		8051	8052	8053	8054
1. Projectile Material		P-Al	P-Al	Fe	Fe
2. Projectile Bulk Density (gm/cm ³)		.44	.44	7.86	7.86
3. Impact Velocity (cm/μsec)		2.0	7.2	2.0	7.2
4. Target Material		Al	Al	Al	Al
5. Target Density (gm/cm ³)		2.7	2.7	2.7	2.7
INITIAL (1-D) CONDITIONS					
6. Pressure (megabars)		1.36	15.3	7.75	76.8
7. Particle Velocity (cm/μsec)		.446	1.42	1.32	4.64
8. Projectile Compression, ρ/ρ_0		.743	.821	1.89	3.02
9. Projectile Specific Internal Energy (10 ¹² ergs/gm)		1.21	13.9	.232	3.27
10. Target Compression, ρ/ρ_0		1.65	2.87	2.54	4.13
11. Target Specific Internal Energy (10 ¹² ergs/gm)		.0995	1.84	.870	10.8
PENETRATION PREDICTIONS					
12. Penetration/Projectile Diameter, P/d		2.0	4.3	5.8	12.0
13. Penetration/(Projectile Mass) ^{1/3} P/m ^{1/3} (cm/gm ^{1/3})		2.8	6.1	3.2	6.6
14. Crater Volume/Projectile Energy, Ω/E (cm ³ × 10 ¹² /erg)		23	18	34	23
15. Residual Melt Depth/Projectile Diameter, D _m /d		1.7	3.7	5.5	10.6
16. Residual Melt Depth/Crater Depth (or Penetration), D _m /P		.84	.87	.94	.88
NORMALIZED PARAMETERS					
REGION I - ISOLATED SHOCK					
17. Kinetic Energy		.304	.234	.447	.279
18. Internal Energy		.068	.061	.114	.117
19. Axial Momentum		5.68	17.7	4.49	11.5
20. Radial Momentum		10.8	28.6	10.1	22.7
REGION II - CRATERING FLOW AND ADJACENT EJECTA					
21. Kinetic Energy		.181	.180	.219	.169
22. Internal Energy		.009	.009	.054	.085
23. Axial Momentum		-2.32	-9.21	-1.57	-3.49
24. Radial Momentum		4.11	12.1	4.6	13.6
REGION III - EJECTA ABOVE TARGET					
25. Kinetic and Internal Energy		.438	.516	.166	.350
26. Axial Momentum		-2.36	-7.47	-1.92	-7.01

TABLE 3-2 (Con't): SUMMARY OF RESULTS OF IMPACT CALCULATIONS

Current Calculations				Prior Research					
8055	8056	8057	8058	0009	0010	0011	0012	0013	0014
1. Al	Al	P-Al	P-Al	Al	Al	Al	Fe	Fe	Fe
2. 2.7	2.7	.44	.44	2.7	2.7	2.7	7.86	7.86	7.86
3. 2.0	7.2	2.0	7.2	.55	2.7	7.2	.55	2.7	7.2
4. Fe	Fe	Fe	Fe	Al	Al	Al	Fe	Fe	Fe
5. 7.86	7.86	7.86	7.86	2.7	2.7	2.7	7.86	7.86	7.86
6. 7.75	76.8	1.70	19.6	.682	4.88	47.3	1.81	14.9	143
7. .681	2.56	.251	1.17	.275	1.00	3.60	.275	1.00	3.60
8. 2.54	4.13	.782	.886	1.43	2.24	3.85	1.49	2.12	3.48
9. .870	10.8	1.53	18.2	.0378	.500	6.48	.0378	.500	6.48
10. 1.89	3.02	1.41	2.22	1.43	2.24	3.85	1.49	2.12	3.48
11. .232	3.27	.0315	.684	.0378	.500	6.48	.0378	.500	6.48
12. 2.7	4.9	.97	2.5	2.5	4.0	7.8	2.0	3.0	8.0
13. 2.1	3.8	1.4	3.6	1.9	3.1	6.1	1.1	1.6	4.4
14. 9.9	4.4	2.7	3.8	102	32	18	18	9.3	6.7
15. 2.3	4.4	.77	2.3						
16. .85	.90	.80	.90						
17. .218	.117	.104	.047						
18. .103	.074	.079	.067						
19. 7.87	7.11	2.73	6.31						
20. 13.9	13.8	4.60	11.7						
21. .099	.049	.070	.050						
22. .191	.387	.155	.214						
23. -3.81	-2.28	-.38	-2.28						
24. 4.78	6.38	2.86	5.39						
25. .389	.373	.592	.622						
26. -3.06	-3.83	-1.35	-3.03						

original target surface. The material in Region III is effectively decoupled from the cratering process. It consists, to a large extent, of ejecta which has been propelled away from the target at a velocity which is higher than the Region II material which follows, thus precluding further influence upon the cratering motion.

Delineation of the three regions is shown in the final velocity field plot for each impact case in Appendix C. Boundaries between the isolated shock and the cratering flow regions were established in the relatively inactive zones separating these regions. Thus the energy and momentum partitions are insensitive to the somewhat arbitrary locations of the boundaries.

The normalized energies in Lines 17, 18, 21, 22, and 25 represent the kinetic and internal energy in the given region divided by the initial kinetic energy of the projectile. Energy conservation dictates that the sum of these values be unity. The axial and radial momenta are normalized by the initial momentum of the projectile. To conserve momentum, the sum of the normalized axial momenta (lines 19, 23, and 26) must also be unity. The axial symmetry of the solution causes the radial momentum to sum to zero automatically, so that no conservation law is available for this quantity.

All of the axial momentum in the isolated shock (Region I) will be imparted to the semi-infinite target, inasmuch as no physical mechanism exists by which the momentum in this isolated pulse can be reduced or transferred. In addition to the axial momentum in the isolated shock (line 19) further axial momentum can subsequently be imparted to the target by upward diversion of material in Region II. For example, if a downward-moving element of Region II were diverted to move upward, twice its current axial momentum would be imparted to the target. Similarly, the pressure generated when radially moving elements are decelerated causes vertical accelerations. If the upward-accelerated material escapes from the crater, the target ultimately receives an additional net increment of axial momentum. Hence the axial momentum given in line 19 represents a lower bound on the axial momentum the target will ultimately receive.

3.3 Discussion and Interpretation of Important Features

3.3.1 Penetration vs Density and Velocity

Figures 3-1 and 3-2 summarize the penetration predictions obtained from the eight current calculations, supplemented by the results of the six prior hydrodynamic solutions of impact problems. Shown in these figures are points representing crater depth predictions for the specific impact conditions considered. These points are connected with straight lines which can be used, subject to the cautions discussed below, for interpolation to conditions other than those which have been analyzed specifically.

The ordinate in these figures is the parameter $P/m^{1/3}$ in units of $\text{cm/gm}^{1/3}$, representing the ratio of penetration to the cube root of the projectile mass. These curves can be applied to projectiles of any mass, provided that the flow is not influenced in an important way by strain rate or viscous terms, or by unusual projectile geometrical effects. Viscous and strain rate

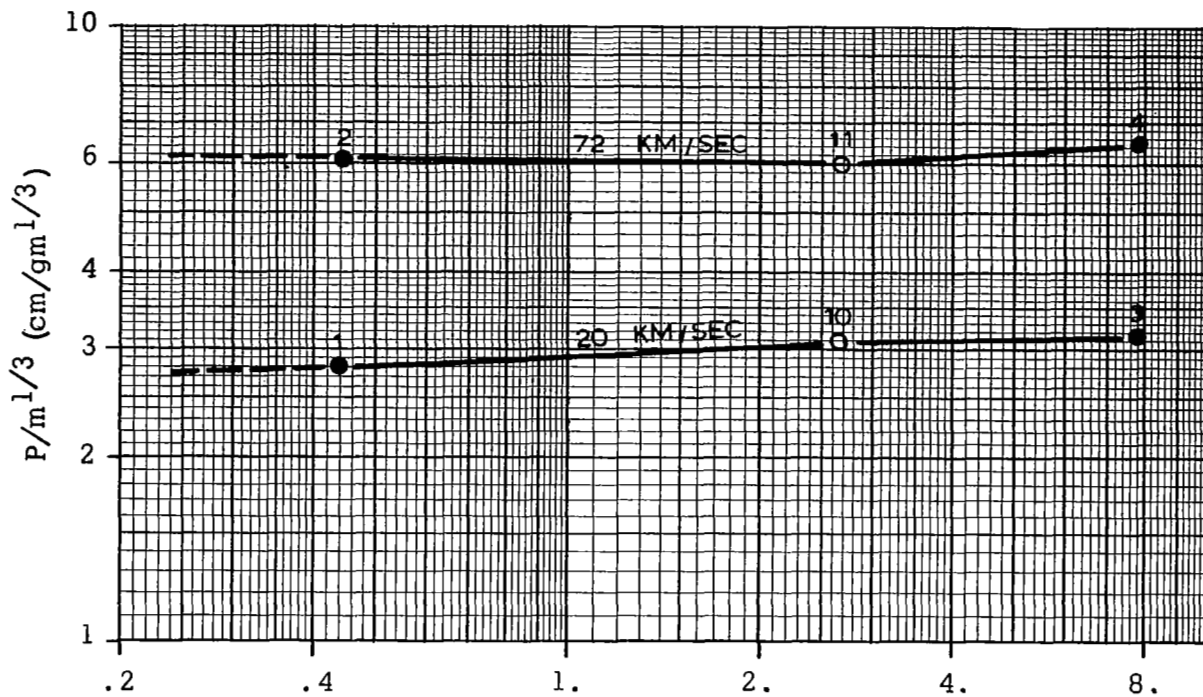


Figure 3-1: PENETRATION INTO ALUMINUM

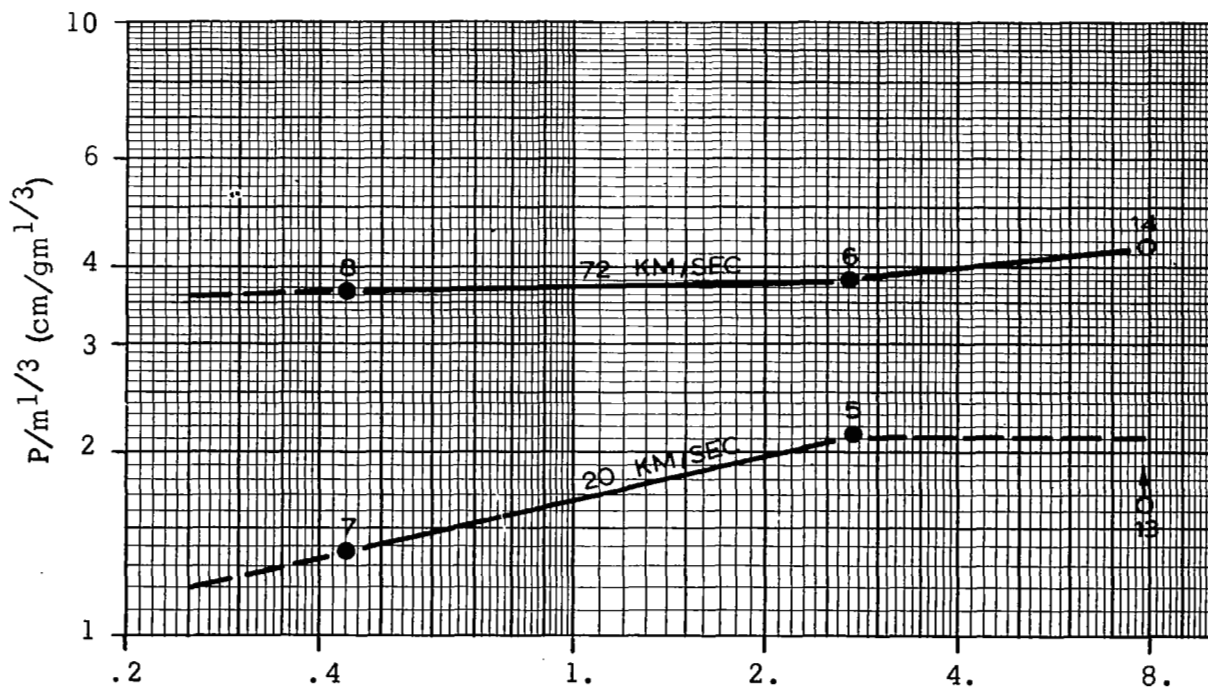


Figure 3-2: PENETRATION INTO STEEL

terms become increasingly important as projectile size diminishes (Bjork 1959). In aluminum, at least, no significant strain rate effect upon material properties is observed at rates up to 10^5 (Lundergan and Herrman, 1963). The effects of thermal conductivity would also produce a deviation from penetration as described by this factor. Order of magnitude considerations, however, indicate that thermal conductivity will not exert an important influence even for the smallest craters considered in this study.

It is seen that $P/m^{1/3}$ is relatively insensitive to the projectile density for 20 and 72 km/sec impacts on aluminum and also for 72 km/sec impacts on steel. At 20 km/sec into steel, however, large variations in $P/m^{1/3}$ are evident. Relative to the porous aluminum impact on steel (Case 8057), lateral expansion of projectile vapor from the shallow crater reduces the effectiveness of blowoff in impacting an impulse to the target. Free surface rarefactions therefore rapidly reduce the pressure in the target shock, minimizing residual target heating. Section 3.3.4.3 discusses this blowoff phenomena further.

With respect to the iron impact on steel at 20 km/sec (Case 13), it is reiterated that thermal softening of the target was not considered in the earlier (Bjork, 1959) impact analyses (Cases 9-14), due to the lack of adequate thermodynamic data. First order corrections were made (Bjork, 1963, Bjork and Olshaker, 1965) on the basis of target melting for the cases involving iron on iron and aluminum on aluminum at 72 km/sec (Cases 11 and 14). A re-examination of the iron on iron point at 20 km/sec (Case 13) suggests that it might also be raised if thermal softening were taken into account. Using the results of the present study as an analogy, it is estimated that an increase of 15 to 20% would be found if the computation were repeated with the more accurate methods utilized here. If the point were so raised, the associated value of $P/m^{1/3}$ would become consistent with that of aluminum on iron at 20 km/sec. Since meteoroids having the density of iron are not sufficiently abundant to pose an important hazard, these speculations do not influence the conclusions of this study on the meteoroid hazard.

A similar re-examination of the aluminum on aluminum point at 20 km/sec (Case 10) suggests that an accurate recomputation might also raise it slightly. In this case, it is estimated that the increase would be on the order of 10%, which borders on the limits of accuracy of crater determination. Therefore, the older point is accepted as it stands.

3.3.2 Interpolation to Intermediate Conditions

The results which are summarized in Figures 3-1 and 3-2 cover a broad range of projectile densities and velocities, and provide a basis for interpolation to assess the effects of impacts under intermediate conditions. For a given projectile, such interpolations can be based on the assumption that $P/m^{1/3}$ varies according to a constant velocity exponent. For a given velocity, assume that $P/m^{1/3}$ varies according to a constant density exponent.

We believe that the penetrating power of meteoroids under intermediate density and velocity conditions can be estimated with reasonable accuracy by such interpolations. Where final design decisions are involved, these estimates should be confirmed by detailed impact analysis. One should bear in mind that

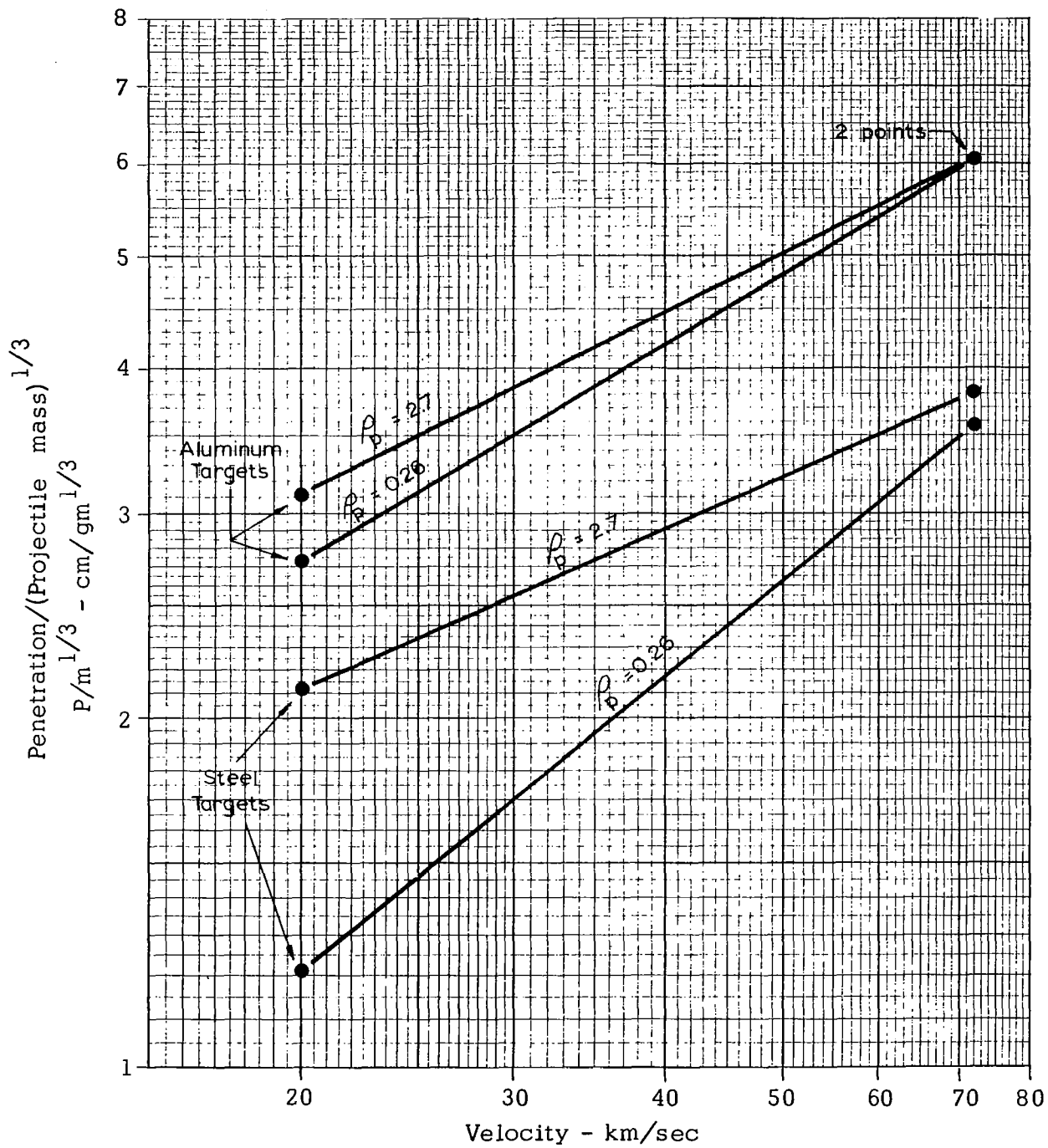


FIGURE 3-3
PENETRATION VS IMPACT VELOCITY

different physical factors determine the crater dimensions in various regions of the velocity-density range. Before accepting an interpolated value for any given projectile, carefully consider whether the properties of that projectile might produce deviations from the physical phenomena which were revealed in the determination of the network of points in Figures 3-1 and 3-2. This caution is even more emphatic for attempted extrapolations.

As an aid in interpolation, the data from Figures 3-1 and 3-2 are plotted to display velocity dependence in Figure 3-3.

To estimate the penetrating power of porous meteoroids ($\rho = 0.26$) at any velocity, the corresponding value of $P/m^{1/3}$ can be directly read from Figure 3-3. For example, at 30 km/sec, the predicted $P/m^{1/3}$ for a porous meteoroid impacting an aluminum target is 2.5. This is equivalent to P/d_s for a spherical projectile of 1.3.

Interpolation for velocities between 20 and 72 km/sec and for densities between 0.26 and 2.7 requires two steps. To illustrate, consider the impact of beryllium ($\rho = 1.85$) on aluminum ($\rho = 2.7$) at 30 km/sec:

First, determine from Figure 3-3 the values of $P/m^{1/3}$ for impacts on aluminum at 30 km/sec of projectiles of densities 0.26 and 2.7. These are 3.50 and 3.85 respectively. Plot these values as shown on Figure 3-1. The intercept of the straight line connecting these points with a density of 1.85 gives the predicted $P/m^{1/3}$ for this impact, or 3.75. For a spherical projectile, this corresponds to a value of P/d_s of 3.71.

Similarly, a beryllium impact on steel at 30 km/sec can be predicted by the same interpolation steps, to obtain a $P/m^{1/3}$ value of 2.4.

3.3.3 Distribution of Energy in Cratering

In comparing lines 18, 19, and 28 in Table 3-2, we note that the major portion of the initial projectile kinetic energy ultimately is deposited into regions of the target which do not directly affect the magnitude of the resulting crater, viz. the isolated shock and ejecta regions (I and III). These regions are effectively detached from the final process of crater formation. Hence, it is only the kinetic energy in the cratering flow field which can enter into the establishment of the ultimate crater dimensions. From line 22 of Table 3-2, it is seen that the kinetic energy in the cratering flow represents only 5 to 10% of the incident energy in the case of iron targets and between 17 and 22% in the case of aluminum targets. It is probable that this fact is responsible for the experimental variability of impact craters. Small variations in experimental conditions which transfer a few percent more or less of the total energy to kinetic energy in the cratering flow would cause a substantial percentage change in the

crater dimensions. It should be further noted that the kinetic energy tabulated for Region II represents an overestimate of the kinetic energy of the flowing material which causes the crater, since a portion of this energy is contributed by the remnants of the projectile which are still within the crater, but which have disengaged themselves from the crater walls and are flying upward.

In the case of porous projectile impacts, a large fraction of the energy is carried away in the ejecta. Between 44 and 52 percent of the energy is carried away in this manner for impacts on aluminum targets, and between 59 and 62 percent leaves in this fashion for impacts on iron targets. In the latter cases, a major portion of the ejecta energy is in the form of internal energy.

3.3.4 Effects of Shock-Induced Residual Temperature on Cratering

3.3.4.1 Target Strength

Section 2.2.3.2 describes the criteria for obtaining crater depth predictions from hydrodynamic solutions. This method, in which the crater growth is assumed to terminate where the dynamic pressure is equivalent to the local target strength, easily accommodates data describing the degradation of strength at elevated temperatures, as well as the ultimate degradation which occurs when the material melts. In this program, the temperature-dependent strength properties are therefore incorporated into the cratering predictions.

In examining Figures B-9 through B-16 of Appendix B, it is seen that the depths at which the dynamic pressure is equivalent to the local target strength occurs in all cases in regions of sharp temperature gradients, and hence of sudden degradation of material strength. Thus temperature effects dominated the final processes of crater formation for these impacts. Strength effects are of course still present, but the steep temperature gradient tends to overwhelm these, at least for the impact cases which are analyzed in this study.

A specific illustration of the temperature dominance is given in Figure 3-4. This shows the dynamic pressure profile as a function of depth for aluminum impacting into steel at 20 km/sec (Case 8054). Residual strengths corresponding to the temperatures are superimposed on this plot for two steels of widely-differing properties - type 301 full hard stainless steel and 1015 low carbon steel. The room temperature ultimate strengths of these steels differ by a factor of nearly three. The intersections of the residual strength curves with the dynamic pressure profile, however, occur at nearly the same depth (i.e., 28.5 cm vs 27.4 cm, or a percentage difference of 4%).

In Figures B-9 to B-16 of Appendix B, the sharper residual strength gradients in the steel targets as compared with the aluminum targets are due to the greater sensitivity of steel strength to temperature.

3.3.4.2 Target Melting

In a previous study (Bjork 1963) it was concluded that in some very high velocity impacts, the final crater dimensions are essentially coincident with the extent of the volume in which residual melting occurs. Finding that this melting dominance was present in aluminum vs aluminum and in iron vs iron

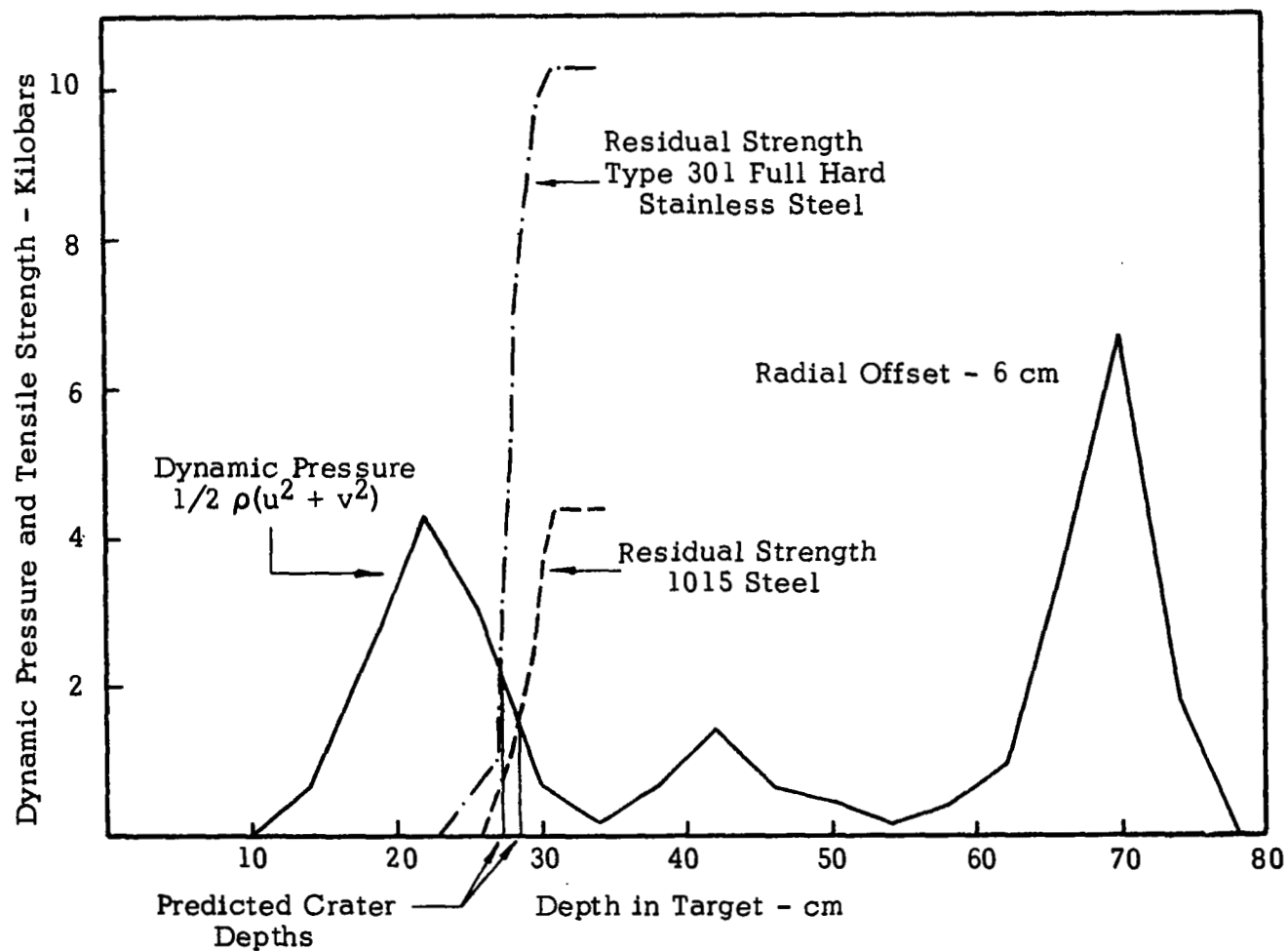


FIGURE 3-4
 DYNAMIC PRESSURE AND RESIDUAL STRENGTH
 PROFILES IN TWO TYPES OF STEEL
 T = 135 MICROSECONDS
 CASE 8055 - ALUMINUM vs IRON (STEEL)
 AT 20 KM/SEC

impacts at 72 km/sec, the earlier predictions (Bjork 1958) for these cases, which had been based upon a simple dynamic pressure-constant target strength equivalence, were adjusted upwards.

The conclusion that crater dimensions coincide with melting in these high velocity impacts contains the implicit assumption that no material which is not melted will be removed from the target. Actually, one would expect that some amount of heated, low strength, material just beneath the melted region would be carried out of the crater, even though the dynamic pressures below the melted region are quite low.

In the current study the incorporation of temperature dependence of strength into the cratering predictions automatically encompasses the effect of melting phenomena, and also makes it possible to determine the additional increment of crater depth due to the carrying out of the hot, relatively weak solid material adjacent to the melted region. Separation of craters into "strength-dominated" and "melting-dominated" categories thereby becomes unnecessary.

It is still of interest to note the extent to which melting of the target material influences the final crater dimensions. An index of this influence is seen in Lines 16 and 17 of Table 3-2, which give the depth reached by residual melting (D_m), and the fraction of the final target depth which this represents (D_m/P).

For the cases analyzed in this study, the ratio of melted depth/crater depth (Line 17) varies through the relatively narrow range from .80 to .94. The largest value occurred in Case 8053 (iron vs aluminum at 20 km/sec), in which melting extended to 94% of the crater depth. In the higher velocity impact involving the same materials (8054), melting extended only to 88% of the crater depth. This apparent anomaly is explained by the strong influence of the vortex phenomena in impact 8054, which is described in Section 3.3.2.

The lowest value of D_m/P was 80%, which occurred in the impact of porous aluminum on iron at 20 km/sec (8057). A significantly higher ratio occurred in the 72 km/sec impact of these same materials (8058). Projectile vaporization and blowoff were present in both of these cases, but the lack of confinement in Case 8057 (discussed in Section 3.3.4.3) diminished the impulse delivered to the target.

The D_m/P ratio is influenced by the spread which occurs between the temperature at which the target material loses most of its strength and the melting temperature. The strength of 2024-T3 aluminum drops to 10% of its room temperature value at about 600°K, and melts at about 850°K. The strength of type 301 full hard stainless, however, drops precipitously to 10% of its room temperature value at 1050°K, but does not melt until about 1675°K. This large spread tends to increase the "soft" zone beneath the melted region, reducing the D_m/P ratio for steel targets.

3.3.4.3 Projectile Vaporization and Blowoff

As is seen by lines 9 and 11 of Table 3-2, hypervelocity impacts impart a very high specific internal energy to the projectile and target materials. For most of the cases considered in this study, the energy levels were sufficient to cause vaporization of portions of the materials.

Table 3-3 summarizes the conditions which are required to cause incipient as well as complete melting in porous aluminum, aluminum and iron. The impact velocities shown are for a one-dimensional geometry. For real impacts, the peak pressure conditions will not be felt throughout the projectile, due to the relief provided by lateral free surfaces. The impact conditions shown in Table 3-3 are nonetheless a useful guide to the incidence of vaporization. Where the energy levels specified for complete vaporization are exceeded by a factor of say two, it is reasonable to assume that the projectile will be vaporized in its entirety, notwithstanding free surface effects.

TABLE 3-3: CONDITIONS FOR VAPORIZATION IN HYPERVELOCITY IMPACTS

	Aluminum		Iron	
	Incipient Vaporization	Complete Vaporization	Incipient Vaporization	Complete Vaporization
Specific internal energy required (ergs/gm x 10^{12})	0.62	3.2	0.08	0.32
Shock pressure required to achieve this level (megabars)	5.8	26	3.5	10
Minimum impact velocity against aluminum which will achieve this condition (cm/ μ sec)	2.2	5.1	1.2	2.3
Minimum impact velocity against iron which will achieve this condition (cm/ μ sec)	1.7	3.9	0.86	1.6

In the current research, it is seen that at least partial vaporization of the projectile occurred in every impact case, with complete vaporization probably taking place in all of the 72 km/sec impacts. Substantial portions of the target

were also vaporized in these same impacts. Only in the 20 km/sec impacts of porous aluminum on aluminum and iron (Cases 8051 and 8057) did at least a portion of the targets fail to reach energy levels necessary for incipient vaporization.

Material vaporization constitutes a major energy sink in the impact process, but the subsequent high velocity blowoff of heated gas out of the crater can impart a large impulse to the target. Blowoff is the major contributor to the large values of negative axial momenta in the ejecta (Region III), as tabulated by line 26 in Table 3-2, and for the correspondingly large momentum multiplication factors in line 19. Since blowoff occurs relatively early in the impact process, its effects are also reflected in the persistence of peak pressures in the target, and in the depth of the cratering flow fields.

It might seem anomalous that the ejecta blowoff momentum is generally larger for aluminum targets than it is for iron targets, since impact with iron produces initially larger specific internal energies. This is especially notable in the porous aluminum impacts. The reason for this phenomena is evident from the plots of Appendix C showing the mass disposition as a function of time for cases 8052 and 8058. These plots indicate that the projectile vapor blows out of a deeper crater in the case of aluminum targets. Lateral expansion of the vapor is therefore inhibited, and the blowoff is more efficiently employed to impart a downward impulse to the target. By contrast, the cratering in iron is relatively shallow, which allows easier lateral expansion of the vapor and consequently reduces the axial momentum delivered to the target. The dynamic geometry of the confining crater is thus important in establishing the impulse imparted by blowoff.

It has been suggested previously (Olshaker and Bjork, 1962) that the effects of projectile density could be accounted for by considering the initial particle velocity in projectiles impart to a target. This hypothesis was shown to be valid over a limited velocity and density range. However, the onset of the blowoff phenomenon increases the penetrating efficiency of very low density projectiles at high impact velocities and causes them to produce crater depths greater than that density scaling relationship predicts.

An index of the cratering efficiency is afforded by the quantity $P/m^{1/3}$. It may be noted in Figure 3-1 that the phenomenon of blowoff causes porous projectiles to be nearly as efficient as iron projectiles in penetrating aluminum targets. Against steel targets, however, the porous projectiles are significantly less effective than iron projectiles, due to the poor lateral confinement provided by the shallow craters to the escaping vaporized material.

3.3.5 Vortex Flow

When a dense projectile strikes a soft target at high velocities, an unusual type of flow develops which we term "vortex flow". This type of flow, which was qualitatively recognized earlier (Bjork 1961b) in the impact of iron on tuff at 30 km/sec, is observed in this study in cases 8053 and 8054 (iron vs aluminum at 20 and 72 km/sec.)

Development of vortex flow is well-represented by the series of mass, velocity, and pressure plots given in Figure C-4 of Appendix C for impact case 8054. The early mass plots, views (a), (b), and (c), show the rapid penetration of the dense projectile into the relatively soft aluminum target, and the converging rebound of vaporized target material from the sides of the crater. In the subsequent mass plots in views (d) and (e), the converging target material closes over the projectile, forming a cavity.

The velocity fields provide the best insight into the material flow. Early vortex action is seen in view (h) when the rebounding target material strikes the trailing sides of the projectile. As the rebounding material closes over the projectile, it converges on the axis, creating high pressures. As seen in view (i), material above about 4 cm is strongly accelerated upward by this pressure, while material below that depth is accelerated downward into the void created previously by the projectile's passage. The downward flow of material interacts with the rear of the projectile, leading to the circular flow pattern in view (l) which suggests a vortex centered at about $y = 30$ and $x = 10$.

The effects of vortex flow on penetration are evident from the pressure fields. In view (r), an isolated high pressure region is seen on the axis down to a depth of about 24 cm. This region is the result of the convergence of the rebounding target material into the void above the projectile, and it is the cause of the high velocity material flow both upward and downward. At $t = 38.1 \mu\text{sec}$, view (t), pressures greater than 100 kb exist in most of the axial region below a point about 4 cm above the original target surface. The persistence of this high pressure, which is evident in views (u), (v), and (w), is responsible for imparting an additional increment of momentum and kinetic energy to the cratering flow field. This forces a given level of dynamic pressure to a greater depth in the target, thereby enhancing the crater dimensions.

These same phenomena are present to a lesser degree in Case 8053. Formation of the cavity by convergence of rebounding target material behind the projectile is evident in views (j) and (k) of Figure C-3 in Appendix C. Formation of a downward jet as the material converges at the axis is also shown clearly in these views, as well as in the velocity field of view (v). In Case 8053, not as much of the vaporized target mass is involved in the vortex flow as compared with Case 8054. This material is able to quickly blow out, thereby relieving the pressure against the rear of the projectile. The added increment of momentum and kinetic energy imparted to the cratering flow due to this process therefore does not significantly increase the crater dimensions.

3.4 Comparisons With Other Work

No other computations of the impact craters produced in the velocity range of interest to this program have been published, so there are no direct bases for comparisons with the crater dimensions which we have calculated. However, we can cite certain aspects of the hydrodynamic calculations by Walsh et al (1964) and an empirical fit by Herrman and Jones (1962). The other hydrodynamic calculations have deduced the dependence of crater dimensions on velocity and projectile density in this velocity range. However, the results contain an undefined constant which must be determined by a suitable experiment. The work of

Herrman and Jones is described by them as empirical and "not based on rational theoretical grounds" and for this reason they caution against extrapolating their expression to higher velocities or other materials. This seems harsh in describing a painstaking and significant study. We wish to point out here a physical mechanism in addition to those which they considered which enters at high velocities and which we believe would cause their expression to underestimate crater dimensions if it were extended to higher velocities.

3.4.1 Other Hydrodynamical Computations

In Appendix D, we discuss the theoretical investigation of hypervelocity impact by Walsh and his co-workers. Briefly, they have derived a velocity scaling exponent based upon examination of the late-time characteristics of isolated target shocks, as predicted by hydrodynamic calculations. The concept of late stage equivalence was then evolved as a means for normalizing the computed velocity dependence of penetration with experimental data. However, experiments in the required velocity range (above $2c_0$, or very roughly twice the sound speed in the target) are not yet available.

From this approach, Walsh concludes that for solid-solid impacts at velocities above $2c_0$:

- a) $P/m^{1/3}$ is constant for a given impact velocity and target material (usually stated in the equivalent form that P/d is proportional to the cube root of projectile density).
- b) For a given target and projectile, penetration varies as the 0.58 power of impact velocity.

In the case of aluminum targets, the data shown in Figure 3-1 (page 37) are consistent with Walsh's conclusion, inasmuch as $P/m^{1/3}$ is essentially independent of density at both 20 and 72 km/sec. In steel targets, agreement is evident in Figure 3-2 for the 72 km/sec impacts. At 20 km/sec, however, the low density projectile point departs significantly from a constant $P/m^{1/3}$ relationship. (The iron vs steel point is also low, but as previously discussed, a recalculation of this impact taking into consideration thermal degradation of target strength would probably raise it by 15 - 20%.)

Walsh's velocity exponent may be compared by using our calculated penetrations at 20 and 72 km/sec, which are within the range above $2c_0$ for both iron and aluminum. In Figure 3-5, the slopes of the straight lines connecting the data points obtained in this study for aluminum targets represent a type of average of the velocity exponent of penetrations between 20 and 72 km/sec. The data on this plot have been used to normalize Walsh's expression. Satisfactory agreement is seen, as the results are consistent to within 7% between 20 and 72 km/sec.

As mentioned previously, values of $P/m^{1/3}$ for impacts into steel at 20 km/sec show a dependence on density for porous projectiles. Comparison with Walsh's constant velocity exponent are therefore not meaningful for the steel target cratering predictions.

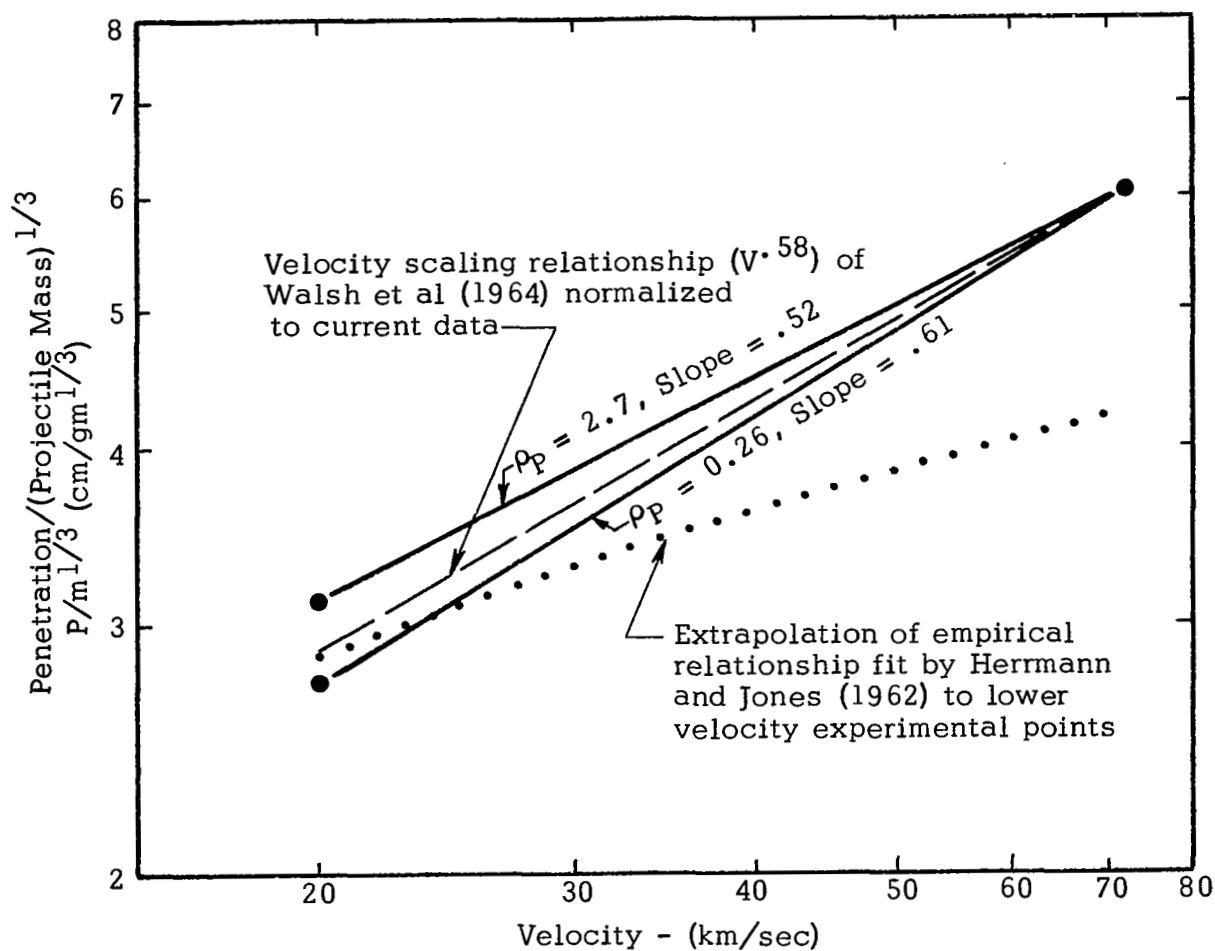


FIGURE 3-5
COMPARISON OF PENETRATION PREDICTIONS
FOR IMPACTS ON ALUMINUM
WITH HYDRODYNAMIC TREATMENT OF WALSH ET AL
AND EMPIRICAL FIT OF HERRMANN AND JONES

The extent of agreement with Walsh's conclusions in aluminum targets is gratifying. We attribute this to the dominance of thermal conditioning effects in the targets for the impacts considered. Peak shock pressures determine the release temperature an element will attain. The impulse profile determines the displacement of these elements into the target. Hence the residual temperature profile in the target is established by the characteristics of the isolated shock. As discussed in Appendix D, Walsh emphasizes the role of the isolated shock, and we would expect to find convergence with his conclusions for those impacts where thermal degradation of target strength is extensive, and where equivalence between shocks for different impacts can be established at relatively early times.

We would again caution, however, against overemphasis upon average velocity exponents*, especially as a basis for extrapolation. The present study does not claim to establish the functional dependence of penetration on projectile density or impact velocity. Rather, our approach has been to exhibit the physics of the impact process which lead to establishment of the final crater, and to evaluate its dimensions quantitatively based on the physical model. The evaluation is conducted at projectile densities and speeds chosen to bracket the meteoroid regime. With reasonable confidence, results can be interpolated to obtain data within that regime, as illustrated in Section 3.3.2.

The physics are seen to be sufficiently complex that it would be surprising if a simple functional dependence could be found which would apply over a broad range of target material, projectile material, and impact velocity.

The computations conducted herein have served to display in detail the interplay among the various physical mechanisms which contribute to the formation of the ultimate crater. These include the formation and propagation of the shock systems, and their interaction with the various rarefactions. These interactions determine the apportionment of energy and momentum among the ejecta, cratering flow, and isolated shock, as well as the thermal conditioning of the target by the isolated shock, and finally the plastic deformation occasioned by the cratering flow in the conditioned material. When one adds to this the complex physics of the equation of state and constitutive relations, one can appreciate the difficulty of describing the total behavior in terms of two or three parameters for a wide class of conditions.

3.4.2 The Fit of Herrmann and Jones

Herrmann and Jones (1962) recommend the use of the following expression to summarize the large body of experimental data which has been accumulated:

$$\frac{P}{d} = k_1 K^{2/3} \ln \left(1 + \frac{K^{2/3} B}{k_2} \right) \quad (3-1)$$

* The velocity exponent is defined by any of the forms

$$\frac{\partial \ln P/m^{1/3}}{\partial \ln V} = \frac{\partial \ln P/d}{\partial \ln V} = \frac{\partial \ln P}{\partial \ln V}$$

where $K = \rho_p/\rho_t$

$$B = \rho_t V^2/H_t$$

H_t = Brinell hardness of target.

The constants, k_1 and k_2 , are prescribed for each target material, and the velocity range where each pair of constants is valid is also specified. The expression is derived by close analogy with the model of Bohn and Fuchs. This model accounts for the static target strength through the Brinell hardness number. The model also indicates the important role of inertial effects in diminishing the velocity exponent at higher velocities.

Besides fitting experimental data well, extrapolation of Eq. 3-1 was shown to provide a good fit to the crater dimensions which had previously been computed on a hydrodynamic model (Bjork, 1959). This is not surprising, since inertial effects are well accounted for in the hydrodynamic model, and the use of the dynamic pressure criteria for crater termination simulates strength effects, as well as their decreasing relative importance.

As previously noted, however, consideration of thermal conditioning (in terms of melting) by the isolated shock caused the original cratering predictions for the 72 km/sec impact to be raised (Bjork, 1963). The more refined model employed for termination of crater growth in this study reinforces those conclusions. Inasmuch as this mechanism of thermal conditioning by the isolated shock was not incorporated in the model of Herrmann and Jones (nor was it needed to describe the lower velocity impacts with which they were concerned) the data from our analyses of very high velocity impacts depart significantly from their model, as is seen in Figure 3-5.

SECTION 4

METEOROID ENVIRONMENT

To compute the probability that a structure will be perforated during a given exposure in space, one must know both the meteoroid environment and the perforating power of an individual meteoroid. Since the perforating power is a function of the meteoroid's mass, density, and velocity, the ideal information would be a complete specification of the meteoroid flux as a function of each of these parameters. However, not enough information is available at present to provide such an extensive description. The data reviewed in this section provides:

- a) an estimate of the average density of meteoroids in a given velocity range, and
- b) the cumulative flux of all meteoroids as a function of mass.

It will be seen that there is some uncertainty in even this limited information. However, the data is improving each year.

The bulk of currently available information regarding the meteoroid environment is derived from four sources:

- a) Photographic observations of the luminous trajectories of meteoroids in the earth's atmosphere (photographic meteors),
- b) Radar observations of the ionization trails of meteoroids in the earth's atmosphere (radio meteors),
- c) Rocket and satellite sounding board measurements of meteoroid impact momentum, and
- d) Penetrating flux measurements by satellites such as those taken by Explorer XVI, Explorer XXIII, and by the Pegasus vehicles.

Photographic observations are possible for meteors of magnitude zero to five, corresponding roughly to masses from 1 gm to 10^{-2} gms. Radio observations overlap this range, but are found most useful for meteors in the 5 to 9 magnitude range, corresponding to about 10^{-2} to 10^{-6} gms. For convenience, meteors in the 1 to 10^{-2} gm range are referred to as photographic meteors, and those in the 10^{-2} to 10^{-6} gm range are referred to as radio meteors. Since meteoroids in the mass range from 1 to 10^{-6} gms constitute the greatest hazard to a vehicle in space, the continuing progress of the photographic and radar observation techniques, and in the interpretation of data obtained by these techniques, is of particular importance to those concerned with the meteoroid hazard to spacecraft.

4.1 Meteoroid Densities

4.1.1 Photographic Observations

Jacchia, Verniani, and Briggs (1965) have published a precise analysis of the atmospheric trajectories of 413 meteors. These cases were selected from the group of 3,500 meteors doubly photographed by Super-Schmidt cameras in the Harvard photographic meteor program. The authors stress that the cases selected were those which were likely to yield excellent deceleration measurements, and that a bias might be introduced by this method of sample selection.

As an input to reducing the data, Verniani's (1964a) value of 1.0×10^{-19} (cgs) was used as the photographic luminous efficiency coefficient. On the basis of this analysis, it was found that the average density of the observed meteoroids was 0.26 gm/cm^3 . Whereas each meteor shower appears to have characteristic average density which differs from other showers, the average of all shower meteors was found to have the same density as the sporadic meteors, which is consistent with the hypothesis that the sporadic component arises from dispersed showers.

A search for meteors of asteroidal origin (i.e., high density) disclosed only one of the 413 reduced cases which might qualify as a member of this group. While little weight can be given to an individual density determination, it may be noted that the computed density of this meteor was 4.9 gm/cm^3 , which is the right order of magnitude for an asteroidal meteor.

4.1.2 Radar Observations

Verniani (1964b), using the ionizing efficiency given by Verniani and Hawkins (1964), deduced that the radio meteors with an average magnitude of 8 which were observed in the Harvard radio meteor program have an average density of about 0.5 gm/cm^3 .

More recently, Verniani and Hawkins (1965) have examined the radar observations of the trails of 320 meteors. Although they observed some masses in the range of 1.5×10^{-5} to $2 \times 10^{-3} \text{ gm}$, most of the observations were made on meteors having masses near 10^{-4} gm . The median of the observed densities was close to 1 gm/cm^3 . Included were 32 Geminid meteors, 19 of which yielded acceptable deceleration measurements. The mean density of the 19 Geminid meteors was $1.0 \pm 0.3 \text{ gms/cm}^3$, which is in good agreement with the average density of $1.0 \pm 0.2 \text{ gms/cm}^3$ found for photographic Geminid meteors by Jacchia, Verniani, and Briggs (1965).

Verniani and Hawkins (1965) examined the possible errors in their computed densities, and cite the need to consider the average values given by a group of measurements, rather than to accept individual measurements.

The total group yielded 285 individual density measurements, of which 44 percent were less than 1 gm/cm^3 , 46 percent were between 1 and 12 gms/cm^3 , and the remainder were larger than 12 gms/cm^3 . Both the median and mean of the densities were close to 1 gm/cm^3 .

When those meteors having a deceleration error greater than half the deceleration itself were rejected, a group of 185 remained. 51% of these had densities less than 1 gm/cm^3 , with a mean of $0.37 \pm .03 \text{ gms/cm}^3$. 45% had densities between 1 and 12 gms/cm^3 , with a mean of $2.8 \pm .2 \text{ gms/cm}^3$. The remaining 4 percent had unrealistically high densities.

When those meteors with standard deceleration errors greater than $1/5$ the deceleration are rejected, a group of 58 cases remained. These cases subdivide into 60% which had densities less than 1 gm/cm^3 , with a mean of $0.36 \pm .05 \text{ gms/cm}^3$, with the remainder (in the density range above 1 gm/cm^3) having a mean density of $2.4 \pm 0.3 \text{ gms/cm}^3$. In this group, only three meteors had computed densities greater than 12 gms/cm^3 .

4.1.3 Conclusions Regarding Densities

It had been previously supposed that as many as 10% of the photographic and radio meteors are asteroidal in origin, and hence of relatively high density. The above-quoted observations, however, fail to show evidence of such a significant high density component.

To compute the perforating hazard during this program, we have accepted the density of photographic meteors (mass greater than 10^{-2} gms) as 0.26 gm/cm^3 , and have assumed that equal numbers of meteors with densities of 0.37 and 2.8 gms/cm^3 exist in the mass range from 10^{-2} to 10^{-10} gms . Further, we have assumed that the number of meteoroids having densities substantially larger than 3.0 gms/cm^3 is negligible.

4.2 Meteoroid Flux as a Function of Mass

4.2.1 Photographic Meteors

The best current estimate of the flux of photographic meteors as a function of mass comes from the work of Hawkins and Southworth (1958) and Hawkins and Upton (1958). It is important that in these studies a homogeneous sample of the meteoroid flux was considered, all observed cases being retained for consideration. However, the results of Jacchia, Verniani, and Briggs (1965) may be expected to exert an influence on the flux of photographic meteors as deduced by Hawkins and Upton.

Jacchia et al found that the classical theories of meteor magnitude as a function of mass, velocity and zenith angle are not adequate to compute magnitudes accurately. Almost all meteors break up when they enter the atmosphere, a factor which complicates the analysis in a major way. The onset of breakup correlates better with the ρv^3 than with ρv^2 , which suggests that heat transfer rather than dynamic air pressure is the cause of breakup. (In the preceding expression, ρ is the atmospheric density.) The most conclusive evidence for breakup is the lengthening of the luminous trail as the meteor travels through the atmosphere. This leads to the phenomena of terminal blending described by Jacchia et al. Another indication of breakup is the fact that the meteor's deceleration does not obey single body deceleration theory. These factors were given careful attention in the preceding reference.

From a least-squares fit of their reduced data, Jacchia et al deduced the following dependence of peak photographic magnitude on the mass, initial velocity, and zenith angle of a meteoroid:

$$\log M_{pm} = 55.34 - 8.75 \log v - 2.25 \log m - 1.5 \log \cos Z_R \quad (4-1)$$

where M_{pm} is the peak visual magnitude, m is the initial meteoroid mass in gm, v is the initial velocity in km/sec, and Z_R is the zenith angle.

Although the flux deduced by Hawkins and Upton may be corrected to first order by assigning a corrected mass to the zero magnitude meteor, such a treatment tacitly assumes that the effects of velocity and zenith angle average out for a given mass. In view of the strong dependence on these quantities suggested in Eq. (4-1), this might represent a poor assumption, and the subject merits further consideration.

For our present purposes, the flux is estimated by correcting the mass of a zero magnitude, 30 km/sec meteor as follows: Table 4-1 specifies the mass of a zero visual magnitude meteoroid as a function of initial velocity and zenith angle. One should note that the photographic magnitude specified in Eq. (4-1) must be corrected by the color index to obtain peak visual magnitude (Jacchia, 1957). Based on an average velocity of 30 km/sec, and a zenith angle between 45 and 60°, we take the mass of a zero visual magnitude meteor to be 2.5 grams. This quantity was used to further correct the expression of Hawkins and Upton (1958) which had previously been corrected by Whipple (1963) to account for earth shielding and to correct to a 1 gram zero visual magnitude meteor. The final expression which we use here as the best estimate of the photographic meteor flux as a function of mass is:

$$\log N = - 1.34 \log m - 14 \quad (4-2)$$

where N is the cumulative flux per square meter per second of meteoroids having mass greater than m grams. The effect of earth shielding has been included so that this represents the flux on a randomly oriented body in space near Earth. That is, it expresses the flux in 2π steradians of solid angle. The expression is taken to hold over the mass range from 10^{-2} to 1 gram.

TABLE 4-1: THE MASS (in gm) OF A ZERO VISUAL MAGNITUDE METEOROID
AS A FUNCTION OF VELOCITY AND ZENITH ANGLE
(from Jacchia, Verniani, and Briggs, 1965)

		Velocity (km/sec)						
		10°	20°	30°	40°	50°	60°	70°
Zenith Angle	0°	120	8.13	1.66	0.55	0.23	0.11	0.062
	30°	132	8.91	1.82	0.63	0.25	0.12	0.068
	45°	151	10.2	2.09	0.69	0.29	0.14	0.078
	60°	191	12.9	2.63	0.87	0.36	0.18	0.098
	75°	269	18.2	3.72	1.23	0.51	0.25	0.14
	85°	617	41.7	8.51	2.82	1.17	0.58	0.32

4.2.2 Radio Meteors

Radar observations of the ionized trail produced by radio meteors permit the computation of the number of electrons produced in a unit length of the trail. The computation of meteoroid mass requires a substantial amount of additional information which is only approximately known at the present time. As outlined in many places (e.g., Elford, Hawkins, and Southworth, 1964), the total number of electrons in the trail is:

$$Q = \beta \frac{m}{\mu} \quad (4-3)$$

where Q is the number of electrons produced in the trail, m is the original mass of a meteoroid, and β is the ionizing efficiency, or average number of electrons ionized per ablated meteoroid atom. The value of μ depends on the composition by atomic species of the meteoroid body, and Elford et al take its value to be 3.8×10^{-23} gm. The ionizing efficiency is also a function of composition, since it is different for each atomic species. A more serious error arises in assessing the velocity dependence of β . It varies strongly with velocity, usually being expressed as proportional to velocity raised to a high power. Unfortunately, the uncertainty lies in the velocity exponent. Elford et al used the value computed by Verniani and Hawkins (1964), namely $\beta = 1.0 \times 10^{-20} v^4$, where v is in meters per second.

Assuming an idealized trail of constant line density over a height range Δh leads to $Q = q_z \Delta h$, where q_z is the zenithal line density. In actuality the line density varies considerably along the trail. In computing the response of the Harvard radar system, Elford (1964) assumed that the maximum line density, q_m , is related to q_z by $q_m = q_z \cos \chi$, where χ is the radiant zenith distance. Elford advocates the use of

$$m = 23 q_z v^{-4}$$

(4-4)

to estimate the initial mass of radio meteors. This expression assumes the typical value of Δh to be 6 km.

The flux of meteors producing trails having zenithal line densities greater than $q_z = 4.5 \times 10^{10}$ electrons per meter had previously been estimated by Elford and Hawkins (1964) to be $40 \text{ km}^{-2} \text{ hr}^{-1}$, or about 10^{-8} per square meter per second.

In the following table we calculate the mass and velocity of meteors which produce 4.5×10^{10} electrons per meter as derived from Eq. (4-4). Also shown in this table are the penetration depth in semi-infinite targets of steel and aluminum derived from the present study.

TABLE 4-2: VELOCITY, MASS, AND PENETRATING POWER OF RADIO METEORS WHICH PRODUCE LINE DENSITIES OF 4.5×10^{10} ELECTRONS/METER

Velocity km/sec	Mass (gm)	Density (gm/cm ³)	Penetration	
			in Steel (cm)	in Aluminum (cm)
20	6.5×10^{-6}	0.26	.022	.050
		2.7	.039	.058
30	1.3×10^{-6}	0.26	.019	.038
		2.7	.027	.042
72	3.9×10^{-8}	0.26	.012	.021
		2.7	.013	.021

The flux of $10^{-8} \text{ met}^{-2} \text{ sec}^{-1}$ should be reduced by a factor of two to yield the flux on a randomly-oriented body in space near earth.

4.2.3 Rocket and Satellite Sounding Board Data

Figure 4-1, from Alexander et al (1962), is a collection of data gathered by various sounding rockets and satellites which carried microphone sounding board pickups. Such sounding boards are assumed to be sensitive to the momentum of the incoming particle, so that the threshold mass is the threshold momentum divided by the meteoroid velocity. Computation of mass from these measurements thus requires the assumption of a nominal velocity. Alexander et al fitted the data in Figure 4-1 with the solid line. An average velocity of 30 km/sec was assumed. Account was taken of the shielding effect of the earth as well as the directional properties of the sounding board detectors used.

The impact computations conducted in the present study and summarized in Table 3-2, indicate that the momentum imparted to the sounding board is about an order of magnitude larger than the momentum of the particle itself, due to the recoil momentum created by the ejection of material "splashed" from the target

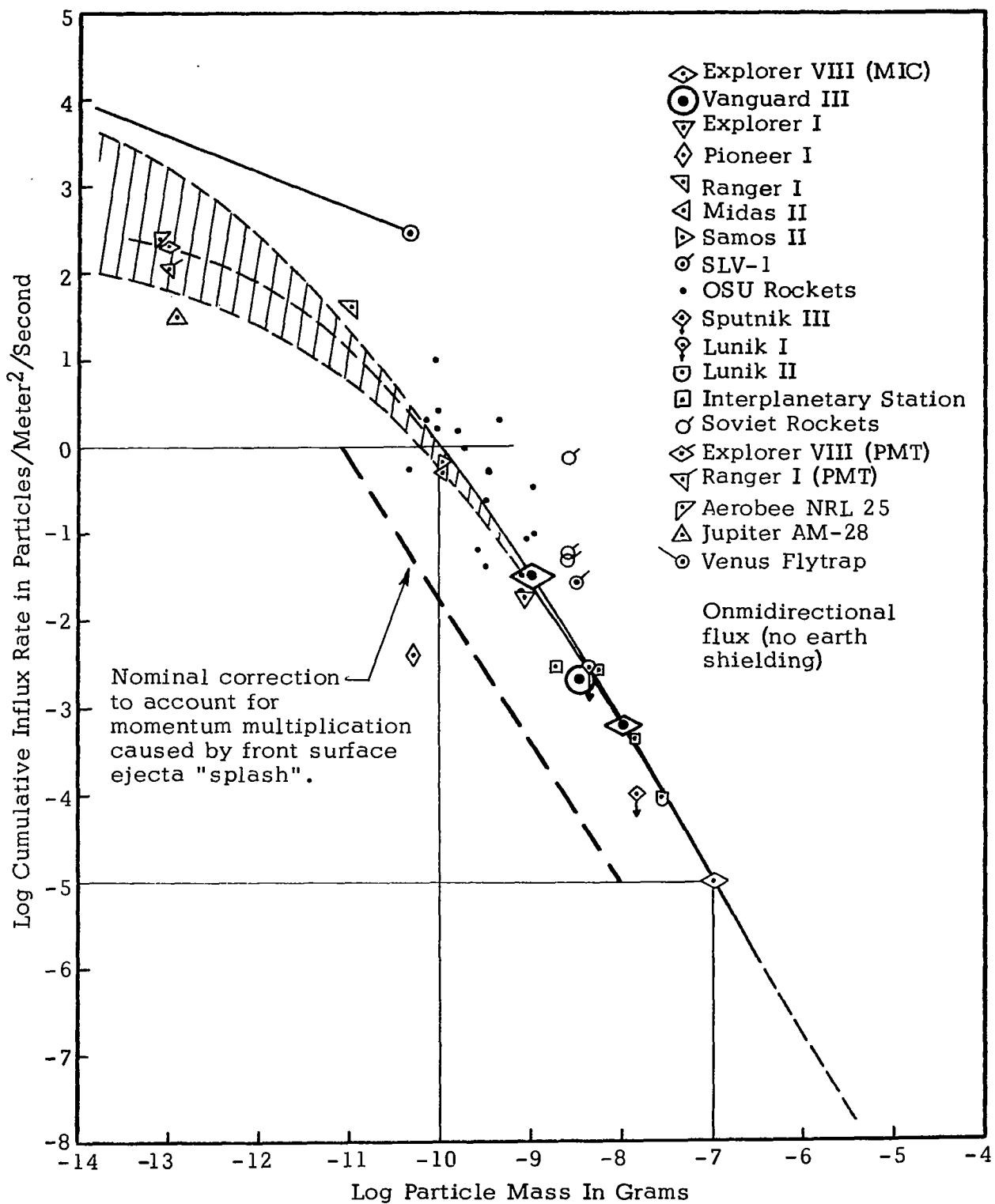


FIGURE 4-1
 AVERAGE CUMULATIVE MASS DISTRIBUTION CURVE FOR THE
 VICINITY OF EARTH, AS DERIVED FROM AVAILABLE MEASUREMENTS
 OBTAINED WITH MICROPHONE AND PHOTOMULTIPLIER SYSTEMS
 (from Alexander et al, 1962)

surface. Consequently, the fit by Alexander et al should be corrected by shifting it by an order of magnitude towards smaller masses. Such a correction assumes that the splash momentum is a constant factor larger than the particle momentum. This is only approximately true, and more refined corrections may be made for individual cases by using the data presented in Table 3-2.

4.2.4 Direct Measurements of Penetrating Flux

The Explorer XVI and XXIII, and the Pegasus I, II, and III satellites have made direct measurements of the flux of meteors capable of penetrating certain thicknesses of metals. These observations are of major importance in assessing the hazard to spacecraft due to meteoroid encounters.

In the Explorer XVI experiment, pressurized beryllium-copper containers having wall thicknesses of 1, 2, and 5 mils were exposed in space for a period of a few months. In Explorer XXIII, similar pressurized containers were exposed, except that 1/2-hard type 302 stainless steel was used, with wall thicknesses of 1 and 2 mils.

The Pegasus satellites exposed electrical condenser-type detectors. In these experiments the exposed metal layer comprised one plate of a condenser, which was discharged when a meteoroid perforated this plate. Complete perforation of the first plate was required to produce a count. The plate thicknesses used in the experiments were 40, 200, and 400 microns (approximately 1.6, 8, and 16 mils). The 40 micron plates were 1100-0 aluminum, while the 200 and 400 micron plates were 2024-T3.

The total number of perforations, and the penetrating flux for these direct observations, as reported by Hastings (1964) for Explorer XVI, O'Neal (1965) for Explorer XXIII, and Naumann (1966) for Pegasus, are summarized in Table 4-3. No correction has been made for earth shielding. Standard deviations are also shown in Table 4-3. The indicated deviation for the Pegasus experiments is small because of the large number of total perforations.

The close agreement between the Explorer XVI and Explorer XXIII data for corresponding wall thicknesses suggests rather strongly that beryllium-copper and type 302, 1/2 hard stainless steel have similar perforation properties. This would also be concluded from rough consideration of the probable hydrodynamic properties of Be-Cu. The computational results from Section 3 permit us to estimate the mass required to perforate the stainless steel containers of Explorer XXIII, and by analogy, the beryllium-copper containers of Explorer XVI.

The pressurized container walls are unsupported and the cratering effects are confined to a region which is small compared with the container's radius of curvature. Thus the wall behaves as a flat plate of given thickness with an unsupported rear free surface. As discussed in Section 2.2.6, meteoroids will strike the wall with an average obliquity angle of 45° , which reduces the average crater depth by a factor of about 1.4. On the other hand, a meteoroid which would penetrate to a depth P in a semi-infinite target will marginally penetrate a plate of thickness $1.4 P$. These two effects are assumed to cancel each other and one may use the penetration results summarized in Figure 3-2 directly to compute the required mass. The plate thickness is set equal to the penetration as given in that figure. Thus the mass which will marginally perforate a plate

TABLE 4-3: SATELLITE PENETRATING FLUX DATA

Experiment	Target	Recorded Perforations	Penetrating Flux $\text{met}^{-2} \text{sec}^{-1}$	Mass Range Required for Perforation (gm)
Explorer XVI (from Hastings, 1964)	1 mil Cu-Be	44	$(3.9 \pm 1.2) \times 10^{-6}$ a	$3.0 \times 10^{-10} - 9.5 \times 10^{-9}$
	2 mil Cu-Be	11	$(2.0^{+1.6}_{-1.0}) \times 10^{-6}$ a	$2.4 \times 10^{-9} - 7.6 \times 10^{-8}$
	5 mil Cu-Be	0	$< 1.1 \times 10^{-6}$ a	
Explorer XXIII (from O-Neal, 1965)	1 mil 302 Stainless Steel, 1/2 Hard	24	$(4.5^{+2.1}_{-1.6}) \times 10^{-6}$ a	$3.0 \times 10^{-10} - 9.5 \times 10^{-9}$
	2 mil 302 Stainless Steel, 1/2 Hard	25	$(2.1^{+1.0}_{-.7}) \times 10^{-6}$ a	$2.4 \times 10^{-9} - 7.6 \times 10^{-8}$
Pegasus I, II, and III (from Naumann, 1966)	40 μ 1100 Al	582	$(1.85 \pm .08) \times 10^{-6}$ b	$2.8 \times 10^{-10} - 3.3 \times 10^{-9}$
	200 μ 2024-T3 Al	49	$(2.08 \pm .35) \times 10^{-7}$ b	$3.5 \times 10^{-8} - 4.1 \times 10^{-7}$
	400 μ 2024-T3 Al	194	$(4.4 \pm .35) \times 10^{-8}$ b	$2.8 \times 10^{-7} - 3.3 \times 10^{-6}$

a 95% Confidence Limits

b 1 - Sigma Limits

of thickness T is given by

$$M_{\text{marg}} = \left(\frac{T}{P/m^{1/3}} \right)^3 \quad (4-5)$$

Since neither the density nor velocity of the perforating meteoroid is known to us, there is an uncertainty in M_{marg} . The review of the meteoroid environment given above indicates that the impacting meteoroid will probably have a velocity between 20 and 72 km/sec and a density between 0.26 and 2.7 gm/cc. The extremes in M_{marg} will correspond to the extremes of $P/m^{1/3}$ which occur with those ranges of velocity and density. From Figure 3-2, the extremes are:

a) Maximum $P/m^{1/3} = 3.8 \text{ cm/gm}^{1/3}$, corresponding to a density of 2.7 gm/cm³ and a velocity of 72 km/sec. At 72 km/sec, $P/m^{1/3}$ is nearly independent of density. Thus if the velocity of the meteoroids were measured to be near 72 km/sec, M_{marg} would be determined quite accurately, no matter what the meteoroid density.

b) Minimum $P/m^{1/3} = 1.2 \text{ cm/gm}^{1/3}$, corresponding to a density of 0.26 gm/cm³ and a velocity of 20 km/sec.

The corresponding marginal perforating masses are included in Table 4-3 for the 1 and 2 mil thicknesses in Explorer XVI and XXIII.

By similar reasoning the results of Figure 3-1 are directly applicable to the 200 μ and 400 μ plates of the Pegasus experiments. These plates are backed by 12 μ of mylar and .635 cm of open cell foam, which does not provide enough support to significantly effect the perforation properties. Moreover, the 200 μ and 400 μ plates are made of 2024-T3 aluminum, which is the alloy used in computing the results shown in Figure 3-1.

The 40 μ plates, however, are made from 1100-0 aluminum. An even more significant difference is that they are backed by 12 μ of mylar and 125 μ of hard epoxy resin. This backup structure provides enough support to materially modify the perforative properties of the aluminum plate. A quantitative assessment of the mass required to perforate the detector structure would require a numerical computation, and we only note here that the requisite mass will be larger than for an unsupported thickness of aluminum.

For the range of probable meteoroid parameters considered, the following extremes in $P/m^{1/3}$ are abstracted from Figure 3-1:

a) Maximum $P/m^{1/3}$: 6.1 cm/gm^{1/3}, corresponding to a density of 2.7 gm/cm³ and a velocity of 72 km/sec.

b) Minimum $P/m^{1/3}$: 2.7 cm/gm^{1/3}, corresponding to a density of 0.26 gm/cm³ and a velocity of 20 km/sec.

The corresponding marginal perforating masses are tabulated in Table 4-3 for plate thicknesses of 40μ , 200μ , and 400μ . As noted previously, the mass tabulated for the 40μ plate is probably lower than that actually required to produce a response in the Pegasus 40μ detector.

4.2.5 Summary of Mass Flux Data

The observational data on the meteoroid flux as a function of mass are summarized in Figure 4-2. All of these data have been adjusted to yield the flux on a randomly-oriented body in space near Earth. The photographic meteor data of Hawkins and Upton, analyzed by correcting the mass of a zero order, 30 km/sec meteor as outlined in Section 4.2.1, lie in the range between 10^{-2} and 1 gm. Proceeding toward larger fluxes, the radio meteor data of Elford et al are shown at a flux level of $5 \times 10^{-9}/\text{met}^2/\text{sec}$. Plotted are cumulative masses corresponding to velocities of 20, 30, and 72 km/sec. Heavier weight should be given to the 20 and 30 km/sec points, since most meteoroids are believed to fall in this range.

Next come the Explorer and Pegasus perforating flux data, which have been reduced to mass flux terms by use of the results of impact calculations in this program.

The average height of the Explorer XVI and XXIII orbits was such as to produce Earth shielding about $1/4$ of the time. In other words, the satellites were exposed to 3π steradians on the average. In Figure 4-2 the fluxes from Table 4-3 are reduced by a factor of 1.5 to yield the flux on a randomly-oriented body in space near Earth.

The rocket and satellite sounding board data summarized by Alexander et al and by McCracken fall at the highest flux levels. These data are also shown with a nominal correction of an order of magnitude towards smaller masses to account for the splash momentum.

It is seen in Figure 4-2 that most of the data for the photographic and radio meteors, and the perforating flux measurements of Explorer and Pegasus can be adequately represented by the smooth curve presented in the figure.

Two exceptions are the extreme velocity end of the radio meteors, and the 40μ Pegasus point. Undue significance should not be attached to the location of the radio meteor points, in view of the uncertainty in ionizing efficiency discussed in Section 4.2.2. The 40μ Pegasus point should probably be corrected to larger masses as discussed in Section 4.2.4.

Although the photographic, radio and satellite perforating flux data can be adequately represented by a smooth curve in Figure 4-2, it is seen that the sounding board data depart significantly from this curve. Indeed, even with the correction of splash momentum, the sounding board data differ from the perforating flux data by from one to two orders of magnitude. We are unable to account for this major discrepancy. However, it is noteworthy that the Explorer XVI satellite

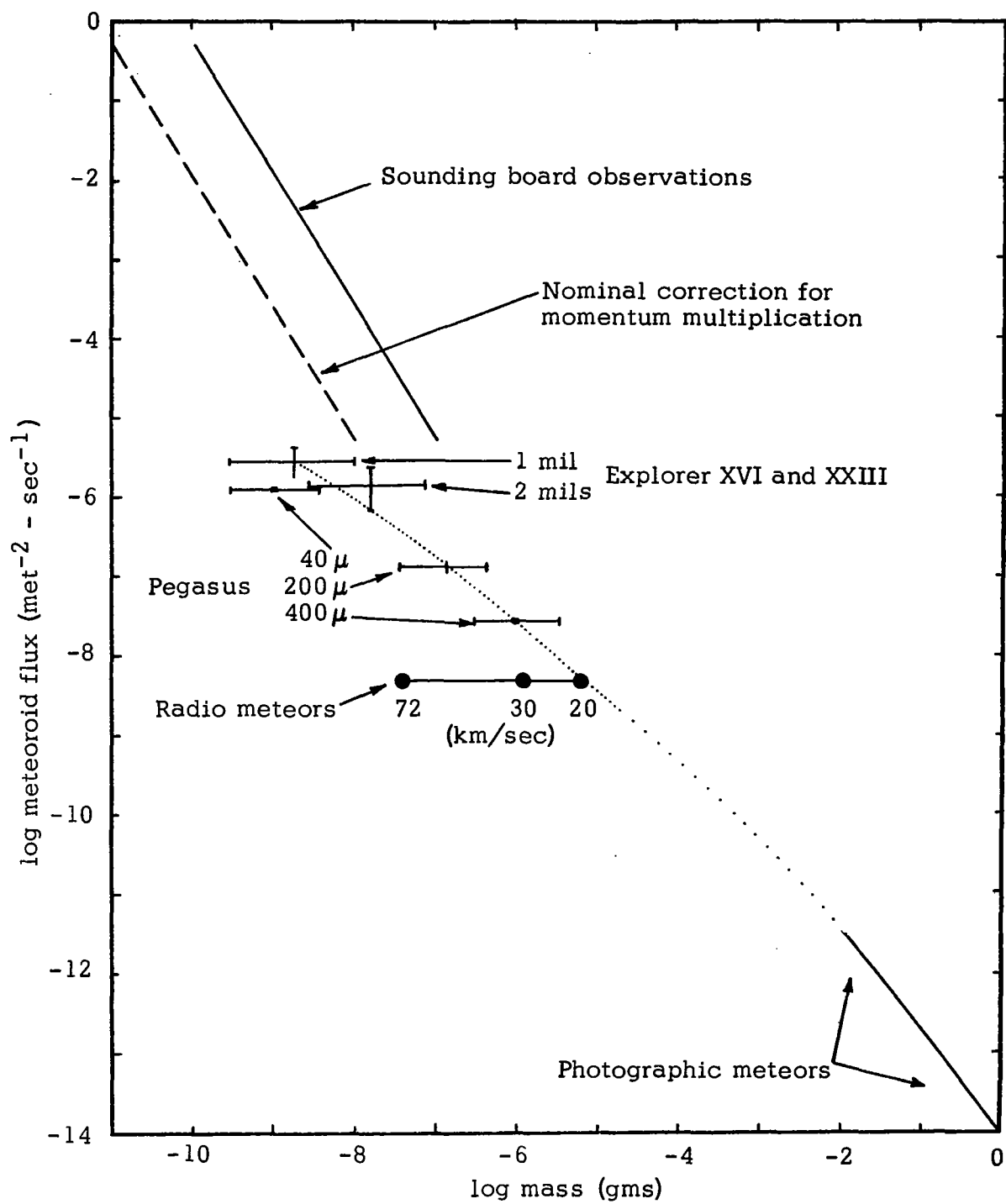


Figure 4-2
METEOROID MASS FLUX
NEAR EARTH

carried both pressurized container and sounding board experiments; the sounding board gave a substantially higher counting rate than did the pressurized cans. One must regard the fact that many containers were exposed for a long period of time and remained pressurized as placing an unambiguous upper limit on the penetrating flux for 1 and 2 mil copper-beryllium sheets. That this upper limit is substantially less than the counting rate of the microphone equipment carried on the same satellite thus weighs heavily in drawing the conclusions that the sounding board flux data are too high.

SECTION 5

CONCLUSIONS REGARDING PERFORATING FLUX

Figure 4-2 summarized the meteoroid mass flux data. To have direct relevance to the meteoroid hazard, these data can be reconstructed in terms of penetrating flux as a function of target thickness. Figure 5-1 shows the penetrating flux which we propose for aluminum and steel targets. In all cases, the data include the effect of earth-shielding. Hence, the penetrating flux pertains to exposure of a body near Earth.

Knowledge of the penetration rate of thin steel sheets permits us to compute the penetration rate of the equivalent aluminum thickness, and conversely. (Equivalent is used to imply that the same meteoroid will marginally perforate both sheets.) The concept of equivalent thickness is valid because the ratio of aluminum and steel thicknesses which a given meteoroid will marginally penetrate is remarkably constant over the regime of meteoroid parameters. As discussed in Section 4.1.3, we consider meteoroids of density .37 and 2.8 gm/cm³. The ratio of steel and aluminum marginally perforated by such meteoroids at 20 and 72 km/sec is tabulated in Table 5-1 for each encounter. Over the whole range the ratio is 1.8 ± 0.3 , and we take this to be the thickness ratio of aluminum and steel sheets which will experience the same penetration rate.

TABLE 5-1

Projectile Density (gm/cm ³)	Impact Velocity km/sec	$\frac{(P/m^{1/3})_{Al}}{(P/m^{1/3})_{Fe}}$
.37	20	2.1
.37	72	1.7
2.8	20	1.5
2.8	72	1.6

Thus 2024-T3 aluminum sheets of thickness 1.8 and 3.6 mils are computed to have the same penetration rates as measured by the 1 and 2 mil detectors of the Explorer XVI and XXIII satellites. Similarly, steel sheets of thickness 110 μ and 220 μ are computed to have the same penetration rates as the 200 μ and 400 μ Pegasus detectors. These computed equivalent thicknesses are used to make the appropriate entries in Figure 5-1.

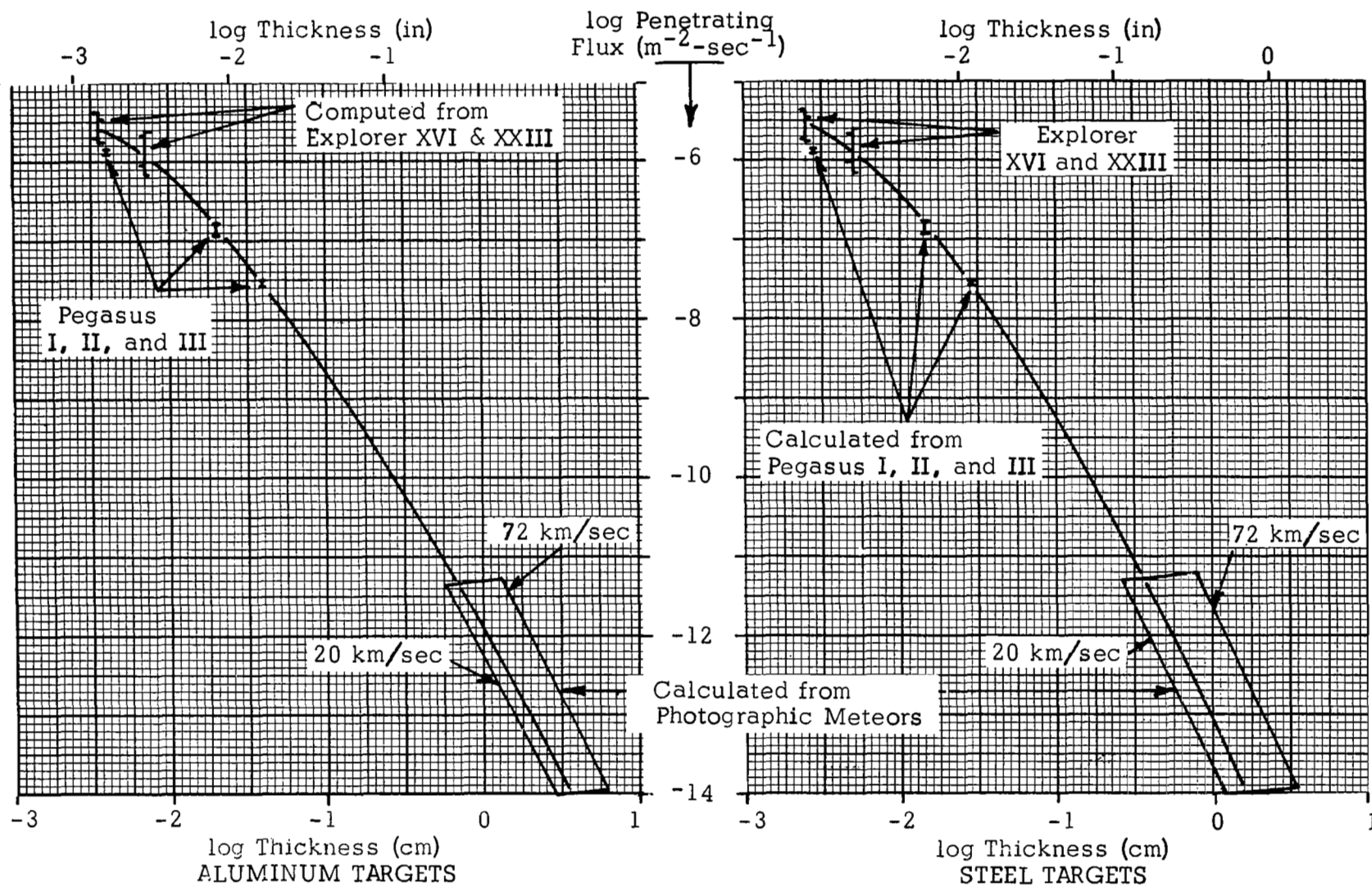


Figure 5-1: PENETRATING FLUX NEAR EARTH

The penetrating flux in the photographic meteor range was computed assuming meteoroids of density $.26 \text{ gm/cm}^3$ (Section 4.1.3), perforation powers as given in Figures 3-1 and 3-2, and the mass flux given by Eq. 4-2. The lines labeled 20 and 72 km/sec are penetration rates which would occur if every meteoroid impacted at that velocity. The preferred curve was constructed by assuming a median velocity of 28 km/sec.

APPENDIX A

ANALYTICAL FORMULATION OF AN EQUATION OF STATE FOR ALUMINUM

M. H. Wagner and R. L. Bjork

As part of this study, impacts by porous meteoroids having specific gravity of 0.44 are considered. In a hypervelocity impact, an extremely high specific internal energy is imparted to a porous substance. At a given impact pressure, this specific internal energy is far greater than that imparted to a substance whose density is initially normal. Therefore, equations of state based only on experimental observations of the Hugoniot involving initially solid materials are prone to be inaccurate in the state region attained by porous particles upon impact.

In the past few years, Russian scientists (Kormer, et al, 1962) have generated experimental equation of state data by shocking porous samples. The states so produced are much closer to the states achieved by porous meteors when they strike aluminum or iron structures. Accordingly, it was felt necessary to lay heavy emphasis on these experiments. To this end, existing equations of state were modified to agree with the experiments conducted by the Russian scientists on porous metal samples, and to fit other available data.

The equation of state data generated by Kormer, et al (1962) in hitherto inaccessible state regions has indicated that most equations of state currently in general use may be in error in states not close to the Hugoniot. This error has arisen largely from the inability to satisfactorily determine the variation of specific heat and the Gruneisen coefficient with temperature at high temperatures. The form of the equation of state proposed by Kormer et al has been evaluated and found to adequately predict the new experimental data as well as all of the old data. However, it was discovered that their fit was in error with respect to the electronic thermal contributions in the Thomas-Fermi region, due to their use of interpolation equations to predict intermediate temperature states. Specifically, this error leads to too low a value for the "limiting" compression of a metal. In addition, it was noted that these equations did not satisfy the requirement for thermodynamic consistency, viz.,

$$\left(\frac{\partial E}{\partial V}\right)_T = T^2 \frac{\partial}{\partial T} \left(\frac{P}{T}\right)_V \quad (A-1)$$

An evaluation of the equation of state formulation by Tillotson (1962) was made to see if it might be in agreement with the new data on porous samples. A comparison of predicted Hugoniot points using this formulation with the experimental data is given in Table A-1. As may be seen, the agreement is not sufficiently close to warrant its use without modification.

A translation of the Russian equation of state into a general computer code has been made by McCloskey (1964), after certain modifications and extensions of the Russian work.

TABLE A-1: COMPARISON OF RUSSIAN EXPERIMENTAL DATA WITH
TILLOTSON'S EQUATION OF STATE

Porosity	Compression	Pressure (Mb)	
		Experimental	Tillotson
- Tungsten -			
1.80	1.212	3.58	3.547
1.80	1.065	1.31	1.071
1.80	1.017	0.31	0.248
2.06	1.00	0.285	0.227
2.096	1.00	1.174	0.904
2.59	1.00	2.865	2.689
4.00	0.789	2.160	1.779
4.00	0.773	0.727	0.382
4.00	0.938	0.187	0.197
- Aluminum -			
1.00	2.185	4.93	4.813
1.43	1.498	1.391	1.404
2.08	1.176	1.003	0.790
2.98	1.015	0.702	0.559
- Copper -			
1.00	1.960	9.55	10.321
1.57	1.395	2.626	3.457
1.57	1.595	7.01	9.309
2.00	1.219	2.204	2.975
2.00	1.402	5.95	8.231
3.01	1.045	1.582	2.595
4.00	0.927	1.260	2.228
4.00	1.018	3.54	5.676
- Nickel -			
1.00	1.946	9.56	8.811
1.43	1.364	2.908	2.678
1.75	1.261	2.469	2.372
1.75	1.295	6.87	4.517
3.00	0.941	1.639	1.251
3.00	0.949	4.67	2.845

This equation of state assumes that the pressure and specific internal energy may be represented as the superposition of three effects.

$$P(\eta, T) = P_C(\eta) + P_n(\eta, T) + P_e(\eta, T) \quad (A-2)$$

$$E(\eta, T) = E_C(\eta) + E_n(\eta, T) + E_e(\eta, T) \quad (A-3)$$

where the terms in the above equations represent respectively the effect of atomic lattice interaction at 0°K, thermal vibration of the lattice ions, and the thermal excitation of the electrons (McCloskey, 1964).

ZERO DEGREE ISOTHERM

At 0°K only the electrons contribute to the pressure and specific internal energy. The only contribution which the nuclei can make to the pressure and energy is through their kinetic energy, but their kinetic energy is essentially zero at 0°K so that they affect neither of these quantities significantly. The contribution of the electrons arises from their resistance to compressive forces. One may regard the increase in electronic energy as arising from the individual electronic quantum states being raised due to compression and the pressure as the partial derivative of the energy increase with respect to volume.

The Thomas-Fermi model is incorrect at low densities and pressure, since it neglects the binding energy of the solid. However, it becomes correct at high densities and pressures when this binding energy is negligible compared with the total energy. Thus, at high densities, the cold curves should approach the T-F curves. Information on the pressure and energy due to the electrons can be derived from compressibility data at near normal densities and low pressures. In this regime, compression results in distortion of the electronic wave function about the individual nuclei and it is the resistance of electrons to this deformation which constitutes the strength of solids.

For values of η up to about 2.5 in the solid phase, McCloskey uses the formulation of Al'tshuler, et al (1962) to approximate P_C :

$$P_C = A_1 \{ \eta^{2/3} \exp [b_1 (1 - \eta^{-1/3})] - \eta^{4/3} \} \quad (A-4)$$

This expression is supposed to account for the resistance of electrons to compression at 0°K and at densities near normal. Accordingly the constants A_1 and b_1 may be derived from experimental measurements at low pressures. McCloskey effectively describes how they may be derived from γ_0 and K_0 , which are the Gruneisen constant and bulk modulus respectively. In this regime, the electronic energy is given by:

$$E_C = \frac{1}{\rho_0} \int P \frac{d\eta}{\eta^2} \quad (A-5)$$

which leads to:

$$E_C = \frac{3A_1}{\rho_0} \left\{ \frac{1}{b_1} \left(\exp [b_1 (1 - \eta^{-1/3})] - 1 \right) - \eta^{1/3} + 1 \right\} \quad (A-6)$$

At high pressures P_C and E_C must join smoothly onto the zero temperature Thomas-Fermi curve. McCloskey makes this fit by appending a quadratic term to expression (A-4) at high pressures. More precisely the high pressure fit is given by:

$$P_C = P_C(\eta_b) + \frac{dP_C}{d\eta}(\eta_b)(\eta - \eta_b) + A_2(\eta - \eta_b)^2, (\eta \geq \eta_b) \quad (A-7)$$

Use of the derivative in the linear term assures a smooth first derivative and the constant A_2 is fit by picking on arbitrary point on the TFC zero temperature curve. As McCloskey points out, this procedure leads to a discontinuous second derivative. The consequences of this are discussed in the next section.

At the point where the slope of the cold curve is zero, it is assumed that for smaller compressions only the gas phase can exist. In this region, P_C is chosen to be:

$$P_C(\eta) = A_3\eta^2 \quad (A-8)$$

consistent with van der Waals equation of state.

No basic changes were made in the above formulation for P_C and E_C ; however, the value of η_b was adjusted such that the Hugoniot pressure fitted a high experimental point, and corrections on the total pressure and energy were made to eliminate the critical values arising from use of van der Waals equation of state in the gas phase.

NUCLEAR THERMAL CONTRIBUTION TO PRESSURE AND ENERGY

In the framework that has been specified, the nuclei contribute to the energy only through their kinetic energy. At low temperatures, the kinetic energy assumes the form of lattice vibrations, i.e., vibrations of each nucleus about its equilibrium position. In this regime, one cannot draw a sharp distinction between the nuclear and electronic energy for in the process of vibrating, both components of energy (potential and kinetic) are present. It is clear that since the majority of the mass of the solid resides in the nuclei, the kinetic energy is almost entirely due to the nucleus. However, the potential energy, which on the average equals the kinetic energy, must reside in the mechanism which comprises the "spring constant." As may be seen from the Born-Oppenheimer model, this mechanism is the potential energy of the electronic configuration. Thus, the energy specified by the Debye formulation contains an element of electronic potential energy. However, this potential energy arises from distortion imposed upon the average electronic density which is a function only of compression. Therefore, it is reasonable to regard the distortional component of electronic energy separate from P_C and E_C . At temperatures a few times the Debye temperature each lattice vibration is fully excited, leading to an energy of kT per vibrational degree of freedom. As is well known, half of this energy is due to kinetic energy of the nucleus and half is due to the potential energy of the electronic cloud. As a result, the total energy is equal to $3NkT = 3RT$. This is a manifestation of the fact that there are three N independent modes of lattice vibration in a material sample containing N atoms. When the material is raised to very high temperatures, the nuclei can translate with-

out perturbing the electronic wave function. Therefore, in this limit, the nuclear energy is entirely due to kinetic energy, which is equal to $1/2 kT$ for each degree of freedom. Consequently in this limit, E_n is equal to $3/2 RT$. When the Debye formulation is valid, the pressure may be calculated from the Gruneisen formulation:

$$P_n(\eta, T) = \eta \rho_0 \gamma E_n \text{ (low temperature)} \quad (A-9)$$

whereas at the limit of high temperature it assumes the form of an ideal gas:

$$P_n(\eta, T) = \eta \rho_0 T \text{ (high temperature)} \quad (A-10)$$

The transition between these regimes is accomplished mathematically by use of the interpolation equations proposed by Kormer et al (1962):

$$E_n(\eta, T) = \frac{3}{2} \frac{2+Z}{1+Z} RT \quad (A-11)$$

$$P_n(\eta, T) = \eta \rho_0 \frac{3\gamma + Z}{1+Z} RT \quad (A-12)$$

where
$$Z = \rho_0 \frac{RTA}{K(dP_C/d\eta)} \quad (A-13)$$

This formulation provides, in effect, reduction of the Gruneisen coefficient, through Z , with increasing temperature. It was noted in the previous section that $\frac{d^2 P_C}{d\eta^2}$ was discontinuous at the point, η_b . Since the Gruneisen coefficient is dependent upon $\frac{d^2 P_C}{d\eta^2}$:

$$\gamma = \frac{1}{3} + \frac{\eta}{2} \frac{d^2 P_C / d\eta^2}{dP_C / d\eta} \quad (A-14)$$

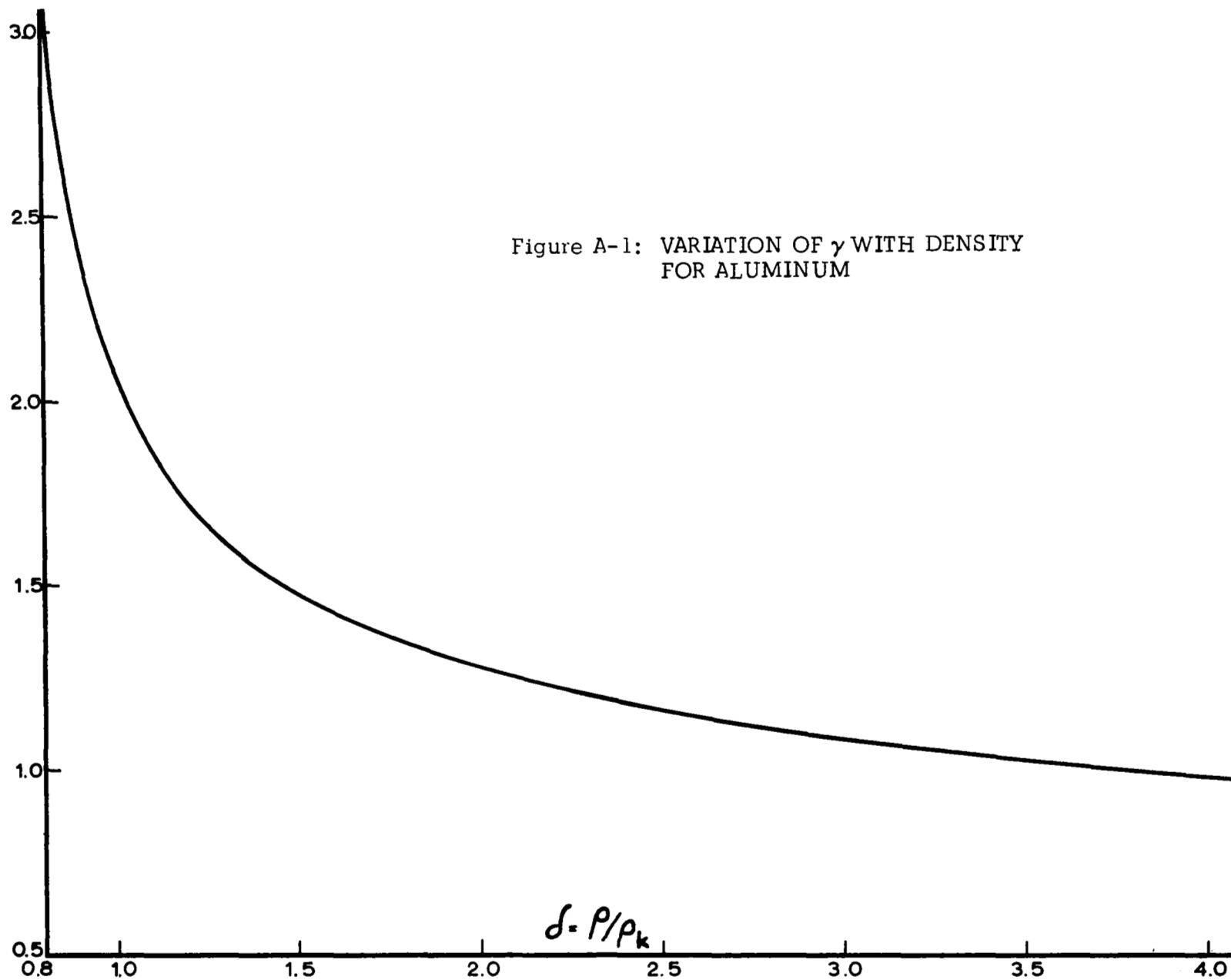
P_n will also be discontinuous at this point. This effect produced a marked break in the Hugoniot. To rectify this, the calculation for γ was changed to be

dependent on $\frac{d^2 P_{C1}}{d\eta^2}$ for both regions, where P_{C1} is given by the equation for

the lower compression region (Eq. A-4). The variation of γ with density for aluminum is shown in Figure A-1. The error in P_n that might be expected, due

to the fact that γ is not exactly dependent on $\frac{d^2 P_C}{d\eta^2}$ above the branch point,

is not significant since the Z factor predominates at physically attainable states where $\eta \geq \eta_b$.



ELECTRONIC THERMAL CONTRIBUTION TO PRESSURE AND ENERGY

It was noted in the first section that compression raises the electronic quantum states of each electron and therefore the electronic energy of the whole solid is raised. This effect was taken into account in computing P_c and E_c . In addition, at any given volume, increasing the temperature also raises the electronic energy, because the higher quantum states become more highly populated as temperature increases. At low temperatures, the electronic thermal contribution can be expressed as:

$$E_e(\eta, T) = \frac{1}{2} \beta(\eta) T^2 \quad (A-15)$$

$$P_e(\eta, T) = \frac{1}{2} \eta \rho_0 g(\eta) \beta(\eta) T^2 \quad (A-16)$$

where β has the form:

$$\beta = \beta_0 \eta^{-g} \quad (A-17)$$

At very high temperatures, the electrons become completely ionized and behave as an ideal gas. In the intermediate region, Latter's (1955) solutions of the Thomas-Fermi equation for $T \neq 0$ are applicable. Both Kormer and McCloskey have proposed equations that approximate these solutions, and which assume the proper limiting forms. However, as noted previously, these equations are not in agreement with Latter's results in the transition region and are also not thermodynamically consistent.

A new fit, based on Latter's data, was derived in the form:

$$E_e = A(T) \sum_i a_i \ln^i \left[\frac{V}{B(T)} \right] \quad (A-18)$$

where A and B were the coordinates (E, V) of the intersections of the E_e isotherms with the cold compression curve. The pressure was found from integration of Eq. (A-1) and fitting the constant of integration $g(V)$ to Latter's data. The resultant expressions provided a satisfactory fit but were of a rather unwieldy form. They are presented in a later section of this appendix.

EQUATION OF STATE FOR HYDRODYNAMIC CODE CALCULATIONS

Having at hand a complete analytical equation of state, it was then necessary to determine how it could be efficiently incorporated into the hydrodynamic code. Since the code requires that successive values of the pressure must be determined from given sets of (η, E) , it would be necessary to first perform iterations on T until the given internal energy was found before the pressure could be computed. It was evident that each computational cycle would be quite long, due to the complexity of the equations involved in determining each contribution.

It was therefore decided to construct a table of the equation of state, consisting of a matrix of pressure elements P_{ij} , where i and j correspond to certain values of η and E . The hydrodynamic code could then compute the pressures it needed by two-way interpolation in the table, which is a rapid process. A disadvantage of the table is that storage in core must be allotted for it; however, this was determined to not be a prohibiting factor, if the table was well-structured. This was achieved by setting the intervals in η and E to constant increments of $\ln \eta$ and $\ln E$. This structure (1) eliminated the necessity of storing the η and E values, (2) permitted a wide range of pressures to be covered with a relatively small number of elements, and (3) shortened the interpolation process time.

The following values of η and E were chosen:

$$\eta_i = \exp(-4.7 + 0.1 i) \quad i = 1, \dots, 70 \quad (\text{A-19})$$

$$E_j = \exp(-7.1 + 0.2 j) 10^{12} \text{ ergs/gm} \quad j = 1, \dots, 70 \quad (\text{A-20})$$

Thus, the approximate ranges of $10^{-2} \leq \eta \leq 10^1$ and $10^9 \text{ ergs/gm} \leq E \leq 10^{15} \text{ ergs/gm}$ would be covered in the table by 4900 pressure elements.

The $P_{ij}(\eta, E)$ elements were computed by interpolation in a table of $P_{ik}(\eta, T)$ and $E_{ik}(\eta, T)$ computed from the previously described equation of state, with the following modifications:

a) Since each element was separately computed there was no need to use the analytic fit of the Thomas-Fermi data to evaluate the electronic contribution, so that instead direct interpolation of Latter's results could be used. Since these results did not cover all the lowest temperature states, extrapolation according to an $\alpha_1 T^2$ dependence was made from the lowest temperature Thomas-Fermi point for each η_i . This in effect permitted a separate evaluation of the coefficient of electronic specific heat (β) for each compression, rather than using a form such as:

$$\beta = \beta_0 \eta^{-9} \quad (\text{A-17})$$

as was done by McCloskey and Kormer.

b) In McCloskey's formulation of the zero temperature isotherm, it is assumed that only the gas phase can exist below a certain minimum compression (η_a) and that in this region the form of P_C is consistent with van der Waals equation of state for gases, while his basic equation for P_C represents the behavior of the solid in tension for compression between η_a and 1. This choice leads to the characteristic cubic fit with two critical values lying between the liquid and gaseous states of the isotherm. This form can result in erroneous paths of release adiabats and therefore incorrect values of the residual temperatures after passage of a shock wave through a material. Each isotherm exhibiting this effect was corrected by inserting a constant value of pressure P_k in the two-phase region such that:

$$\int_{V_1}^{V_2} [P(V) - P_k] dV = 0 \quad (A-21)$$

two-phase
region

Here V is volume and $P(V)$ is the total pressure along the isotherm before corrections. Having P_k , the energy was simply found from:

$$E = f E_1 + (1 - f) E_2 \quad (A-22)$$

where E_1 and E_2 are the energies at the ends of the two-phase region (100% liquid, 100% gas, respectively) and f is the fraction of liquid by weight, found from:

$$V = fV_1 + (1 - f) V_2 \quad (A-23)$$

P_k was determined by iteration of the integral equation.

The table of $P_{ik}(\eta, T)$, $E_{ik}(\eta, T)$ correspond to the same η_i values as before, and the following temperatures:

$$T_k = \exp(4.5 + 0.1 k) ^\circ K \quad k = 1, \dots, 116 \quad (A-24)$$

giving a range of $\sim 10^2 ^\circ K \leq T \leq \sim 10^7 ^\circ K$.

For positions in the $P_{ij}(\eta, E)$ table not covered by this range, values were obtained from linear extrapolation in a particular column.

The foregoing procedure was followed to construct a table of the equation of state of aluminum. After examination of the trend of the $P_{ij}(\eta, E)$ elements, and keeping the anticipated P, η, E limits of a given problem in mind, the size of the table was able to be reduced, by selecting particular rows and columns, to a 25 x 27 matrix.

Figure A-2 shows the new aluminum equation of state in the form of the P - V - T surface. The solid region occupies the front left side of the figure (low temperature and specific volume). A group of five isotherms is presented between $\sim 2000^\circ K$ and the critical isotherm and illustrates the behavior in the two-phase region wherein the liquid and vapor are in equilibrium. This region may be identified by the well-known property of isotherms within it, namely that pressure is constant along them. It is clear that at temperatures much larger than the critical temperature, the isotherms become straight lines on this logarithmic plot corresponding to ideal gas behavior. However, it is noted that in a wide temperature region above the critical temperature, the isotherms differ markedly from ideal gas behavior.

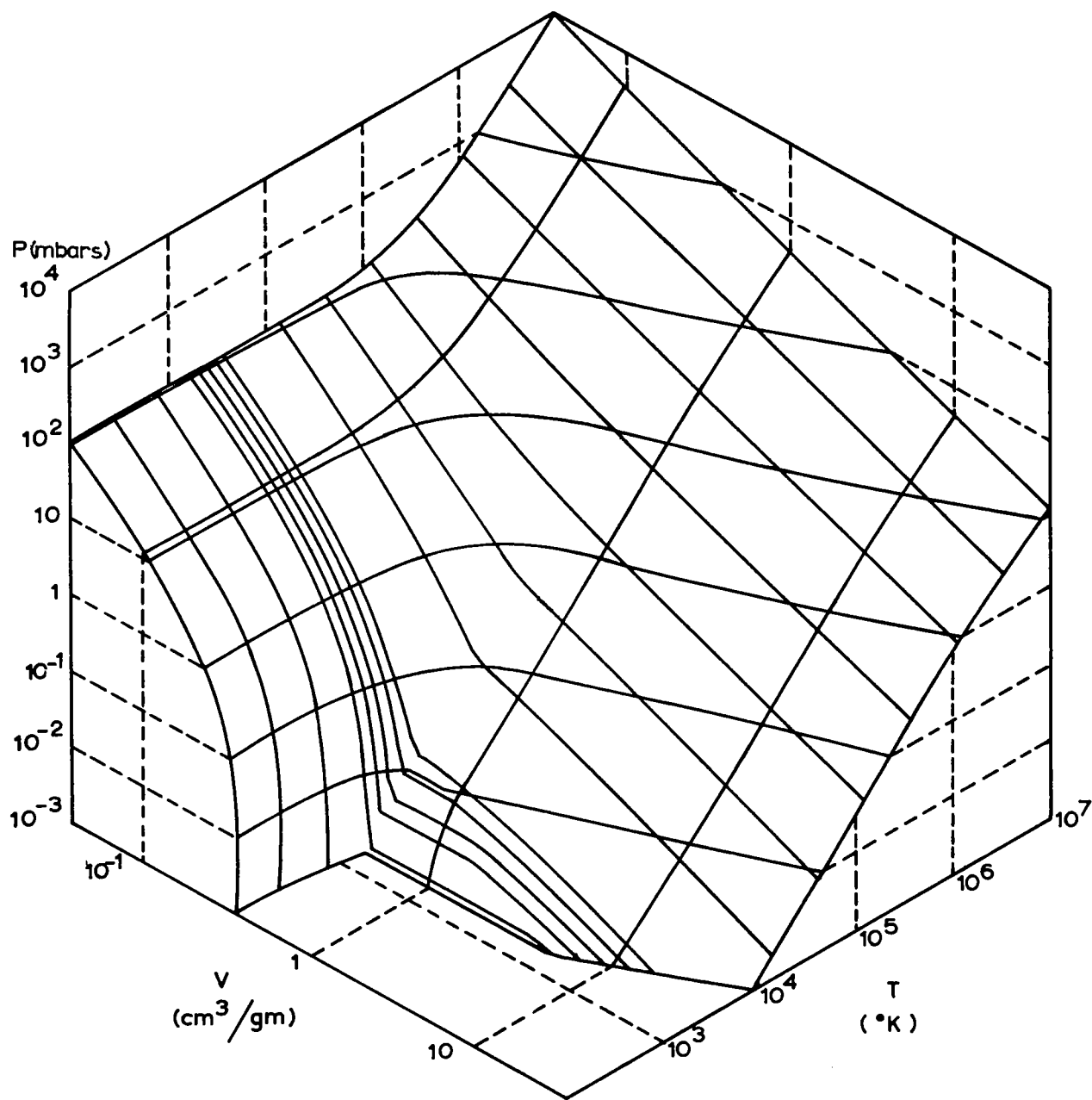


Figure A-2: ALUMINUM P-V-T SURFACE

CALCULATION OF HUGONIOTS, ADIABATS AND RELEASE TEMPERATURES

Based on the equation of state table compiled as described above for aluminum, $\rho_0 = 2.702$, the Hugoniot was computed for the following porosities: 1.00, 1.43, 2.08, 1.98, and 6.14. These curves are shown on the aluminum P-V-E surface in Figure A-3, along with the Russian experimental points (Kormer, et al 1962 and Al'tshuler, et al 1960).

A comparison was also made with experimental data recently given by Anderson, et al (1965), for Hugoniots of 1.4, 1.7, and 2.0 porous aluminum (Figure A-4). The apparent discrepancy for the 2.0 porous Hugoniot is probably due to experimental uncertainties (Anderson, et al 1965).

Comparisons of the Hugoniot for solid and 2.98 porous aluminum computed from other equations of state are shown in Figures A-5 and A-6. The aforementioned discontinuity in the Hugoniot at a compression of 2.0 is seen in the McCloskey formulation. The values of compression at high pressures in the McCloskey formulation (which is similar to that of Kormer in this region) are significantly less than that given by the Los Alamos (Harlow 1960) or this formulation, which are based on Thomas-Fermi theory. The Los Alamos fit, however, is in disagreement with the experimental data on porous samples, as at lower pressures it is based on the Mie-Gruneisen approximation and experimental data on solid aluminum.

The Hugoniot of the projectile in the impact problems of this study is shown in Figure A-7.

The Hugoniot pressure as a function of particle velocity is shown in Figure A-8. Shock velocity versus particle velocity is shown in Figure A-9.

The Hugoniot states were found by comparing the Hugoniot condition for pressure at a constant energy (E'),

$$P_i = \frac{2 \rho_0 \eta (E' - E_0)}{m\eta - 1} - P_0 \quad (A-25)$$

with the corresponding $P_{ij}(\eta, E)$ elements in the column of the table for $E = E'$.

The Hugoniot pressure was then calculated from linear interpolation between neighboring elements with differences ($P_i - P_{ij}$) of opposite sign. The compression and particle and shock velocities were computed from:

$$\eta = \frac{P + P_0}{m(P + P_0) - 2 \rho_0 (E - E_0)} \quad (A-26)$$

$$U = \left[\frac{m\eta - 1}{\rho_0 \eta} (P - P_0) \right]^{1/2} \quad (A-27)$$

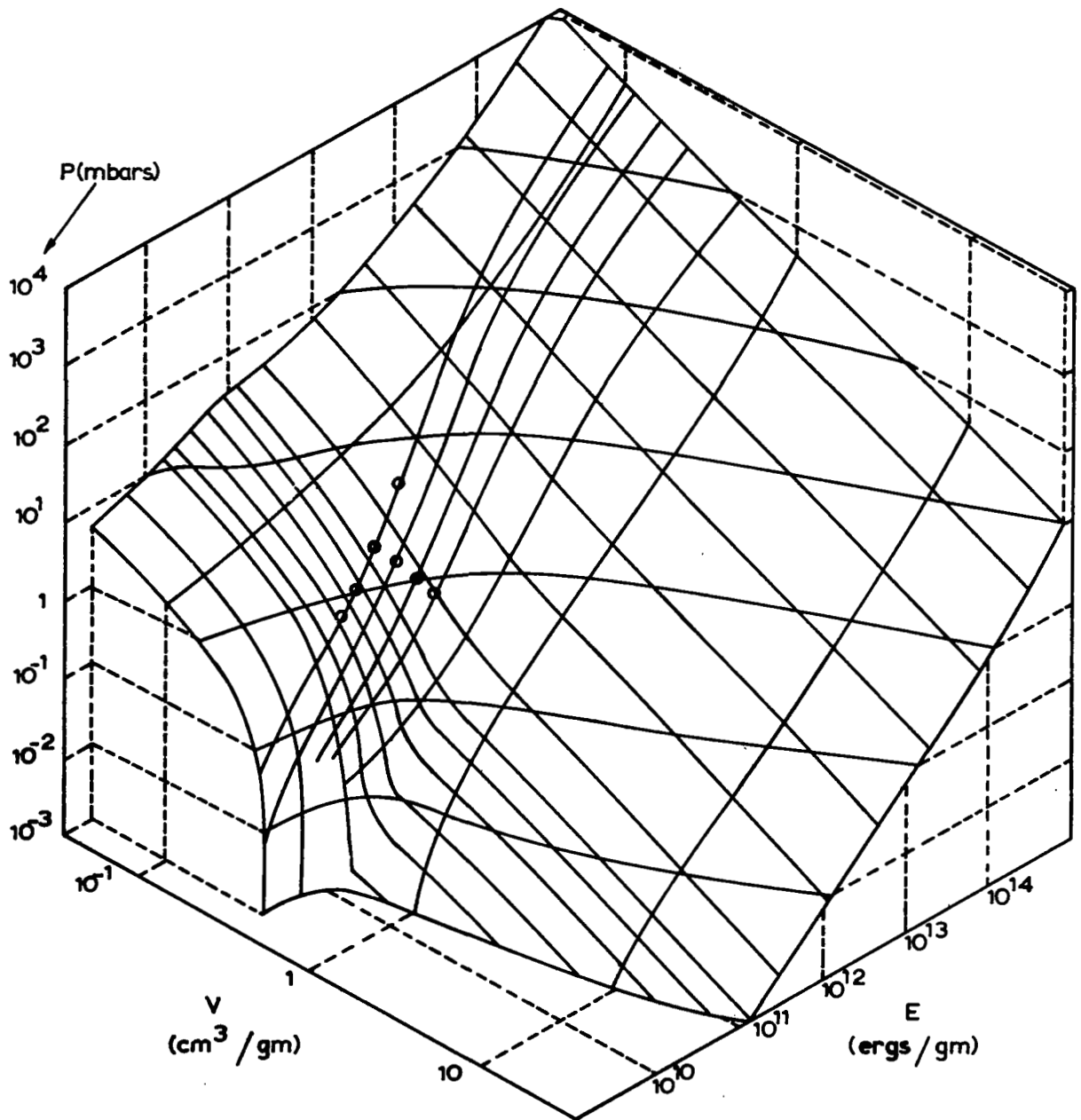


FIGURE A-3 ALUMINUM P-V-E SURFACE SHOWING HUGONIOTS
FOR POROSITIES = 1.00, 1.43, 2.08, 2.98, 6.14
(L. TO R.), AND RUSSIAN EXPERIMENTAL POINTS (\circ).

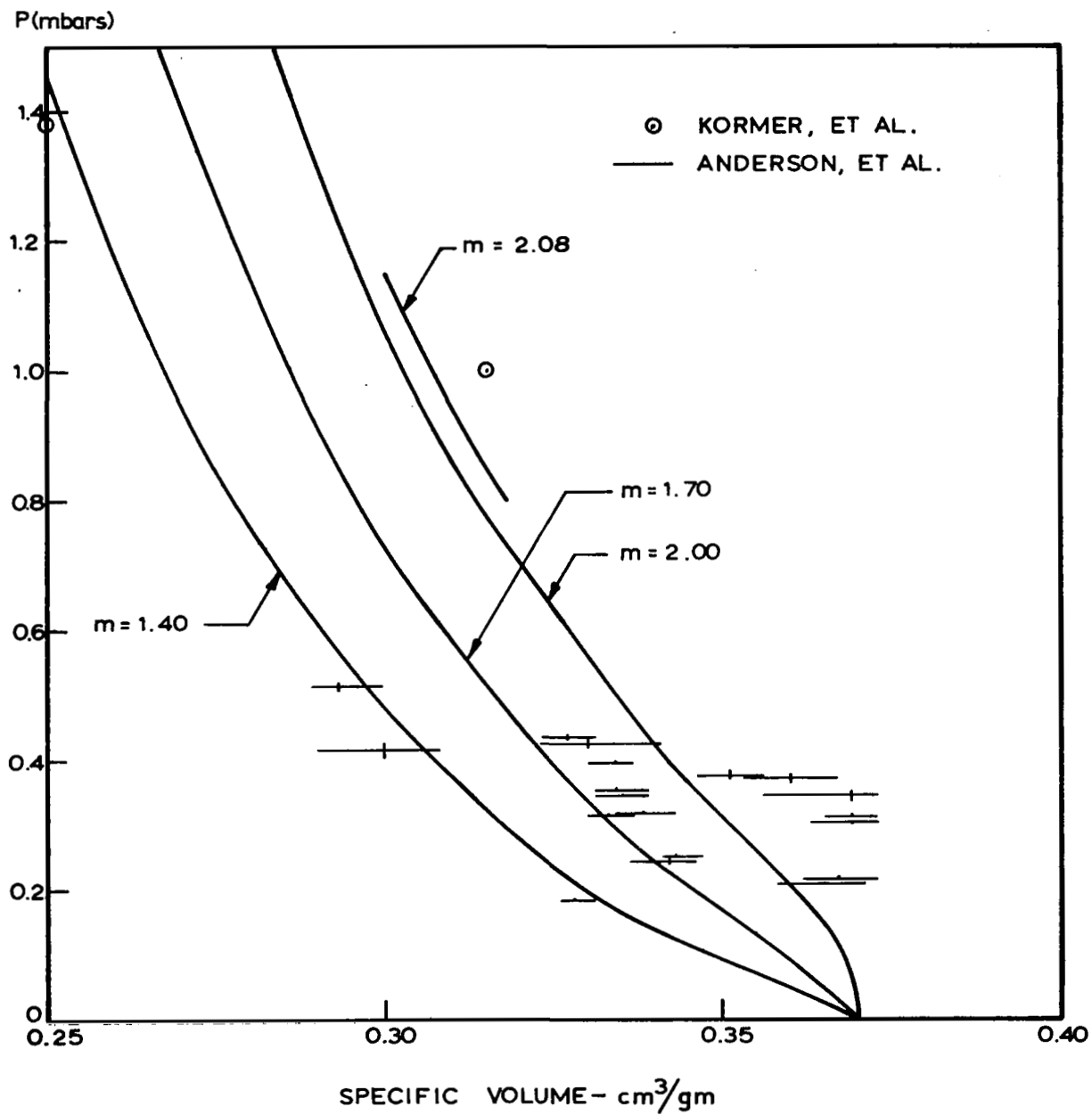


FIGURE A-4: COMPARISON OF ALUMINUM HUGONIOTS WITH EXPERIMENTAL DATA

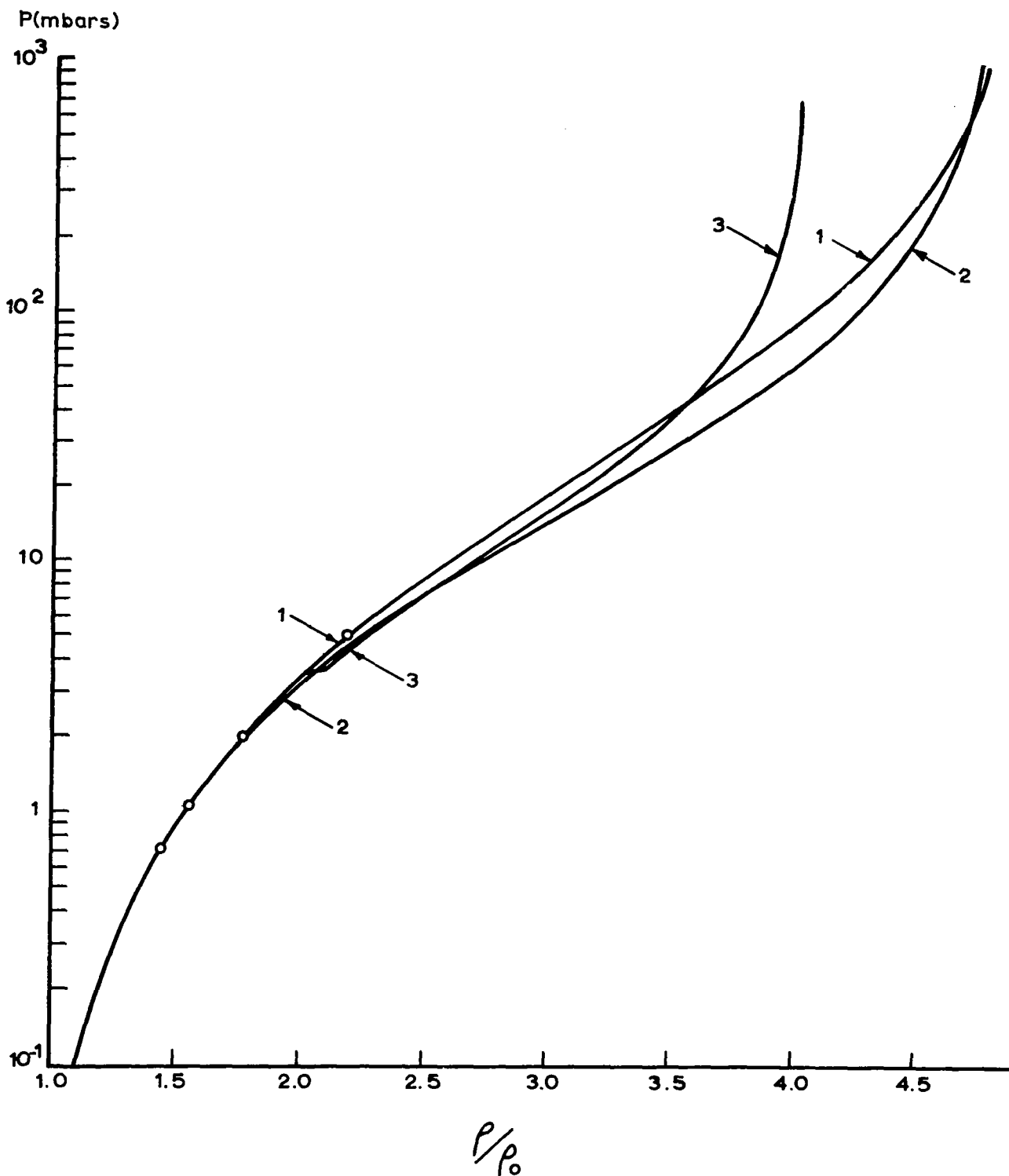


FIGURE A-5 ALUMINUM HUGONIOT, (1) THIS WORK, (2) AFTER LASL, (3) AFTER McCLOSKEY, ° SOVIET EXPERIMENTAL DATA

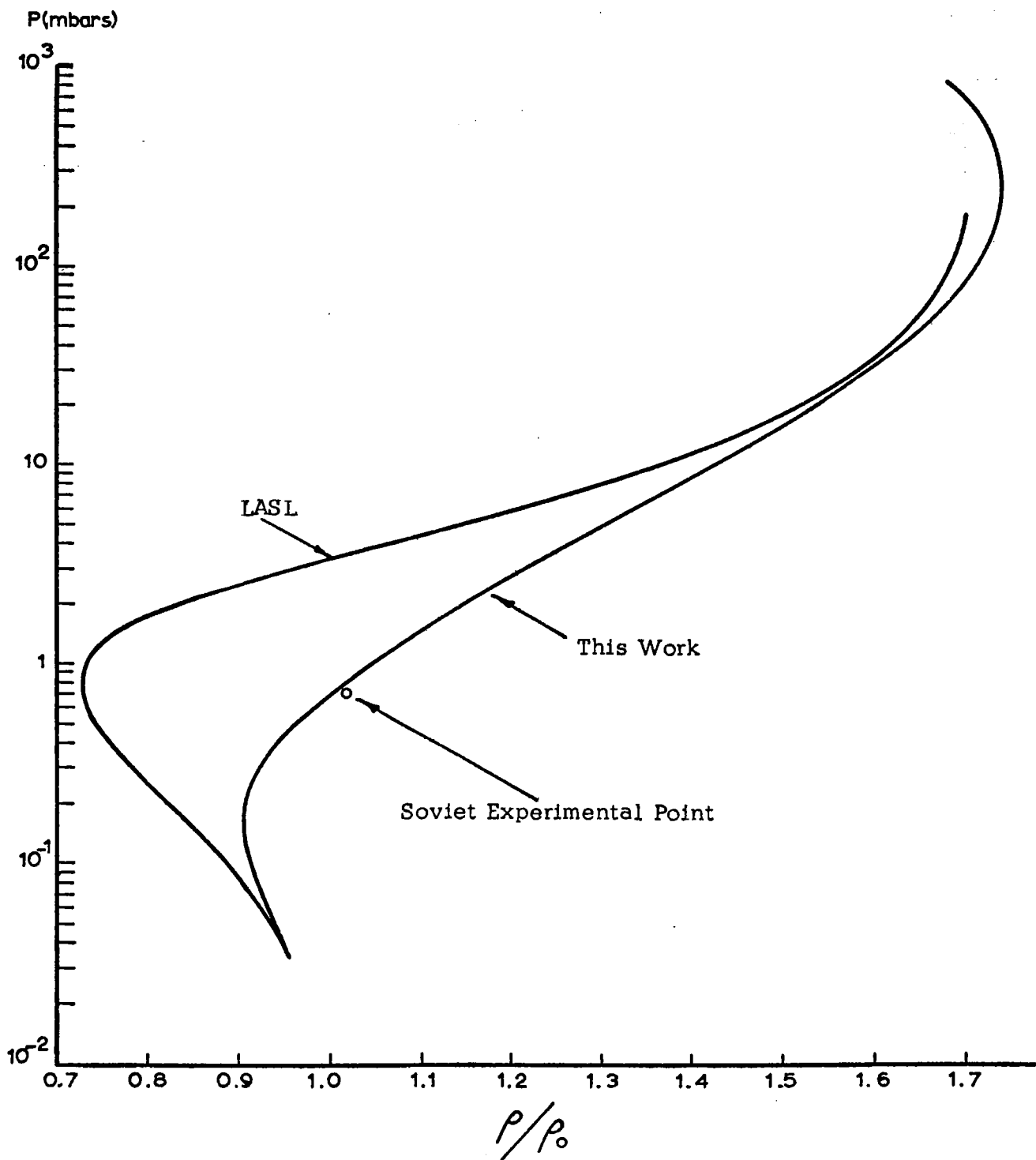


Figure A-6: ALUMINUM HUGONIOT
POROSITY = 2.98

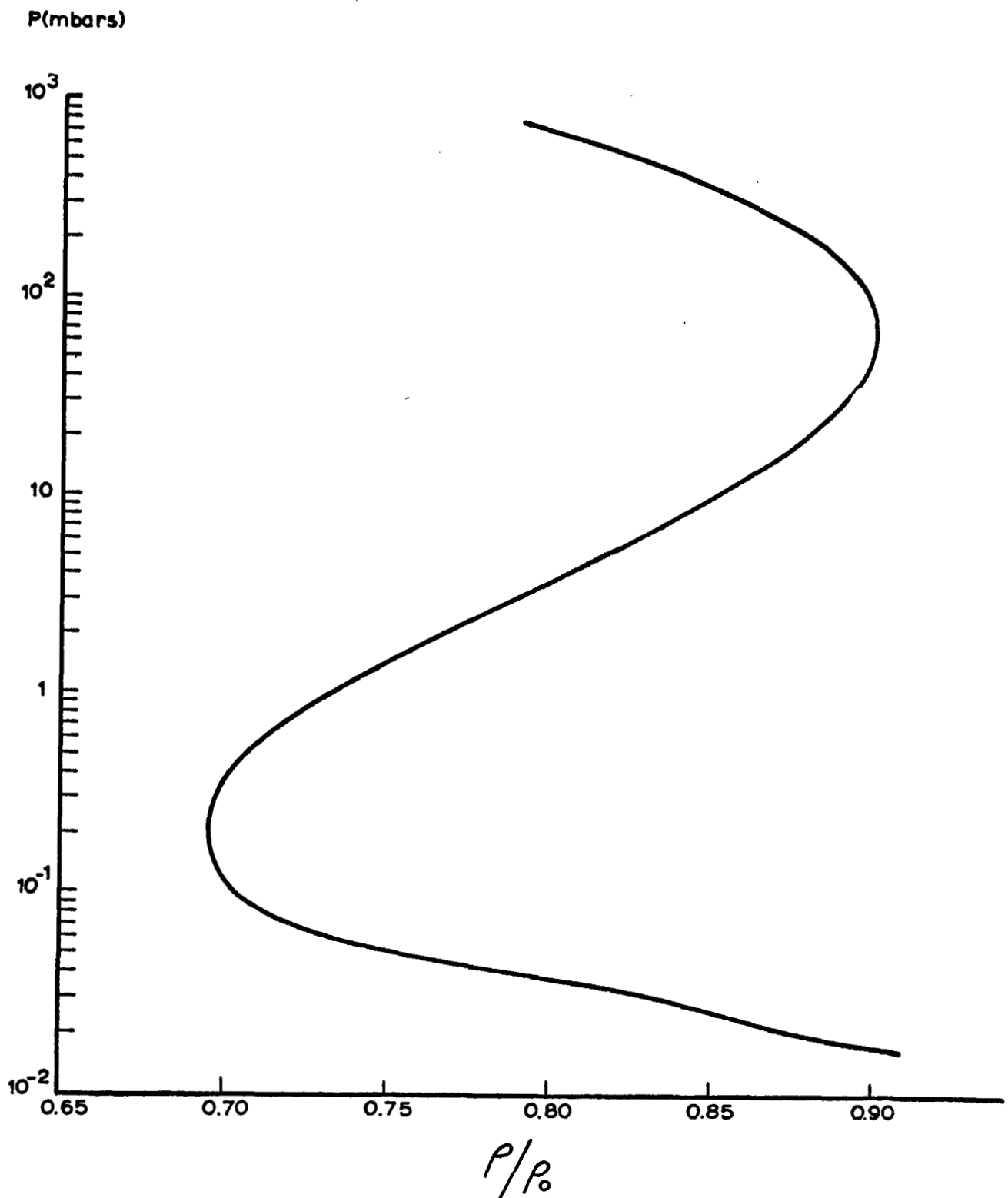


FIGURE A-7 ALUMINUM HUGONIOT, POROSITY = 6.14

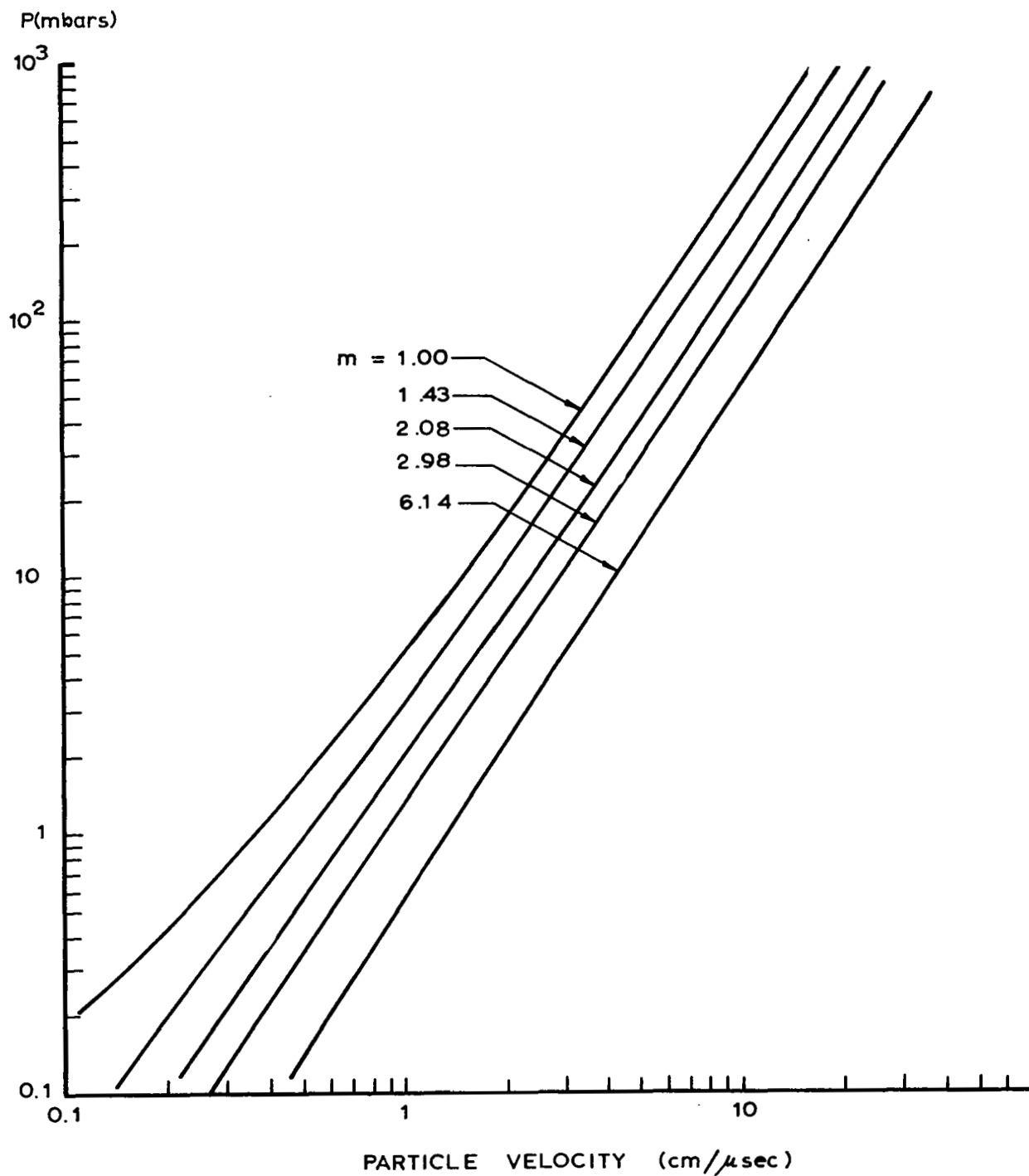


FIGURE A-8 PRESSURE VS PARTICLE VELOCITY FOR ALUMINUM HUGONIOT STATES FOR SEVERAL POROSITIES

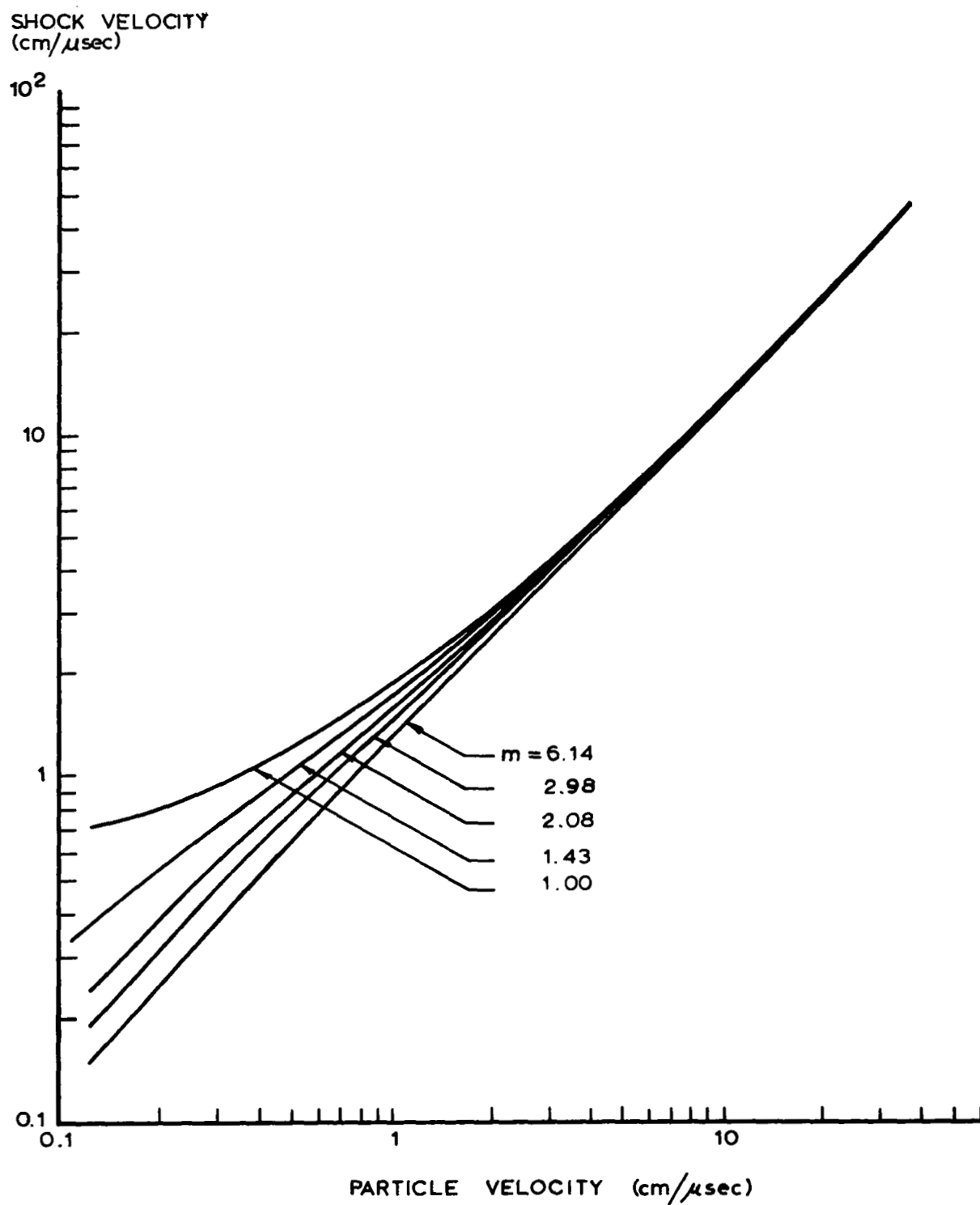


FIGURE A-9 SHOCK VELOCITY VS PARTICLE VELOCITY FOR ALUMINUM HUGONIOT STATES FOR SEVERAL POROSITIES

$$D = \frac{m (P - P_O)}{\rho_O U} \quad (A-28)$$

Release adiabats from the Hugoniot for $m = 1$ were calculated for over 65 spaced initial (Hugoniot) energies. Along an adiabat

$$dE = - PdV$$

or

$$dE = \frac{P}{\rho_O \eta^2} d\eta \quad (A-29)$$

The first point is the Hugoniot point. The second point was calculated from:

$$\begin{aligned} E_2 &= E_H - \frac{P_H}{\rho_O \eta^2} \Delta \eta_1 \\ \eta_2 &= \eta_H - \Delta \eta_1 \\ P_2 &= f(\eta_2, E_2) \end{aligned} \quad (A-30)$$

where $\Delta \eta_1 = 7.8125 \times 10^{-5}$ and P_2 was obtained from two-way interpolation in the table. The next eight points were calculated from:

$$\begin{aligned} E_{i+1} &= E_H - \frac{2P_i}{\rho_O \eta_i^2} \Delta \eta_{i-1} \\ \eta_{i+1} &= \eta_i - \Delta \eta \\ P_{i+1} &= f(\eta_{i+1}, E_{i+1}) \\ \Delta \eta_i &= 2 \Delta \eta_{i-1} \end{aligned} \quad (A-31)$$

At this point $\Delta \eta = .01$ and was held constant for the remaining points (i=8)

$$\begin{aligned} E_{i+1} &= E_{i-1} - \frac{2P_i}{\rho_O \eta_i^2} \Delta \eta \\ \eta_{i+1} &= \eta_i - \Delta \eta \\ P_{i+1} &= f(\eta_{i+1}, E_{i+1}) \end{aligned} \quad (A-32)$$

The above scheme is a centered-difference numerical integration technique, which requires two previous points. The second point is first generated by an ordinary difference integration step, but with an extremely small delta. Succeeding points are generated with the centered-difference technique using the first and last point, thus enabling delta to be doubled until the desired integration step is obtained. The remaining points are generated with the centered-difference technique, using the last two previous points.

Successive points in the path were computed until the first negative pressure was obtained. The release state was then calculated from interpolation between the last two points. In those cases where $\eta_i - \Delta\eta$ would become negative before release, $\Delta\eta$ was reduced by factors of ten as necessary at such points. From thermodynamic data given in Stull and Sinke (1956) the release temperatures were computed from the release energies. For temperatures above 3000°K (upper limit of data), the temperatures were calculated assuming a constant heat capacity of 4.97 cal/deg/gfw in the vapor state.

A few of the adiabats that were calculated are shown in Figures A-10 and A-11. A graph of release temperature vs shock pressure is shown in Figure A-12. Shock strengths required for the following phase changes are:

Incipient melting (932°K)	0.67 Mb
Complete melting	0.95 Mb
Incipient vaporization (2720°K)	5.8 Mb
Complete vaporization	26. Mb

ANALYTICAL FIT TO ELECTRONIC THERMAL CONTRIBUTION

The results of the numerical solution of the Thomas-Fermi equation obtained by Latter (1955, 1956) were used as the basis for deriving analytic expressions for the electronic pressure and energy. At selected temperatures, a set of pressure, energy, volume values was obtained by executing a 4 point, Lagrangian interpolation routine on the solutions to the Thomas-Fermi equation. These solutions were in the form of a series of 67 tables totaling about 1500 sets of values. To obtain the values of the electronic pressure and energy, the pressure and energy on the zero-temperature isotherm, for each particular volume, obtained from interpolation of data given in Latter (1956) were subtracted from the previously obtained values for the total pressure and energy. This procedure yielded sets of the electronic pressure and energy for particular volumes and temperatures.

The forms of $E(V, T)$ and $P(V, T)$ that might be chosen to fit the data were restricted to those that satisfied the requirements for thermodynamic consistency as given by Eq. A-1. From examination of graphs of the energy isotherms, it was noted that their shape $(\frac{V}{E} \frac{\partial E}{\partial V})$ was reasonably uniform and that the offset in temperature and volume approximately followed the intersections of the iso-

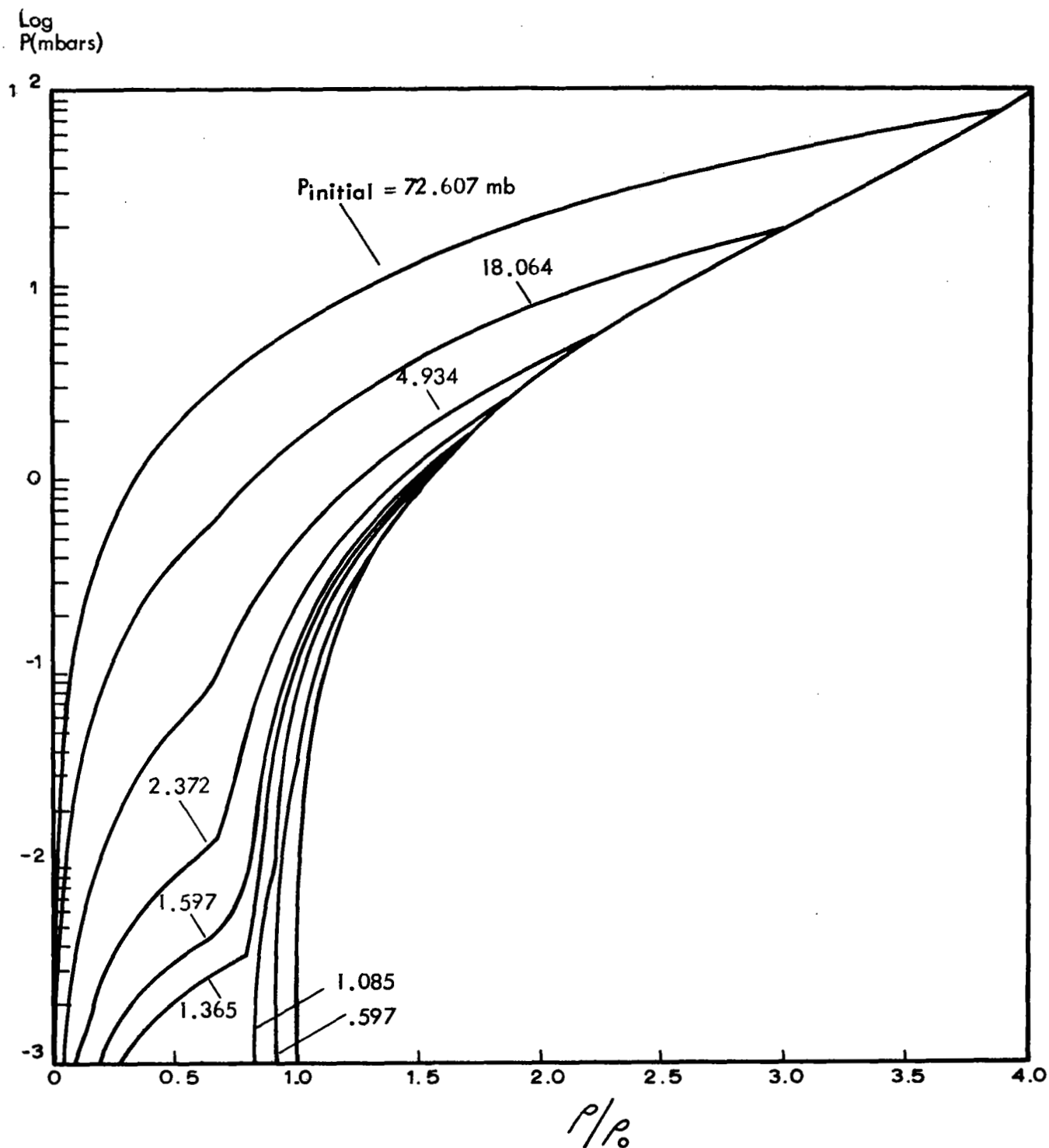


FIGURE A 10 ALUMINUM HUGONIOT AND REPRESENTATIVE ADIABATS

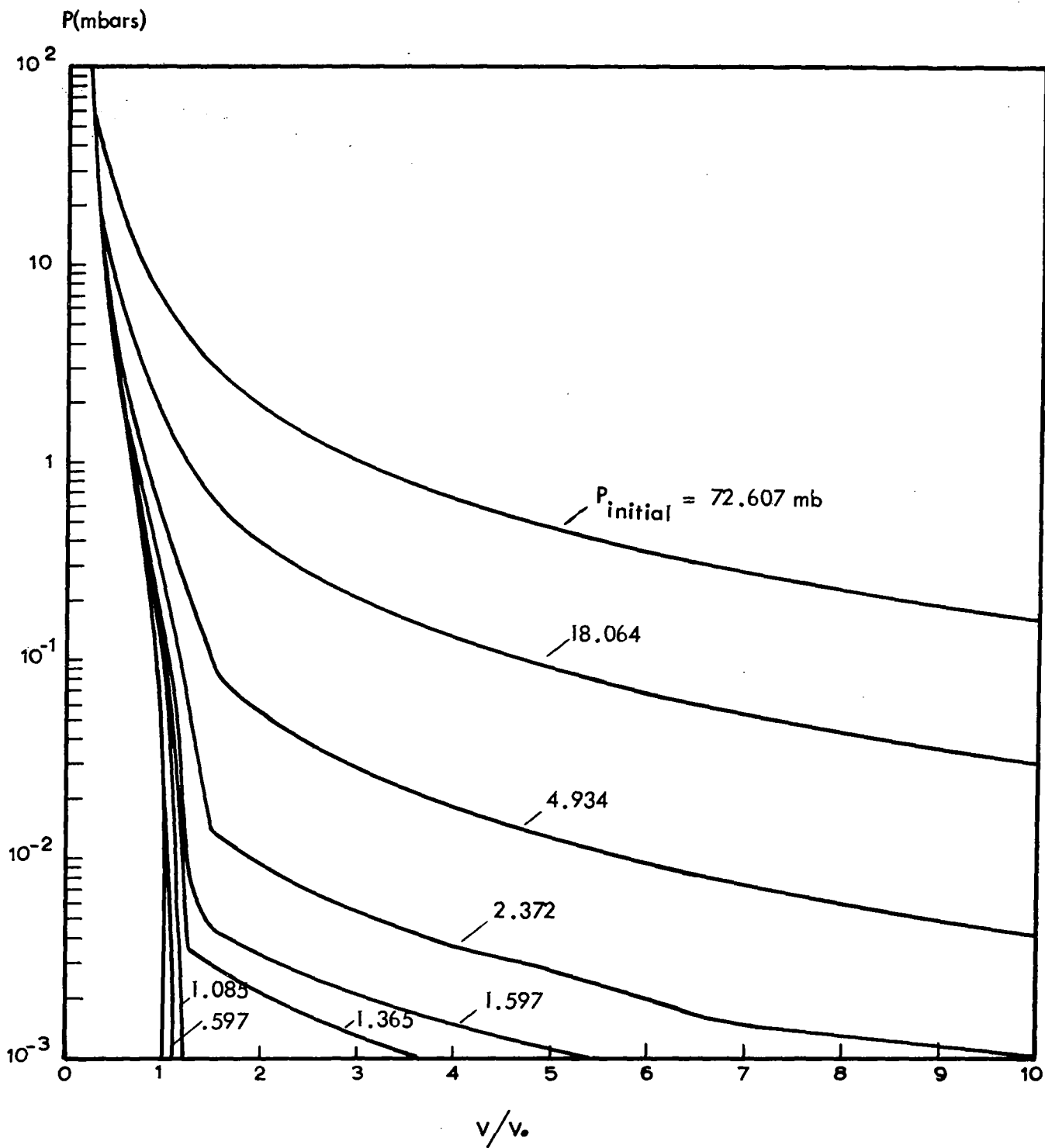


FIGURE A11 ALUMINUM HUGONIOT AND REPRESENTATIVE ADIABATS

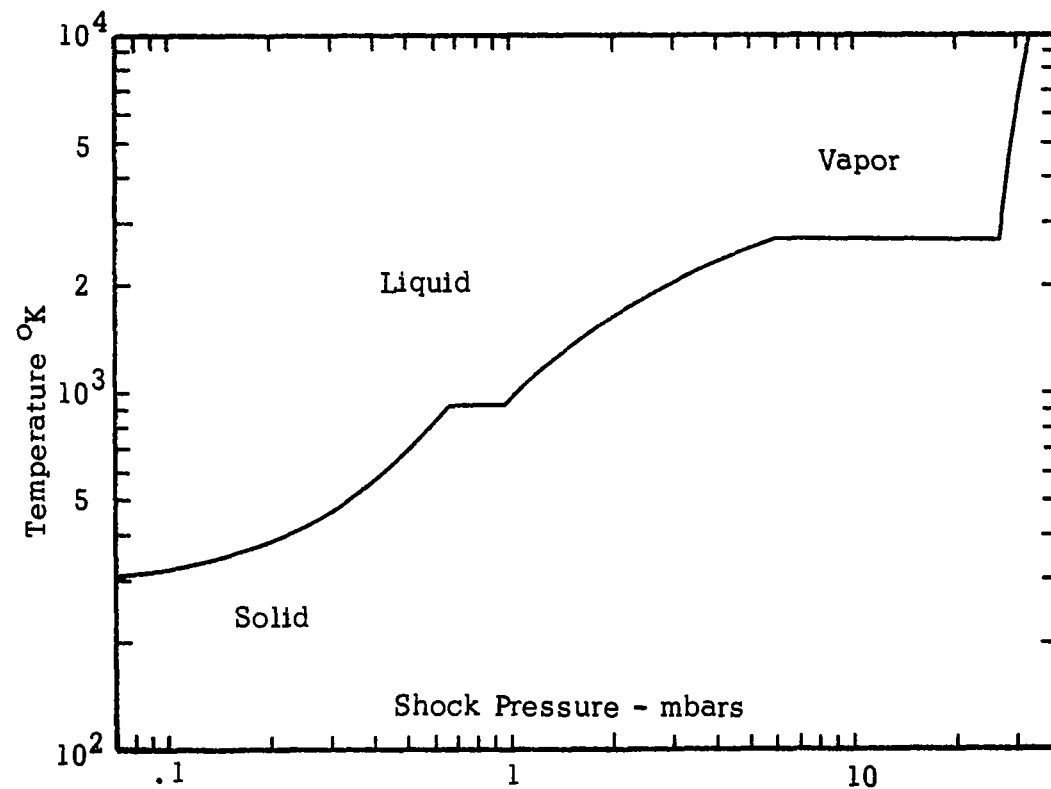


FIGURE A-12 TEMPERATURE AFTER SHOCK RELEASE
FOR ALUMINUM

therms with the cold compression curve. Denoting the coordinates of the intersections by $E_C(T)$, $V_C(T)$, it thereby appeared appropriate to express the electronic energy in the form

$$\frac{E}{E_C} = f\left(\frac{V}{V_C}\right) \quad (A-33)$$

From examination of graphs of $E_C(T)$ and $V_C(T)$ vs T , it was evident that a polynomial function of the form: $\ln V_C = \sum_{n=1} c_n \ln^{n-1} T$ would provide a satisfactory

fit to the data. A similar expression for E_C would have also been desirable;

however, requirements for integration of $\frac{1}{T^2} \left(\frac{\partial E}{\partial V} \right)_T$ to obtain the pressure precluded this. Instead a weighted least-square polynomial fit was selected of the form:

$$E_C = \sum_{n=1} a_n T^{n-1} \quad (A-34)$$

where

$$\sum_{i=1}^N \left(\frac{1}{E_{Ci}} \right)^2 \left(\sum_{n=1}^M a_n T_i^{n-1} - E_{Ci} \right)^2 \text{ was minimized.}$$

Least-square polynomial coefficients were then determined for

$$\frac{E}{E_C} = \sum_{n=1} b_n \ln^{n-1} \left(\frac{V}{V_C} \right) \quad (A-35)$$

The resultant expression for the electronic energy was selected as:

$$E = E_C \left[b_1 + b_2 \ln \frac{V}{V_C} + b_3 \ln^2 \frac{V}{V_C} \right] \quad (A-36)$$

where

$$E_C = \sum_{i=1}^7 a_i T^{i-1} \quad (A-37)$$

$$\ln V_C = c_1 + c_2 \ln T + c_3 \ln^2 T \quad (A-38)$$

The next step was to determine the expression for the pressure from the thermodynamic relation (Eq. A-1). From Eqs. A-36, A-37, and A-38,

$$\begin{aligned} \frac{1}{T^2} \left(\frac{\partial E}{\partial V} \right)_T &= V^{-1} (b_2 + 2b_3 \ln V) \sum_{i=1}^7 a_i T^{i-3} \\ &\quad - 2b_3 V^{-1} \sum_{i=1}^7 a_i T^{i-3} (c_1 + c_2 \ln T + c_3 \ln^2 T) \end{aligned} \quad (A-39)$$

Substituting Eq. A-39 in Eq. A-1, and integrating

$$\begin{aligned}
 \int \frac{1}{T^2} \left(\frac{\partial E}{\partial V} \right)_T dT &= V^{-1} \left\{ \sum_{\substack{i=1 \\ i \neq 2}}^7 a_i T^{i-2} \left[\frac{b_2 - 2b_3 c_1 + 2b_3 \ln V}{i-2} \right. \right. \\
 &\quad \left. \left. - 2b_3 c_2 \left(\frac{\ln T}{i-2} - \frac{1}{(i-2)^2} \right) - 2b_3 c_3 \left(\frac{\ln^2 T}{i-2} \right. \right. \right. \\
 &\quad \left. \left. - \frac{2 \ln T}{(i-2)^2} + \frac{2}{(i-2)^3} \right) \right] + a_2 (b_2 - 2b_3 c_1 + 2b_3 \ln V) \ln T \\
 &\quad \left. - a_2 b_3 c_2 \ln^2 T - \frac{2}{3} a_2 b_3 c_3 \ln^3 T \right\} \\
 &= \frac{P}{T} + g(V)
 \end{aligned} \tag{A-40}$$

where $g(V)$ is the constant of integration.

To find an expression for $g(V)$, Eq. A-40 was solved for $g(V)$, and a set of $(g(V), V)$ data was then obtained by evaluating $g(V)$ at the Thomas-Fermi data points (P, E, T, V) previously determined. A least-square polynomial fit of this data was then made to determine coefficients of the equation:

$$\ln [-g(V)] = \sum_{i=1}^n d_i \ln^{i-1} V \tag{A-41}$$

The result for $g(V)$ was selected as:

$$g(V) = - \exp (d_1 + d_2 \ln V + d_3 \ln^2 V) \tag{A-42}$$

The expression for P could then be written from Eqs. A-40 and A-42:

$$\begin{aligned}
 P = T \left\{ V^{-1} \left[\sum_{\substack{i=1 \\ i \neq 2}}^7 a_i T^{i-2} \left\{ \frac{b_2 - 2b_3 c_1 + 2b_3 \ln V}{i-2} - 2b_3 c_2 \left(\frac{\ln T}{i-2} \right. \right. \right. \right. \right. \\
 \left. \left. - \frac{1}{(i-2)^2} \right) - 2b_3 c_3 \left(\frac{\ln^2 T}{i-2} - \frac{2 \ln T}{(i-2)^2} + \frac{2}{(i-2)^3} \right) \right\} \right. \\
 \left. + a_2 (b_2 - 2b_3 c_1 + 2b_3 \ln V) \ln T - a_2 b_3 c_2 \ln^2 T \right. \\
 \left. - \frac{2}{3} a_2 b_3 c_3 \ln^3 T \right] + \exp (d_1 + d_2 \ln V + d_3 \ln^2 V) \left. \right\} \tag{A-43}
 \end{aligned}$$

The foregoing procedure was followed to evaluate the constants in the equations for the electronic energy and pressure in a predetermined region of interest. This region was bounded by temperatures ($kT/Z^{4/3}$) between .02 and 2 ev and volumes, along an isotherm of the electronic energy, within 2 magnitudes of the volume, $V_C(T)$, at the intersection of the isotherm with the cold compression curve. The calculated values for the constants are given in Table A-2. The units used were E(ev), T(ev), and V(10^{-20} cm³). Thus the expression

for pressure (Eq. A-43) is in units of ($\frac{\text{ev}}{10^{-20} \text{ cm}^3}$). To convert P to dynes/cm², the right side of Eq. A-43 should be multiplied by 1.60206×10^8 . Graphs of E(V, T) and P(V, T) (Eqs. A-36 and A-43), along with the data points determined from Latter's numerical solutions of the Thomas-Fermi equation, are shown in Figures A-13 and A-14.

TABLE A-2: CALCULATED VALUES FOR EQUATION CONSTANTS

$a_1 = -6.2590 \times 10^{-4}$	$b_1 = 1.0099$	$d_1 = -1.8852$
$a_2 = 8.9514 \times 10^{-2}$	$b_2 = 3.5464 \times 10^{-1}$	$d_2 = -1.0487$
$a_3 = 9.7628 \times 10^{-1}$	$b_3 = 3.8865 \times 10^{-3}$	$d_3 = -2.2678 \times 10^{-2}$
$a_4 = -1.8143$		
$a_5 = 1.9575$	$c_1 = -6.1857$	
$a_6 = -1.0071$	$c_2 = -1.0766$	
$a_7 = 1.9189 \times 10^{-1}$	$c_3 = -2.3440 \times 10^{-2}$	

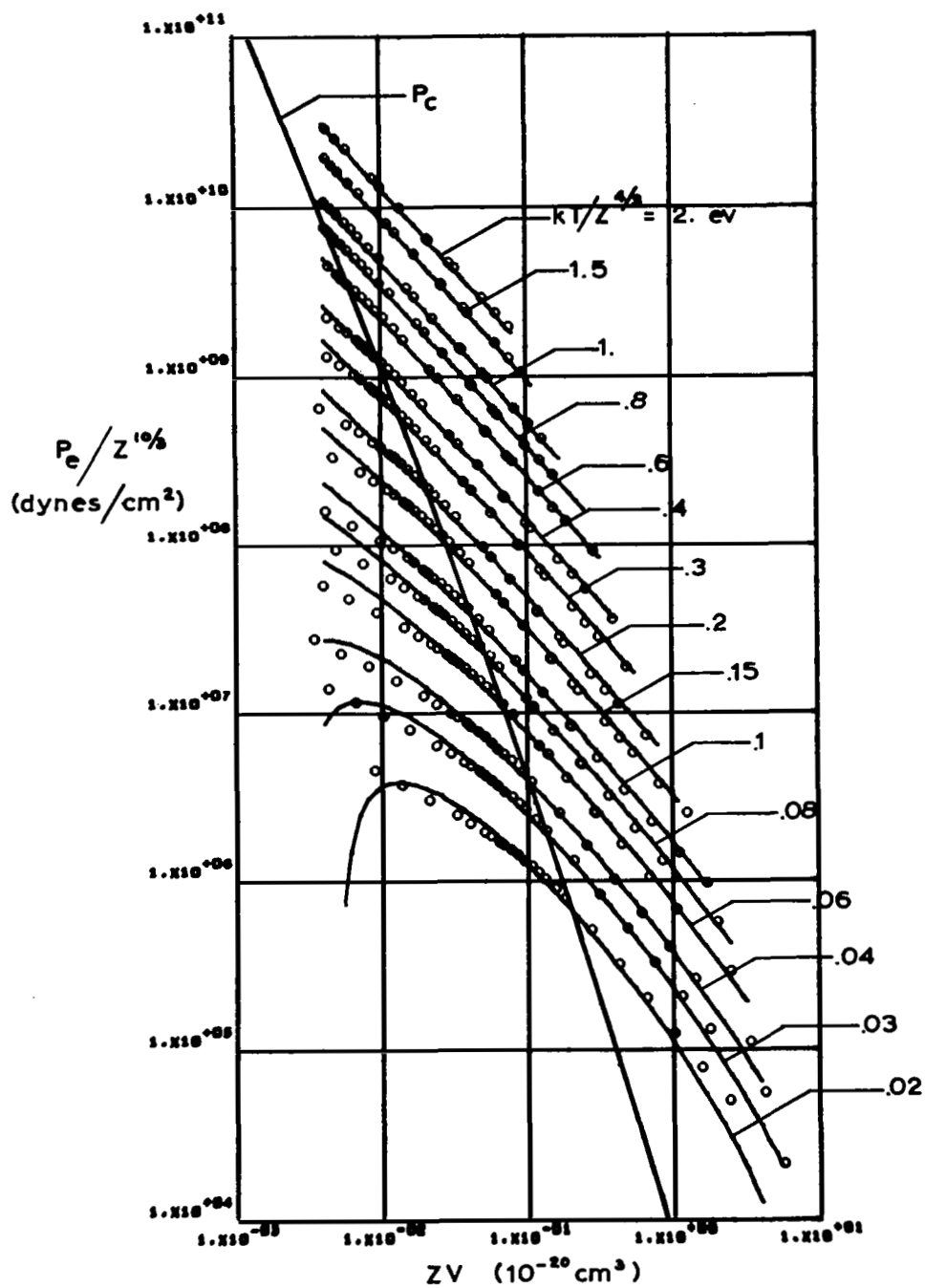


FIGURE A-13 ELECTRONIC ENERGY vs
VOLUME FOR FIXED TEMPERATURE

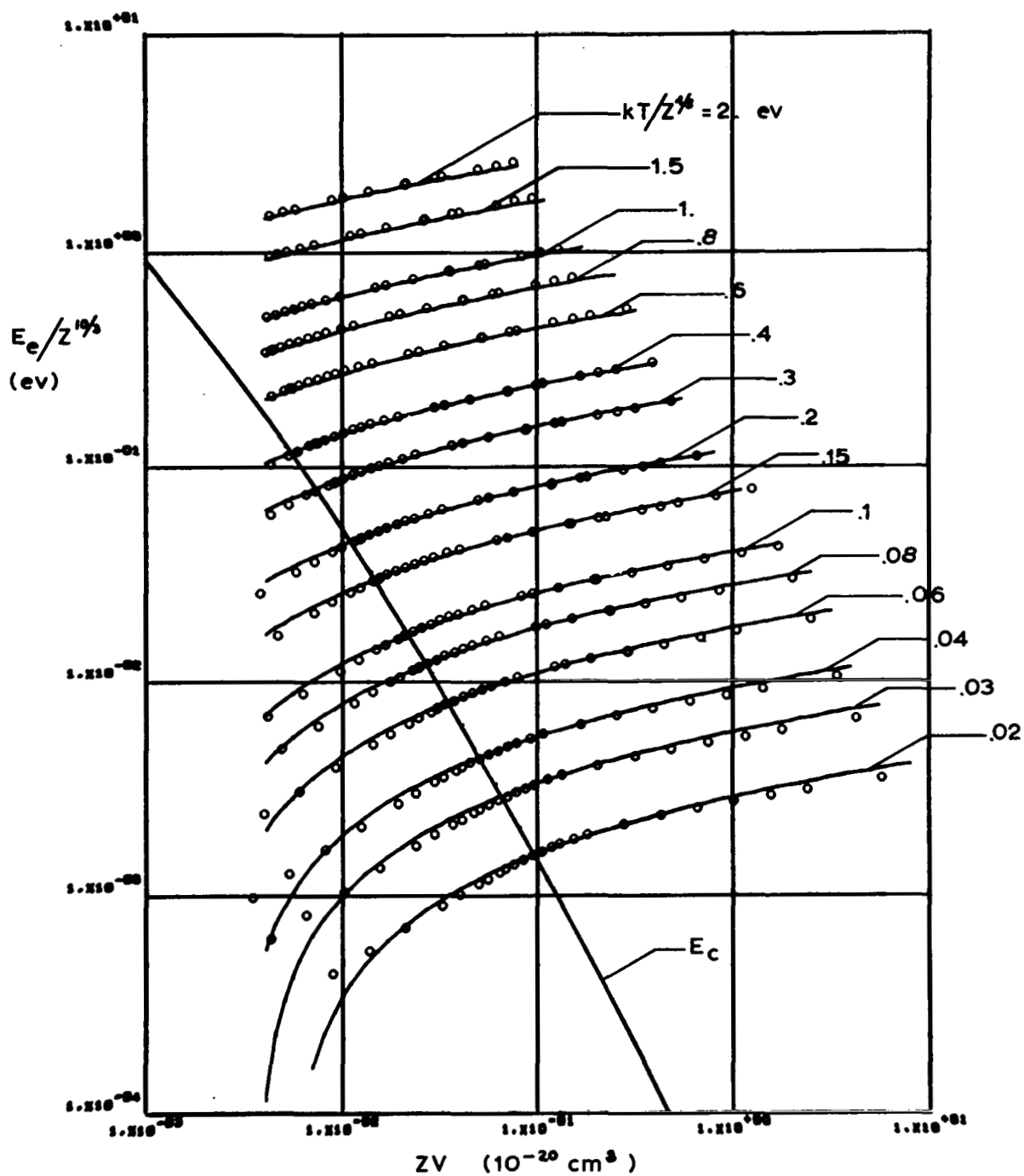


FIGURE A-14 ELECTRONIC PRESSURE vs
VOLUME FOR FIXED TEMPERATURE

APPENDIX B

USE OF SPECIFIC INTERNAL ENERGY AND DYNAMIC PRESSURE PROFILES FOR PENETRATION PREDICTIONS CASES 8051 - 8058

This appendix contains the specific internal energy and dynamic pressure profiles from which penetration predictions are made for each of the eight impact cases in this study.

The technique for predicting penetration is described in Section 2.2.1 of the text. Application of this technique in the plots in this Appendix involves the following steps:

- a. Figures B-1 through B-8 are specific internal energy profiles versus depth in the target at late times in each solution, after detachment of the isolated shocks from the cratering flow regions. These profiles are drawn at small radial offsets from the axis of each problem to avoid minor oscillations along the axis.
- b. Using the conversions from Tables B-1 or B-2, temperatures corresponding to the specific internal energies are flagged in Figures B-1 to B-8. Thus residual temperature as a function of depth is determined.
- c. Residual strength as a function of depth is determined by use of the tabulations of strength vs temperature in Tables B-1 or B-2.
- d. Figures B-9 through B-16 are dynamic pressure and residual strength profiles versus depth in the target at times and offsets corresponding to the specific internal energy plots. The relatively stable cratering flow regions are identified on each of these plots. Compression profiles are also shown.
- e. The intersection of the dynamic pressure curves with the residual strength curves is taken as the predicted crater depth for each case. (Either residual yield or residual ultimate strength can be used, since the prediction is insensitive to the exact strength profile.)

TABLE B-1
SPECIFIC INTERNAL ENERGY AND ULTIMATE STRENGTH
VS TEMPERATURE FOR ALUMINUM

Temperature (°K)	Specific Internal Energy ¹ (erg/gm x 10 ⁹)	Strength of 2024-T3 Al ² (kilobars)
350	0.47	3.4
400	0.93	3.1
450	1.4	2.24
500	1.9	1.02
600	2.9	0.39
700	4.0	---
800	5.1	---
850	5.7	0
900	6.3	---
1000	11.0	---

TABLE B-2
SPECIFIC INTERNAL ENERGY AND ULTIMATE STRENGTH
VS TEMPERATURE FOR IRON

Temperature (°K)	Specific Internal Energy ¹ (erg/gm x 10 ⁹)	Strength of Type 301 Full Hard Stainless Steel ³ (kilobars)
800	2.8	8.8
900	3.5	7.0
950	4.0	5.2
1000	4.4	3.0
1050	4.9	0.5
1100	5.4	---
1400	7.6	---
1675	9.5	0
2000	14.8	---

¹For pure aluminum and iron. Taken from Thermodynamic Properties of the Elements, by Stull and Sinke, American Chemical Society, New York, 1956.

²From MIL-Hdbk-5.

³From Metals Handbook, 8th Edition, American Society for Metals, 1961.

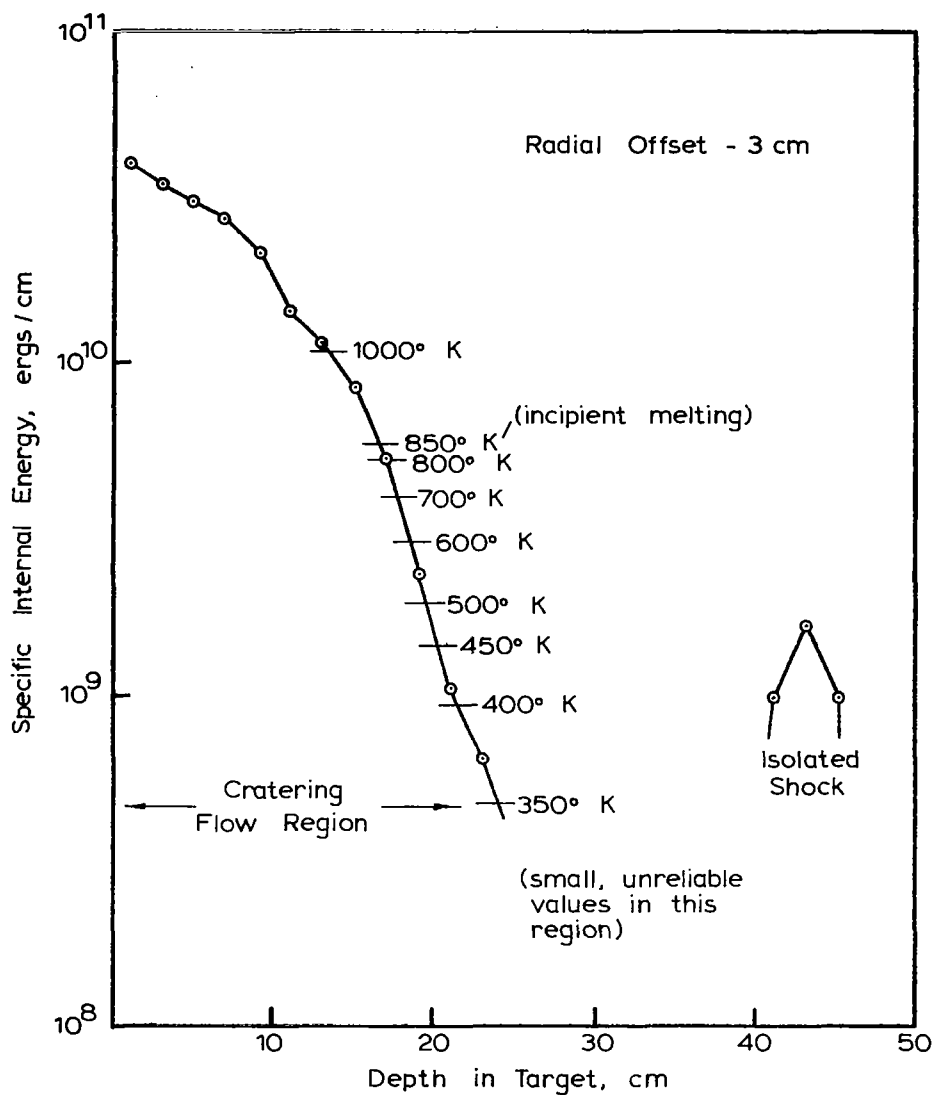


FIGURE B-1
 SPECIFIC INTERNAL ENERGY PROFILE
 60.2 MICROSECONDS AFTER IMPACT
 CASE 8051 - POROUS ALUMINUM ($\rho = 0.44$)
 VS. ALUMINUM AT 20 KM/SEC

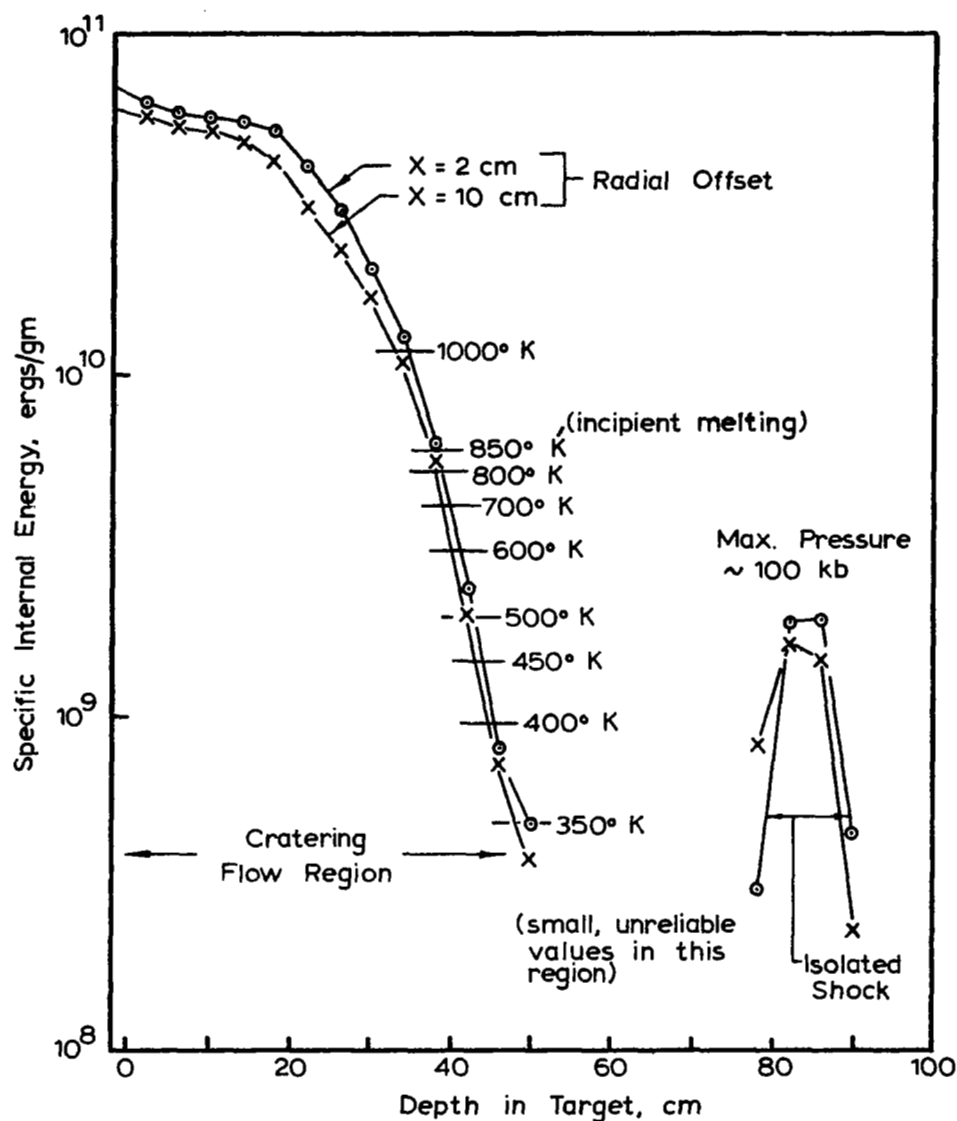


FIGURE B-2
 SPECIFIC INTERNAL ENERGY PROFILES
 103.2 MICROSECONDS AFTER IMPACT
 CASE 8052 - POROUS ALUMINUM ($\rho = 0.44$)
 VS. ALUMINUM AT 72 KM/SEC

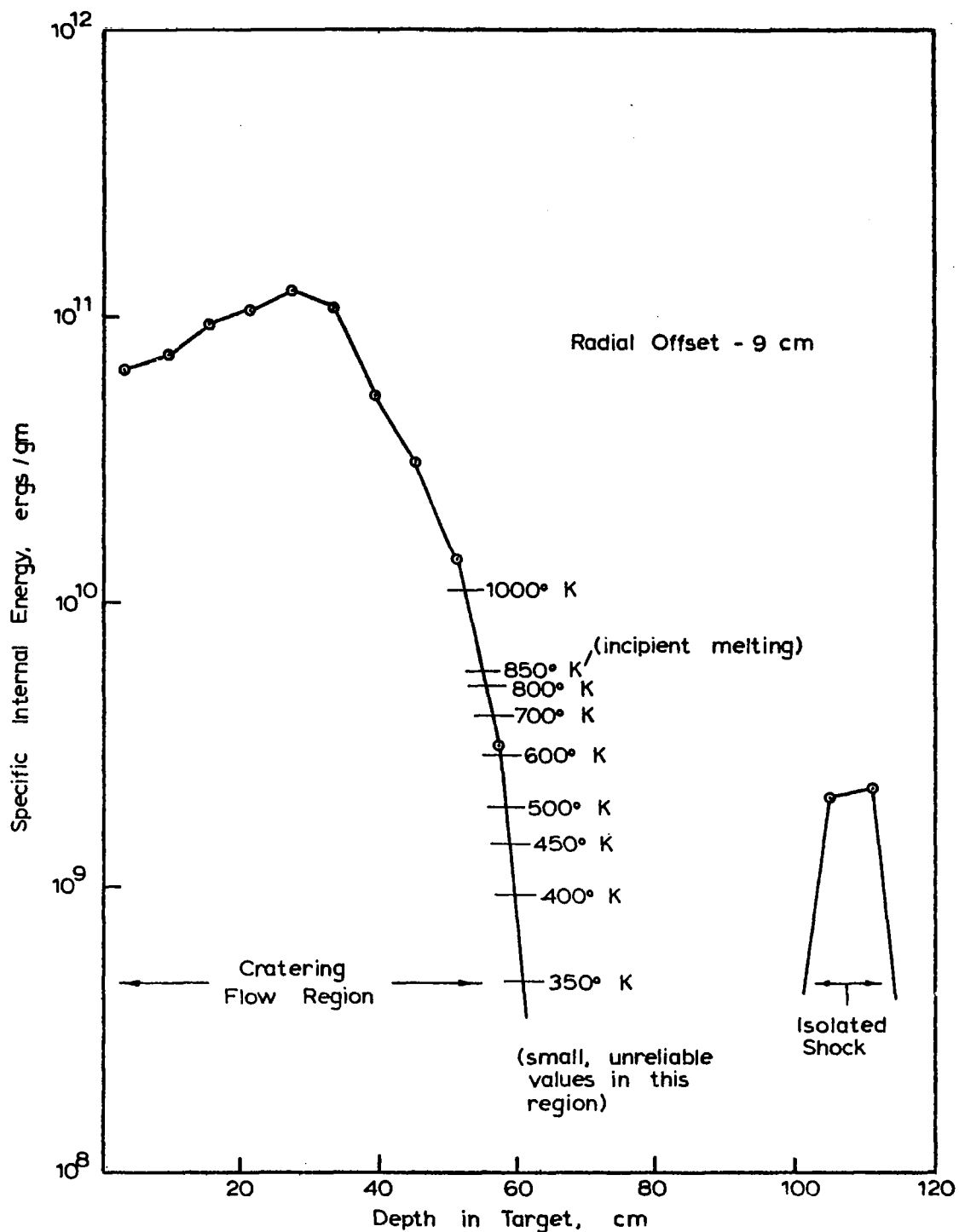


FIGURE B-3
 SPECIFIC INTERNAL ENERGY PROFILE
 135.7 MICROSECONDS AFTER IMPACT
 CASE 8053 - IRON VS. ALUMINUM
 AT 20 KM / SEC

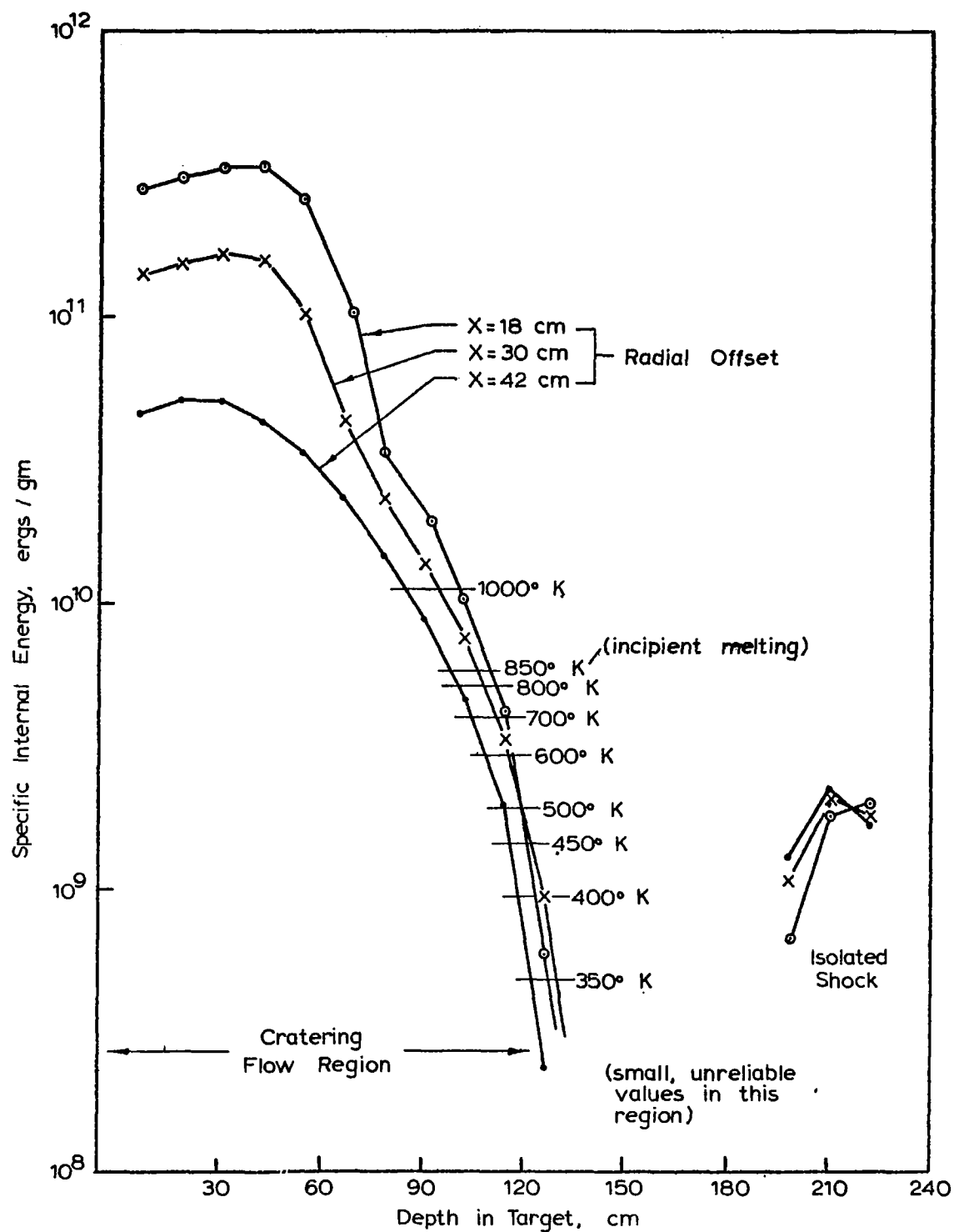


FIGURE B-4
 SPECIFIC INTERNAL ENERGY PROFILES
 257.5 MICROSECONDS AFTER IMPACT
 CASE 8054 - IRON VS. ALUMINUM
 AT 72 KM / SEC

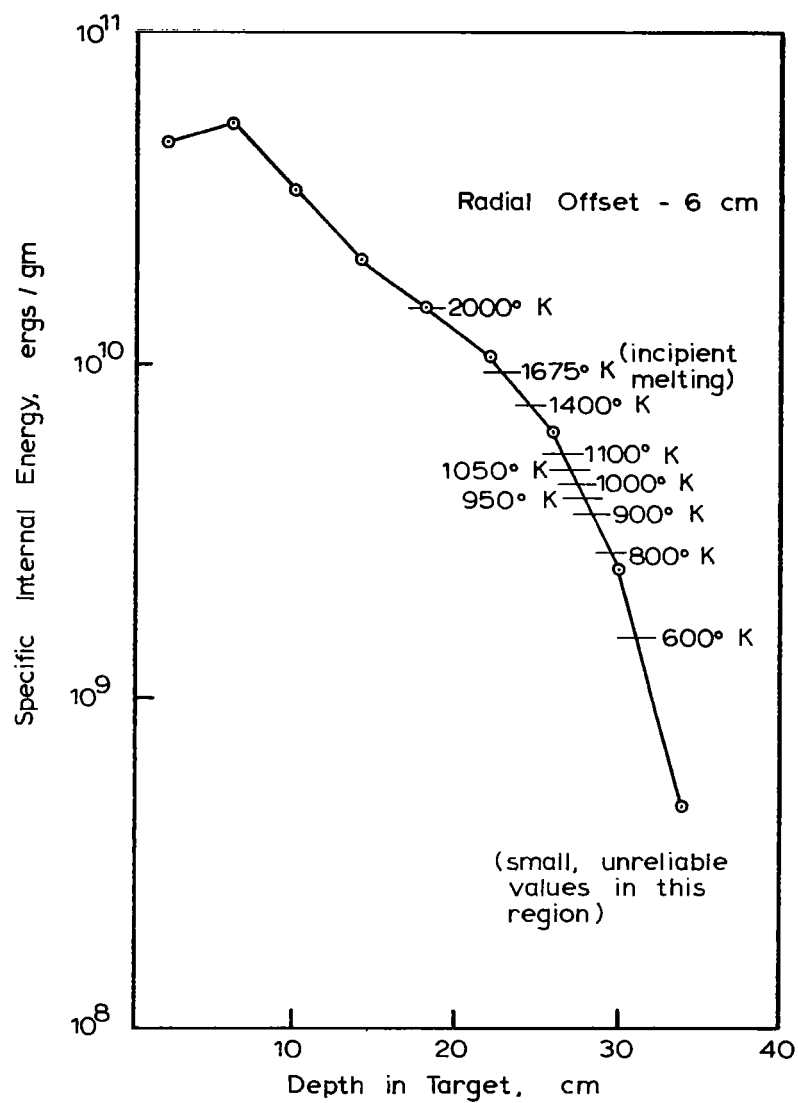


FIGURE B-5
 SPECIFIC INTERNAL ENERGY PROFILE
 135 MICROSECONDS AFTER IMPACT
 CASE 8055 - ALUMINUM VS. IRON
 AT 20 KM / SEC

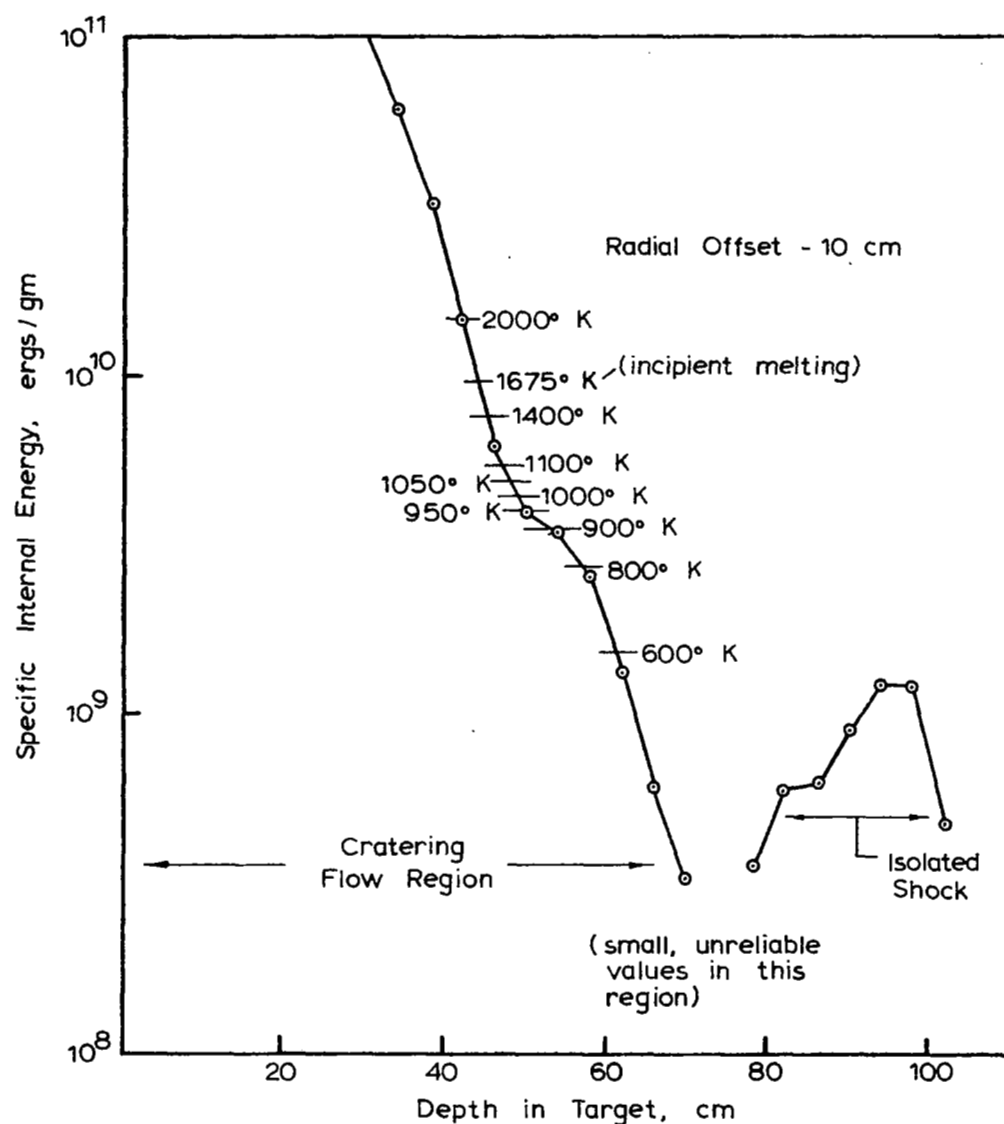


FIGURE B-6
SPECIFIC INTERNAL ENERGY PROFILE
136 MICROSECONDS AFTER IMPACT
CASE 8056 - ALUMINUM VS. IRON
AT 72 KM / SEC

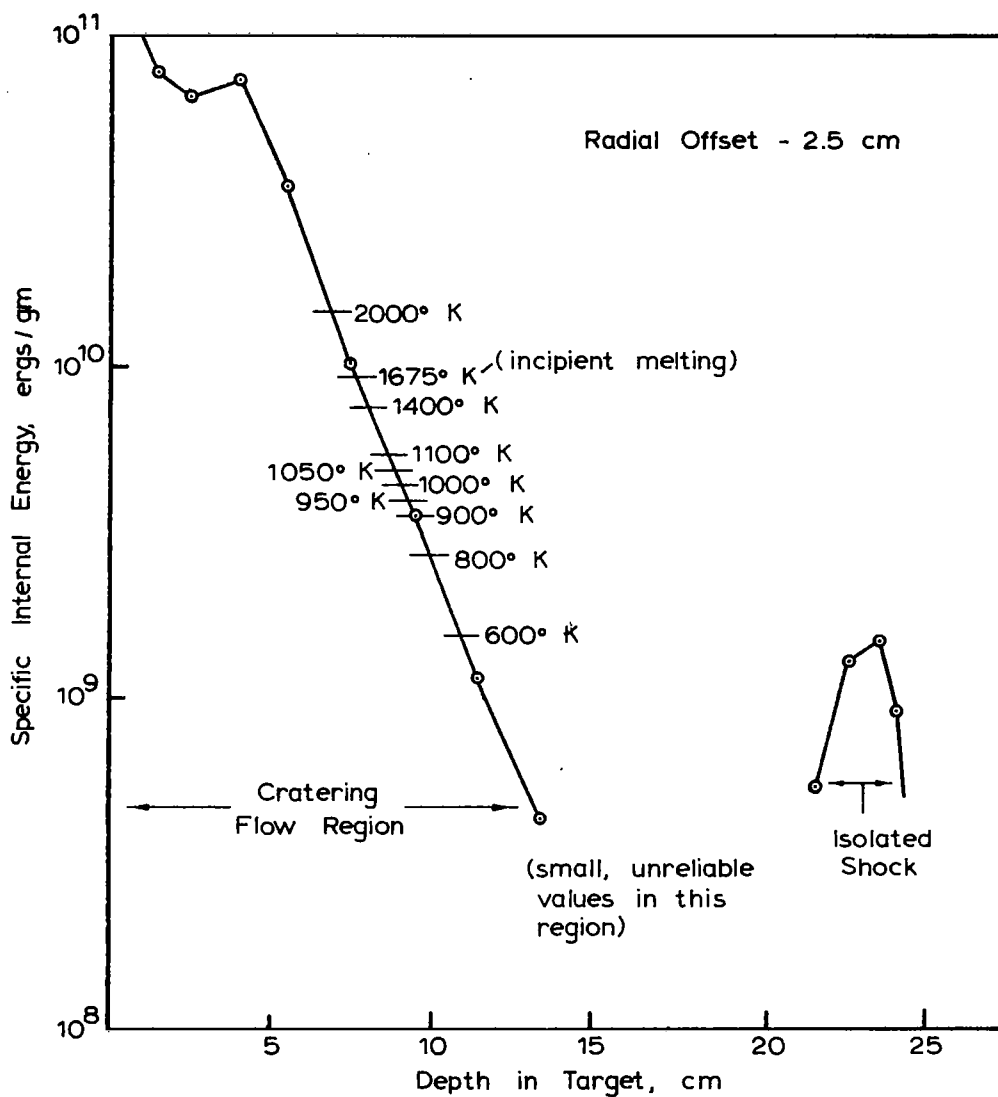


FIGURE B-7
 SPECIFIC INTERNAL ENERGY PROFILE
 41.9 MICROSECONDS AFTER IMPACT
 CASE 8057 - POROUS ALUMINUM ($\rho = 0.44$)
 VS. IRON AT 20 KM/SEC

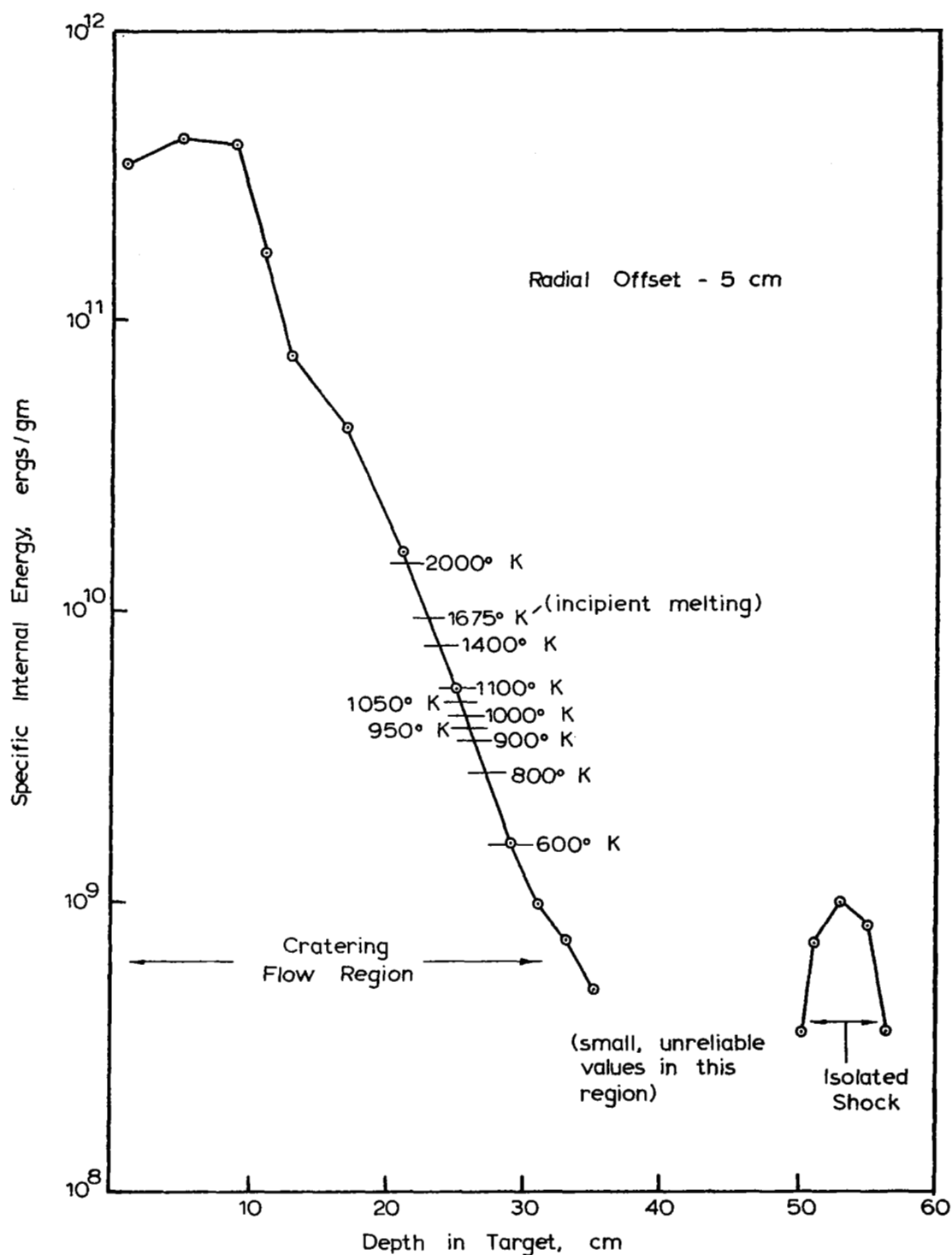


FIGURE B-8
 SPECIFIC INTERNAL ENERGY PROFILE
 84.8 MICROSECONDS AFTER IMPACT
 CASE 8058 - POROUS ALUMINUM ($\rho = 0.44$)
 VS. IRON AT 72 KM/SEC

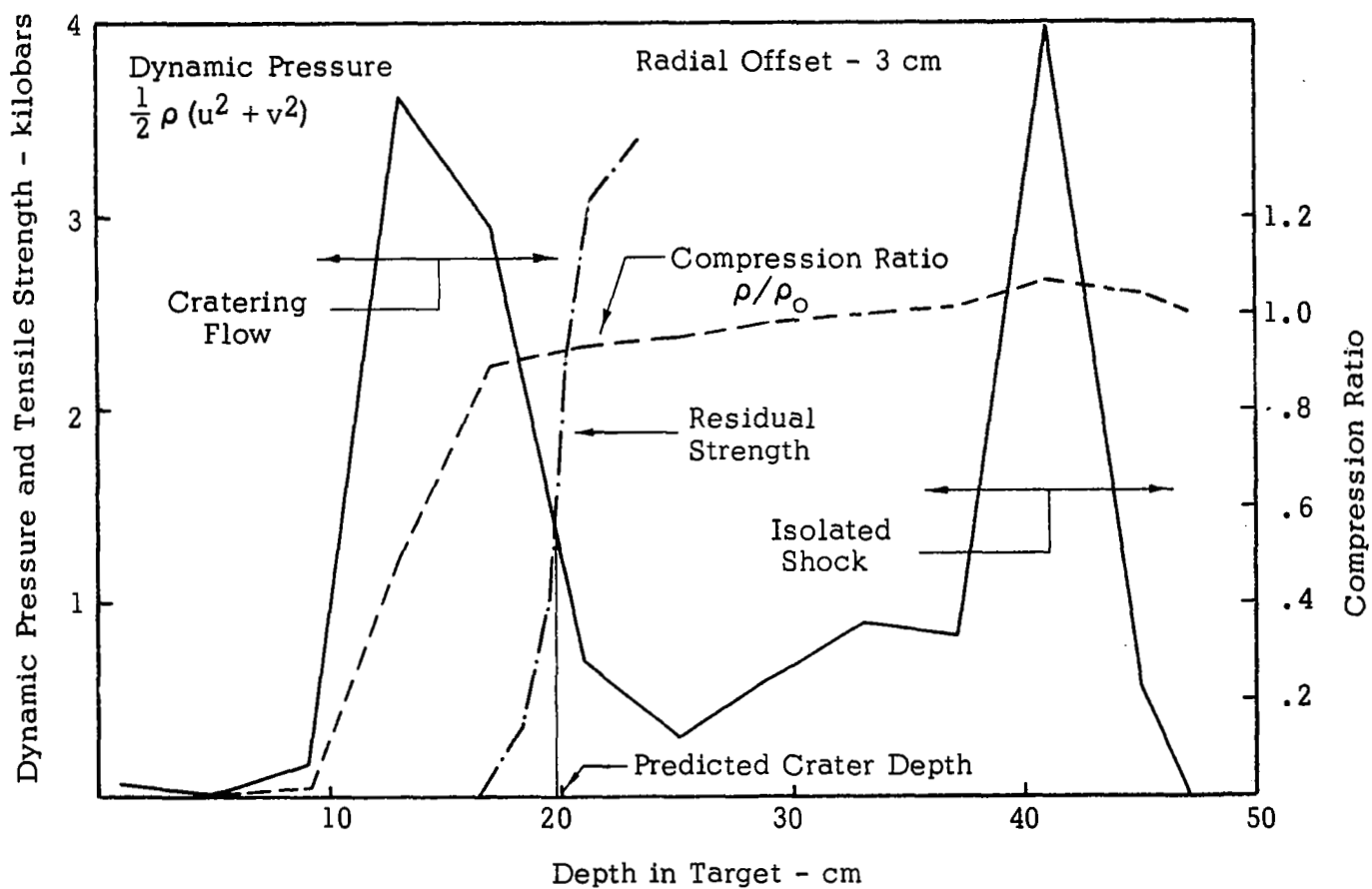


FIGURE B-9
 DYNAMIC PRESSURE VS DEPTH
 $T = 60.2$ Microseconds
 Case 8051 - Porous Aluminum ($\rho = 0.44$)
 vs Aluminum at 20 KM/SEC

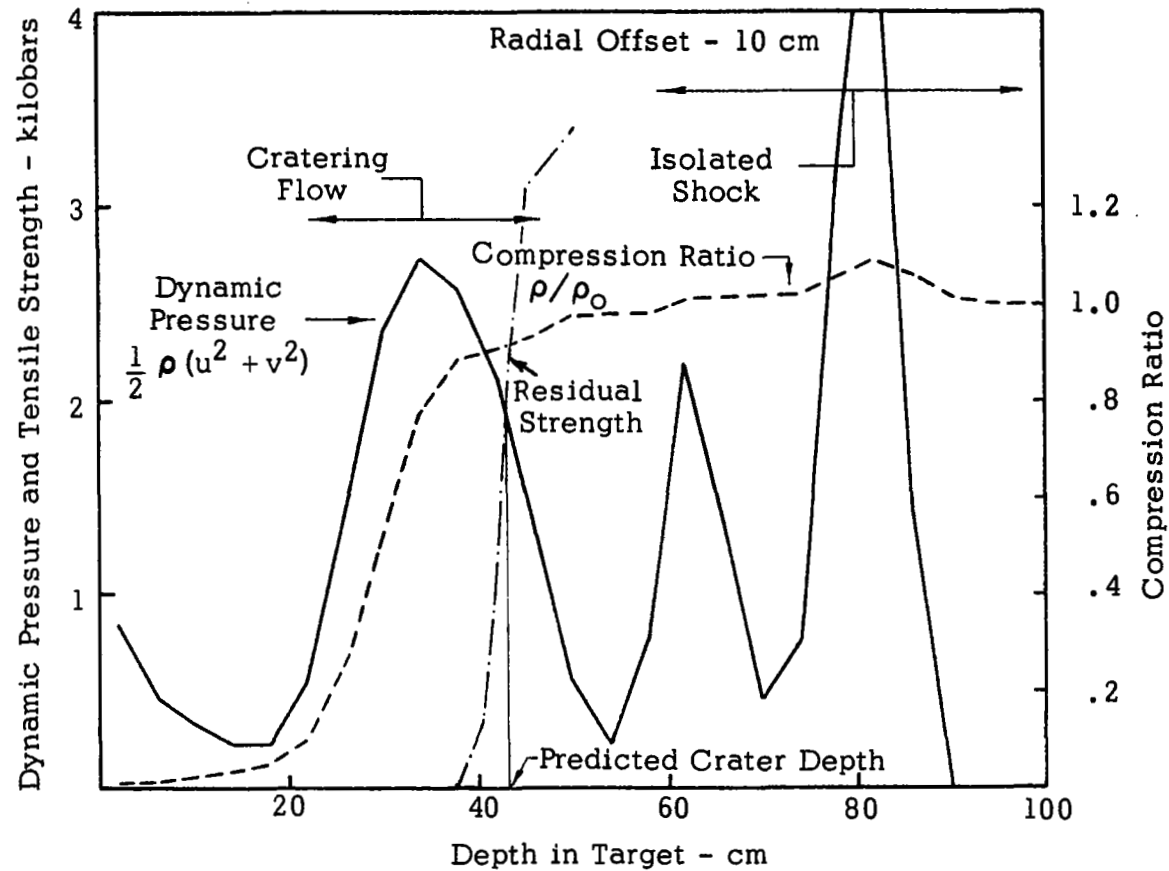


FIGURE B-10
 DYNAMIC PRESSURE VS DEPTH
 $T = 103.2$ Microseconds
 Case 8052 - Porous Aluminum ($\rho = 0.44$)
 vs Aluminum at 72 km/sec

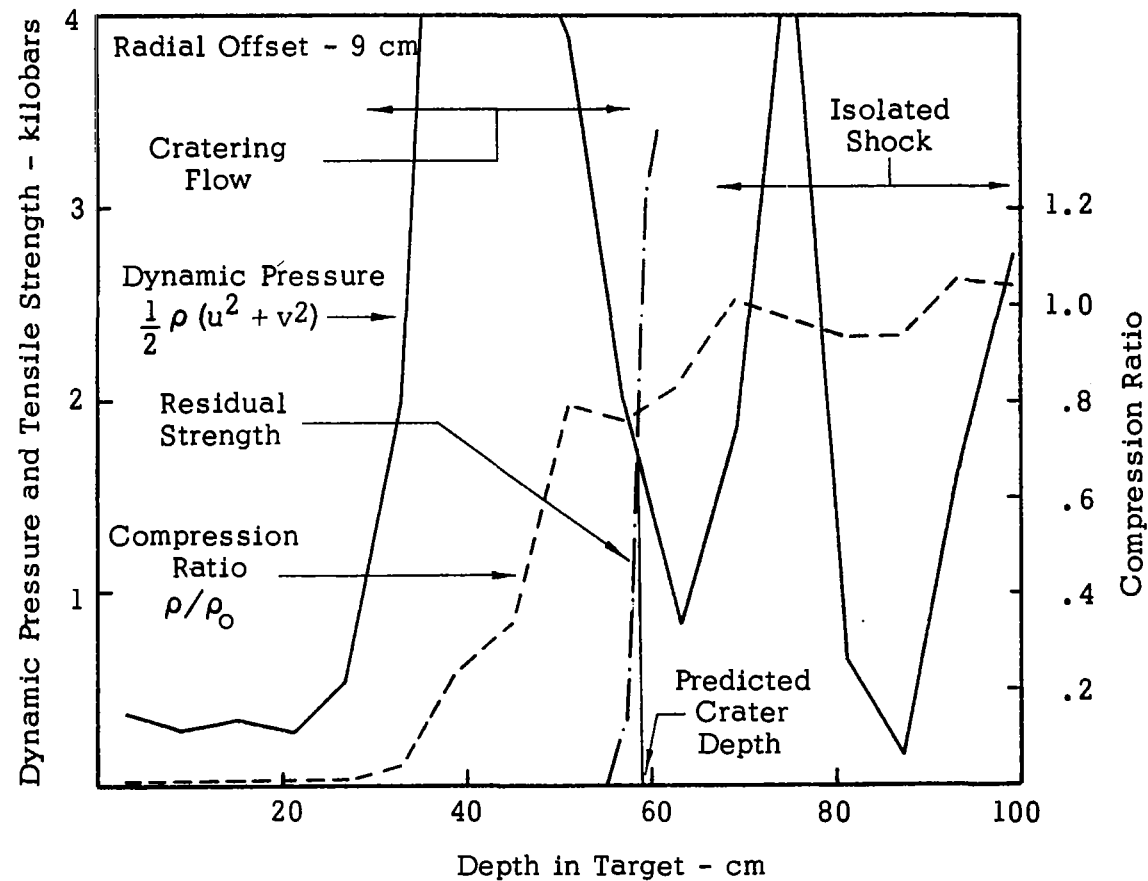


FIGURE B-11
 DYNAMIC PRESSURE VS DEPTH
 T = 135.7 Microseconds
 Case 8053 - Iron vs Aluminum
 at 20 KM/SEC

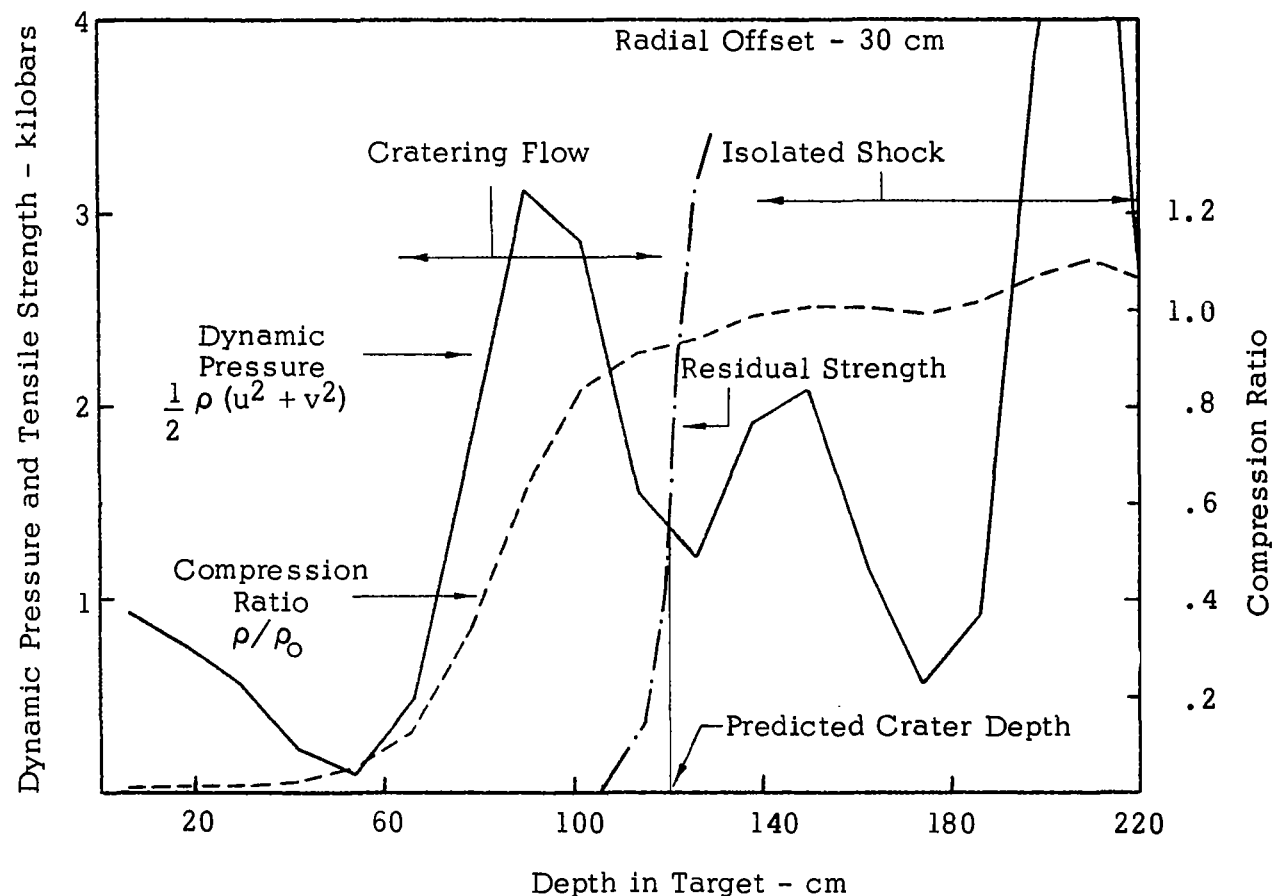


FIGURE B-12
DYNAMIC PRESSURE VS DEPTH
T = 257.5 Microseconds
Case 8054 - Iron vs Aluminum
At 72 km/sec



111

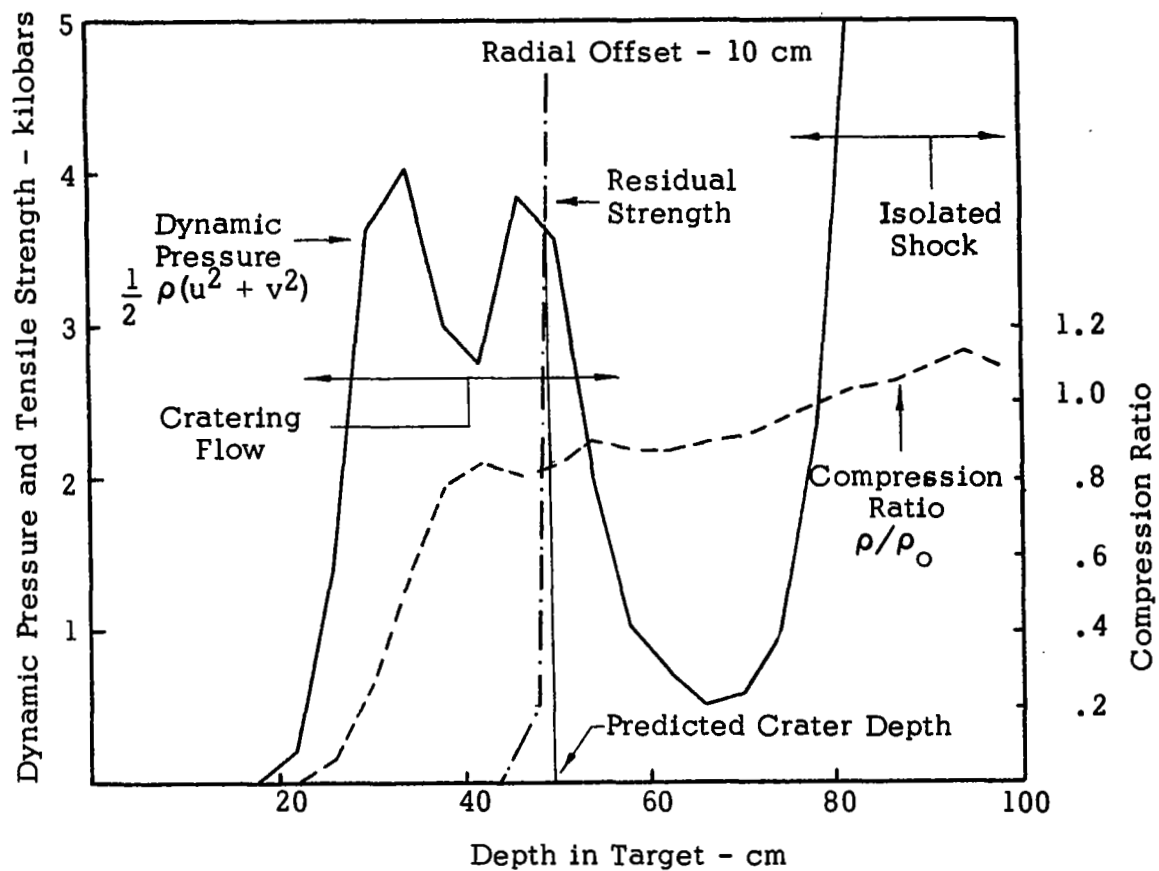


FIGURE B-14
 DYNAMIC PRESSURE VS DEPTH
 $T = 136$ Microseconds
 Case 8056 - Aluminum vs Iron (Steel)
 at 72 KM/SEC

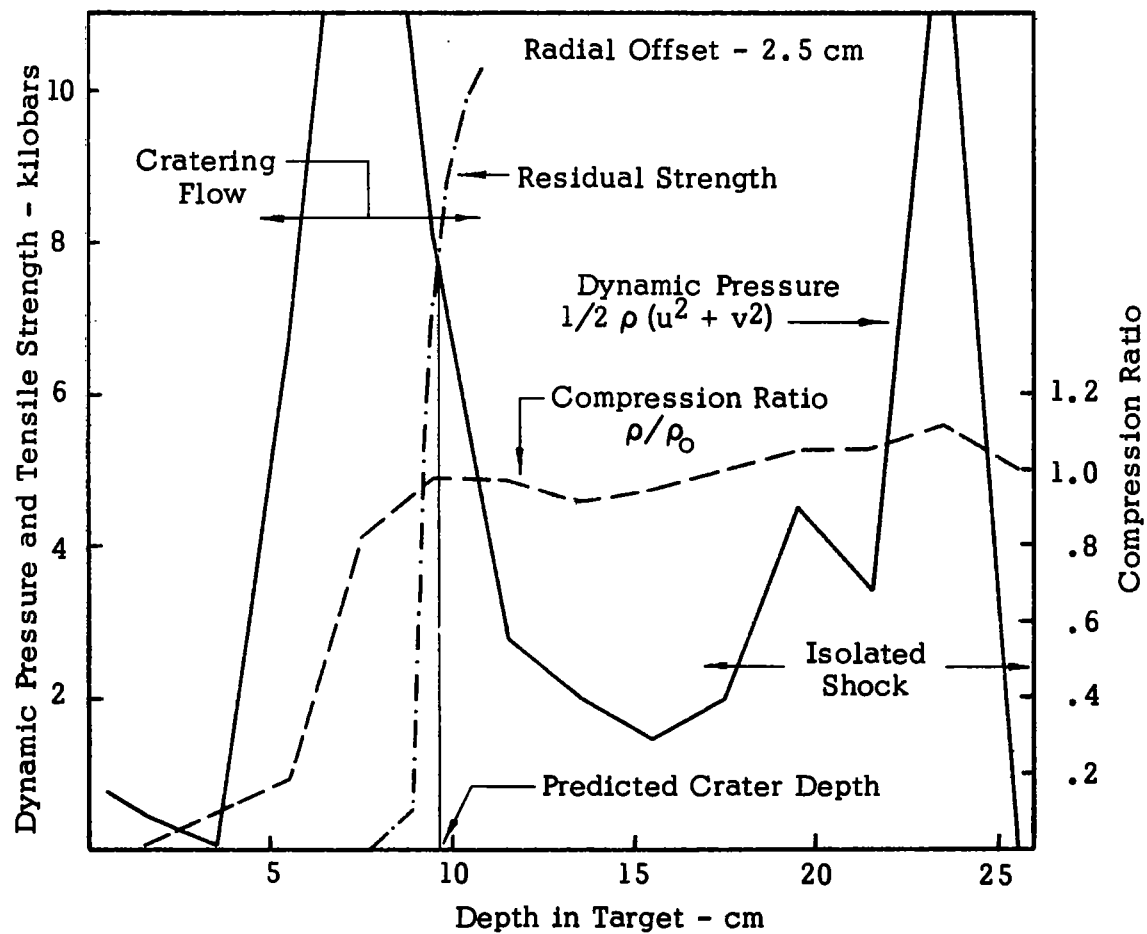


FIGURE B-15
 DYNAMIC PRESSURE VS DEPTH
 $T = 41.9$ Microseconds
 Case 8057 - Porous Aluminum ($\rho = 0.44$)
 vs Iron (Steel) at 20 KM/SEC

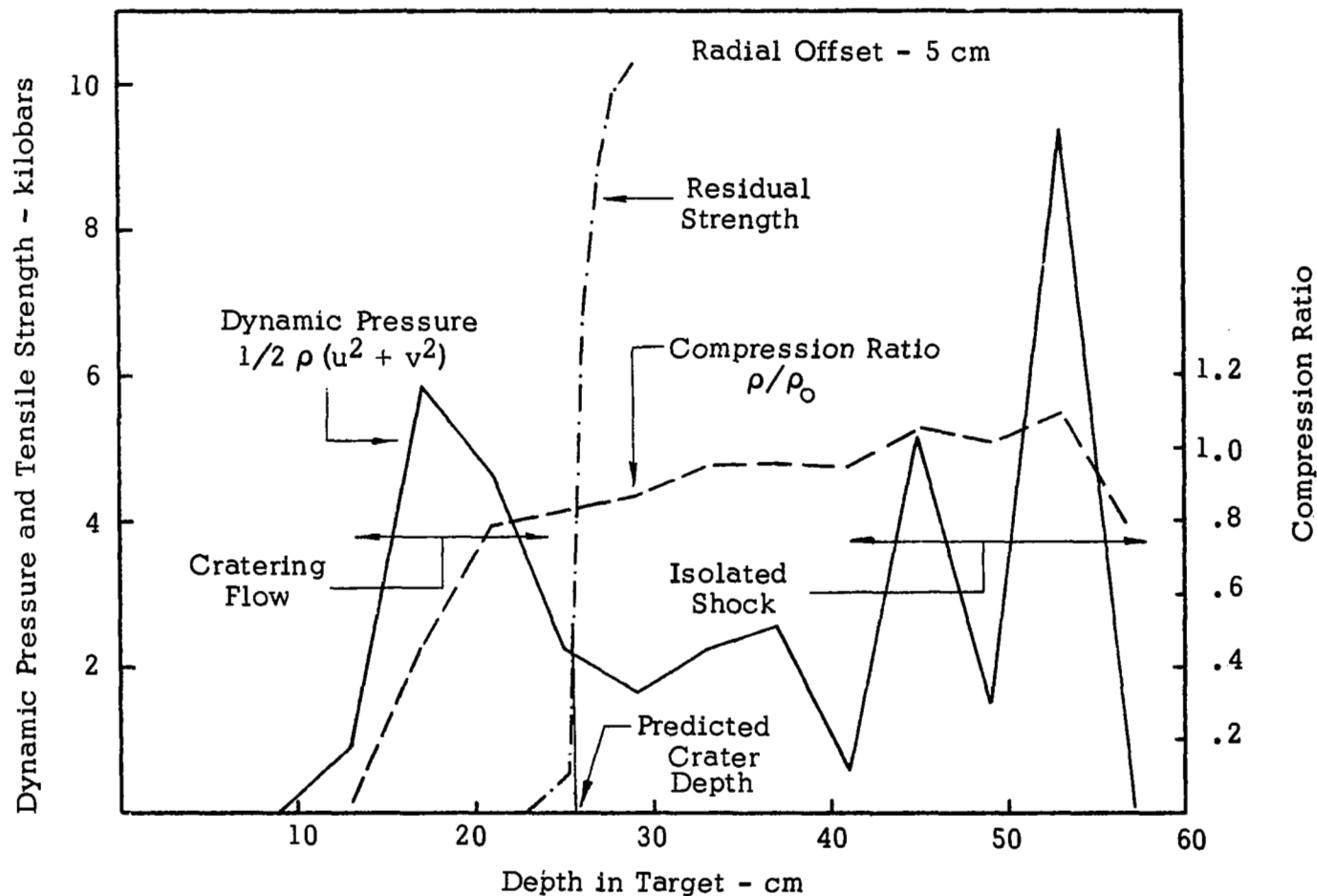


FIGURE B-16
 DYNAMIC PRESSURE VS DEPTH
 $T = 84.8$ Microseconds
 Case 8058 - Porous Aluminum ($\rho = 0.44$)
 vs Iron (Steel) at 72 km/sec

APPENDIX C

DESCRIPTIONS OF NUMERICAL SOLUTIONS OF IMPACT CASES 8051-8058, INCLUDING PLOTS OF MASS POSITIONS, AND VELOCITY AND PRESSURE FIELDS

This appendix contains plots of the numerical solutions obtained during the program for the following eight cases:

<u>Case Number</u>	<u>Projectile</u>	<u>Target</u>	<u>Velocity</u>
8051	Porous Aluminum	Aluminum	20 km/sec
8052	Porous Aluminum	Aluminum	72 km/sec
8053	Iron	Aluminum	20 km/sec
8054	Iron	Aluminum	72 km/sec
8055	Aluminum	Iron (Steel)	20 km/sec
8056	Aluminum	Iron (Steel)	72 km/sec
8057	Porous Aluminum	Iron (Steel)	20 km/sec
8058	Porous Aluminum	Iron (Steel)	72 km/sec

TYPES OF PLOTS

The plots are made by the SC4020, which converts taped data to cathode ray tube displays. Three types of plots are normally made - Mass Positions, Velocity Fields, and Pressure Fields. The Mass Position plots show the locations of the individual mass points as these move through the grid. The Velocity Fields show the velocity of the mass in each cell by means of vectors. The tail of each vector is in the center of each cell, and the length and direction indicate the magnitude and direction of the velocity. Velocity scales in cm/ μ sec are usually given in the lower right hand corner of each plot. A "+" plotted in a cell indicates that the velocity is non-zero, but of insufficient magnitude to be shown by a vector on the scale used. When an "x" is shown in a cell, this means that the proper vector is too long for convenient plotting. The direction of the vector, however, is correctly shown in these cases.

The Pressure Fields show isobars at selected intervals. These are flagged with the pressure levels (in megabars).

All of the impacts analyzed during this program have axial symmetry. Hence the phenomena can be described in two space dimensions, y and r (height and radius). In the following plots, values of y are noted on the left boundary and values of r along the bottom. Positive values of y are below the original target surface; negative values are above (outside) the original surface. The left boundary is the axis of symmetry in all cases.

SCALE

All aspects of hydrodynamic solutions scale. For convenience, the solutions in this program were worked out for 10 cm x 10 cm right cylinders. The results can be scaled to any other dimensions by multiplying all dimensions and times by the same scale factor. For example, to determine target response to

impact by a 10^{-3} gm stony meteoroid ($\rho = 2.7$), dimensions and times would be multiplied by 7.79×10^{-2} .

GRID CHANGING

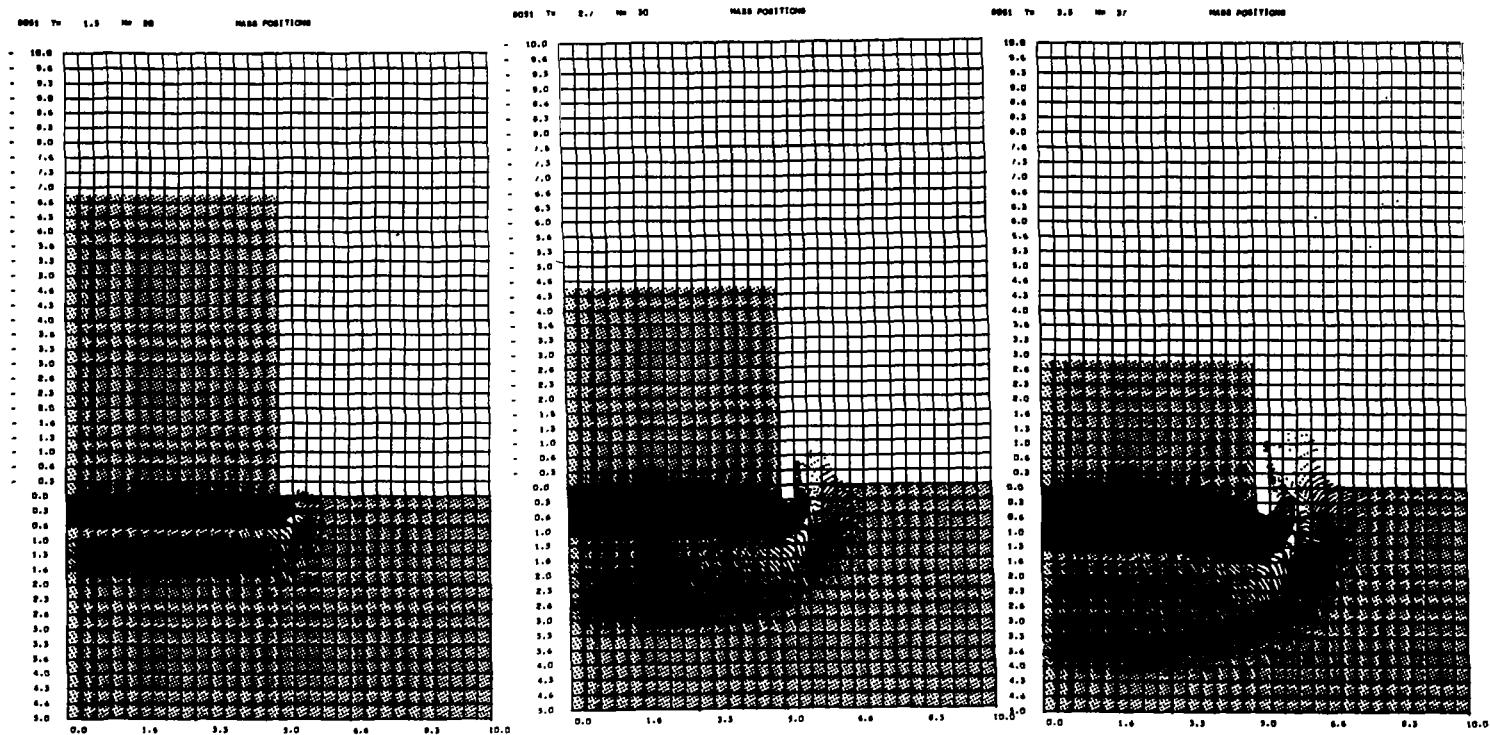
To permit maximum spatial resolution during each stage of a solution, the grid is restricted to a region which is only moderately larger than the area encompassing cells which have been disturbed by the shock front. When the shock front reaches the edge of the "field of view", the grid must be changed to incorporate a larger region of the target. Hence in the plots which follow, the field of view is enlarged in steps as time increases.

ENERGY AND MOMENTUM PARTITIONING

For purposes of partitioning the energy and momentum as discussed in Section 3.2.3 of the text, the impact response fields are divided into three regions at late stages, as follows:

- Region I: Isolated Shock
- Region II: Cratering Flow
- Region III: Ejecta and other material above target surface

Boundaries of these regions have been superimposed on the final velocity plot for each impact case.



(a) Mass Positions
 $t = 1.5 \mu\text{sec}$

(b) Mass Positions
 $t = 2.7 \mu\text{sec}$

(c) Mass Positions
 $t = 3.5 \mu\text{sec}$

FIGURE C-1: CASE 8051, Porous Aluminum ($\rho = 0.44$) into Aluminum at 20 km/sec

The porous projectile is very severely compressed upon impact with the relatively stiff aluminum target. Note that at $t = 3.5 \mu\text{sec}$ approximately 7.5 cm of the original projectile length has been compressed to about 1.5 cm. These plots also show the shock front propagating into the target, and the "spray" of target material from the free surface region adjacent to the projectile.

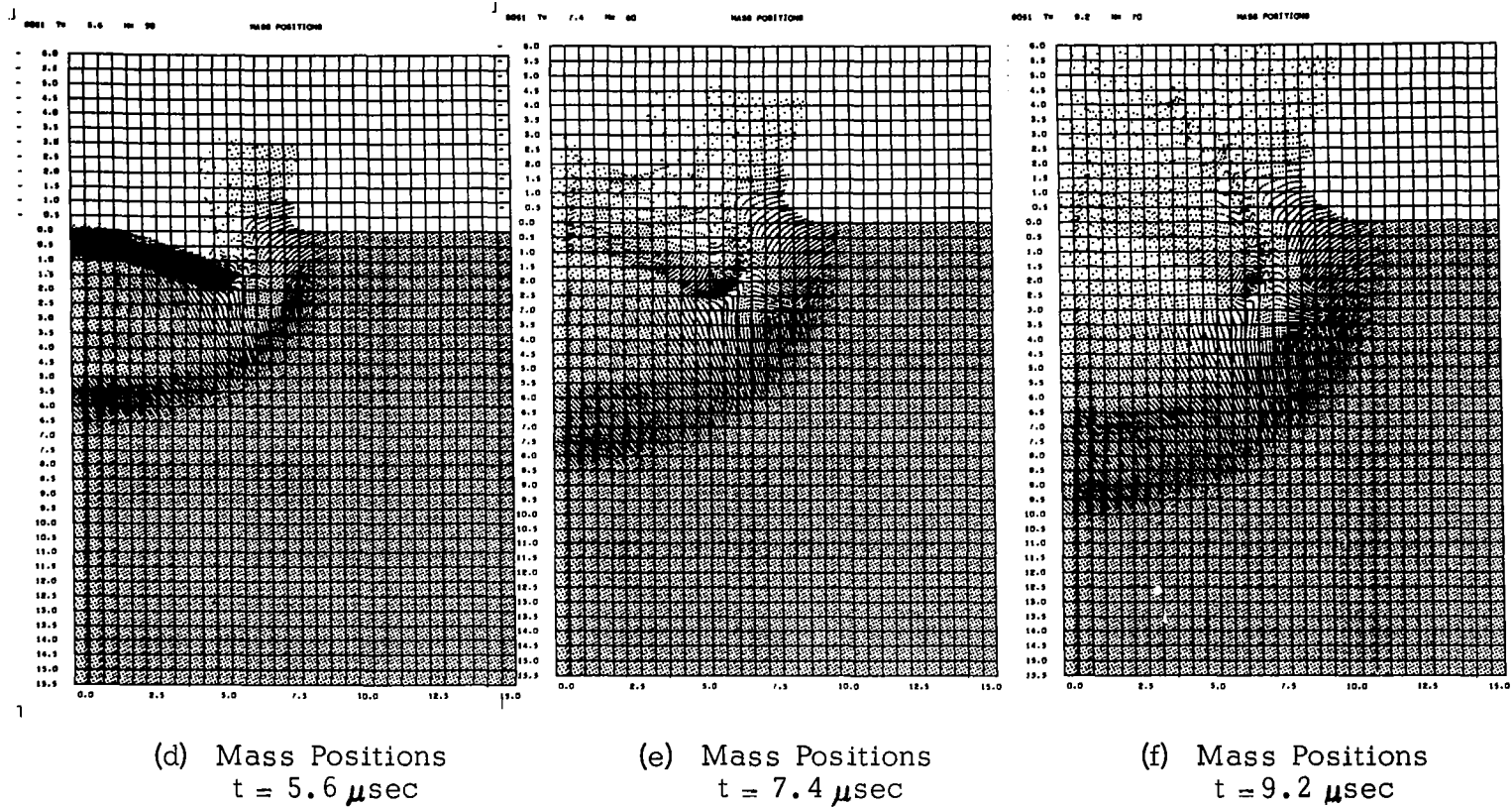
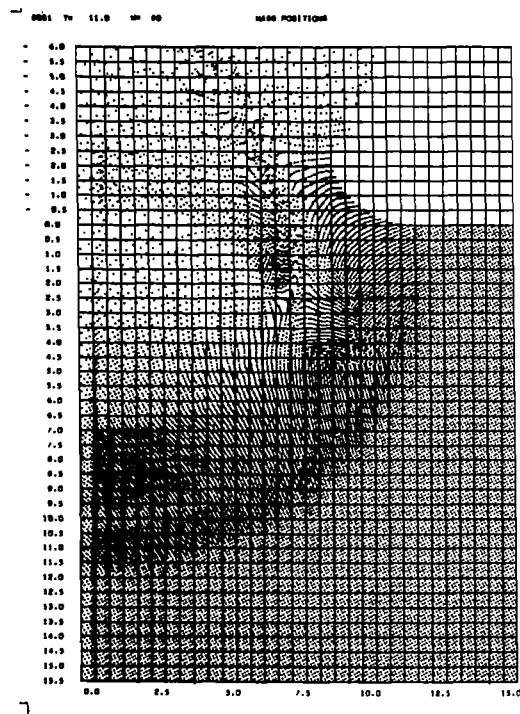
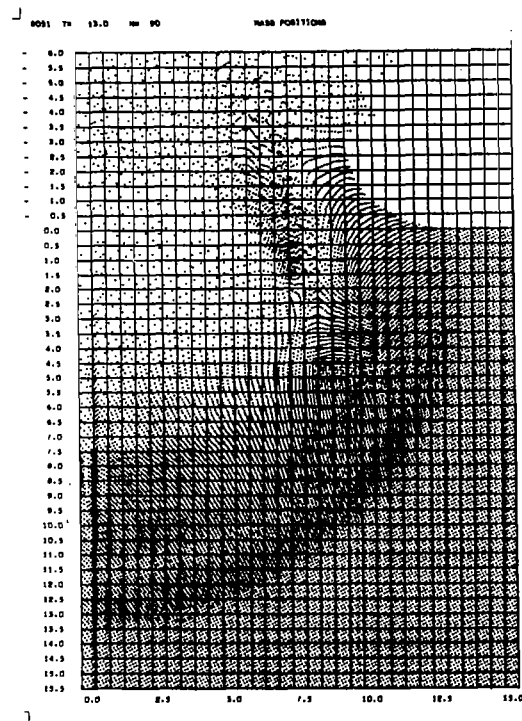


FIGURE C-1 (Con't): CASE 8051, Porous Aluminum ($\rho = 0.44$) into Aluminum at 20 km/sec

A grid change was made at $t = 3.7 \mu\text{sec}$ to incorporate a larger "field of view" as the volume encompassed by the shock front expands. By $t = 5.6 \mu\text{sec}$, all of the porous projectile has been compressed by the impact. This severe compression imparts sufficient internal energy to vaporize the porous aluminum. At $t = 7.4 \mu\text{sec}$, blowoff of the rear surface of the projectile is starting, and this continues at $t = 9.2 \mu\text{sec}$ and at subsequent times.



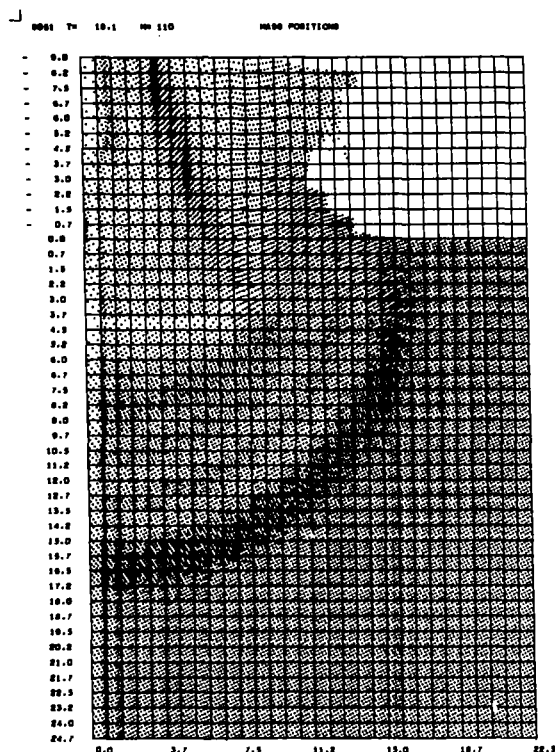
(g) Mass Positions
 $t = 11.0 \mu\text{sec}$



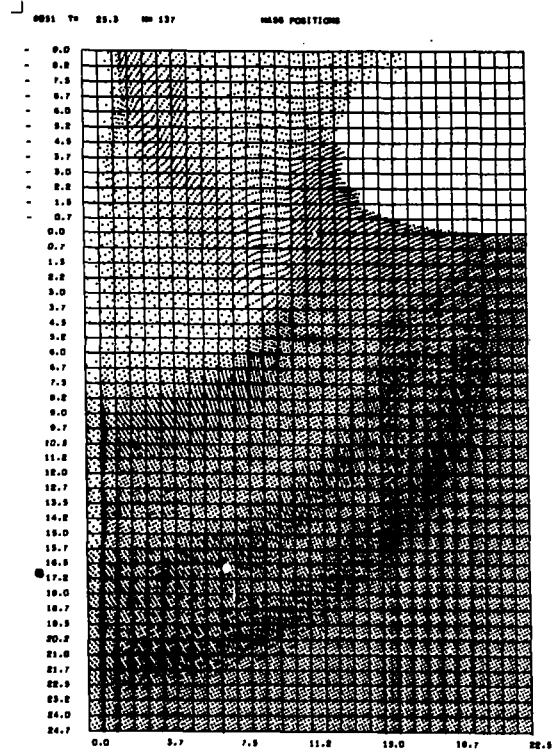
(h) Mass Positions
 $t = 13.0 \mu\text{sec}$

FIGURE C-1 (Con't): CASE 8051, Porous Aluminum ($\rho = 0.44$) into Aluminum at 20 km/sec

Blowoff of the vaporized projectile material continues, relieving pressure behind the target shock. Rebound of this projectile material imparts a strong additional impulse to the target.



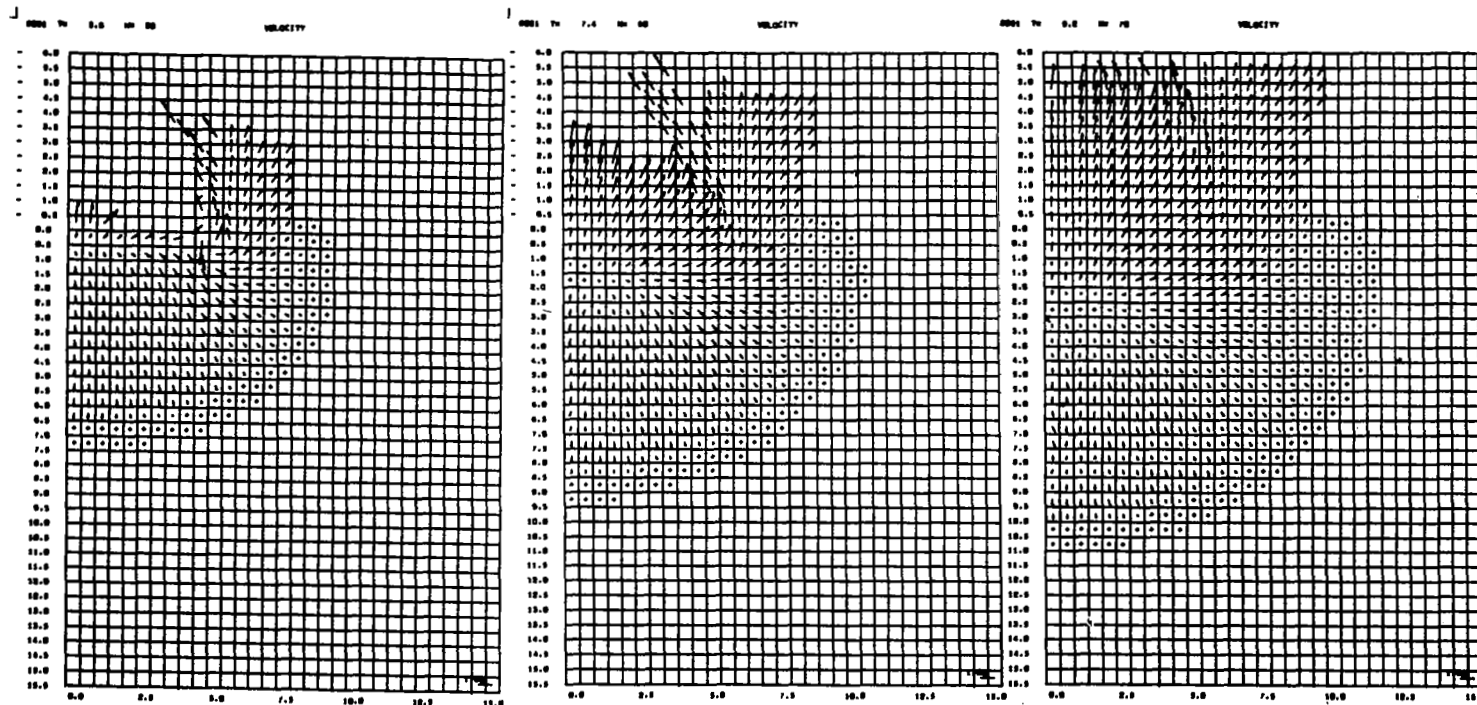
(i) Mass Positions
 $t = 18.1 \mu\text{sec}$



(j) Mass Positions
 $t = 25.3 \mu\text{sec}$

FIGURE C-1 (Con't): CASE 8051, Porous Aluminum ($\rho = 0.44$) into Aluminum at 20 km/sec

A grid change was made at $t = 13.9 \mu\text{sec}$. By $t = 25.3 \mu\text{sec}$, much of the vaporized projectile mass has been ejected from the forming crater region. The target shock has reached a depth of about 22 cm, or two projectile diameters, and is detaching from the remaining cratering flow. The solution continued to $t = 60.1 \mu\text{sec}$, but the continuing plots do not show any further changes of interest in the mass positions.



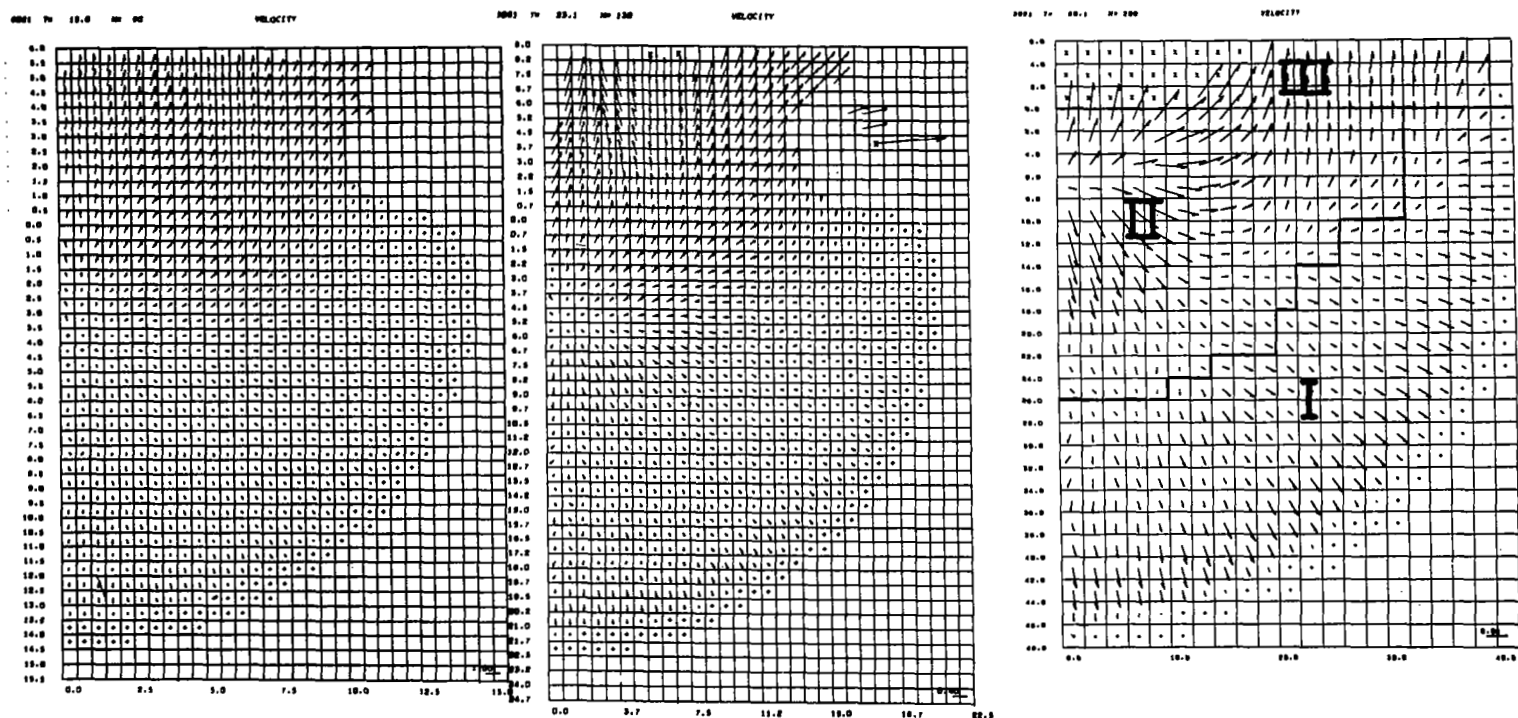
(k) Velocity Field
 $t = 5.6 \mu\text{sec}$

(l) Velocity Field
 $t = 7.4 \mu\text{sec}$

(m) Velocity Field
 $t = 9.2 \mu\text{sec}$

FIGURE C-1 (Con't): CASE 8051, Porous Aluminum ($\rho = 0.44$) into Aluminum at 20 km/sec

In these velocity plots, the length of the arrows is the average velocity of the mass points in each cell, as measured on the scale (cm/ μsec) in the lower right corner. Where a (+) is shown, the velocity is non-zero, but is too small to be plotted. At $t = 5.6$, vapor blowoff from the rear surface of the projectile is just starting. This relatively high velocity blowoff continues until all of the projectile material is ejected.



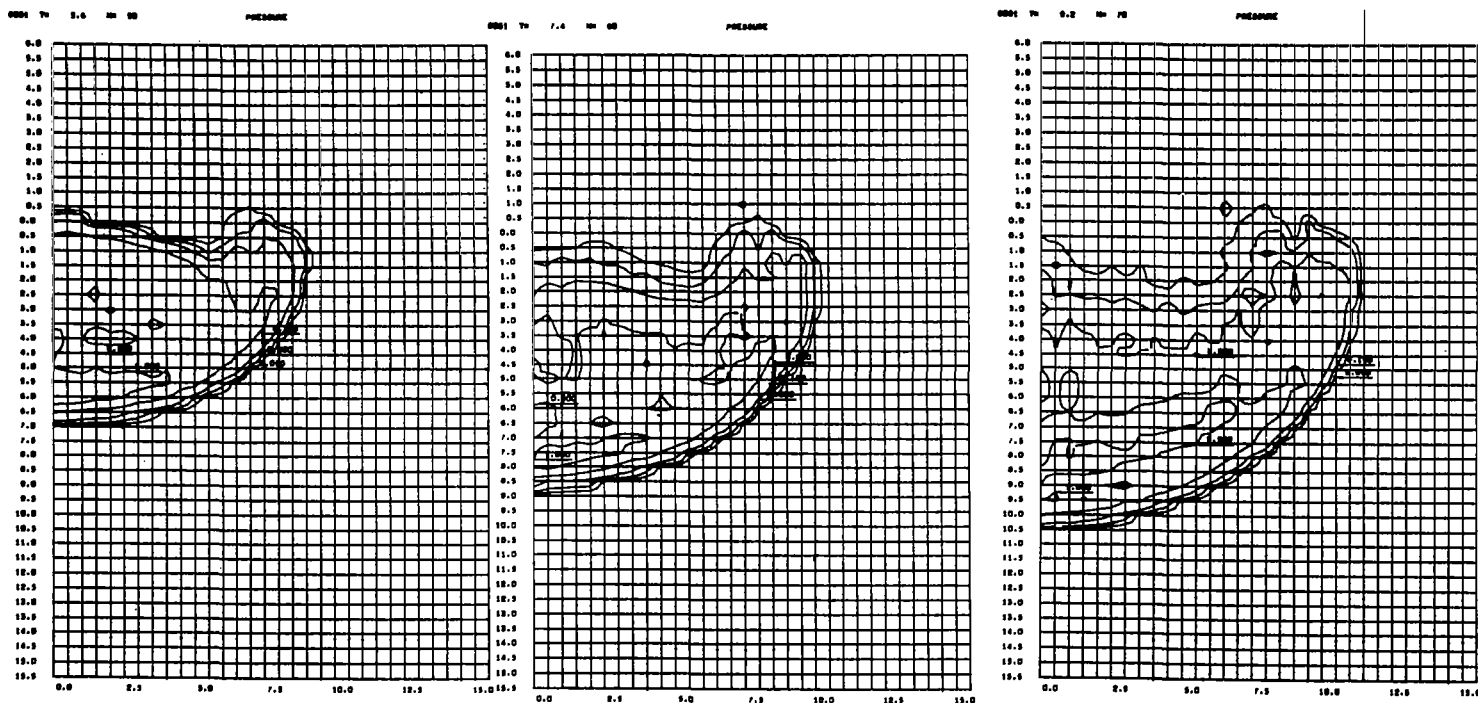
(n) Velocity Field
 $t = 13.0 \mu\text{sec}$

(o) Velocity Field
 $t = 23.1 \mu\text{sec}$

(p) Velocity Field
 $t = 60.1 \mu\text{sec}$

FIGURE C-1 (Con't): CASE 8051, Porous Aluminum ($\rho = 0.44$) into Aluminum at 20 km/sec

The velocity field at $t = 60.1 \mu\text{sec}$ is from the late stages of the impact response. A distinct region of quiescence from about $y = 24$ to $y = 34$ is evident separating the target shock from the vigorous flow in the cratering region.



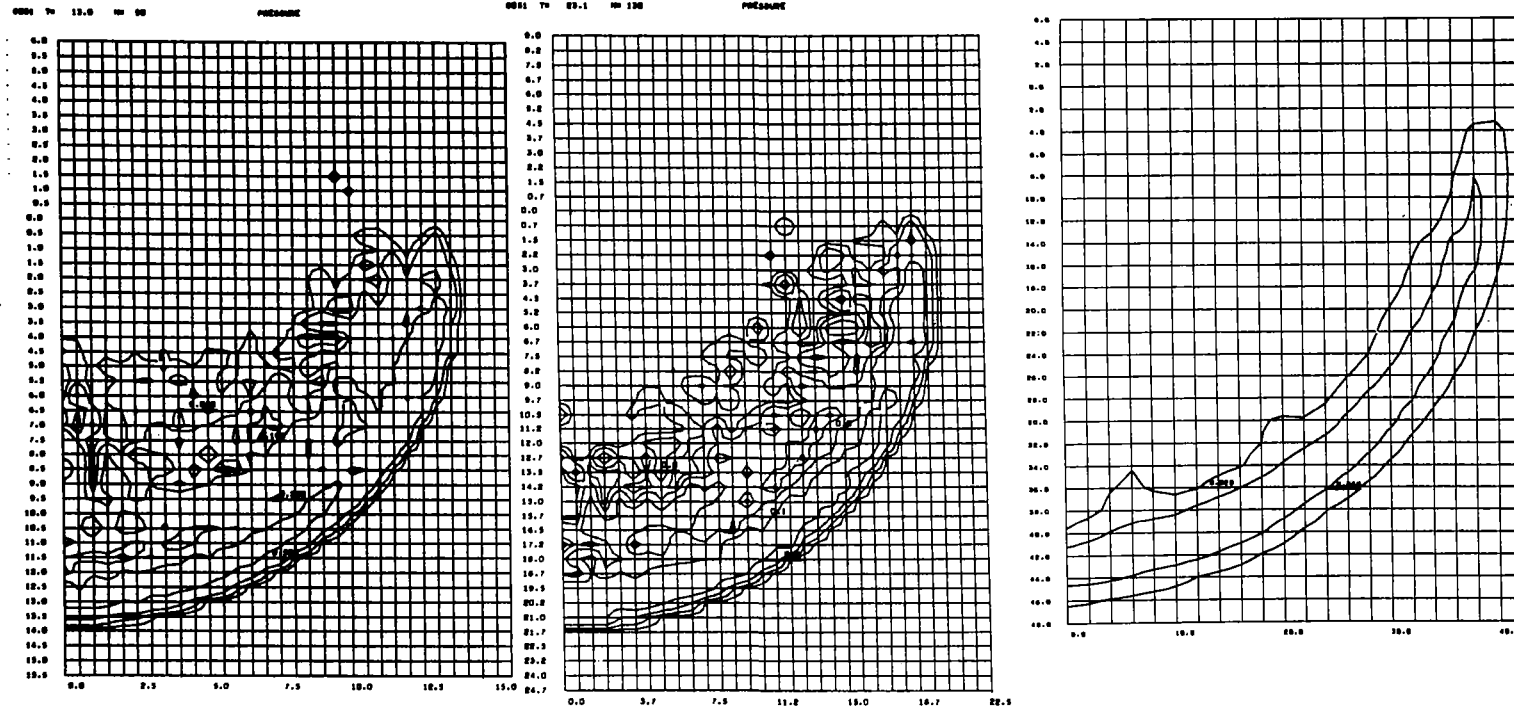
(g) Pressure Field
 $t = 5.6 \mu\text{sec}$

(r) Pressure Field
 $t = 7.4 \mu\text{sec}$

(s) Pressure Field
 $t = 9.2 \mu\text{sec}$

FIGURE C-1 (Con't): CASE 8051, Porous Aluminum ($\rho = 0.44$) into Aluminum at 20 km/sec

These plots show pressure contours, with the contour lines flagged with pressure levels in megabars. By $t = 5.6 \mu\text{sec}$, the initial pressure pulse has reached the rear surface of the projectile. Blowoff of the vaporized material is providing pressure relief, as is evidenced by the declining pressures which are seen in the upper part of the shocked region at $t = 7.4$ and $t = 9.2 \mu\text{sec}$.



(t) Pressure Field
 $t = 13.0 \mu\text{sec}$

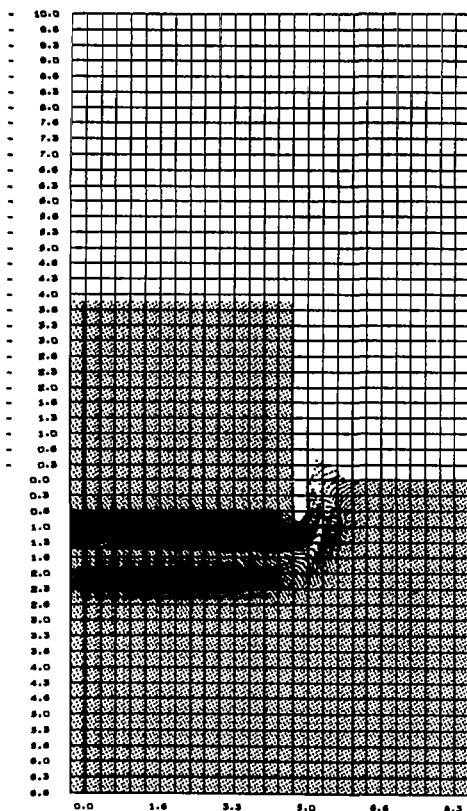
(u) Pressure Field
 $t = 23.1 \mu\text{sec}$

(v) Pressure Field
 $t = 60.1 \mu\text{sec}$

FIGURE C-1 (Con't): CASE 8051, Porous Aluminum ($\rho = 0.44$) into Aluminum at 20 km/sec

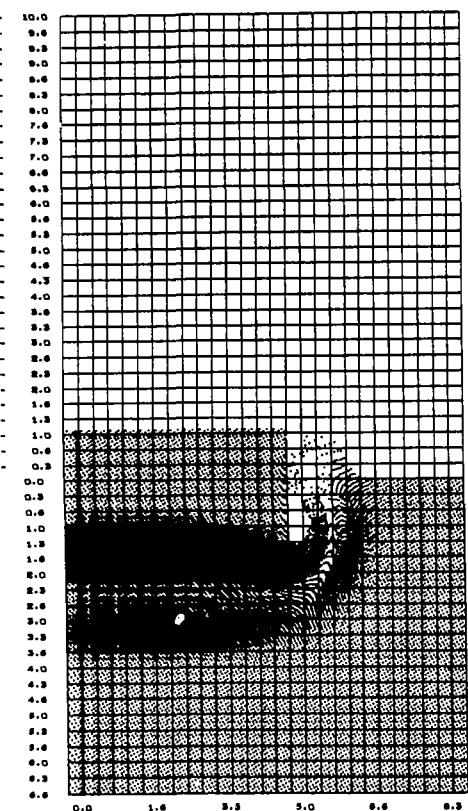
The strong shock front continues to propagate into the target, although it is attenuating rapidly due both to geometrical divergence and to rarefactions from the target surface. At $t = 13.0 \mu\text{sec}$, the peak pressure is over 500 kilobars, declining to somewhat over 200 kb at $t = 23.1 \mu\text{sec}$, and to 50 kb at $60.1 \mu\text{sec}$. Note the complete separation of the shock from the cratering region at late times.

DOSE T= 0.8 N= 80 MASS POSITIONS



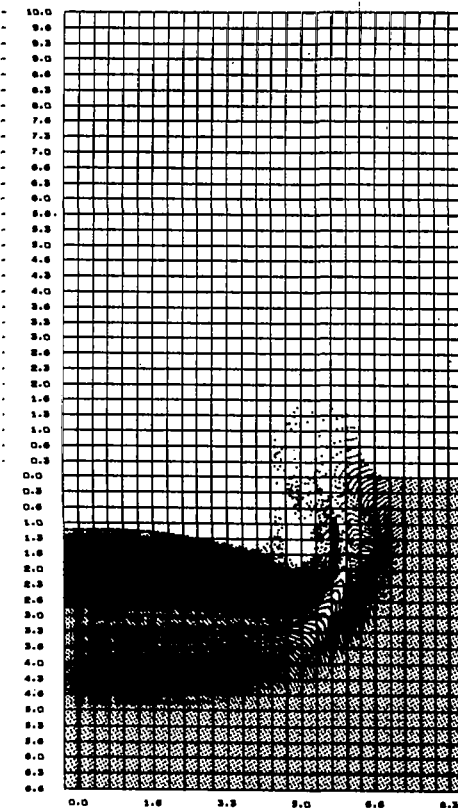
(a) Mass Positions
 $t = 0.8 \mu\text{sec}$

DOSE T= 1.2 N= 30 MASS POSITIONS



(b) Mass Positions
 $t = 1.2 \mu\text{sec}$

DOSE T= 1.6 N= 40 MASS POSITIONS



(c) Mass Positions
 $t = 1.6 \mu\text{sec}$

FIGURE C-2: CASE 8052, Porous Aluminum ($\rho = 0.44$) into Aluminum at 72 km/sec

As in Case 8051, the porous projectile is severely compressed in the initial stages of impact. By $t = 1.6 \mu\text{sec}$, all of the projectile has been engulfed by the impact shock, and it has been compressed to a length of about 1.5 cm. The projectile is vaporized by this severe shocking, and blowoff is just starting at the rear (top) surface. A small vortex is seen forming at $t = 1.2 \mu\text{sec}$ as target ejecta strikes the side of the incoming projectile. (See also Fig. C-2 (k) and (l).)

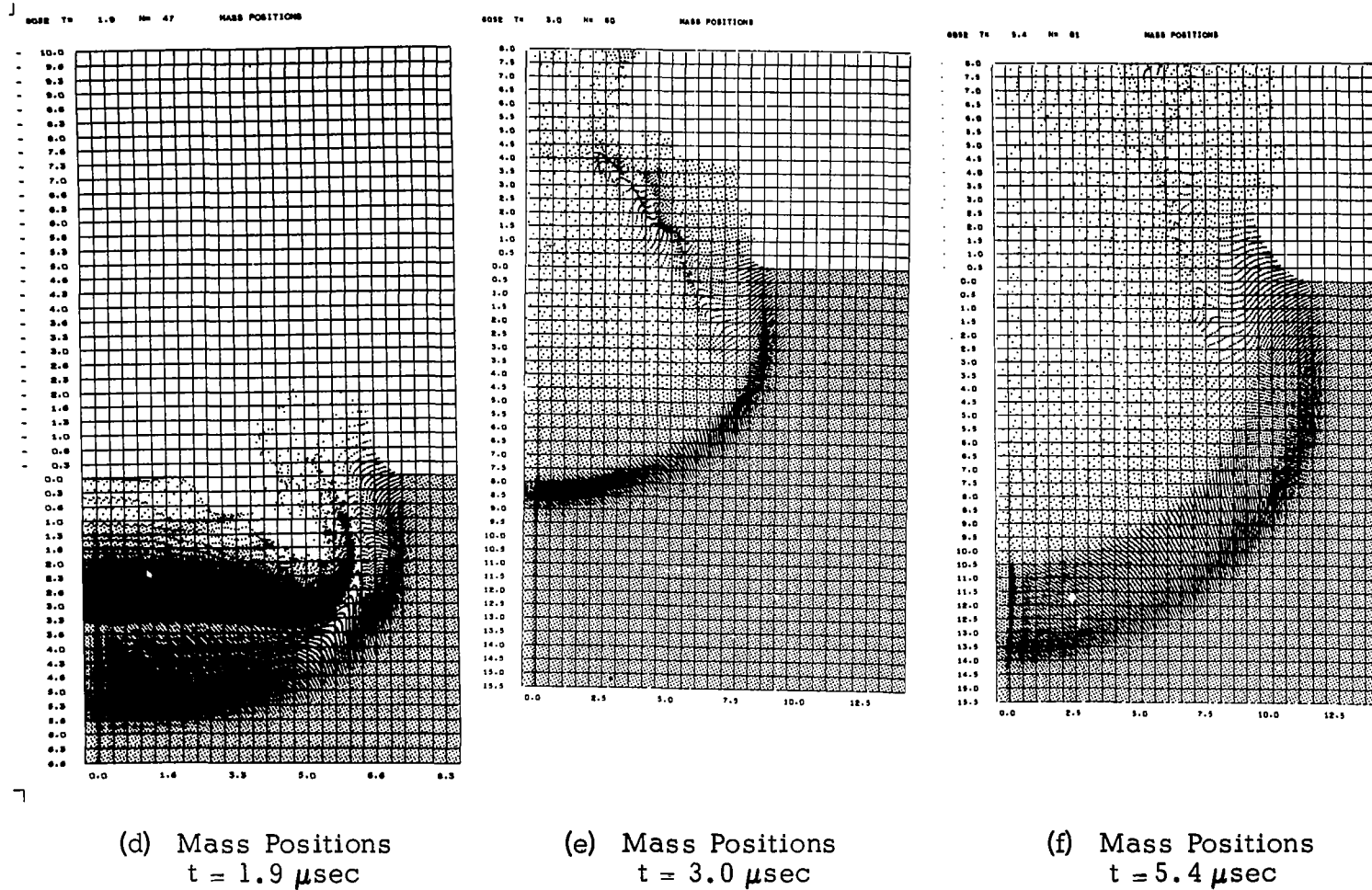
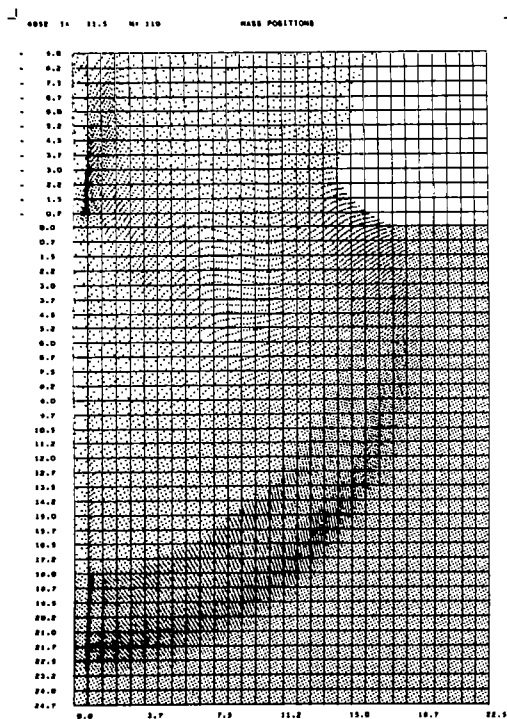
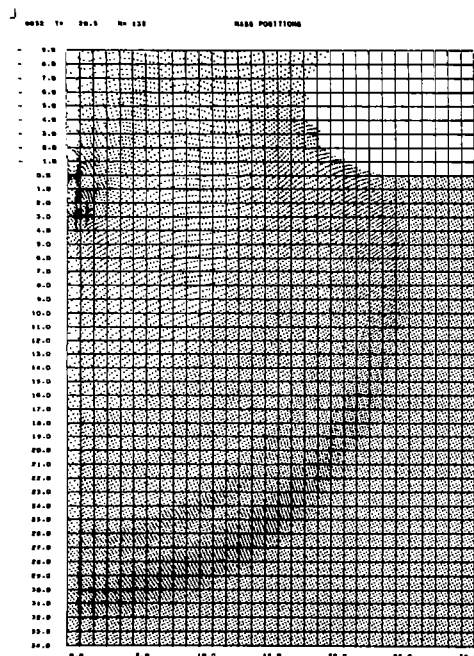


FIGURE C-2 (Con't): CASE 8052, Porous Aluminum ($\rho = 0.44$) into Aluminum at 72 km/sec

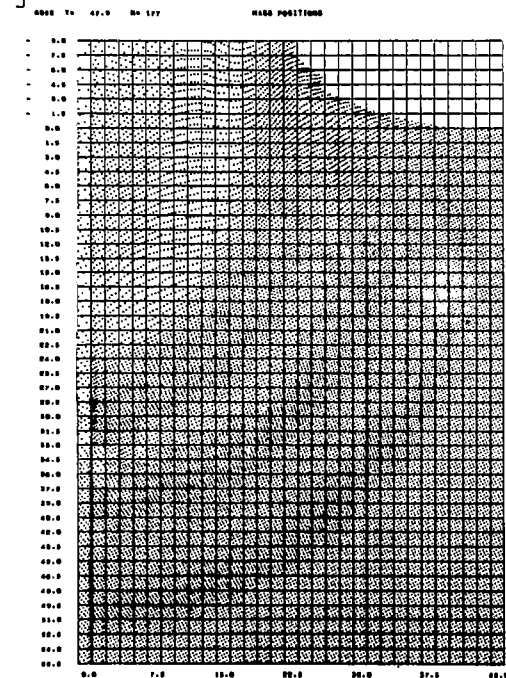
At $t = 1.9 \mu\text{sec}$, blowoff of projectile material continues from the top surface. Target ejecta is seen closing over the projectile mass. At later times, this ejecta is seen to interact with blowoff vapor and to converge towards the axis. A grid change was made after the $t = 1.9 \mu\text{sec}$ plot to enlarge the field of view.



(g) Mass Positions
 $t = 11.5 \mu\text{sec}$

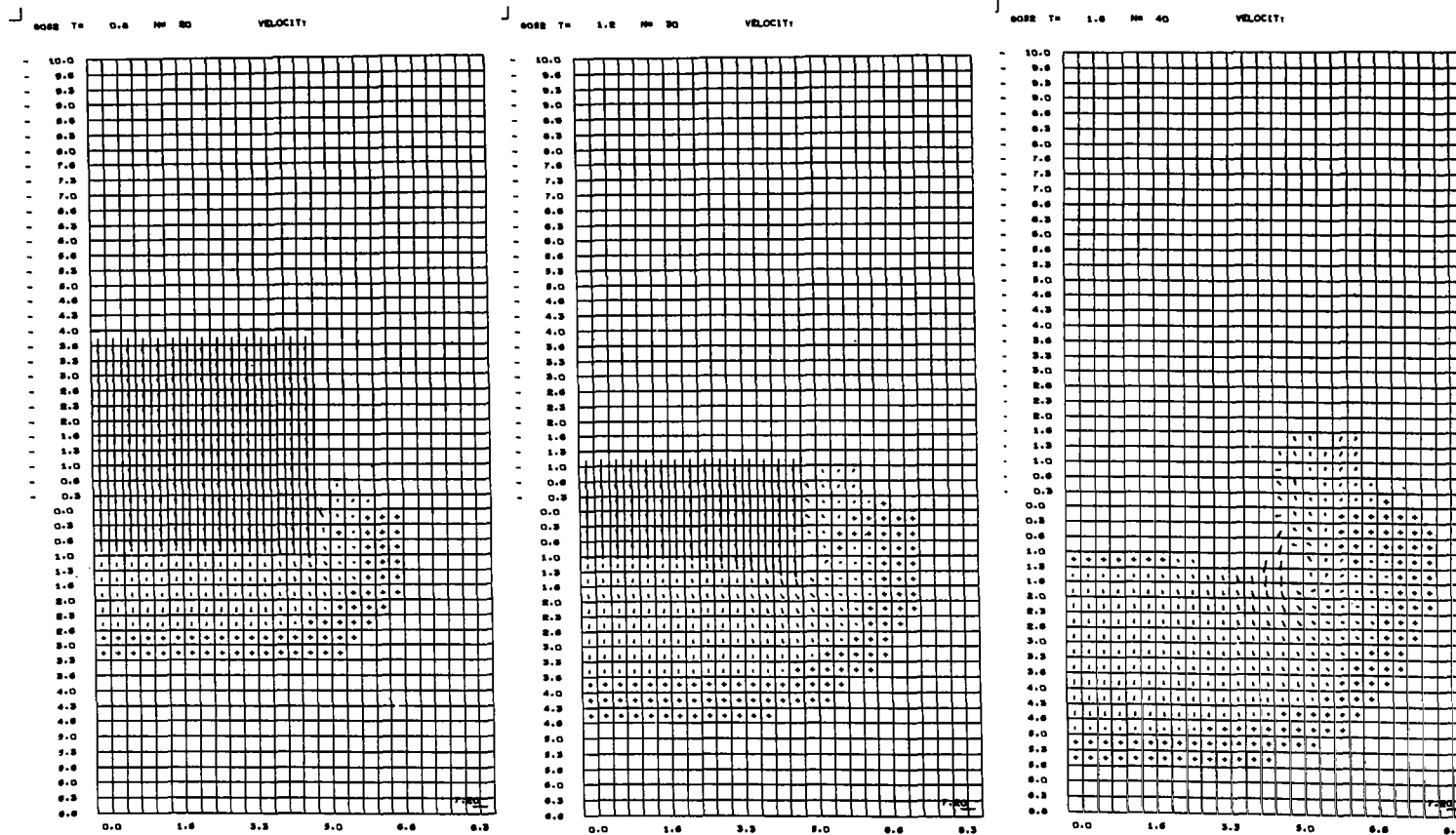


(h) Mass Positions
 $t = 20.5 \mu\text{sec}$



(i) Mass Positions
 $t = 47.9 \mu\text{sec}$

FIGURE C-2 (Con't): CASE 8052, Porous Aluminum ($\rho = 0.44$) into Aluminum at 72 km/sec



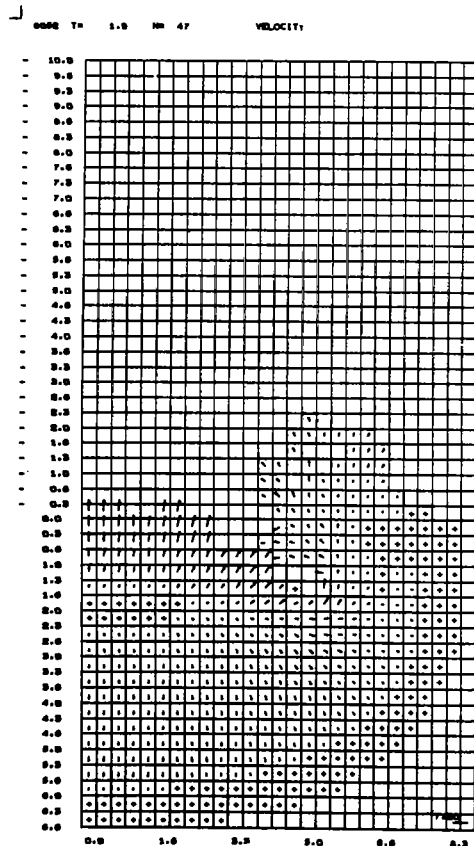
(j) Velocity Field
 $t = 0.8 \mu\text{sec}$

(k) Velocity Field
 $t = 1.2 \mu\text{sec}$

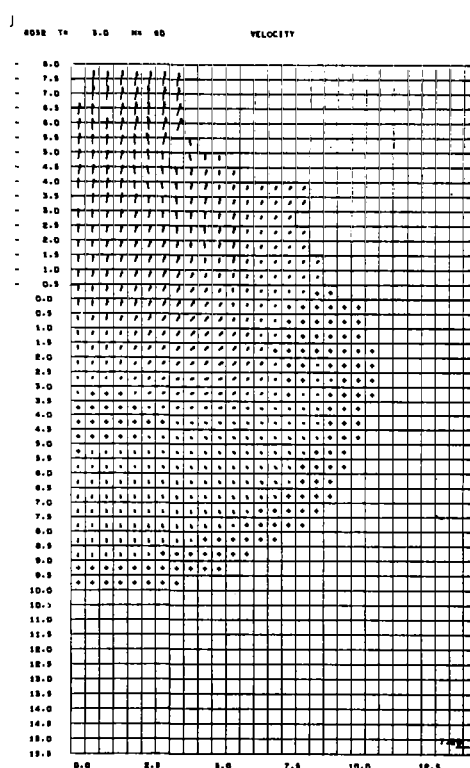
(l) Velocity Field
 $t = 1.6 \mu\text{sec}$

FIGURE C-2 (Con't): CASE 8052, Porous Aluminum ($\rho = 0.44$) into Aluminum at 72 km/sec

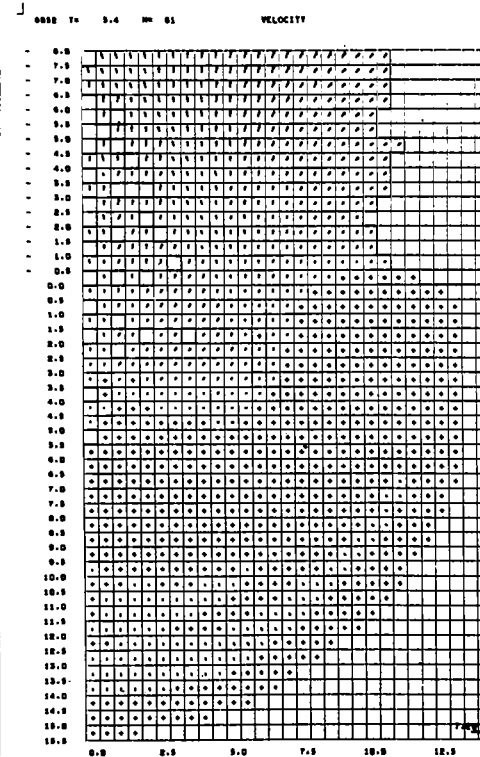
Formation of a small vortex is seen at 1.2 and 1.6 μsec as target ejecta strikes the side of the incoming projectile.



(m) Velocity Field
 $t = 1.9 \mu\text{sec}$



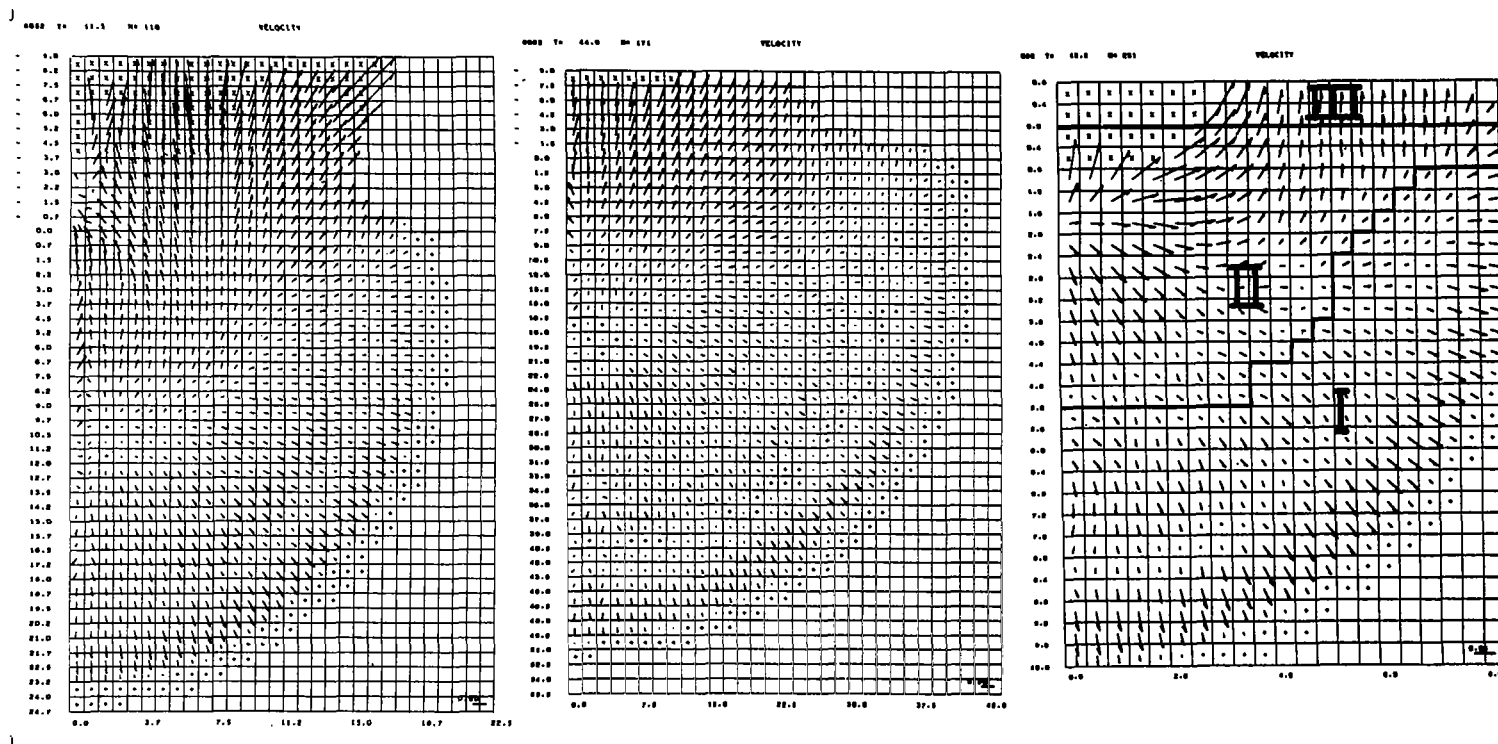
(n) Velocity Field
 $t = 3.0 \mu\text{sec}$



(o) Velocity Field
 $t = 5.4 \mu\text{sec}$

FIGURE C-2 (Con't): CASE 8052, Porous Aluminum ($\rho = 0.44$) into Aluminum at 72 km/sec

A grid change was made after $t = 1.9 \mu\text{sec}$. The very high blowoff velocity of the projectile vapor is seen at $t = 3.0 \mu\text{sec}$.



(p) Velocity Field
 $t = 11.5 \mu\text{sec}$

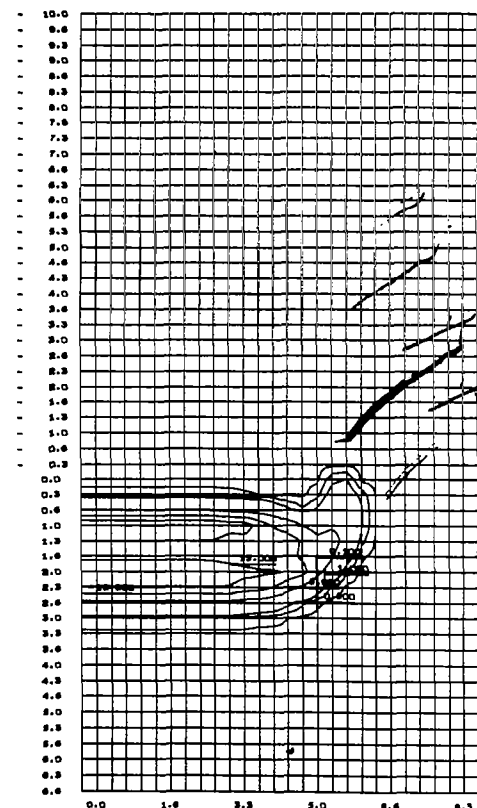
(q) Velocity Field
 $t = 44.0 \mu\text{sec}$

(r) Velocity Field
 $t = 122 \mu\text{sec}$

FIGURE C-2 (Con't): CASE 8052, Porous Aluminum ($\rho = 0.44$) into Aluminum at 72 km/sec

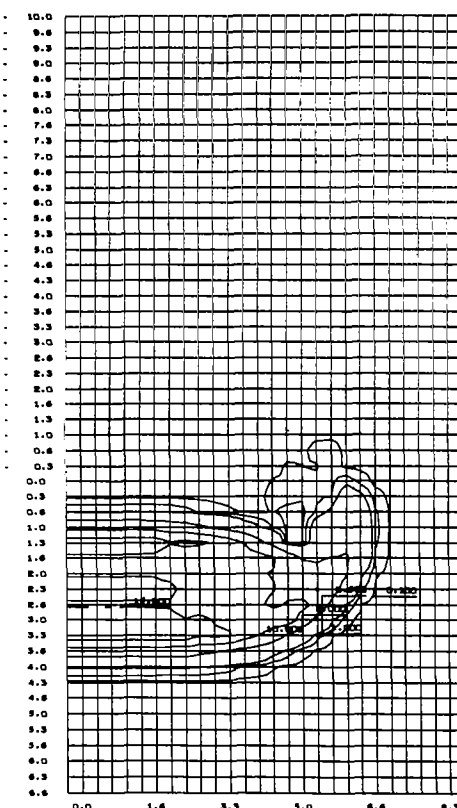
Grid changes were made between each of these views. Separation of the target shock from the cratering region is evident at $t = 122 \mu\text{sec}$.

BOSE T= 0.8 No 80 PRESSURE



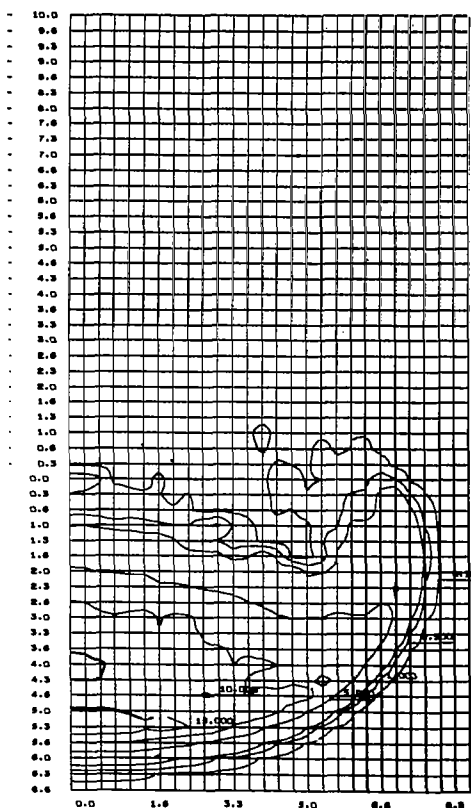
(s) Pressure Field
 $t = 0.8 \mu\text{sec}$

BOSE T= 1.2 No 30 PRESSURE



(t) Pressure Field
 $t = 1.2 \mu\text{sec}$

BOSE T= 1.9 No 47 PRESSURE



(u) Pressure Field
 $t = 1.9 \mu\text{sec}$

FIGURE C-2 (Con't): CASE 8052, Porous Aluminum ($\rho = 0.44$) into Aluminum at 72 km/sec

Initial impact pressure was 15.3 megabars. One dimensional flow occurs adjacent to the axis until about $1.5 \mu\text{sec}$, when lateral rarefactions reach the axis.

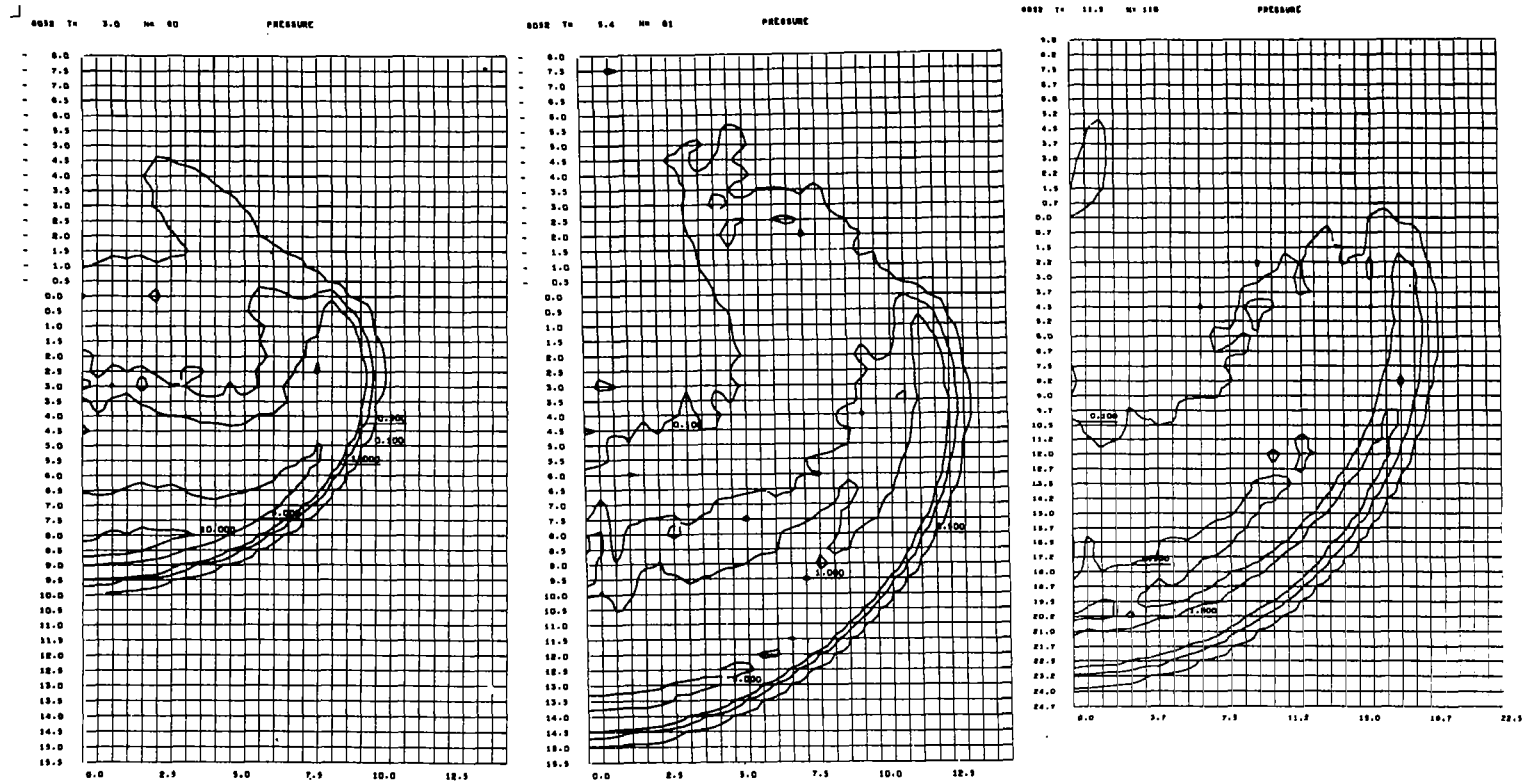
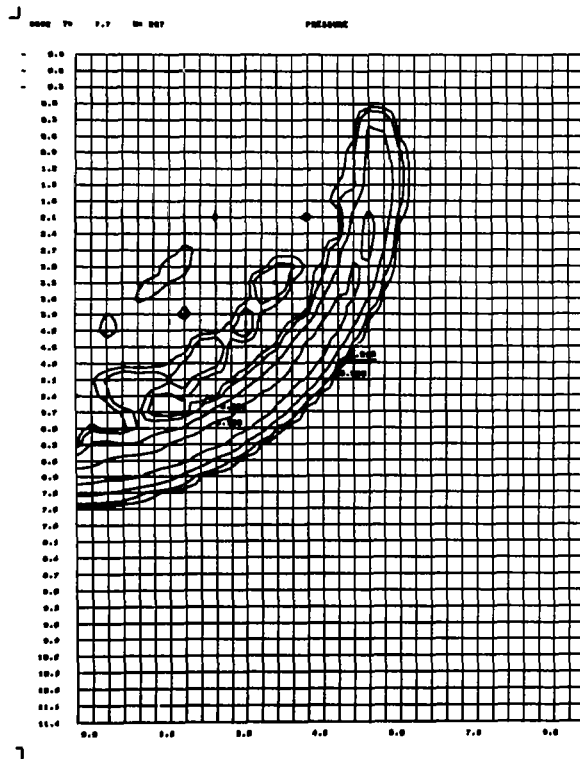
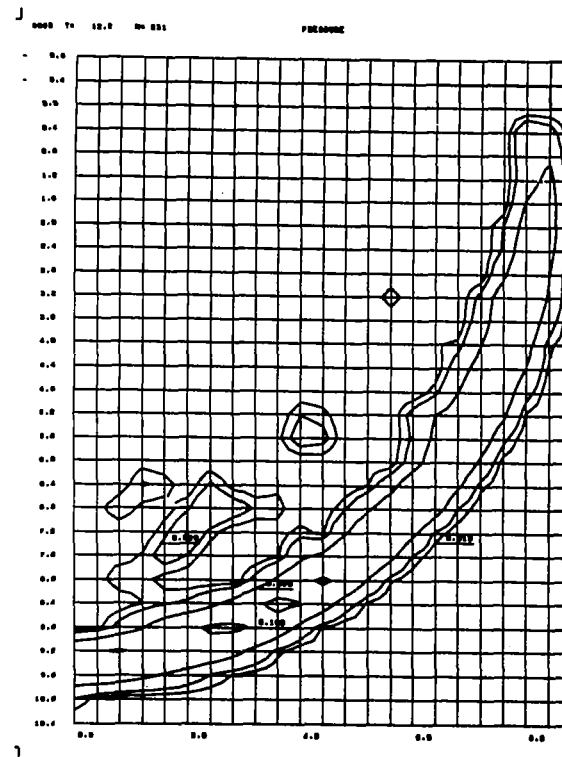


FIGURE C-2 (Con't): CASE 8052, Porous Aluminum ($\rho = 0.44$) into Aluminum at 72 km/sec

Relatively high pressures (>100 kb) persist even in the blowoff region above the projectile.



(y) Pressure Field
t = 77 μ sec



(z) Pressure Field
t = 122 μ sec

FIGURE C-2 (Con't): CASE 8052, Porous Aluminum ($\rho = 0.44$) into Aluminum at 72 km/sec

The target shock continues to expand, with peak pressure dropping due to geometric divergence and to rarefactions from behind. By $t = 122 \mu$ sec, the shock is well-separated from the cratering flow. Peak pressures, however, are still at 100 kb. By comparison, in Case 8051, peak pressures had dropped nearly to 50 kb by 60 μ sec.

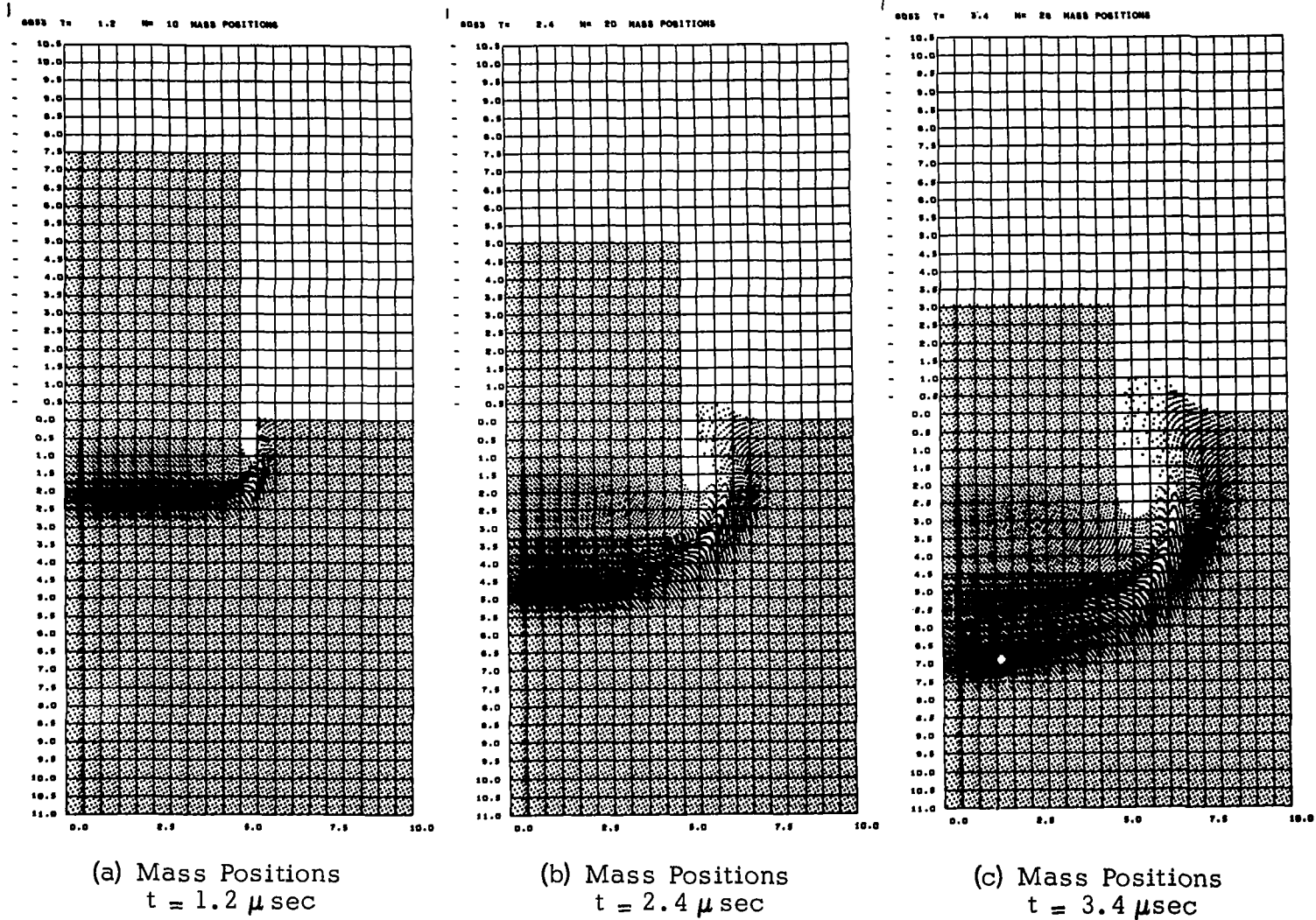
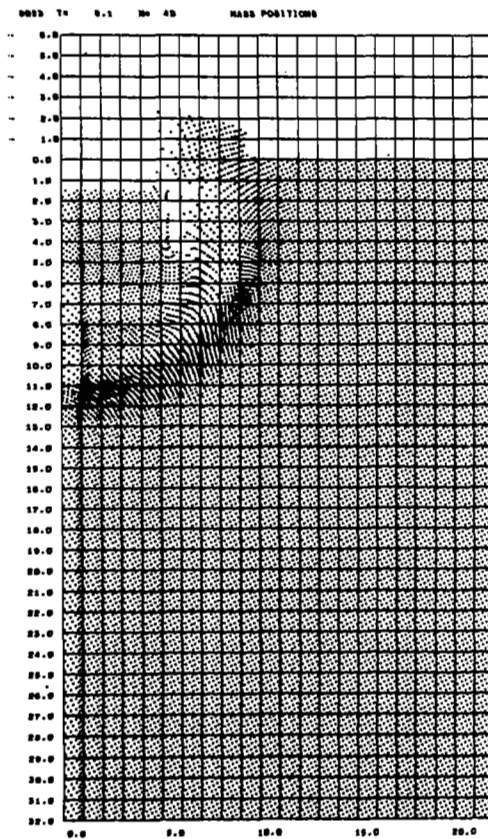
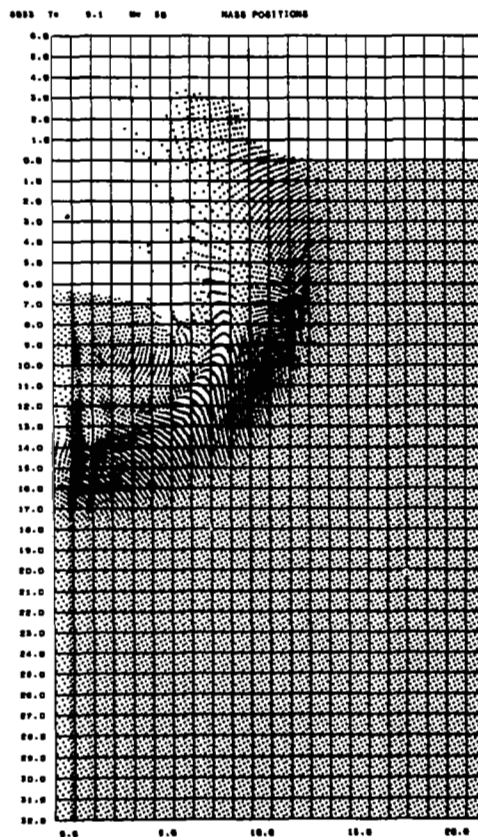


FIGURE C-3: CASE 8053, Iron into Aluminum at 20 km/sec

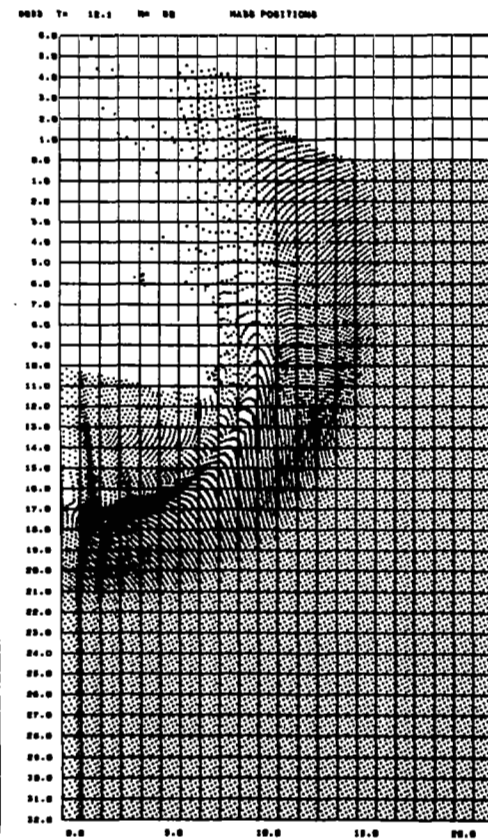
The vortex flow mechanism is well-illustrated in this and the following case (8054). Such flow can occur in impacts of stiff projectile materials into relatively soft targets. Note at $t = 3.4 \mu\text{sec}$ that target ejecta is folding back towards the projectile.



(d) Mass Positions
 $t = 6.1 \mu\text{sec}$



(e) Mass Positions
 $t = 9.1 \mu\text{sec}$



(f) Mass Positions
 $t = 12.1 \mu\text{sec}$

FIGURE C-3 (Con't): CASE 8053, Iron into Aluminum at 20 km/sec

A grid change was made after $t = 3.4 \mu\text{sec}$. Target ejecta continues to close over the back of the projectile. By $t = 12.1 \mu\text{sec}$, the main projectile mass has reached a depth of about 17 cm, or 1.7 diameters into the target.

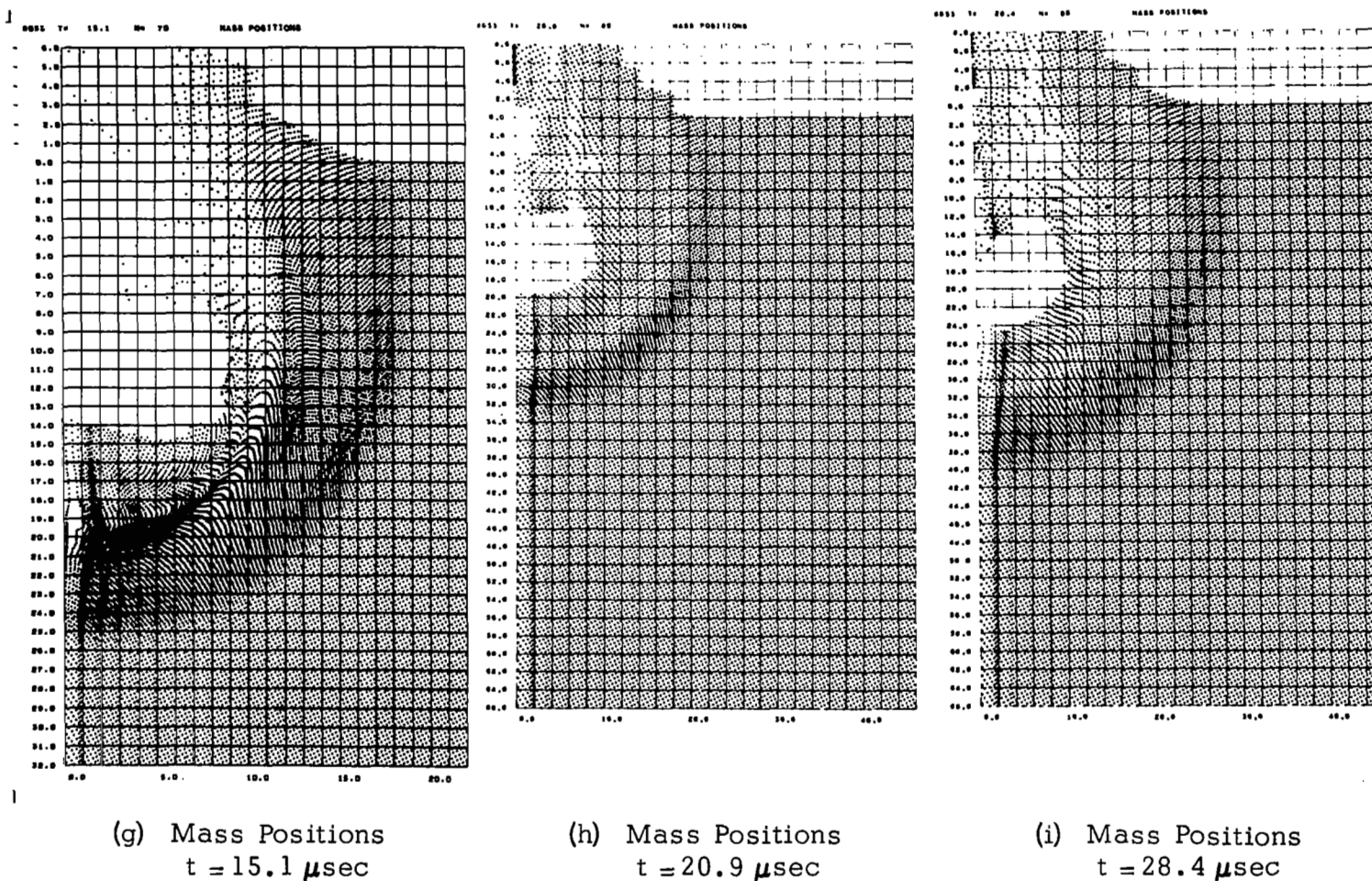
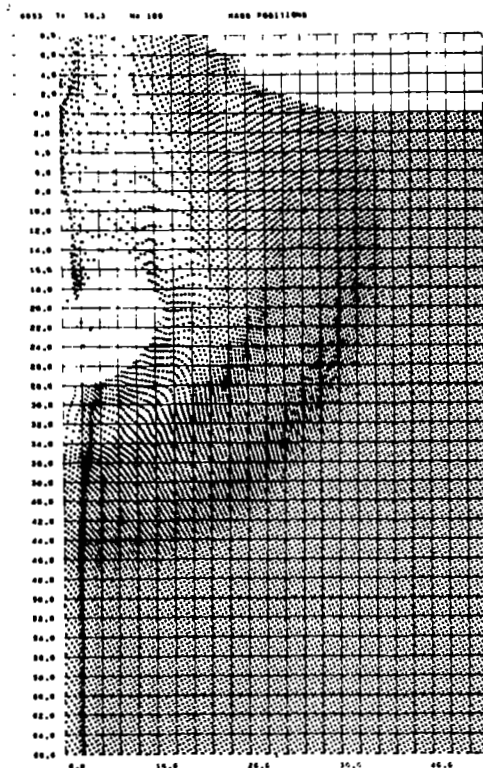
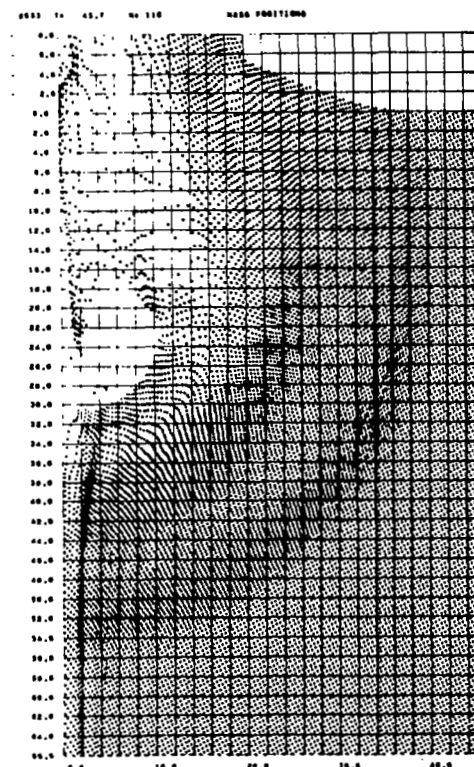


FIGURE C-3 (Con't): CASE 8053, Iron into Aluminum at 20 km/sec

Another grid change was made at $t = 15.4 \mu\text{sec}$. Convergence of ejecta mass towards the axis results in formation of a cavity in the target behind the projectile. This converging material also forms a jet traveling downward into the cavity.



(j) Mass Positions
 $t = 36.3 \mu\text{sec}$



(k) Mass Positions
 $t = 45.7 \mu\text{sec}$

FIGURE C-3 (Con't): CASE 8053, Iron into Aluminum at 20 km/sec

Jetting into the cavity continues. At later times, it will reach the bottom of the cavity (the rear of the projectile mass), applying an additional impulse as it is diverted outward to form a vortex flow. In this impact, the mass involved in the jet was small, so the influence of this vortex mechanism on the cratering was not major.

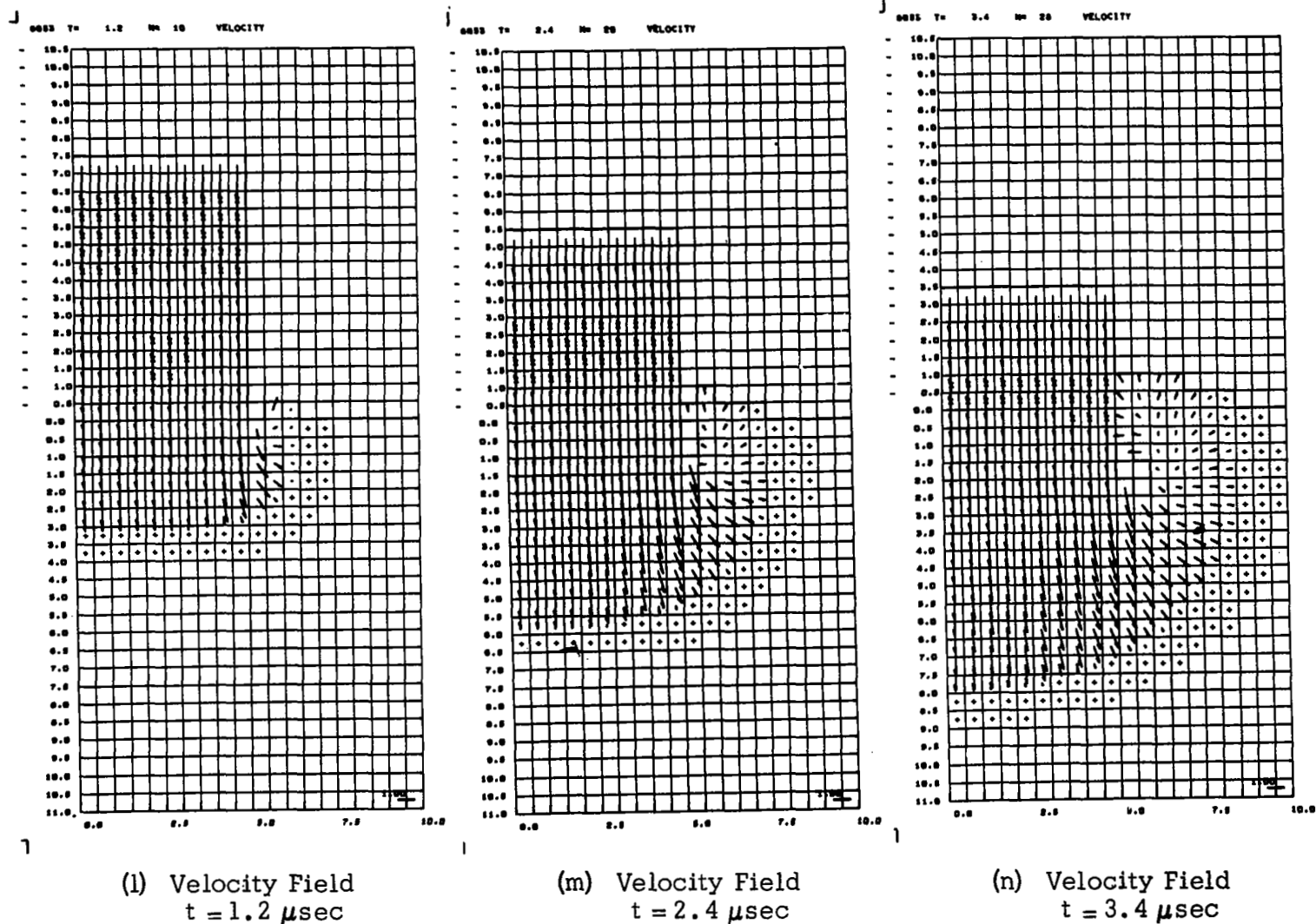
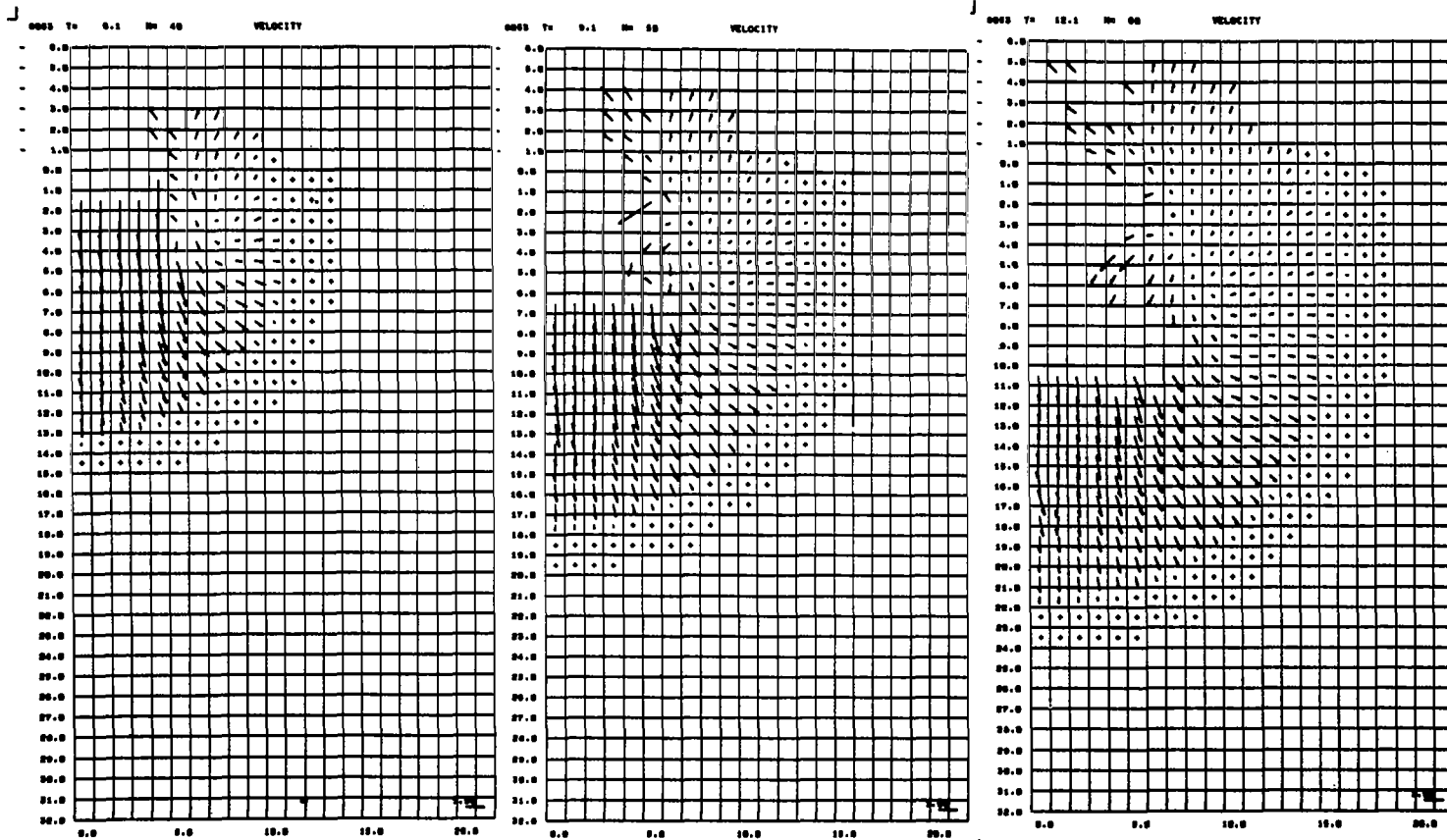


FIGURE C-3 (Con't): CASE 8053, Iron into Aluminum at 20 km/sec

Development of the annular vortex is shown in these and succeeding velocity field plots. At $t = 3.4 \mu\text{sec}$, target ejecta is striking the side of the projectile.



(o) Velocity Field
 $t = 6.1 \mu\text{sec}$

(p) Velocity Field
 $t = 9.1 \mu\text{sec}$

(q) Velocity Field
 $t = 12.1 \mu\text{sec}$

FIGURE C-3 (Con't): CASE 8053, Iron into Aluminum at 20 km/sec

A small vortex has formed where the converging target ejecta interacts with the downward-moving projectile. This vortex persists after the projectile passes, and is enlarging towards the axis at $t = 12.1 \mu\text{sec}$.

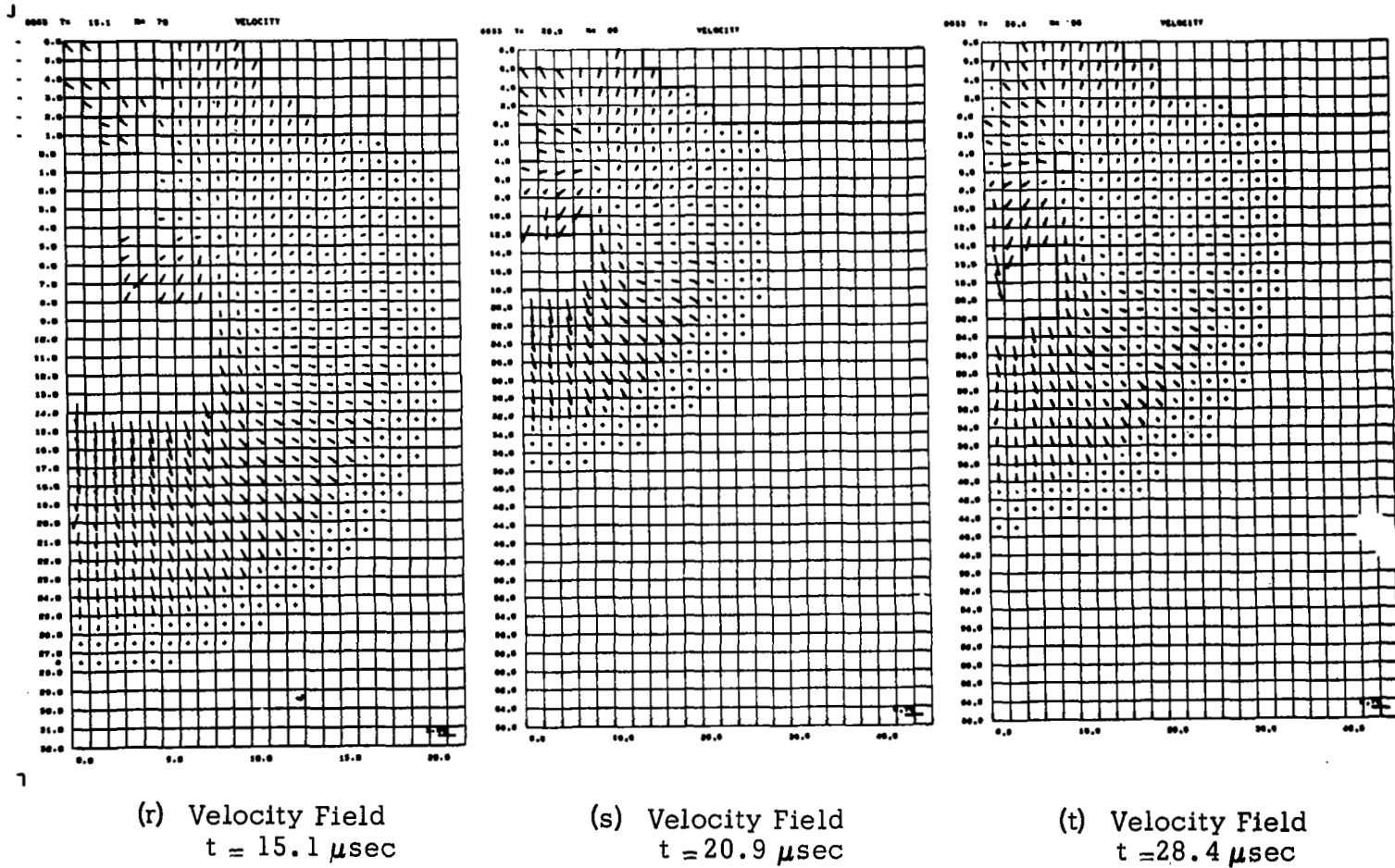
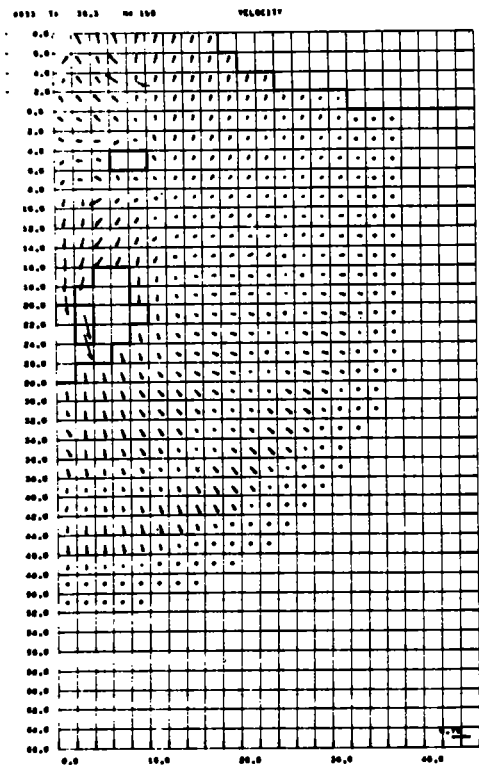
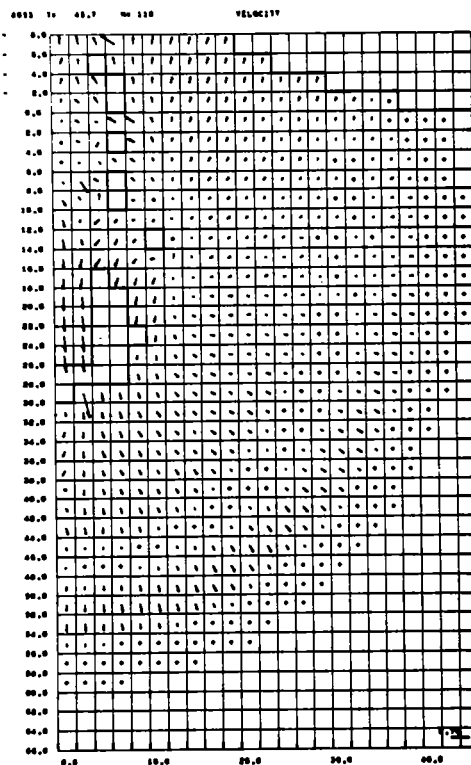


FIGURE C-3 (Con't): CASE 8053, Iron into Aluminum at 20 km/sec

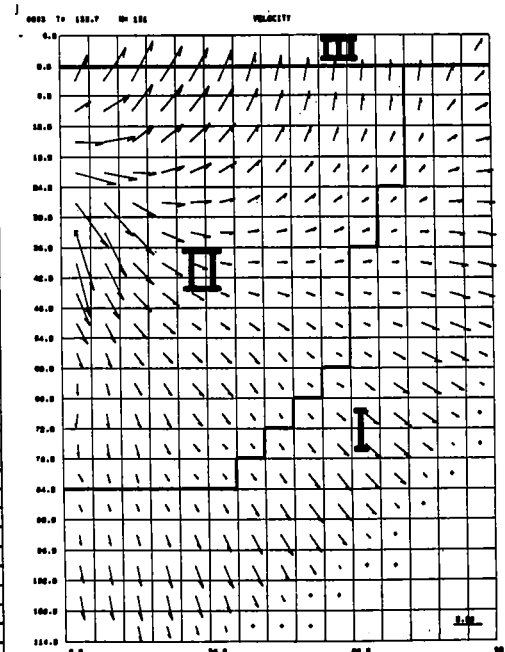
At $t = 20.9 \mu\text{sec}$, the converging material has reached the axis, and downward jetting is evident into the cavity.



(u) Velocity Field
 $t = 36.3 \mu\text{sec}$



(v) Velocity Field
 $t = 45.7 \mu\text{sec}$

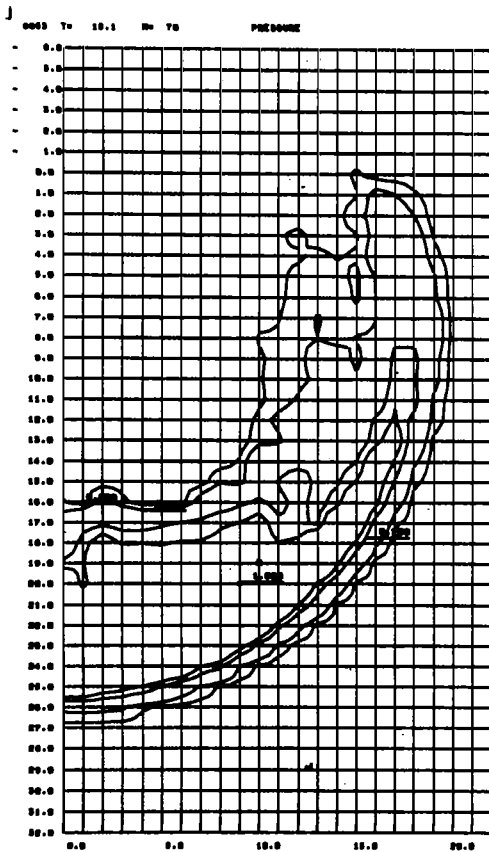


(w) Velocity Field
 $t = 135.7 \mu\text{sec}$

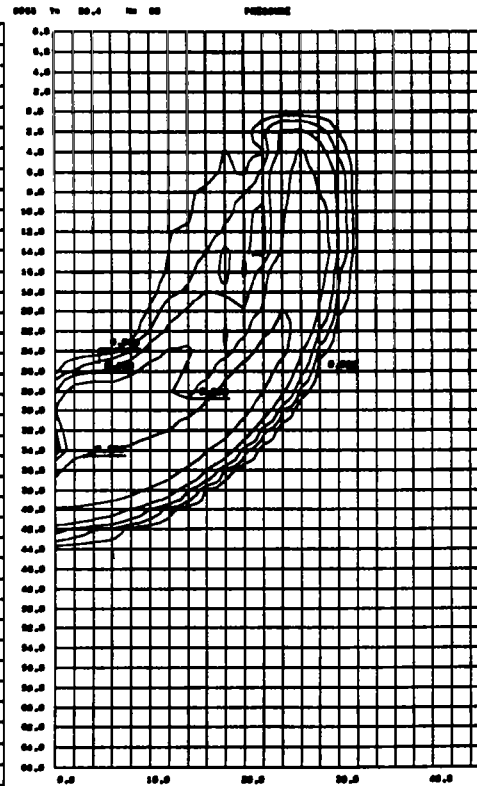
FIGURE C-3 (Con't): CASE 8053, Iron into Aluminum at 20 km/sec

Downward flow of the jet continues, and at $t = 45.7 \mu\text{sec}$, it has nearly reached the rear of the projectile.

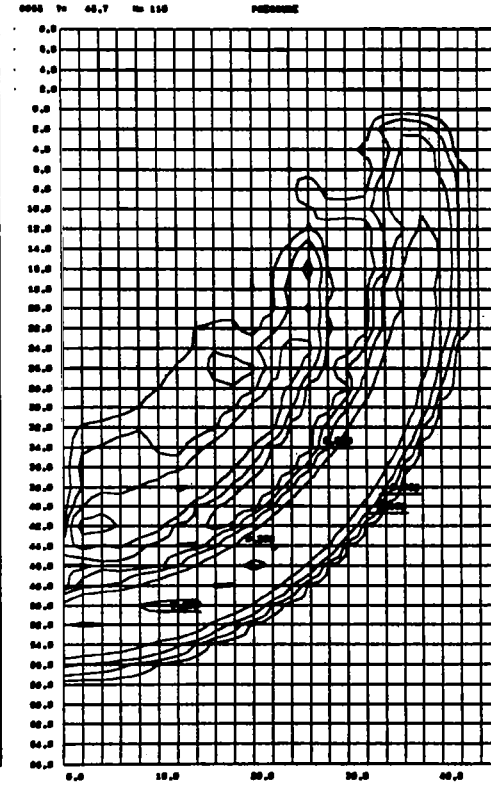
Initial impact pressure was 7.75 megabars. Because only a small mass of target material is involved, the vortex flow does not markedly influence these pressure fields.



(aa) Pressure Field
 $t = 15.1 \mu\text{sec}$



(bb) Pressure Field
 $t = 28.4 \mu\text{sec}$



(cc) Pressure Field
 $t = 45.7 \mu\text{sec}$

FIGURE C-3 (Con't): CASE 8053, Iron into Aluminum at 20 km/sec

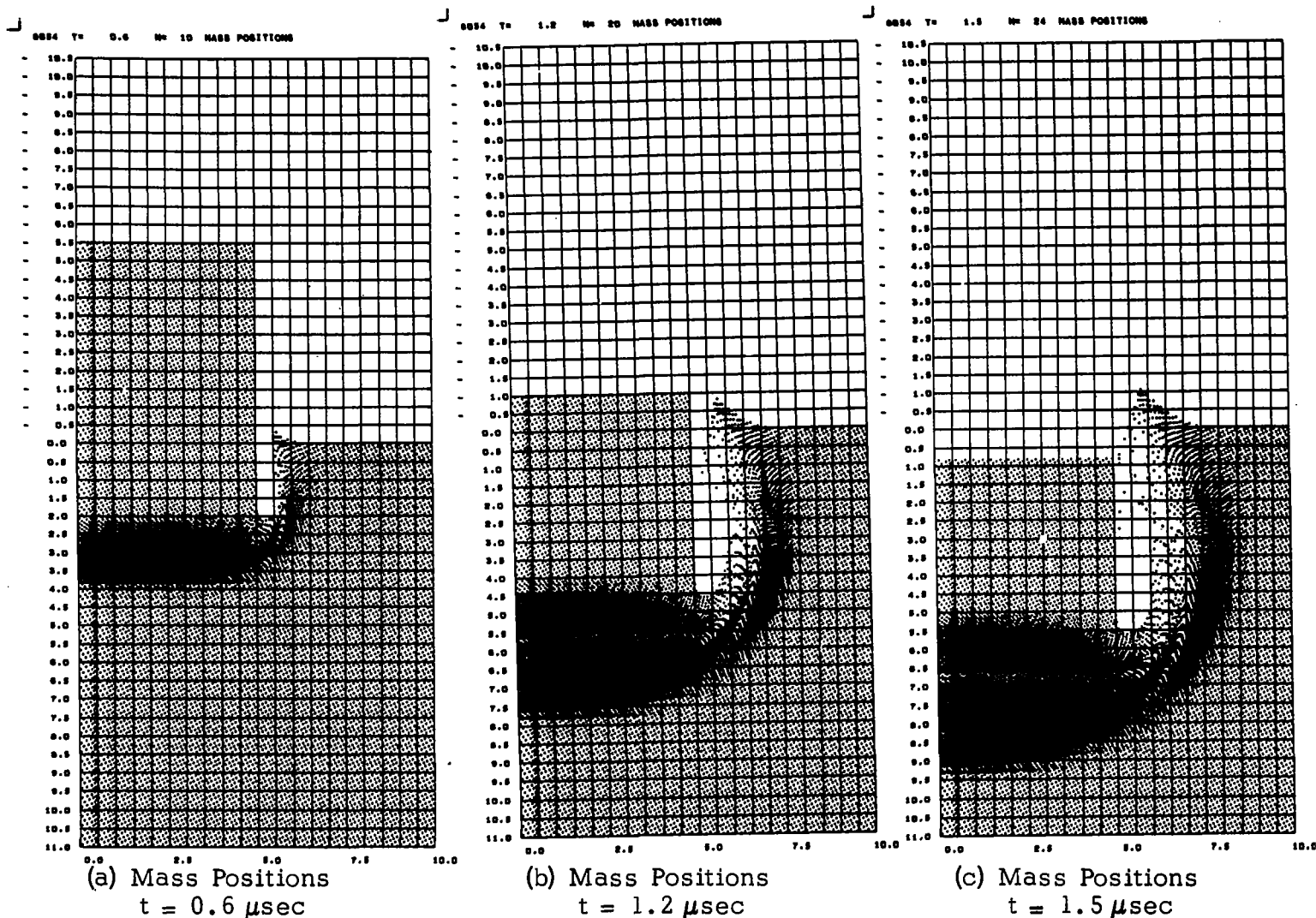
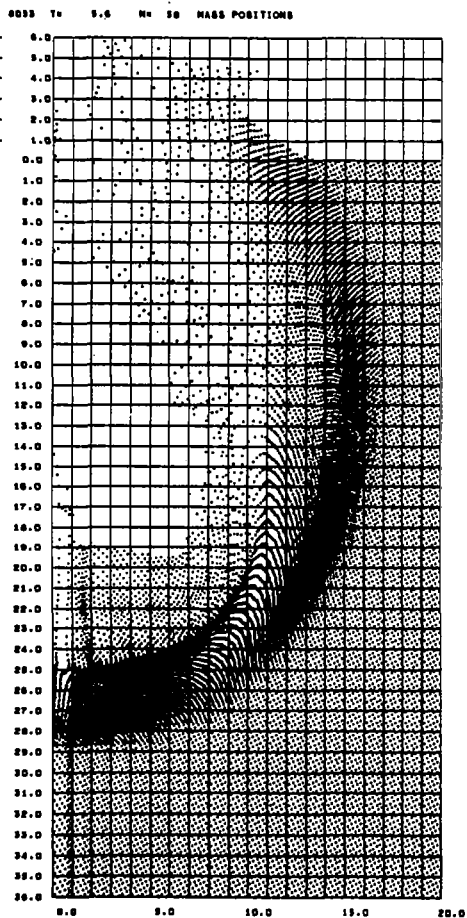
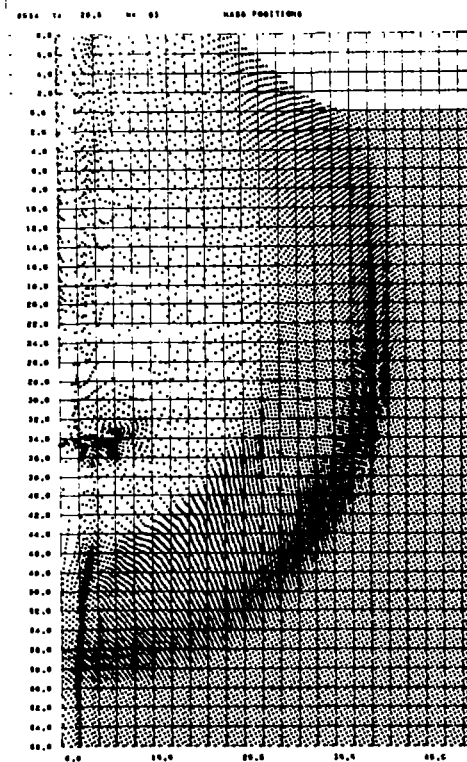


FIGURE C-4: CASE 8054, Iron into Aluminum at 72 km/sec

Vortex flow is strongly evident in this impact. The relatively incompressible steel projectile rapidly penetrates into the soft aluminum target. Initial pressure at impact is 76.8 megabars which is sufficient to cause eventual vaporization of all the projectile and a significant mass of target material. In the above plots, vaporizing target material is seen to rebound from the sides of the crater, converging over the back surface (top) of the projectile.



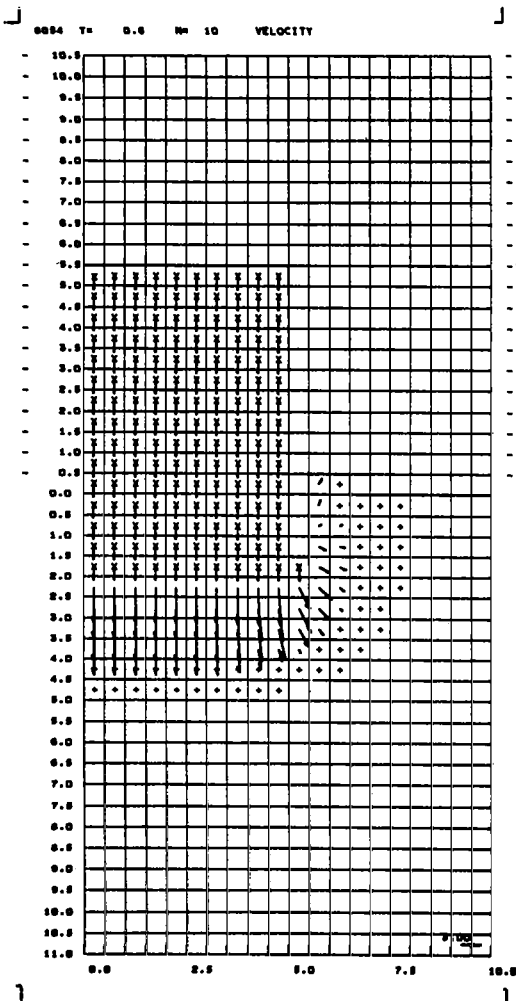
(d) Mass Positions
 $t = 5.6 \mu\text{sec}$



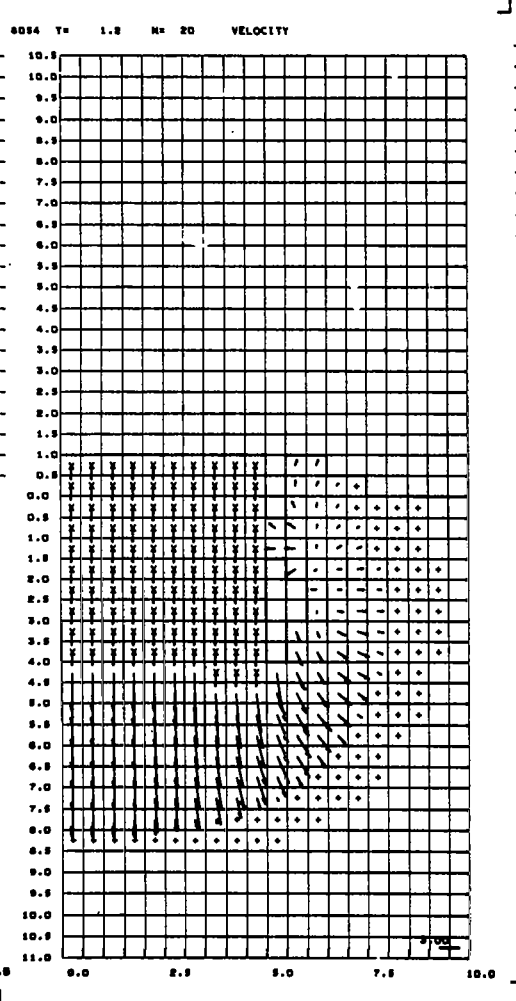
(e) Mass Positions
 $t = 20.6 \mu\text{sec}$

FIGURE C-4 (Cont'd): CASE 8054, Iron into Aluminum at 72 km/sec

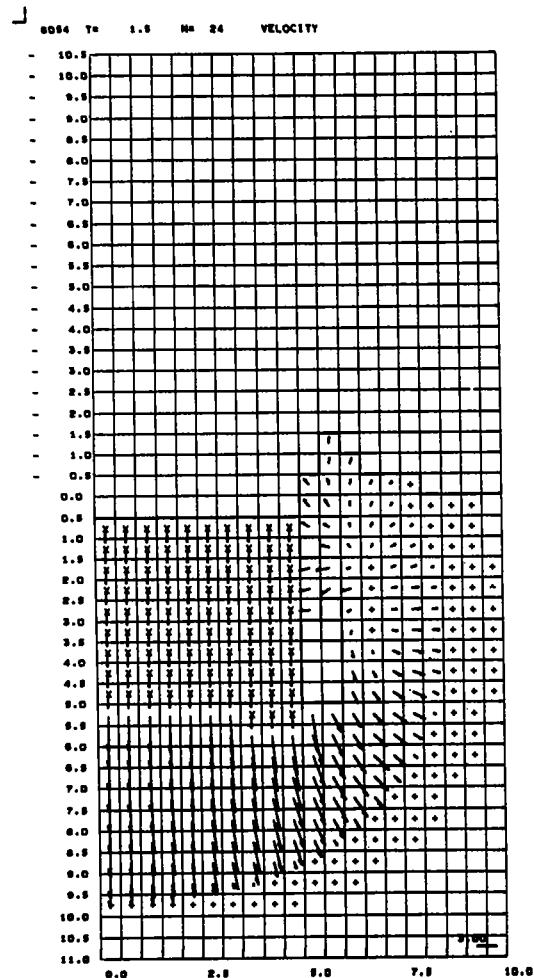
The rebounding sides of the crater have converged to the axis in view (d), enclosing a cavity above the projectile.



(f) Velocity Field
 $t = 0.6 \mu\text{sec}$



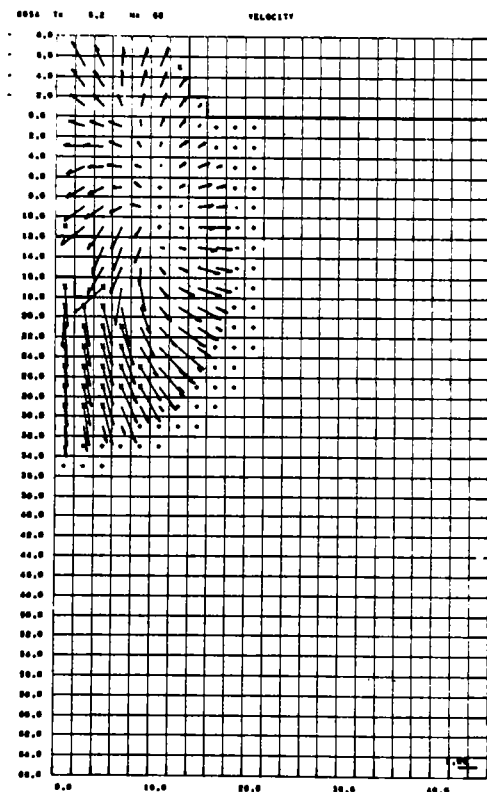
(g) Velocity Field
 $t = 1.2 \mu\text{sec}$



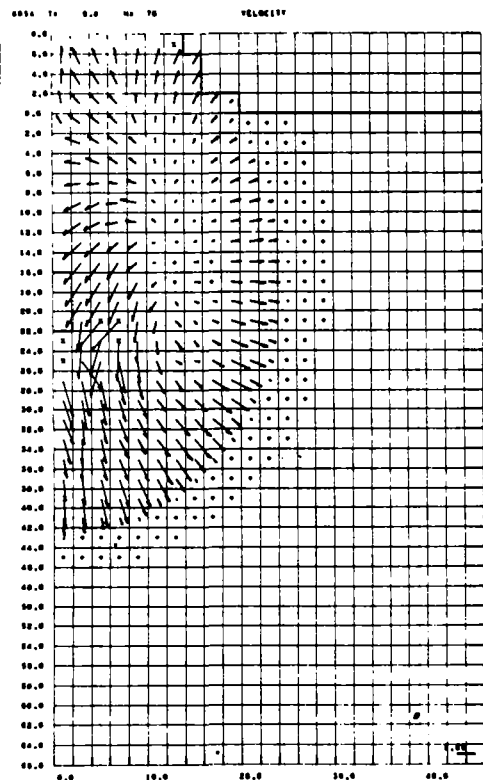
(h) Velocity Field
 $t = 1.5 \mu\text{sec}$

FIGURE C-4 (Con't): CASE 8054, Iron into Aluminum at 72 km/sec

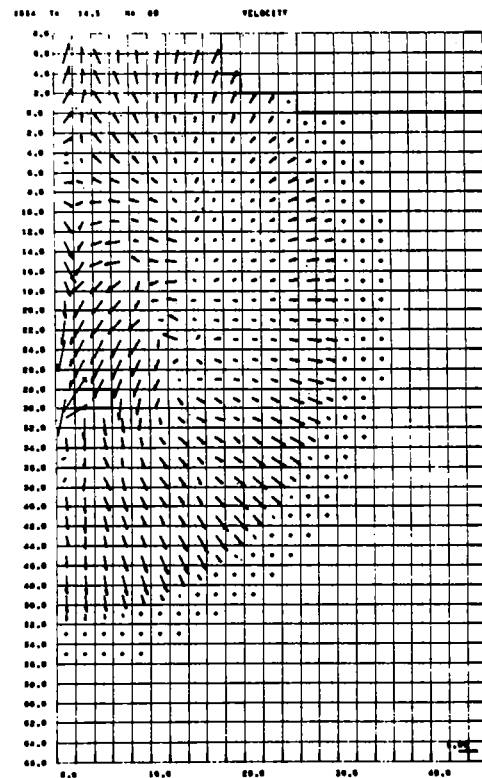
The early stages of rebound of vaporized target material from the sides of the crater are seen here.



(i) Velocity Field
 $t = 6.2 \mu\text{sec}$



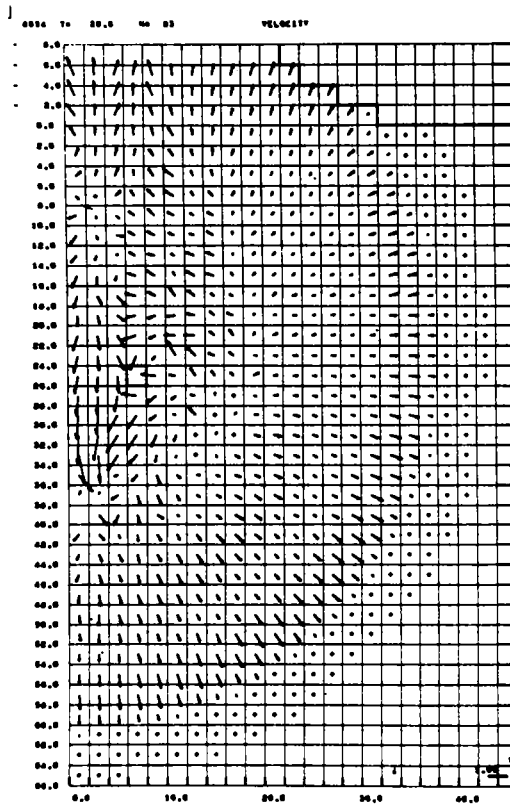
(j) Velocity Field
 $t = 9.8 \mu\text{sec}$



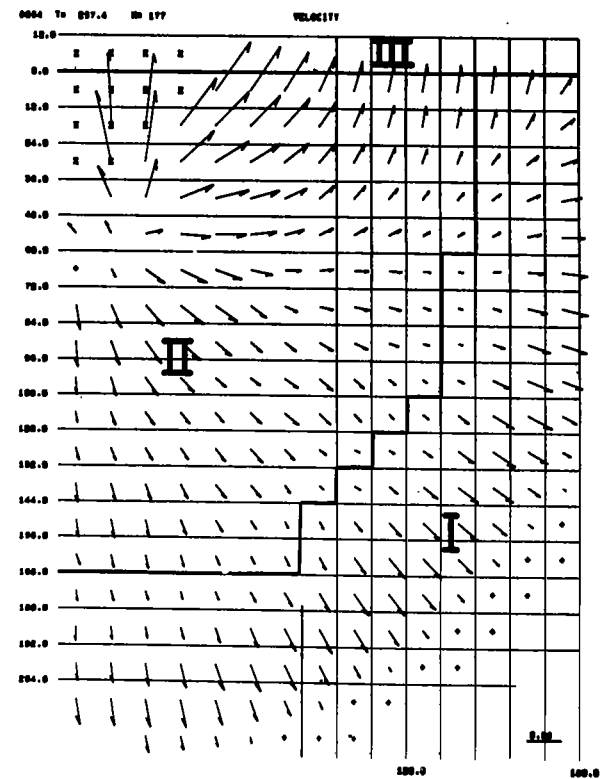
(k) Velocity Field
 $t = 14.5 \mu\text{sec}$

FIGURE C-4 (Con't): CASE 8054, Iron into Aluminum at 72 km/sec

Convergence of the rebounding cavity walls behind the projectile creates high pressures when the material reaches the axis. At $t = 6.2 \mu\text{sec}$ (i) the effect of this high pressure in diverting the converging flow are seen. Above $y = 4$, material is accelerated upwards, while below this depth, material is accelerated downwards into the cavity behind the projectile. This downward flow impinges on the rear of the projectile and the subsequent circular flow pattern suggests an annular vortex.



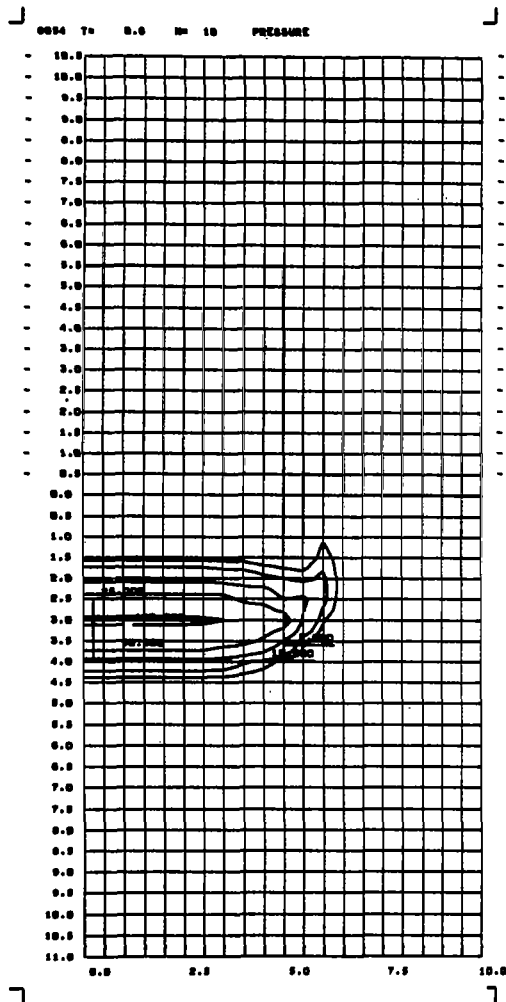
(l) Velocity Field
 $t = 20.6 \mu\text{sec}$



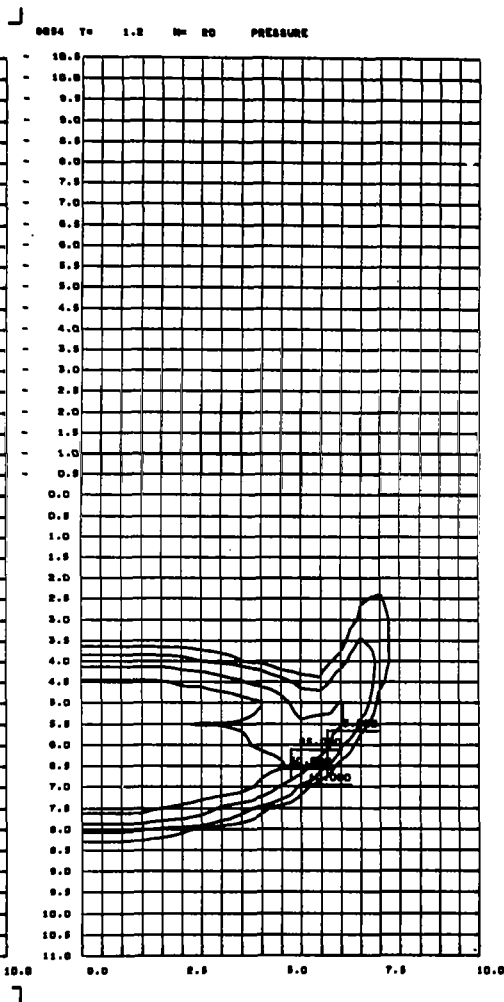
(m) Velocity Field
 $t = 257.4 \mu\text{sec}$

FIGURE C-4 (Con't): CASE 8054, Iron into Aluminum at 72 km/sec

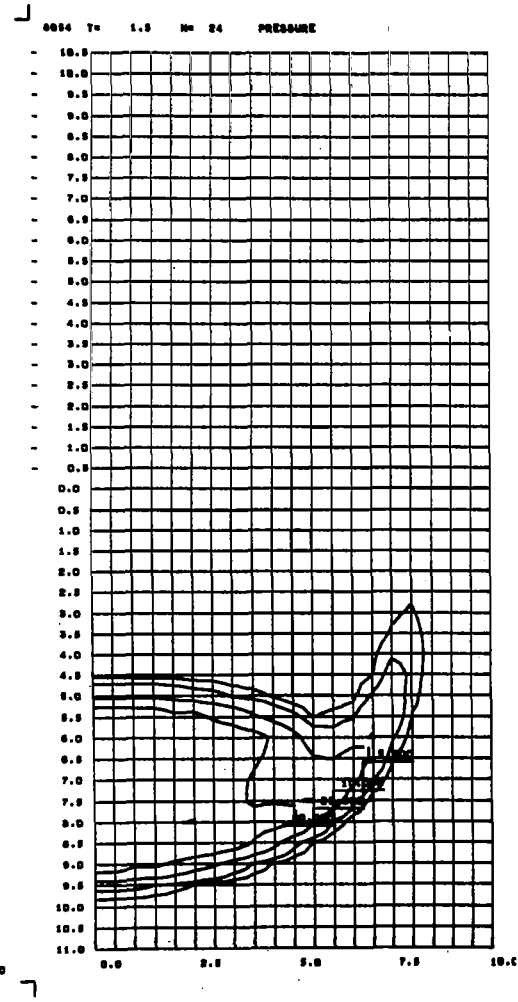
Strong downward flow of material behind the projectile is seen at $t = 20.6 \mu\text{sec}$ (l), with the vortex centered at about $y = 30$, $x = 10$. At the much later stage, in view m, this vortex flow has dissipated.



(n) Pressure Field
 $t = 0.6 \mu\text{sec}$

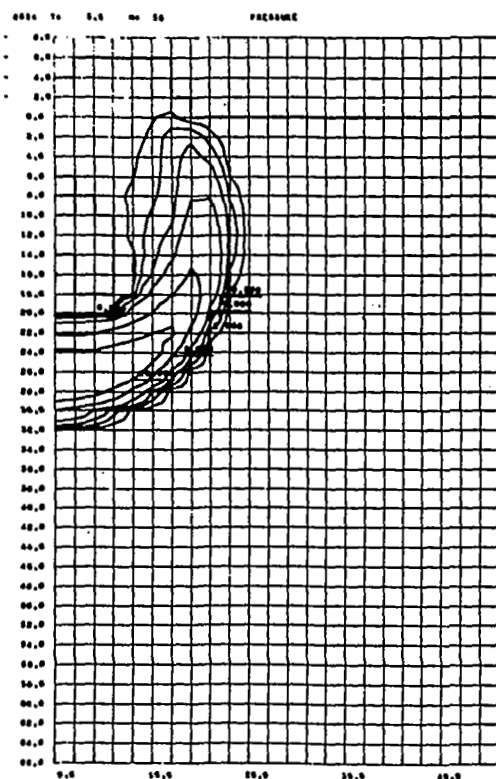


(o) Pressure Field
 $t = 1.2 \mu\text{sec}$

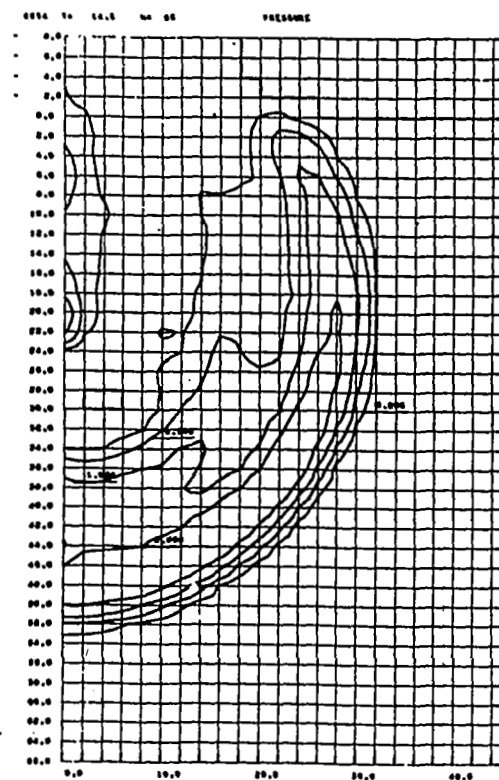


(p) Pressure Field
 $t = 1.5 \mu\text{sec}$

FIGURE C-4 (Con't): CASE 8054, Iron into Aluminum at 72 km/sec



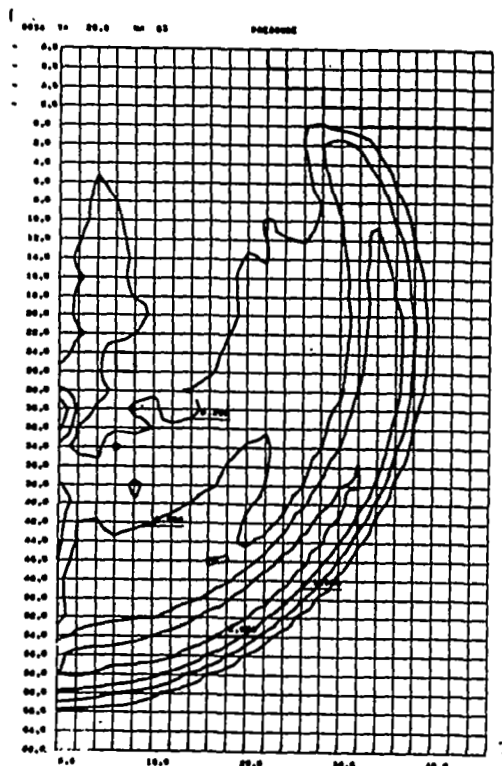
(q) Pressure Field
 $t = 5.6 \mu\text{sec}$



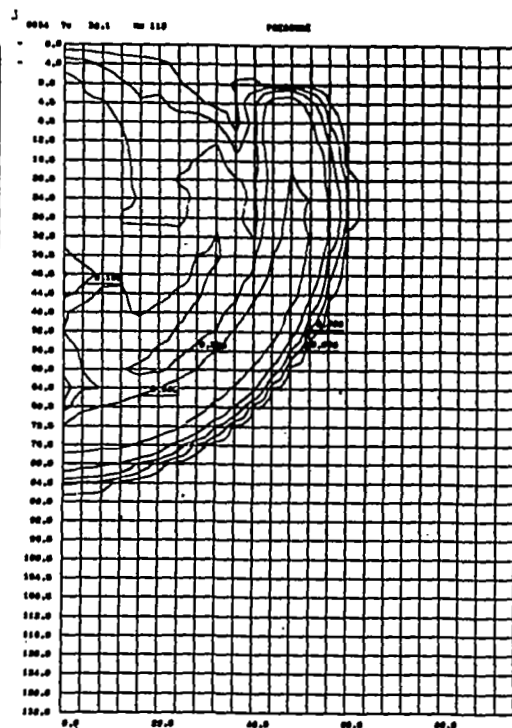
(r) Pressure Field
 $t = 14.5 \mu\text{sec}$

FIGURE C-4 (Con't): CASE 8054, Iron into Aluminum at 72 km/sec

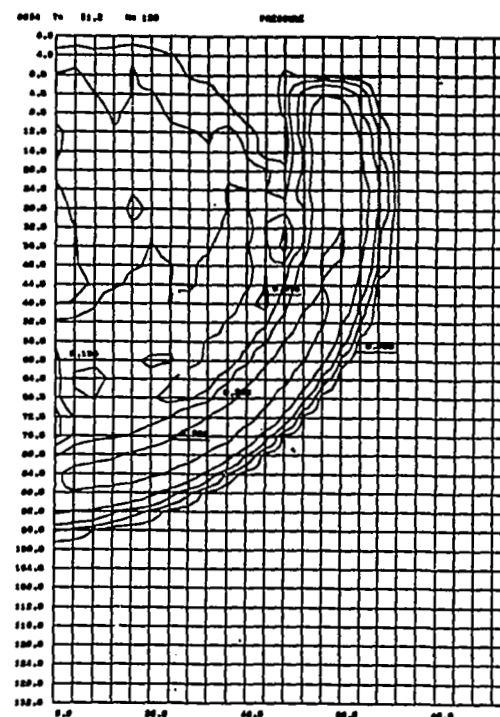
At $t = 14.5 \mu\text{sec}$ (r), an isolated high pressure region appears along the axis behind the projectile. This is caused by the convergence upon the axis of the vaporized, rebounding cavity walls.



(s) Pressure Field
 $t = 20 \mu\text{sec}$



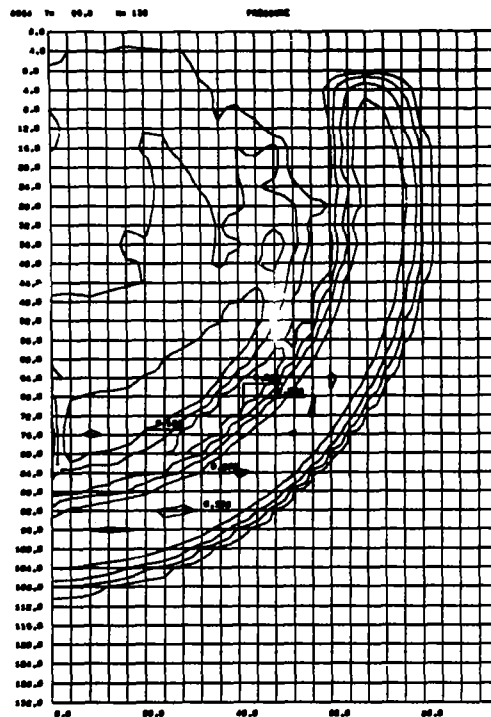
(t) Pressure Field
 $t = 38.1 \mu\text{sec}$



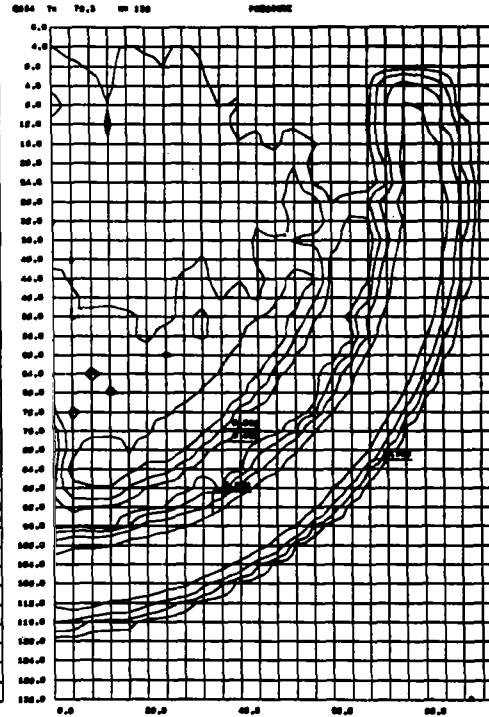
(u) Pressure Field
 $t = 51.2 \mu\text{sec}$

FIGURE C-4 (Con't): CASE 8054, Iron into Aluminum at 72 km/sec

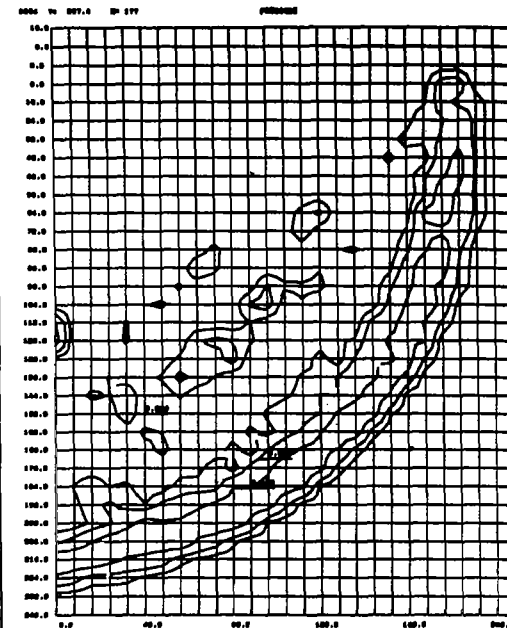
The high pressure region behind the projectile is seen to enlarge in views (s) and (t), and by $t = 51.2 \mu\text{sec}$ (u), pressures above 100 kb fill almost all of the crater.



(v) Pressure Field
 $t = 66.8 \mu\text{sec}$



(w) Pressure Field
 $t = 79.3 \mu\text{sec}$



(x) Pressure Field
 $t = 257.4 \mu\text{sec}$

FIGURE C-4 (Con't): CASE 8054, Iron into Aluminum at 72 km/sec

Persistence of high pressures in the crater are evident in views (v) and (w).

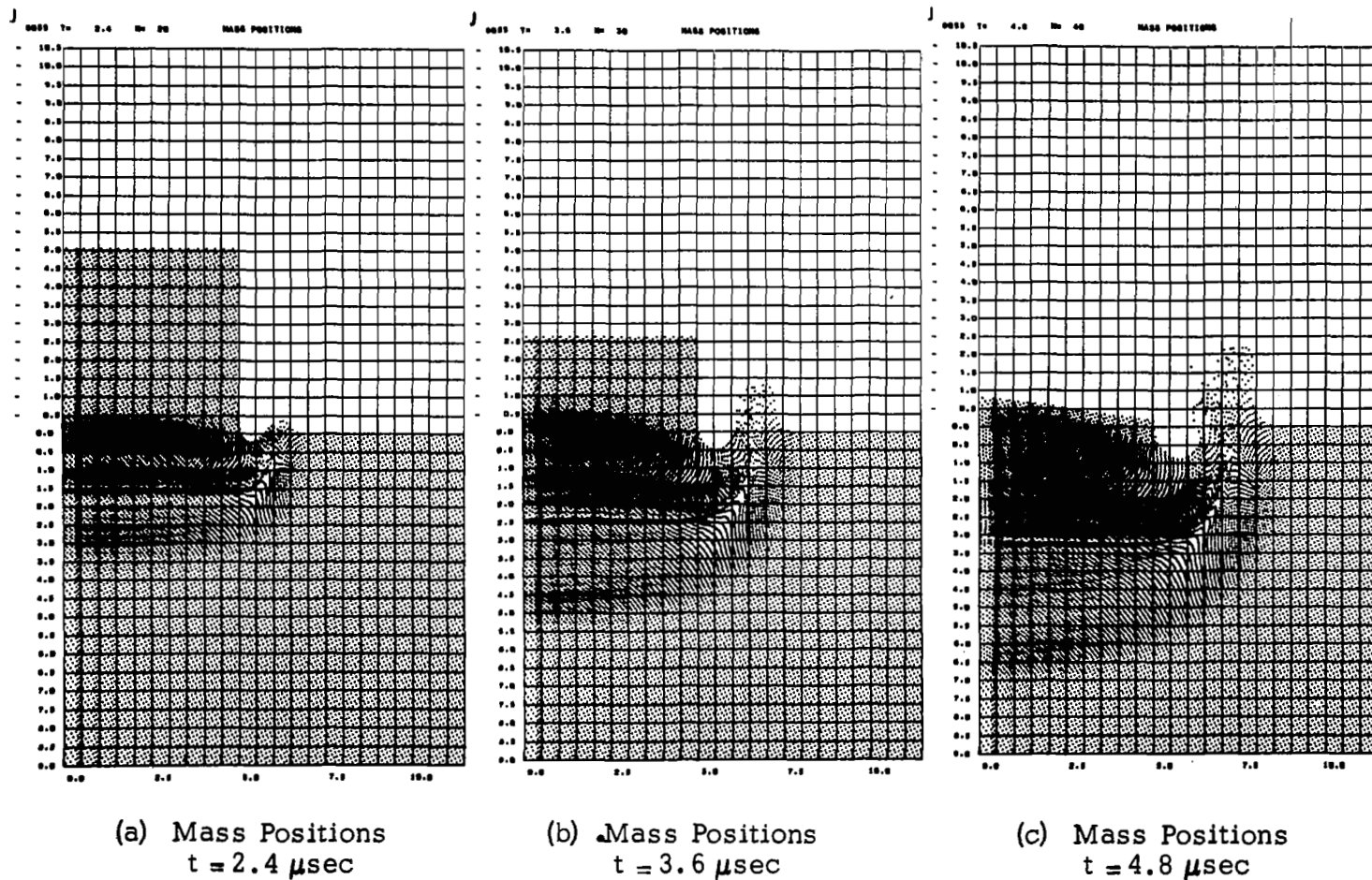
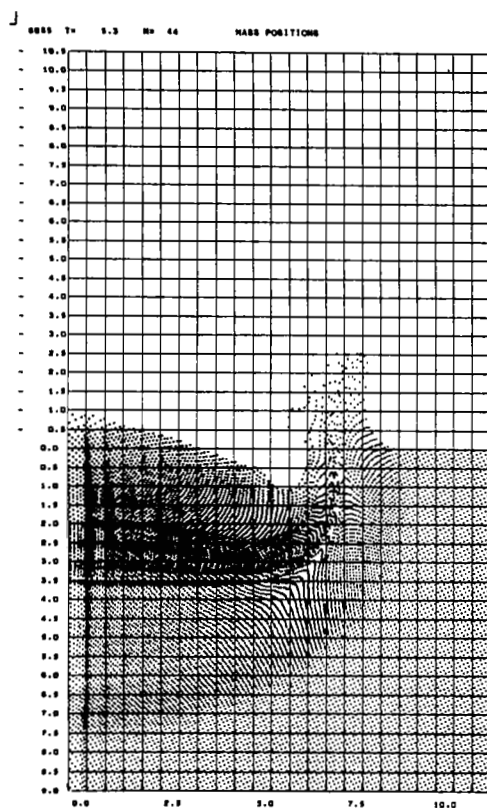
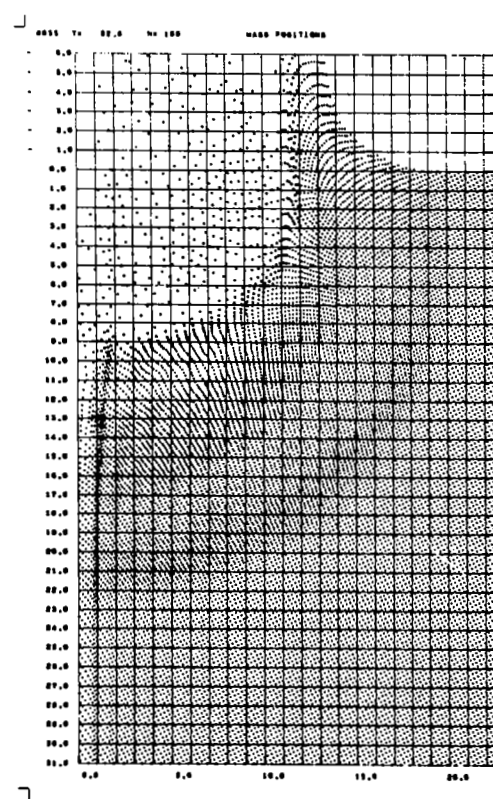


FIGURE C-5: CASE 8055, Aluminum into Iron at 20 km/sec

The initial impact pressure of 7.75 mb is sufficient to compress the aluminum projectile by a factor of 2.5. Release from this pressure will leave a portion of the aluminum in a vapor state.



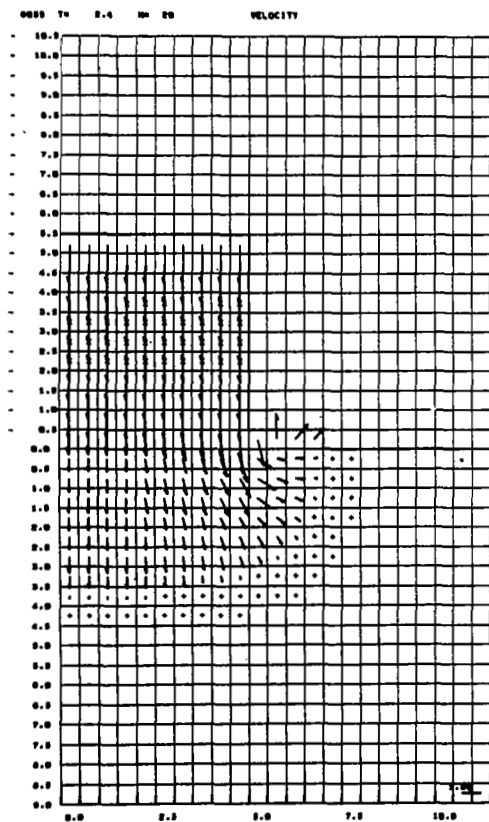
(d) Mass Positions
 $t = 5.3 \mu\text{sec}$



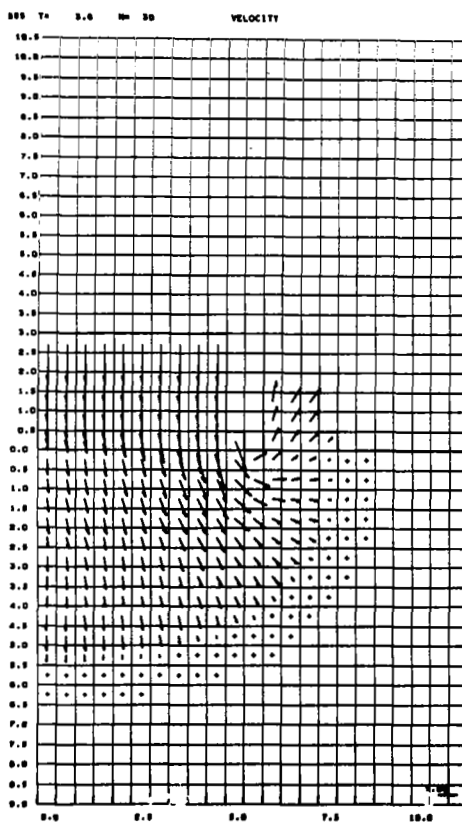
(e) Mass Positions
 $t = 22.8 \mu\text{sec}$

FIGURE C-5 (Con't): CASE 8055, Aluminum into Iron at 20 km/sec

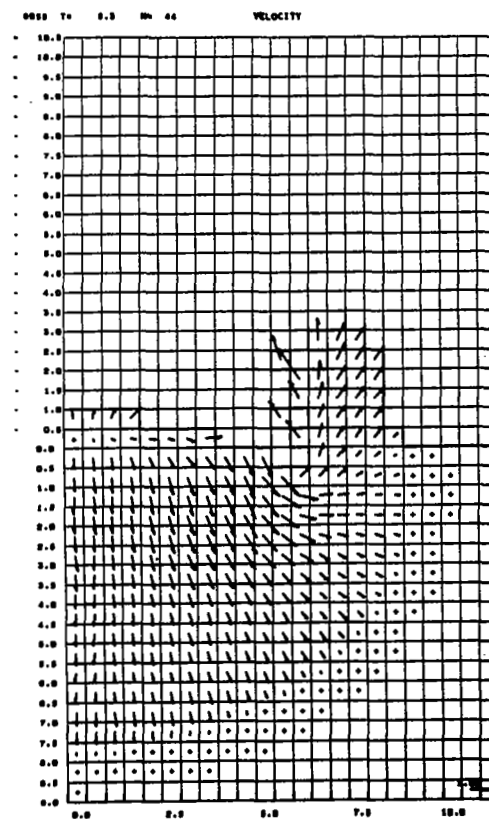
Blowoff caused by projectile vaporization begins at the rear (top) surface in the plot at $t = 5.3 \mu\text{sec}$. A grid change was made after this time. At $t = 22.0 \mu\text{sec}$, efflux of projectile material from the cavity continues.



(f) Velocity Field
 $t = 2.4 \mu\text{sec}$

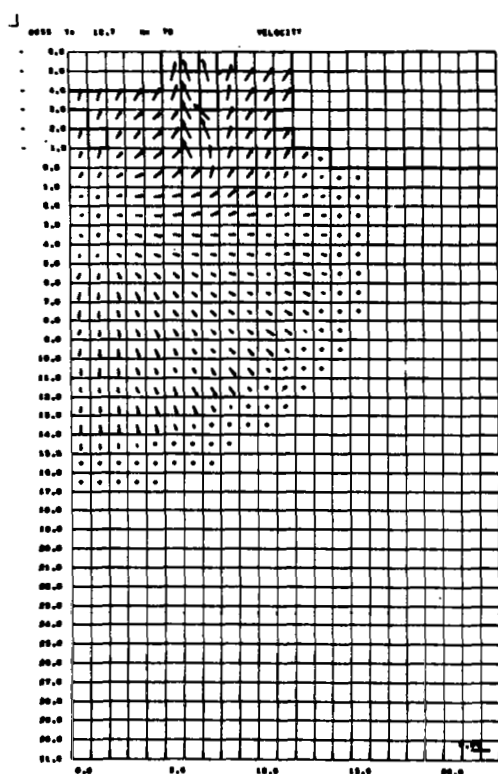


(g) Velocity Field
 $t = 3.6 \mu\text{sec}$

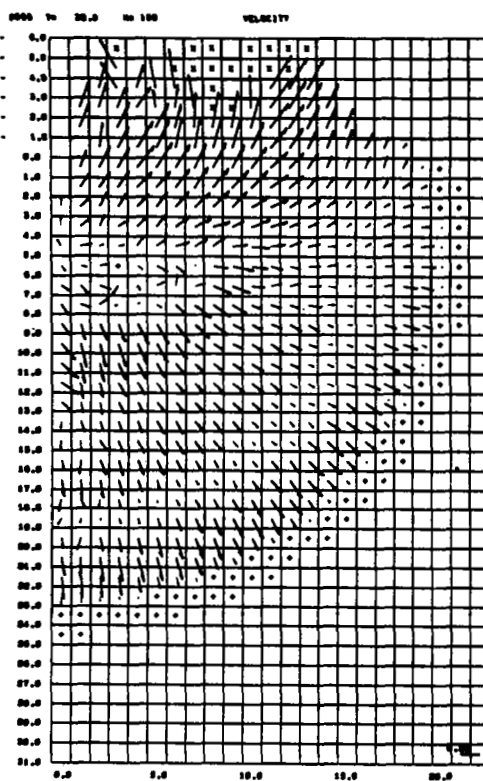


(h) Velocity Field
 $t = 5.3 \mu\text{sec}$

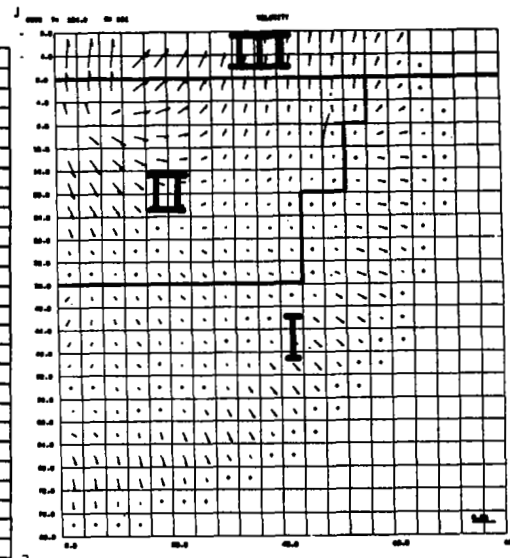
FIGURE C-5 (Con't): CASE 8055, Aluminum into Iron at 20 km/sec



(i) Velocity Field
 $t = 12.7 \mu\text{sec}$

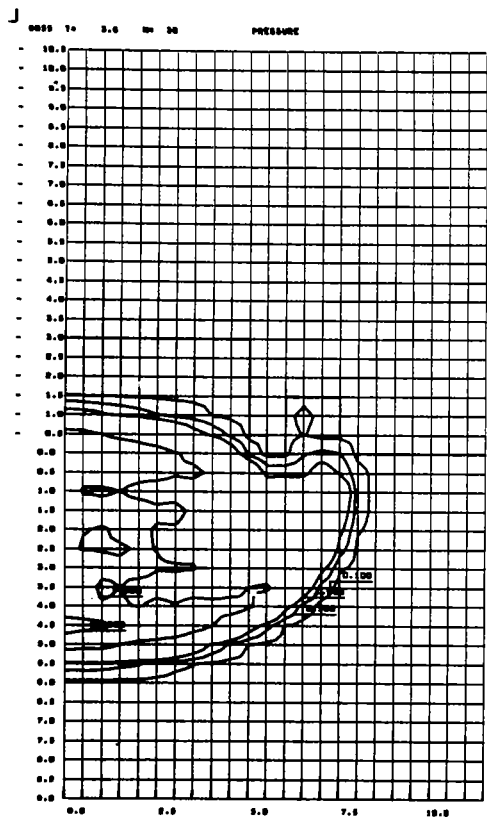


(j) Velocity Field
 $t = 22.8 \mu\text{sec}$

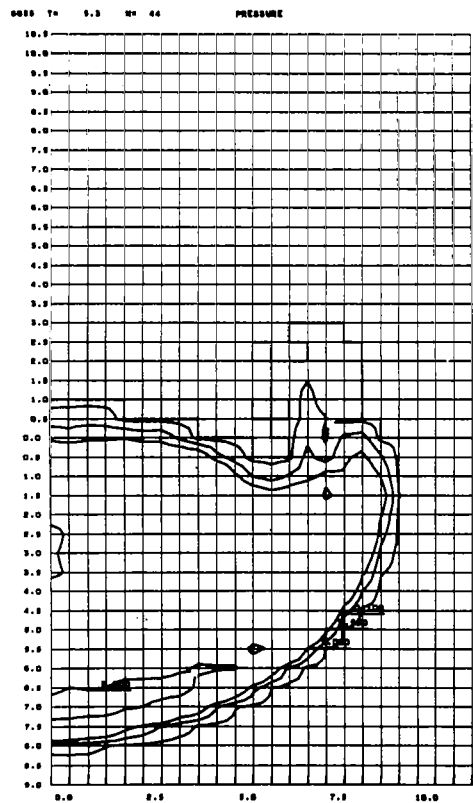


(k) Velocity Field
 $t = 134.9 \mu\text{sec}$

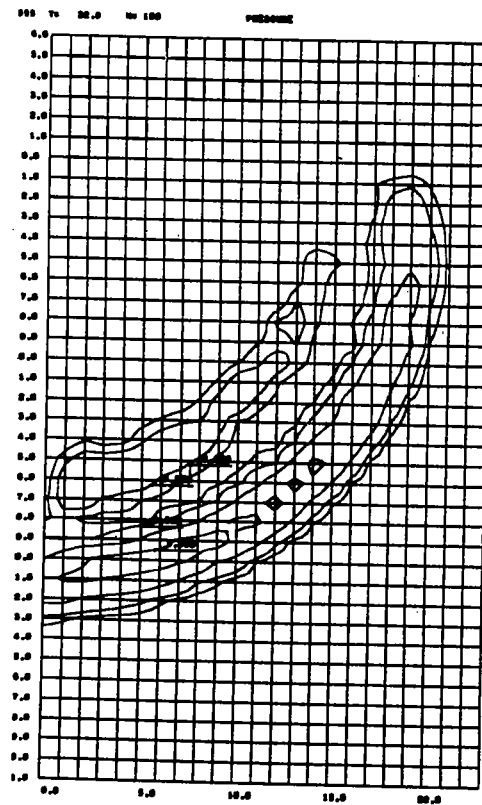
FIGURE C-5 (Con't): CASE 8055, Aluminum into Iron at 20 km/sec



(l) Pressure Field
 $t = 3.6 \mu\text{sec}$



(m) Pressure Field
 $t = 5.3 \mu\text{sec}$



(n) Pressure Field
 $t = 22.8 \mu\text{sec}$

FIGURE C-5 (Con't): CASE 8055, Aluminum into Iron at 20 km/sec

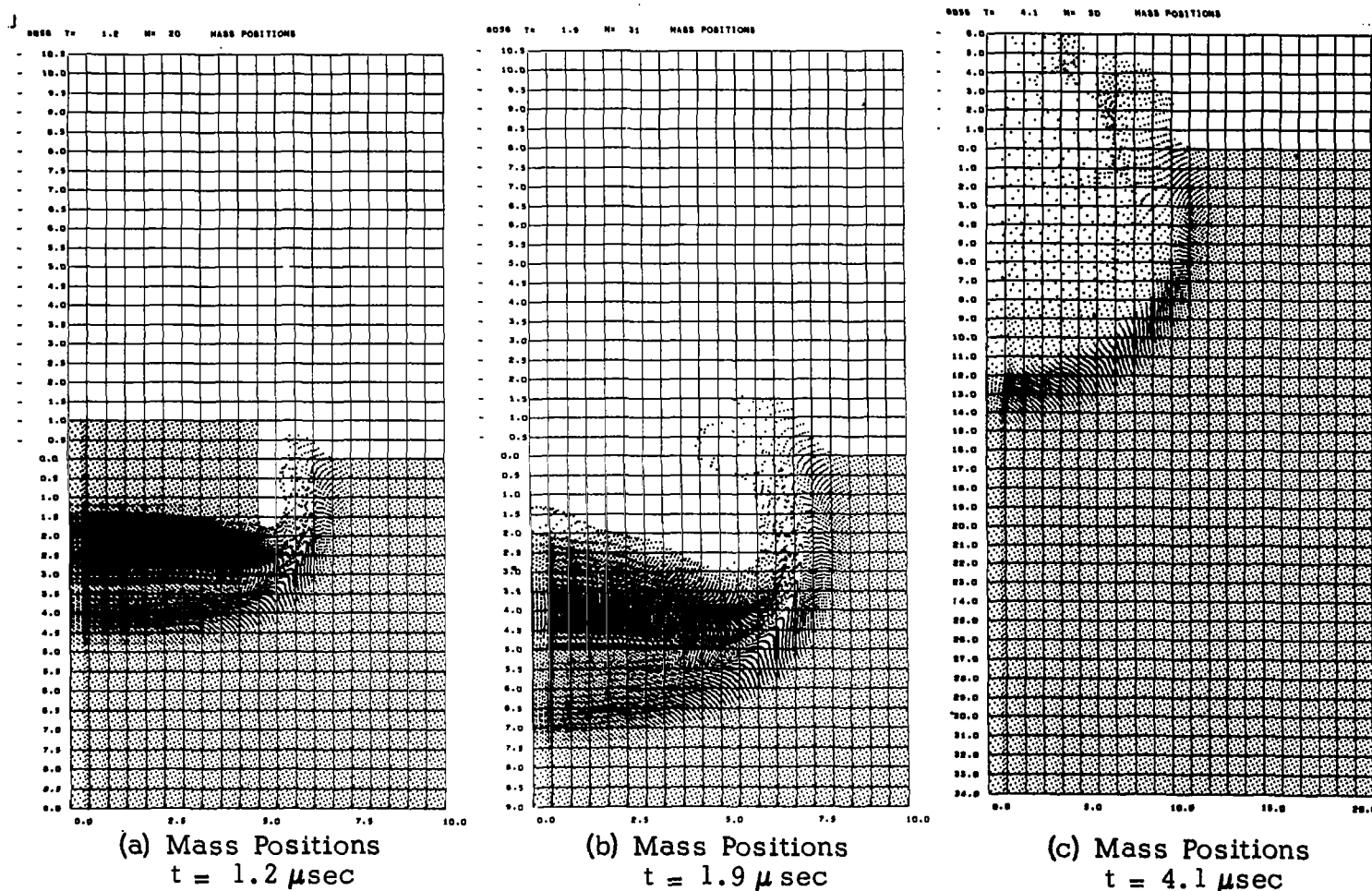
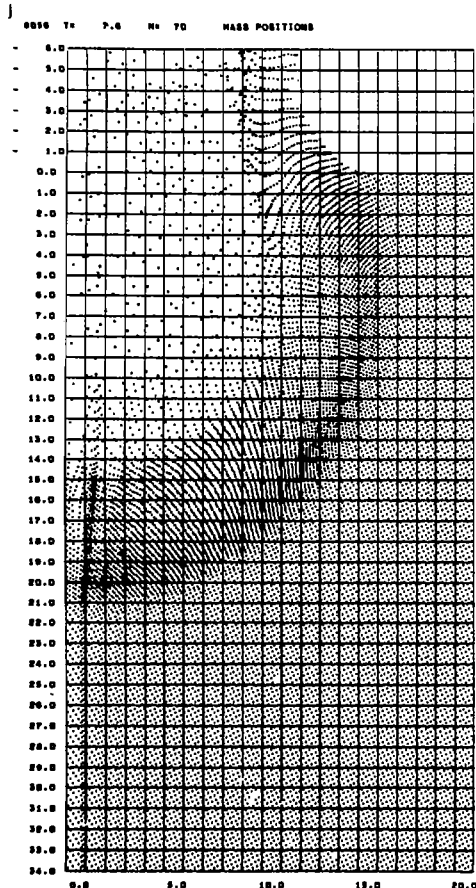
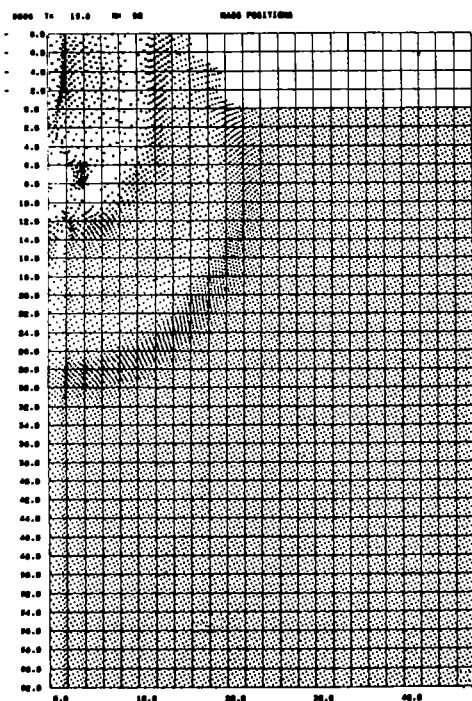


FIGURE C-6: CASE 8056, Aluminum into Iron at 72 km/sec

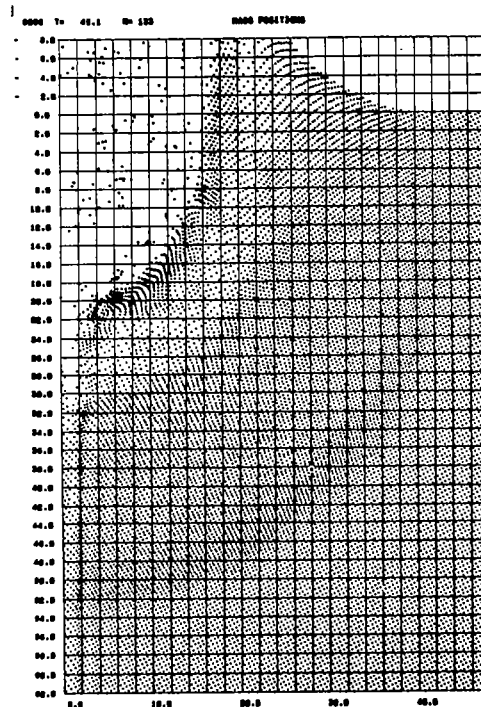
As in Case 8054 (Iron into Aluminum at 72 km/sec), the pressure generated by impact is 76.8 megabars. In Case 8056, the projectile penetrates more slowly (compare Figure C-4-b with Figure C-6-a), resulting in a shallower crater at early stages. Rebound of the vaporizing crater walls is seen starting at $t = 1.9 \mu\text{sec}$ (b), but convergence of this material on the axis is prevented by encounter with vapor which blows off the rear surface of the projectile. The conditions which lead to vortex flow in Cases 8053 and 8054 are therefore absent.



(d) Mass Positions
 $t = 7.6 \mu\text{sec}$



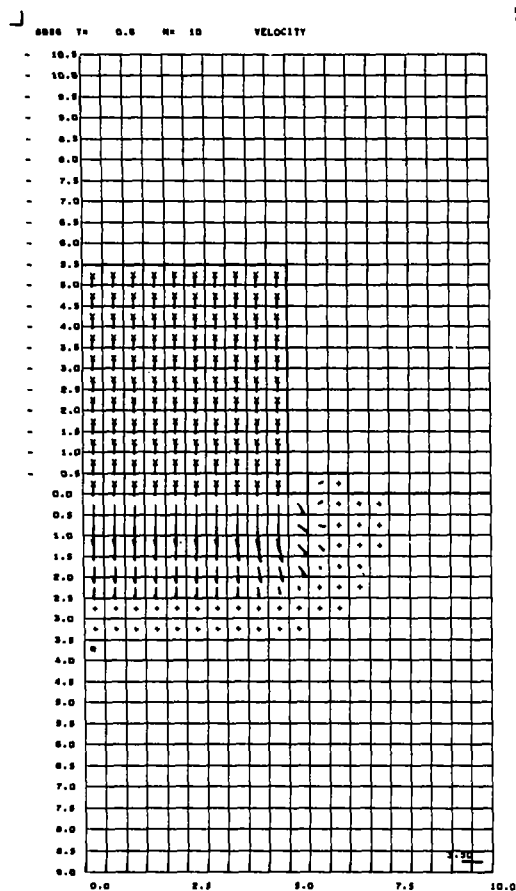
(e) Mass Positions
 $t = 15.8 \mu\text{sec}$



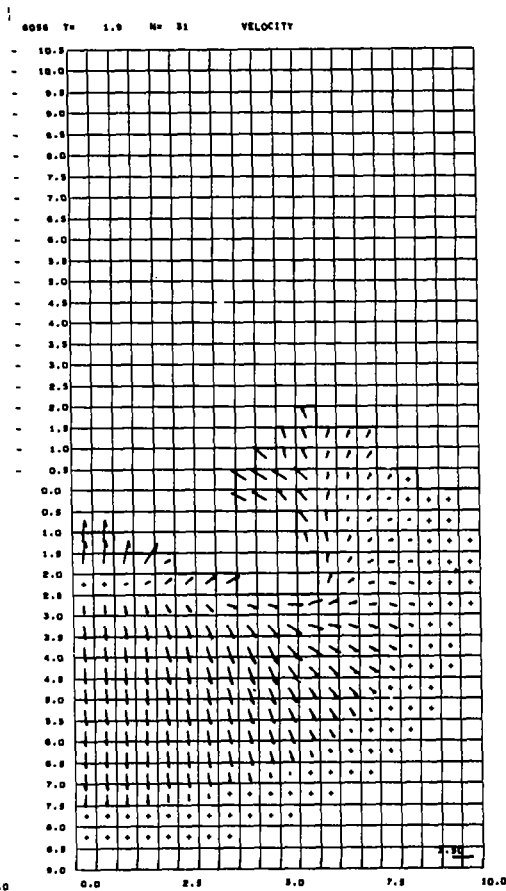
(f) Mass Positions
 $t = 45.1 \mu\text{sec}$

FIGURE C-6 (Con't): CASE 8056, Aluminum into Iron at 72 km/sec

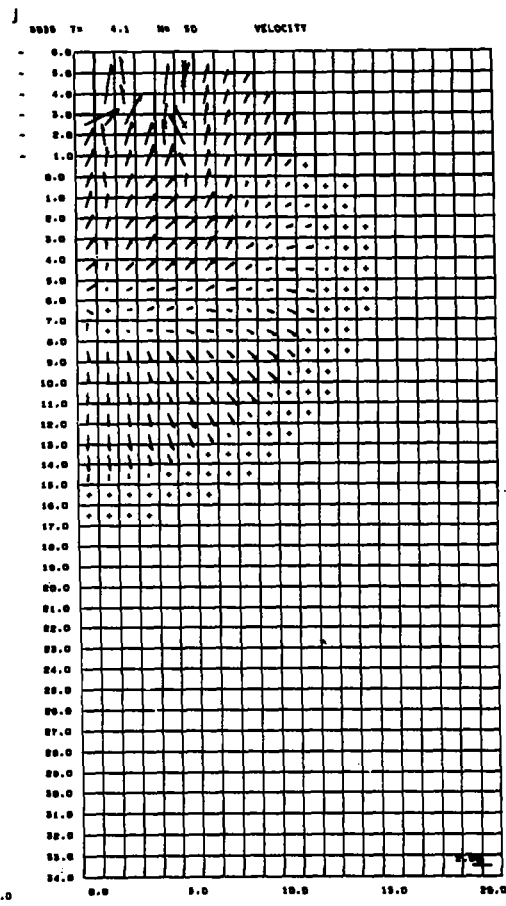
By $t = 45.1 \mu\text{sec}$ (f), most of the projectile has vaporized and blown out of the crater. Cratering flow in the target, however, is still forming.



(g) Velocity Field
 $t = 0.6 \mu\text{sec}$



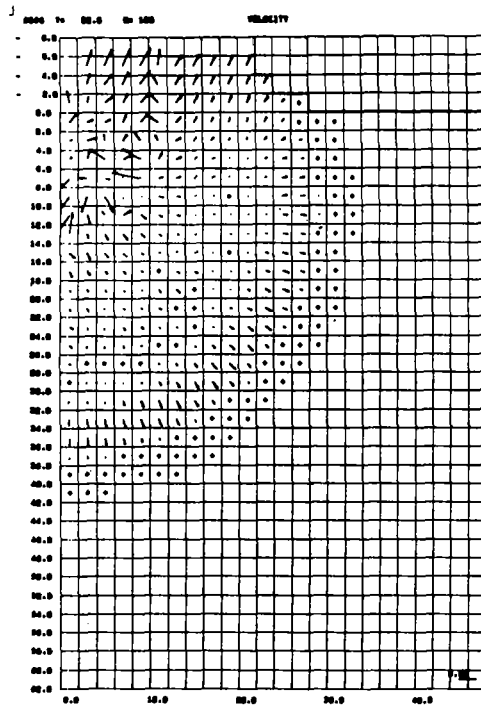
(h) Velocity Field
 $t = 1.9 \mu\text{sec}$



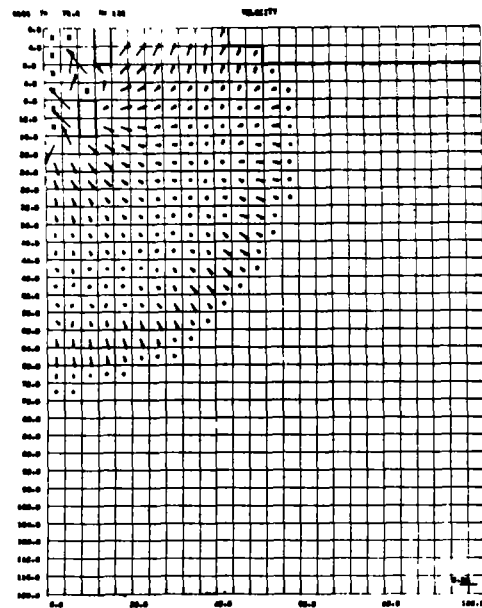
(i) Velocity Field
 $t = 4.1 \mu\text{sec}$

FIGURE C-6 (Con't): CASE 8056, Aluminum into Iron at 72 km/sec

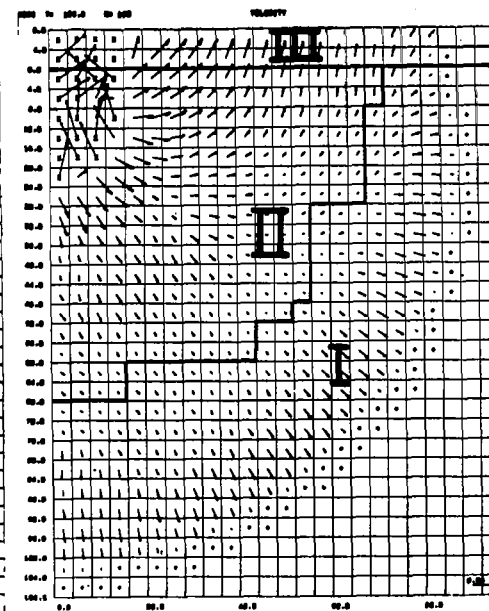
At $t = 1.9 \mu\text{sec}$ (h), the high blowoff velocity of both the crater walls and the rear surface of the projectile are seen. By $t = 4.1 \mu\text{sec}$ (i), these have converged into a strong upward flow.



(j) Velocity Field
 $t = 22.0 \mu\text{sec}$

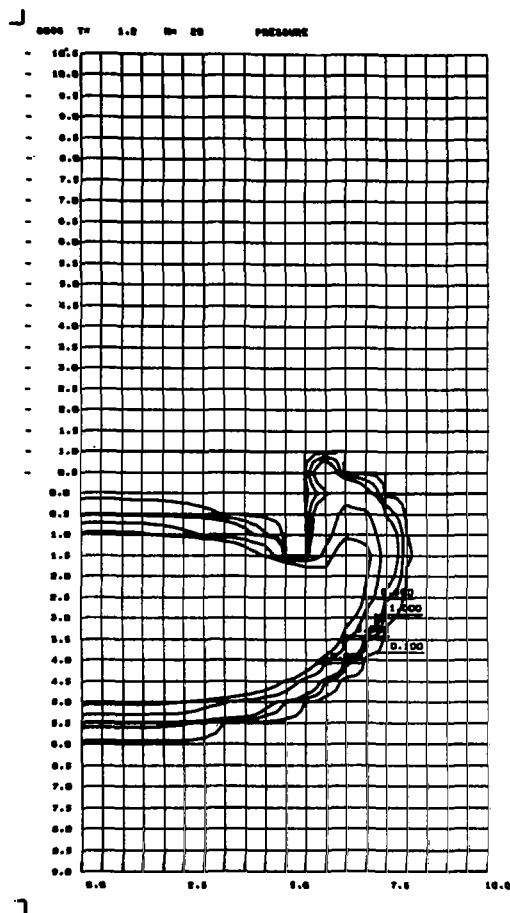


(k) Velocity Field
 $t = 73.6 \mu\text{sec}$

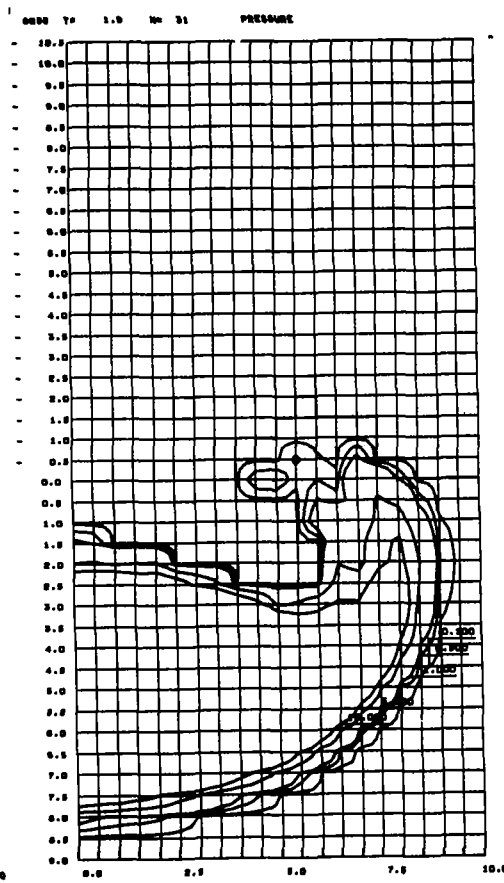


(l) Velocity Field
 $t = 135.9 \mu\text{sec}$

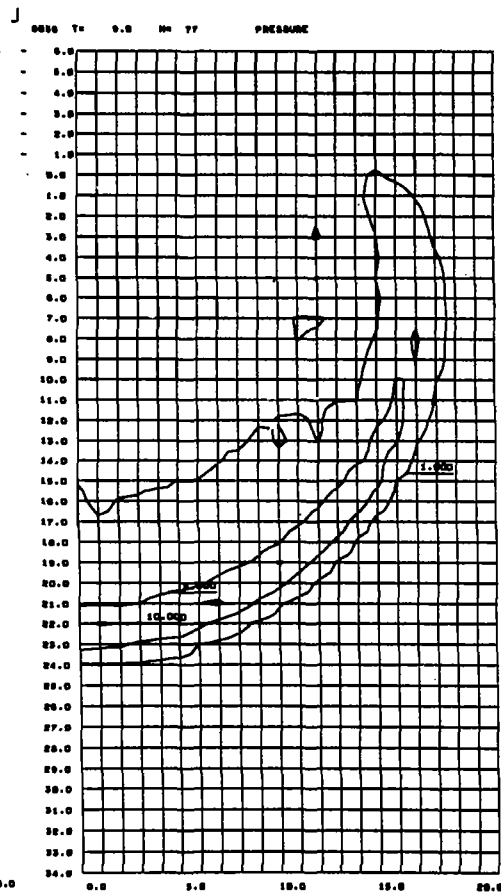
FIGURE C-6 (Con't): CASE 8056, Aluminum into Iron at 72 km/sec



(m) Pressure Field
 $t = 1.2 \mu\text{sec}$

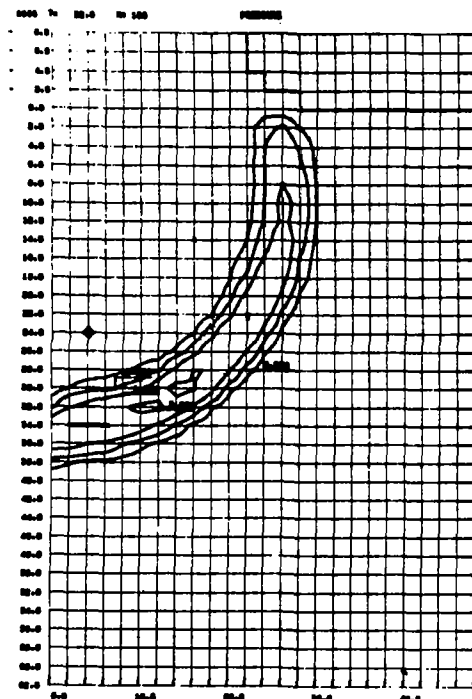


(n) Pressure Field
 $t = 1.9 \mu\text{sec}$

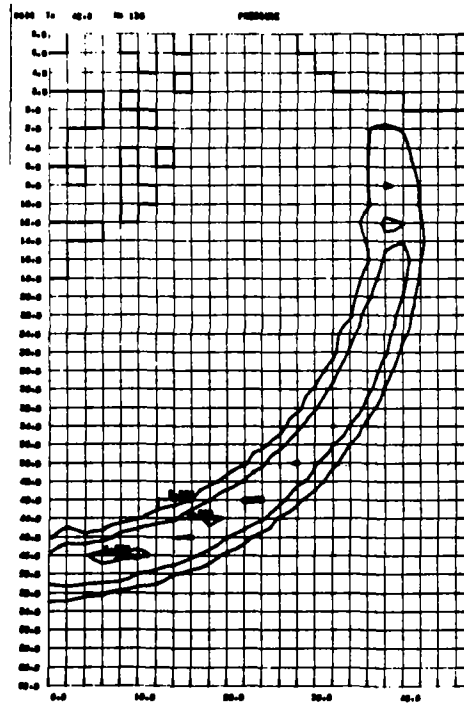


(o) Pressure Field
 $t = 9.0 \mu\text{sec}$

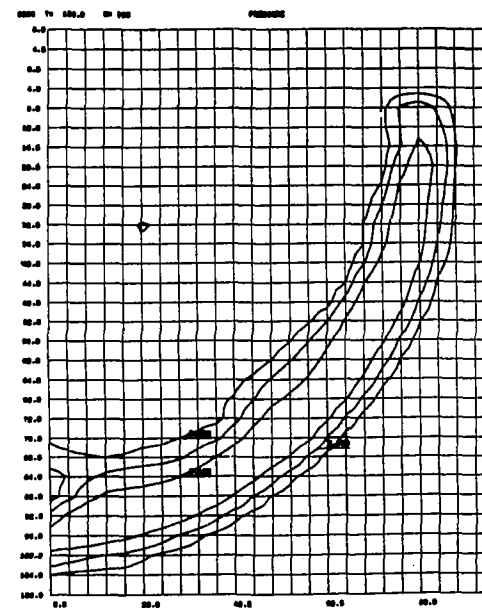
FIGURE C-6 (Con't): CASE 8056, Aluminum into Iron at 72 km/sec



(p) Pressure Field
 $t = 22.0 \mu\text{sec}$



(q) Pressure Field
 $t = 42.0 \mu\text{sec}$



(r) Pressure Field
 $t = 135.9 \mu\text{sec}$

FIGURE C-6 (Con't): CASE 8056, Aluminum into Iron at 72 km/sec

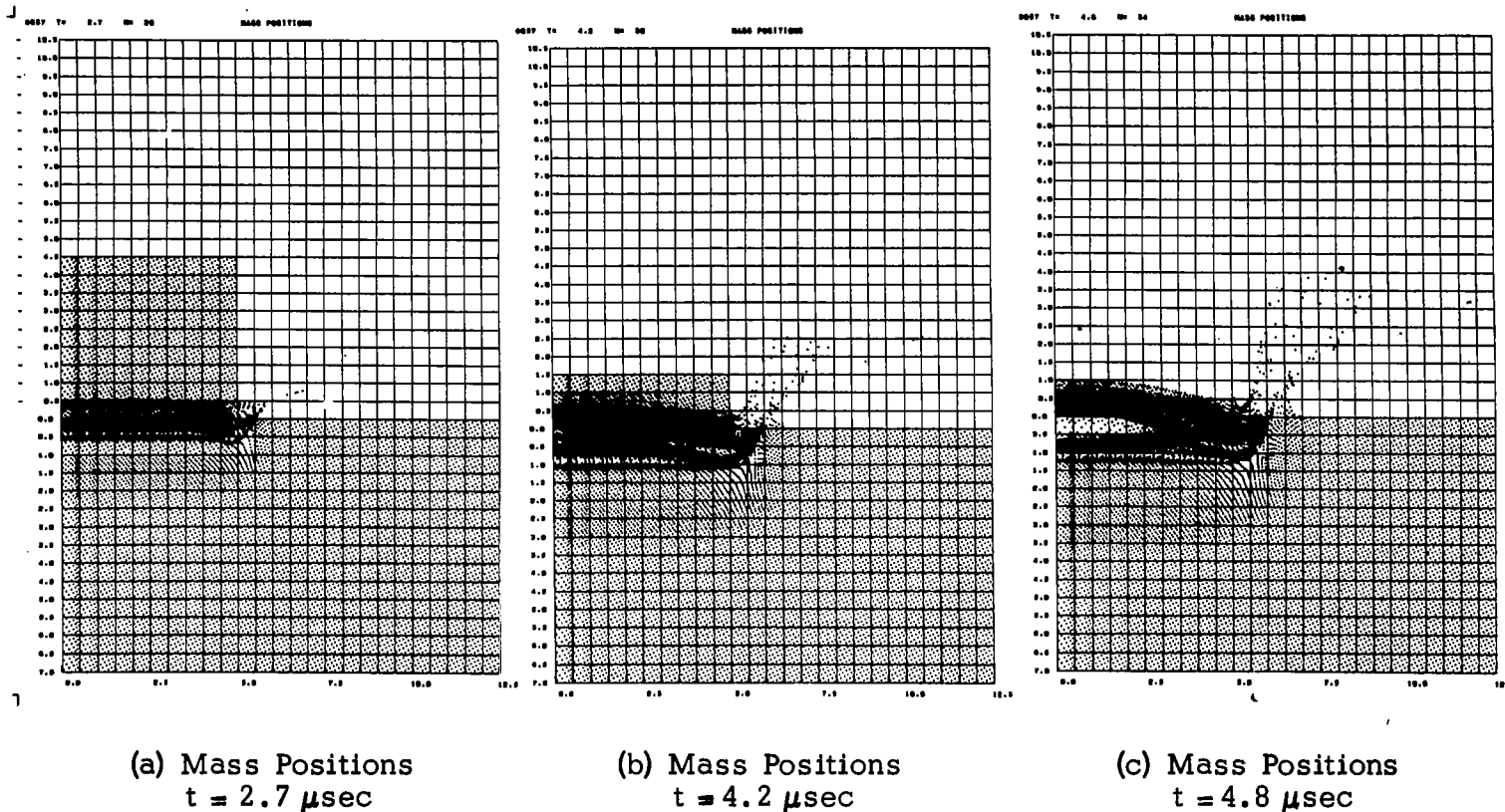
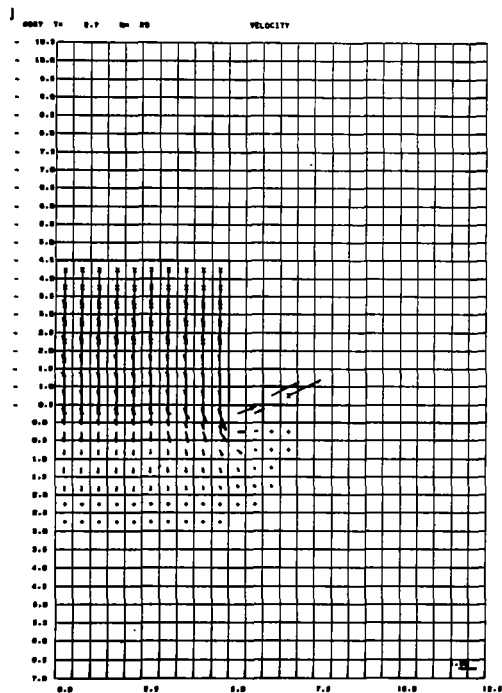
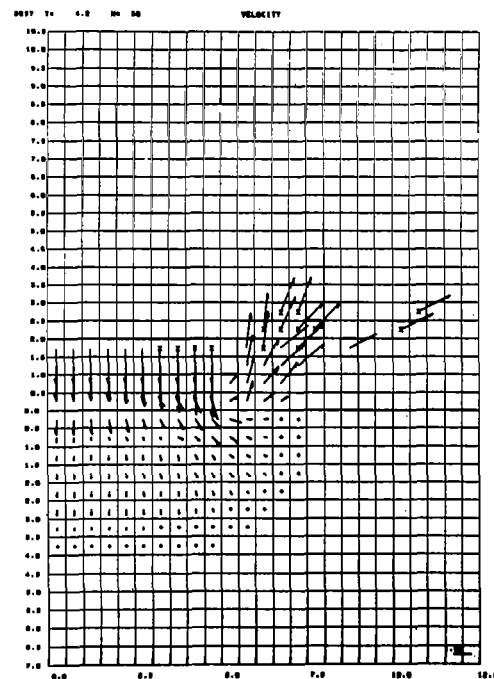


FIGURE C-7: CASE 8057, Porous Aluminum ($\rho = 0.44$) into Iron at 20 km/sec

The major characteristics of the cratering process for this impact of a highly compressible projectile on a stiff target are well established at early stages. By $4.2 \mu\text{sec}$ (b), nearly all of the porous projectile has been compressed into about 2 cm length. The projectile-target interface has advanced to only slightly over 1-cm depth. By $t = 4.8 \mu\text{sec}$ (c), the rear surface of the grossly compressed projectile is starting to rebound. Interactions between the main projectile mass and the target are therefore of relatively short duration, and are confined to shallow depths in the target.



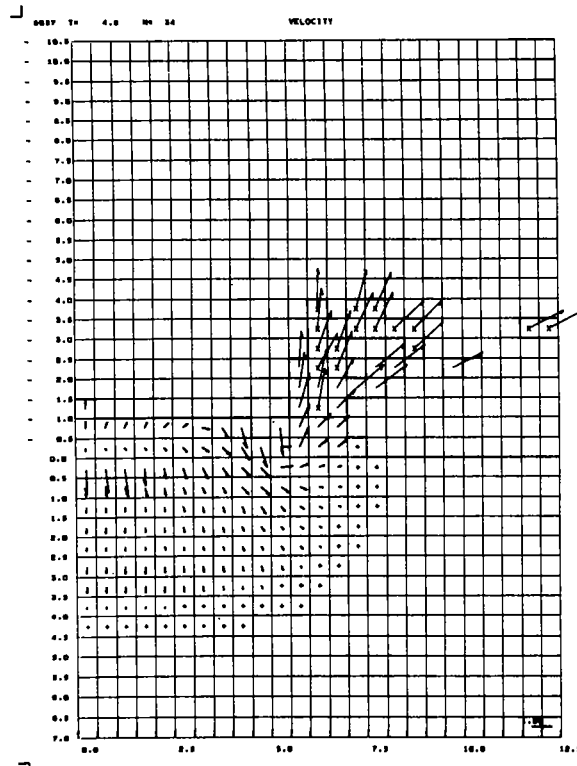
(d) Velocity Field
 $t = 2.7 \mu\text{sec}$



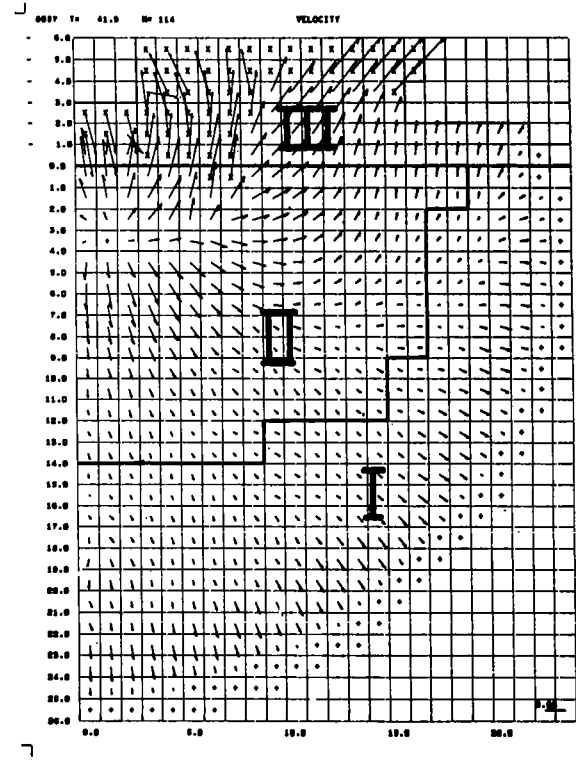
(e) Velocity Field
 $t = 4.2 \mu\text{sec}$

FIGURE C-7 (Con't): CASE 8057, Porous Aluminum ($\rho = 0.44$) into Iron at 20 km/sec

The shallow character of the projectile-target interactions are again evident in these plots.



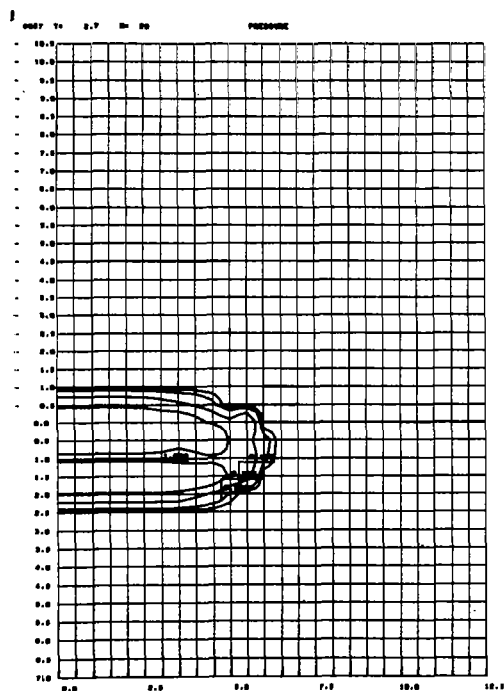
(f) Velocity Field
 $t = 4.8 \mu\text{sec}$



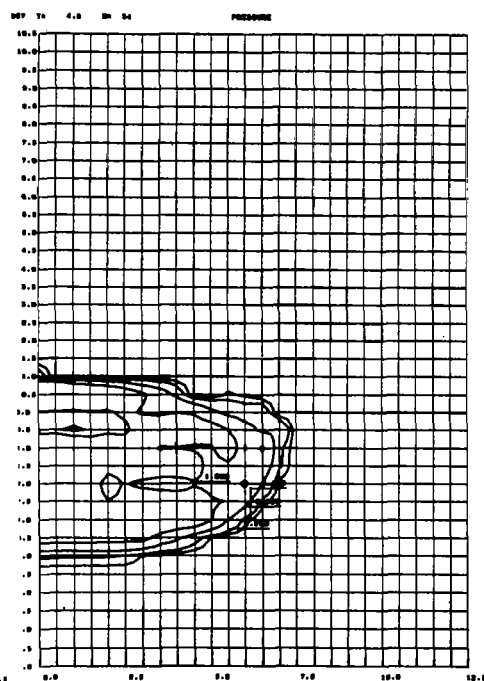
(g) Velocity Field
 $t = 41.9 \mu\text{sec}$

FIGURE C-7 (Con't): CASE 8057, Porous Aluminum ($\rho = 0.44$) into Iron at 20 km/sec

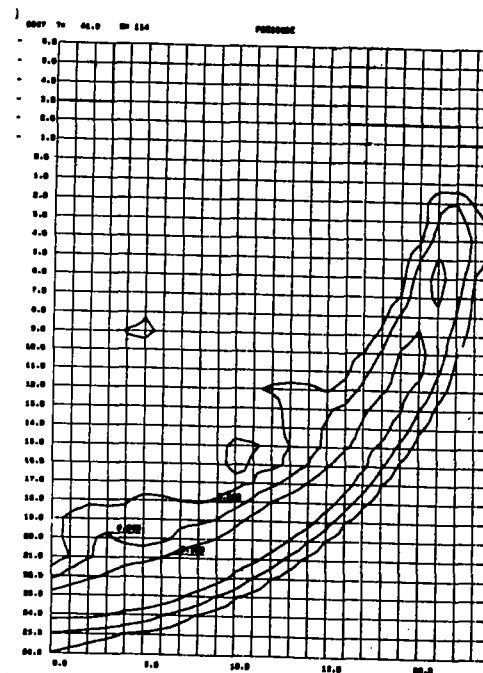
By $t = 41.9 \mu\text{sec}$ (g), the separation of the isolated shock from the cratering flow is evident in the velocity plot.



(h) Pressure Field
 $t = 2.7 \mu\text{sec}$

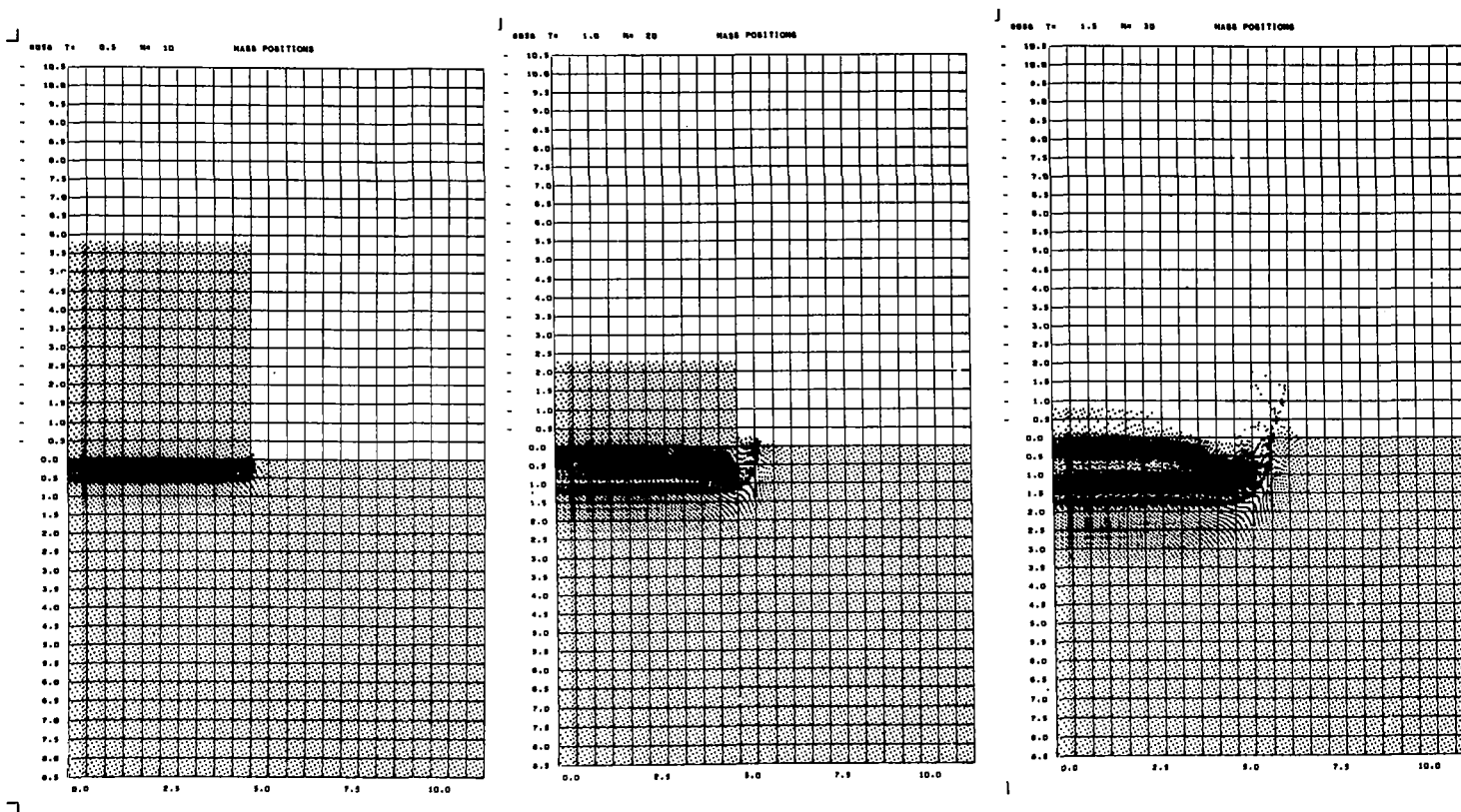


(i) Pressure Field
 $t = 4.8 \mu\text{sec}$



(j) Pressure Field
 $t = 41.9 \mu\text{sec}$

FIGURE C-7 (Con't): CASE 8057, Porous Aluminum ($\rho = 0.44$) into Iron at 20 km/sec



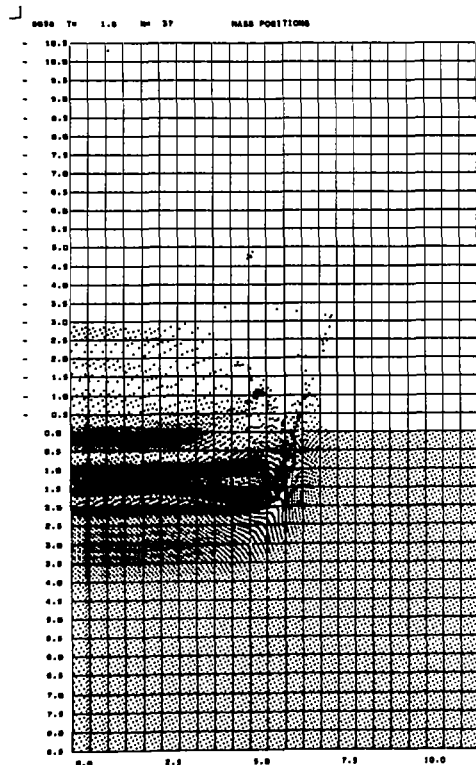
(a) Mass Positions
 $t = 0.5 \mu\text{sec}$

(b) Mass Positions
 $t = 1.0 \mu\text{sec}$

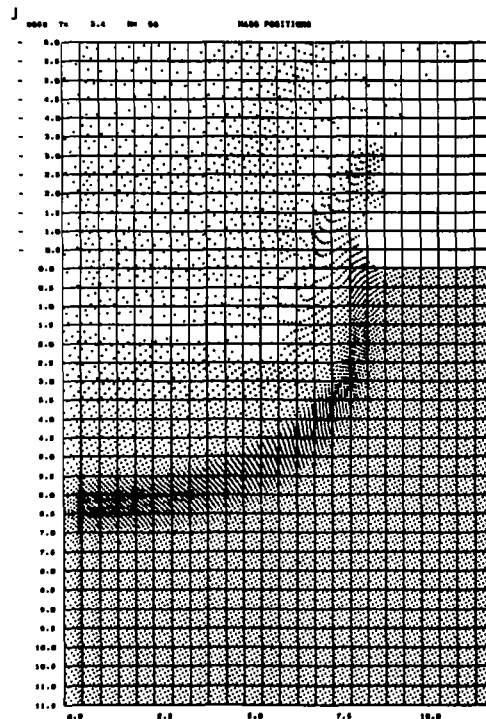
(c) Mass Positions
 $t = 1.5 \mu\text{sec}$

FIGURE C-8: CASE 8058, Porous Aluminum ($\rho = 0.44$) into Iron at 72 km/sec

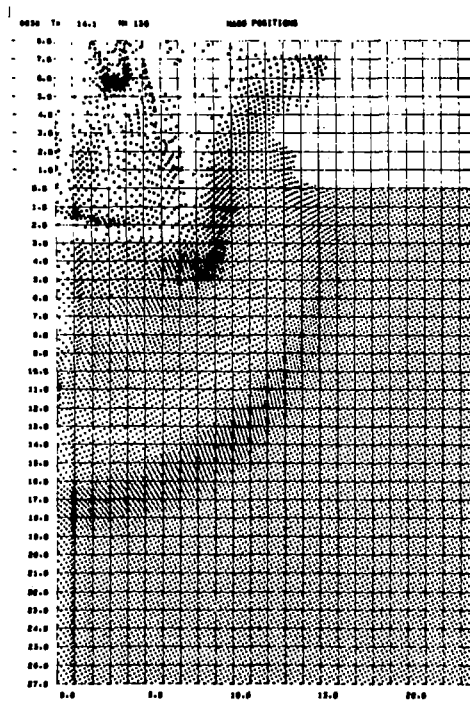
Very rapid compression of the porous projectile into a shallow crater is observed. The initial pressure of 19.6 megabars is sufficient to vaporize all of the projectile upon release, and this blowoff process is seen starting at $t = 1.5 \mu\text{sec}$ (c). Note that the shock velocity in the projectile is approximately the same as the impact velocity, such that the shock front in the projectile remains essentially stationary at the level of the target surface.



(d) Mass Positions
 $t = 1.8 \mu\text{sec}$



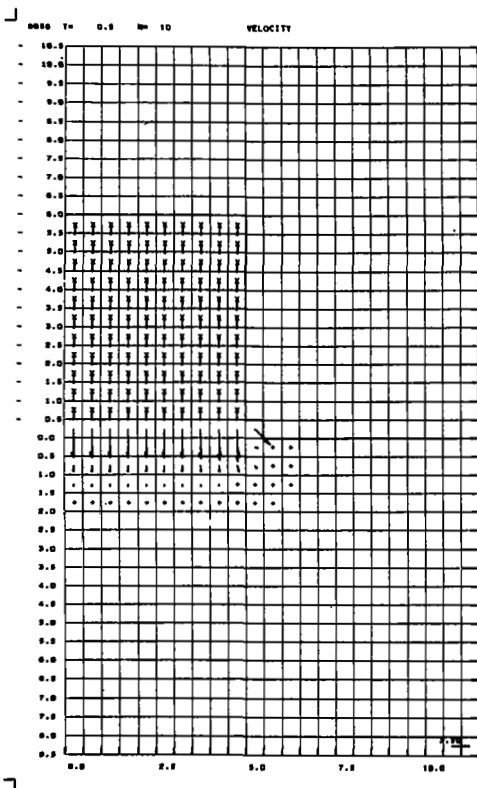
(e) Mass Positions
 $t = 3.4 \mu\text{sec}$



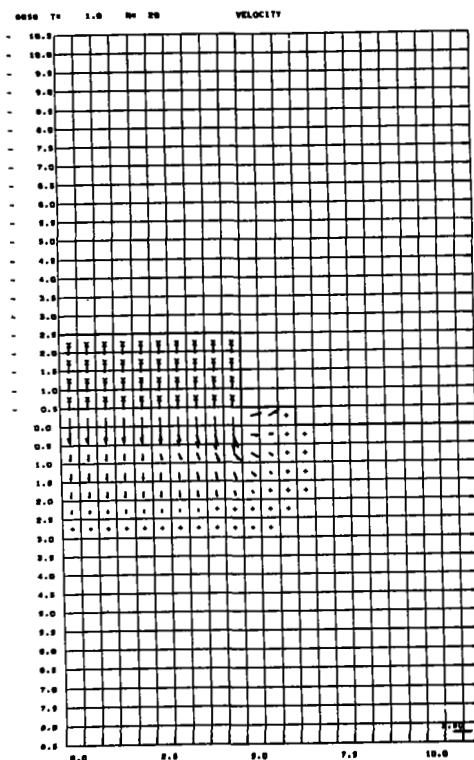
(f) Mass Positions
 $t = 14.1 \mu\text{sec}$

FIGURE C-8 (Con't): CASE 8058, Porous Aluminum ($\rho = 0.44$) into Iron at 72 km/sec

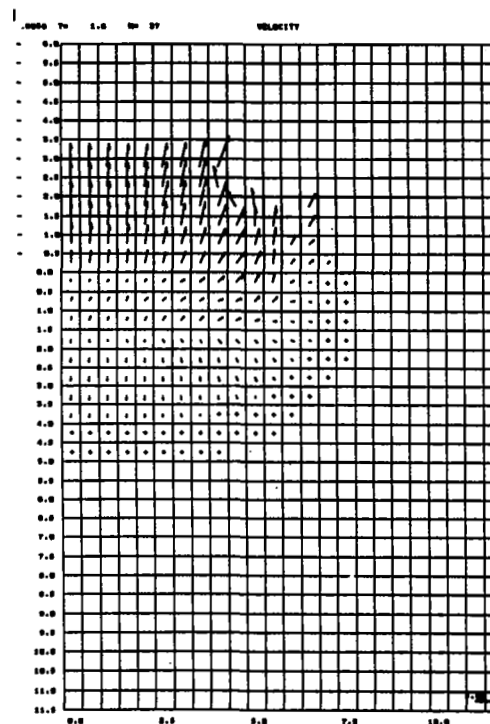
Note the shallow extent of projectile material penetration into the target at $t = 1.8 \mu\text{sec}$ (d). Nearly all of the projectile material has blown out of the crater by $t = 3.4 \mu\text{sec}$ (e).



(g) Velocity Field
 $t = 0.5 \mu\text{sec}$



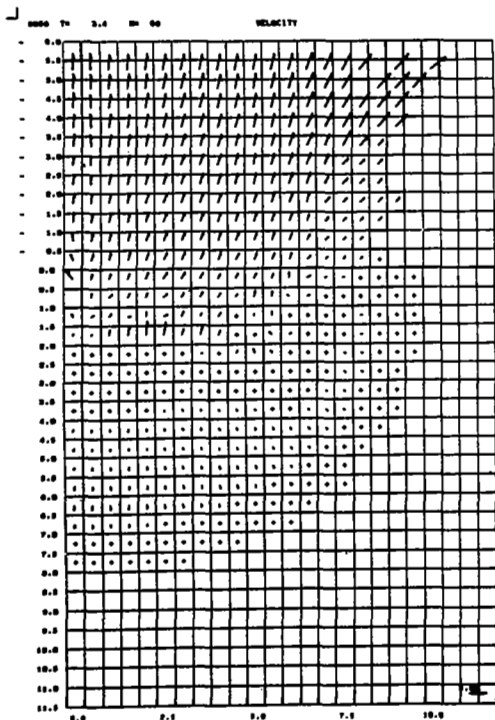
(h) Velocity Field
 $t = 1.0 \mu\text{sec}$



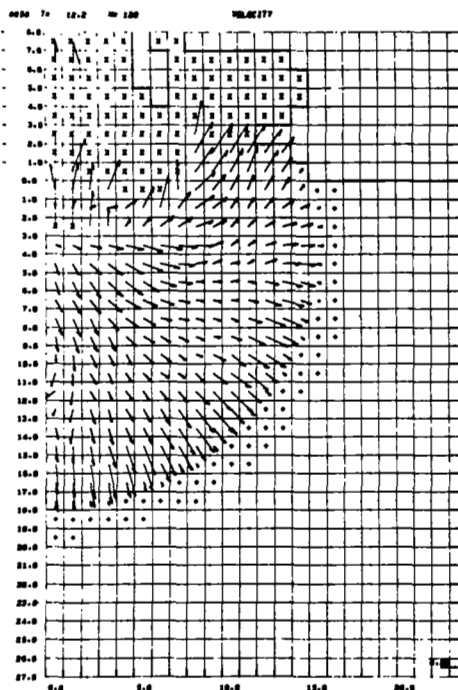
(i) Velocity Field
 $t = 1.8 \mu\text{sec}$

FIGURE C-8 (Con't): CASE 8058, Porous Aluminum ($\rho = 0.44$) into Iron at 72 km/sec

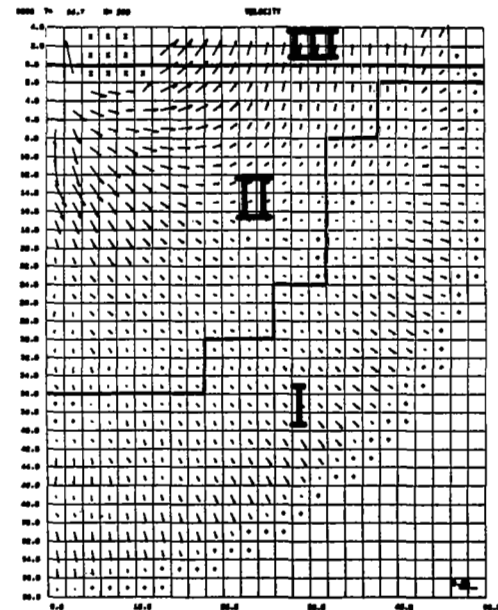
A rapid reversal of velocity is seen between $t = 1.0 \mu\text{sec}$, when the rear of the projectile is still traveling at impact velocity towards the target, and $t = 1.8 \mu\text{sec}$, when the vaporized rear surface is blowing off.



(j) Velocity Field
 $t = 3.4 \mu \text{ sec}$

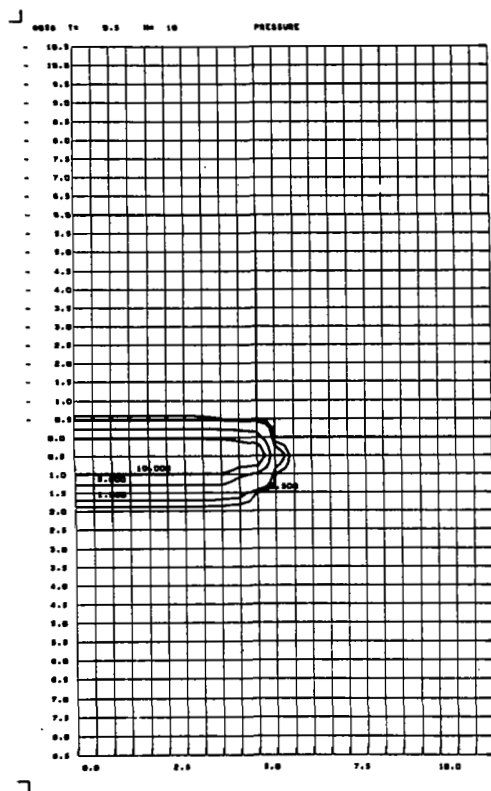


(k) Velocity Field
 $t = 12.2 \mu \text{ sec}$

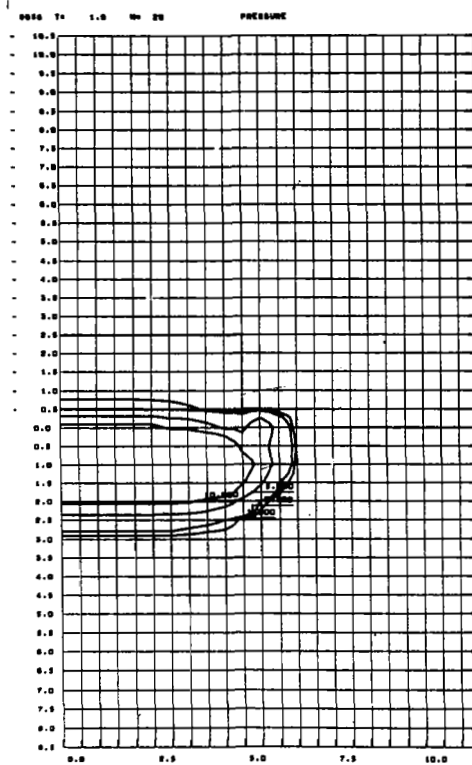


(l) Velocity Field
 $t = 84.7 \mu \text{ sec}$

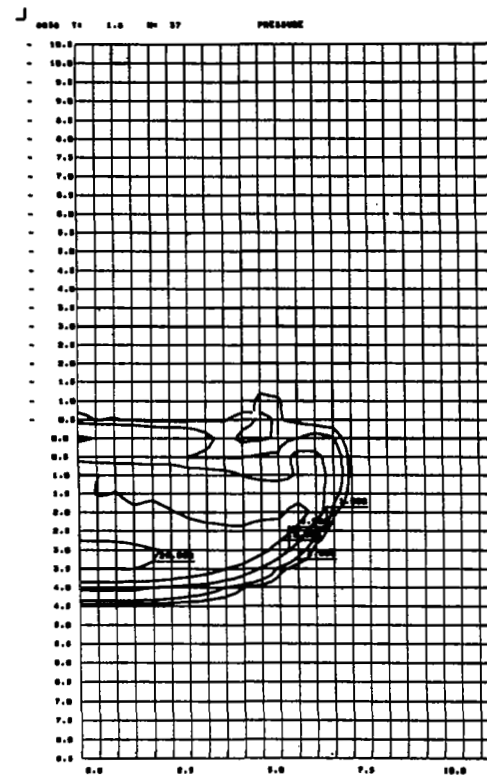
FIGURE C-8 (Con't): CASE 8058, Porous Aluminum ($\rho = 0.44$) into Iron at 72 km/sec



(m) Pressure Field
 $t = 0.5 \mu\text{sec}$

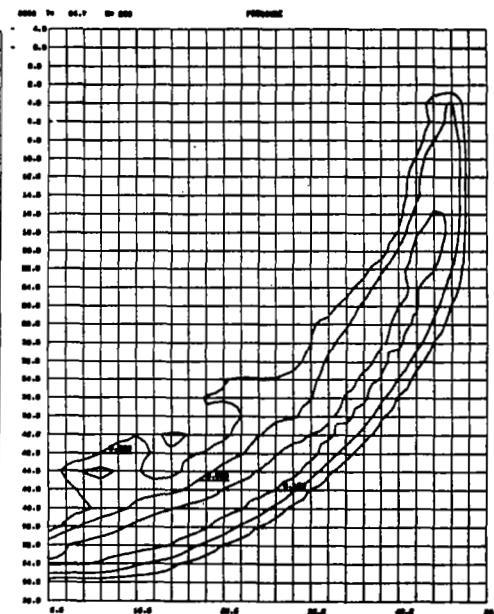
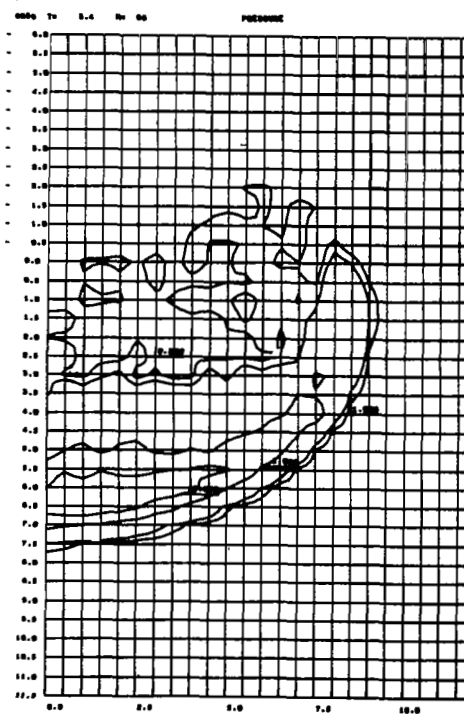
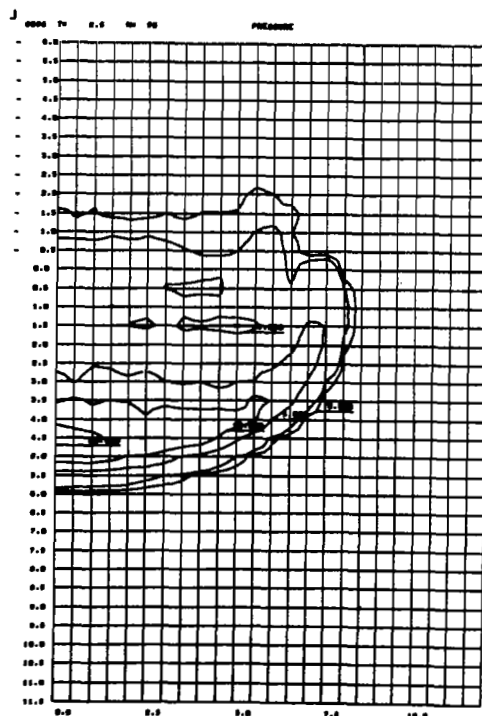


(n) Pressure Field
 $t = 1.0 \mu\text{sec}$



(o) Pressure Field
 $t = 1.8 \mu\text{sec}$

FIGURE C-8 (Con't): CASE 8058, Porous Aluminum ($\rho = 0.44$) into Iron at 72 km/sec



(p) Pressure Field
 $t = 2.5 \mu\text{sec}$

(q) Pressure Field
 $t = 3.4 \mu\text{sec}$

(r) Pressure Field
 $t = 84.7 \mu\text{sec}$

FIGURE C-8 (Con't): CASE 8058, Porous Aluminum ($\rho = 0.44$) into Iron at 72 km/sec



APPENDIX D

REVIEW OF OTHER THEORETICAL TREATMENTS

As outlined in the previous sections, this study has used the basic two-dimensional hydrodynamic PIC code (Bjork 1958, Bjork, Brooks, and Pappetti 1963) to analyze hypervelocity impacts of meteoroid-like materials on space vehicle targets at velocities in the range of interest. The numerical computation treats the initial stages of impact, the subsequent relaxation and break away of the target shock, as well as portions of the final cratering flow. Crater expansion is terminated by a dynamic pressure = local strength criterion, thus providing a specific prediction of the crater dimensions which will result from a given impact. The computations discussed in Section 3 display the physical phenomena which are of importance in determining the impact effects and provide the basis for a quantitative evaluation of damage.

The theoretical treatments of Walsh and Riney also utilize two-dimensional numerical codes based upon the hydrodynamic model. These investigators differ from Bjork in that they make no predictions of specific crater dimensions. Rather, they place heavy emphasis upon interpretation of the flow field in the isolated shock (which is termed "Region II" in this paper) as a means for deriving a velocity scaling law. It is useful to discuss these treatments as a background for the current research, and to draw comparisons, to the extent possible, with the results of the present study.

D.1 Late Stage Equivalence

The concept of late stage equivalence was first introduced by Walsh (1963) from examination of the velocity fields calculated by his numerical solution of the hydrodynamic equations. This concept states that for velocities above $2c_0$,* projectiles having the same parameter $z_w = mv^\alpha$ will produce identical flow fields in the target at late times (m is the projectile mass, v the impact velocity). Initially, a value of 1.86 was assigned to α . More recently (Walsh, 1965) the exponent was refined to 1.74 by comparing integrated features of the flow field, such as the total radial and axial momentum for different impacts. The time at which equivalence occurs has not been specified.

*As used here, c_0 is not the usual sound speed, but rather is given by

$$c_0^2 = \left. \frac{\partial P}{\partial \rho} \right|_s$$

This c_0 is very close to $\sqrt{K/\rho}$, where K is the bulk modulus. For example, in lead, using Bridgeman's measurement of the bulk modulus, c_0 is 2.01 km/sec. This contrasts with the measured rod sound speed of 1.23 km/sec.

Invoking the additional reasonable assumption that identical flow fields in the target at late times lead to identical craters, Walsh deduced that the crater volume is a function of z_w only. Assuming the craters to be hemispherical, he developed an expression to predict penetration, which is

$$\frac{P}{d_s} = K_w \left(\frac{\rho_p}{\rho_t} \right)^{1/3} \left(\frac{v}{c_t} \right)^{0.58} \quad (D-1)$$

where K_w must be determined by some other means. For example, it might be determined by experiments if they could be conducted in a velocity regime where late stage equivalence was valid. Unfortunately, this has been possible only for lead targets because of practical limitations on experimentally-attainable velocities. In Section 3.4, we find K_w for aluminum from the results of the present study. In Eq. (D-1) the values of ρ_t and c_t may be regarded as components of the constant of proportionality which are inserted to make the expression dimensionless. The exponent of $1/3$ appearing on ρ_p arises from the fact that late stage equivalence assumes the process to be a function of the projectile mass only and to be independent of projectile density.

Following the same approach as Walsh, Riney (1965) observes late stage equivalence in his numerical solutions. Riney emphasizes the integrated axial and radial momenta for various impact cases, as well as the dependence of pressure upon depth at late times. However, he concludes that the exponent in the equivalence parameter, mv^α , is 2. Thus his proposed penetration law is

$$\frac{P}{d_s} = K_R \left(\frac{\rho_p}{\rho_t} \right)^{1/3} \left(\frac{v}{c} \right)^{2/3} \quad (D-2)$$

Riney also notes that his observations are valid only above a critical impact velocity, v_c . For the case of aluminum targets, he has estimated this critical velocity to lie in the range

$$7.6 < v_c < 20 \text{ km/sec for } 1/16" \text{ diameter aluminum projectiles}$$

$$v_c \leq 7.6 \text{ km/sec for } 1/2" \text{ diameter aluminum projectiles}$$

D.2 Comments on Identical Flow Fields

Although the concept of "identical flow fields" is invoked in postulating late stage equivalence, it is clear that two flow fields resulting from impacts at different velocities can never be truly identical. Moreover, the region in which they differ is in the region of cratering flow, which we find exerts a critically important influence on the final crater dimension.

To exemplify these remarks, consider two impacts having the same value of mv^α . Let one case pertain to a fast particle with small mass and the other case to a slower particle with larger mass. The faster impact produces higher initial shock pressures, which in turn produce higher entropies in the material

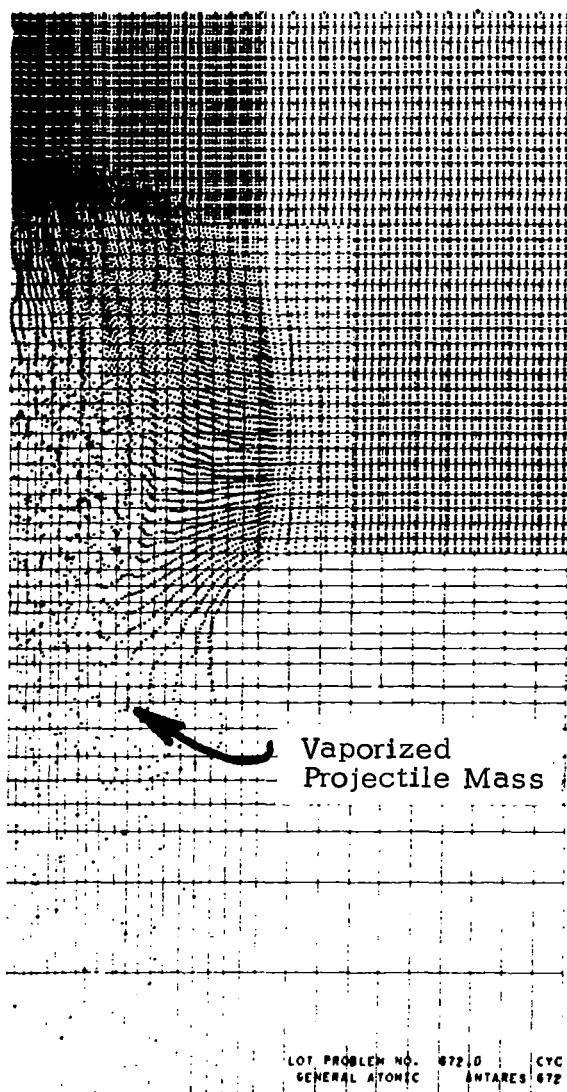
affected by the shock. The shocked material subsequently undergoes adiabatic expansion, in which the entropy remains constant. Therefore in the fast impact there will always be material with higher entropy than can possibly be created in the slow impact. These considerations lead to differences in the cratering flow discussed in Section 2 of the text, even though conditions may be nearly identical in the isolated shock. For example, the faster impact may result in complete projectile vaporization, whereas the slow one may not even melt it. Indeed the mass and velocity fields upon which Walsh (1963) based his initial conclusions exhibit such differences. In the slower impact, a portion of the projectile is still intact and moving into the target. On the other hand the faster projectile has vaporized and blown out from the crater at the time at which the comparison is made. The central point is that differences of this type alter the cratering flow field, while producing only minor differences in the isolated shock. Since the equivalence will be shown to depend strongly on the isolated shock, flows which are equivalent in this sense can produce substantially different craters. These considerations are illustrated in Figures D-1 and D-2.

As an additional illustration of the differences between flow fields, one can compare the impacts of iron and porous aluminum projectiles, on aluminum targets, which are described in detail in Section 3. The initial flows are radically different, being of the deep-penetrating, vortex type in the case of iron projectiles, and of the vapor rebound type in the porous aluminum case.

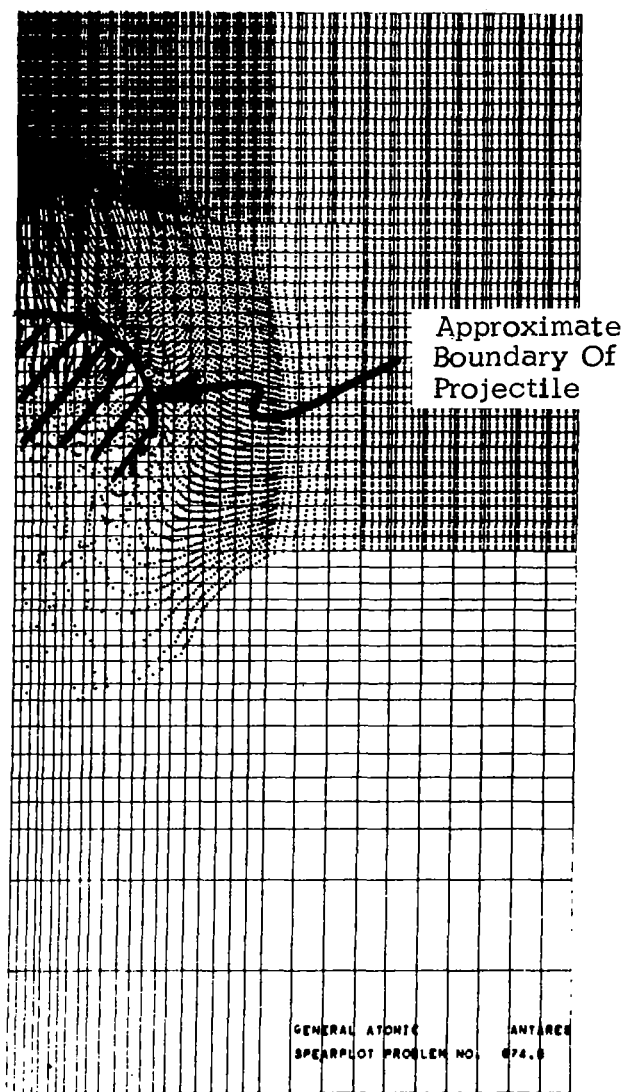
In their most recent work, both Walsh and Riney base the attainment of late stage equivalence on the integrated radial and axial momentum, as given by $\sum_i m_i u_i$ and $\sum_i m_i v_i$. Here i indexes cells, m_i is the cell mass, and u_i and v_i are respectively the radial and axial velocity components. The sum excludes cells which give negative contributions. These parameters are used in lieu of a quantitative comparison of the velocity fields. Use of these parameters places a heavy emphasis on the isolated shock. For example, Table 3-1 reveals that the radial momentum in the isolated shock exceeds that in the crater flow by a factor of about two or more. A similar comment applies to the axial momentum.

For the cases in which thermal softening of the target dominates the final crater dimensions, the isolated shock is the agency which determines the crater dimensions. However, it is not evident a priori that this shock has attained late stage equivalence at the time when it produces the temperature field which determines the final crater. That time, of course, corresponds to the instant at which the peak pulse pressure is just high enough to create the critical release temperature. Neither Walsh nor Riney have identified the depths at which equivalence is attained and so it is not possible to deduce whether late stage equivalence can be applied to this case.

We have discussed many factors which can cause the crater dimensions to depart from the predictions of late stage equivalence. It is important to ascertain that none of them are important before accepting the predictions of that model.

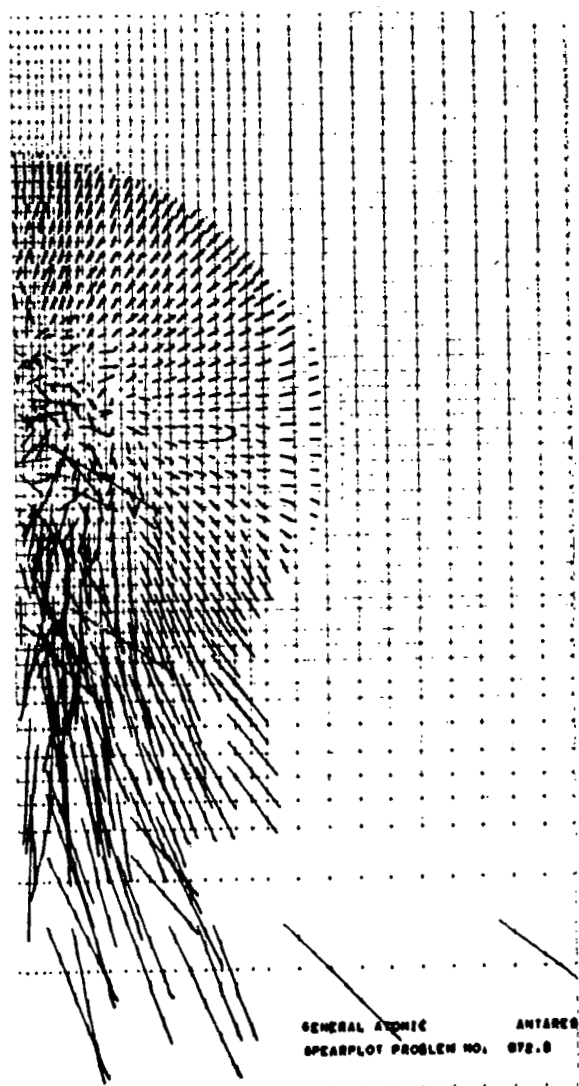


Velocity = 10^7 cm/sec

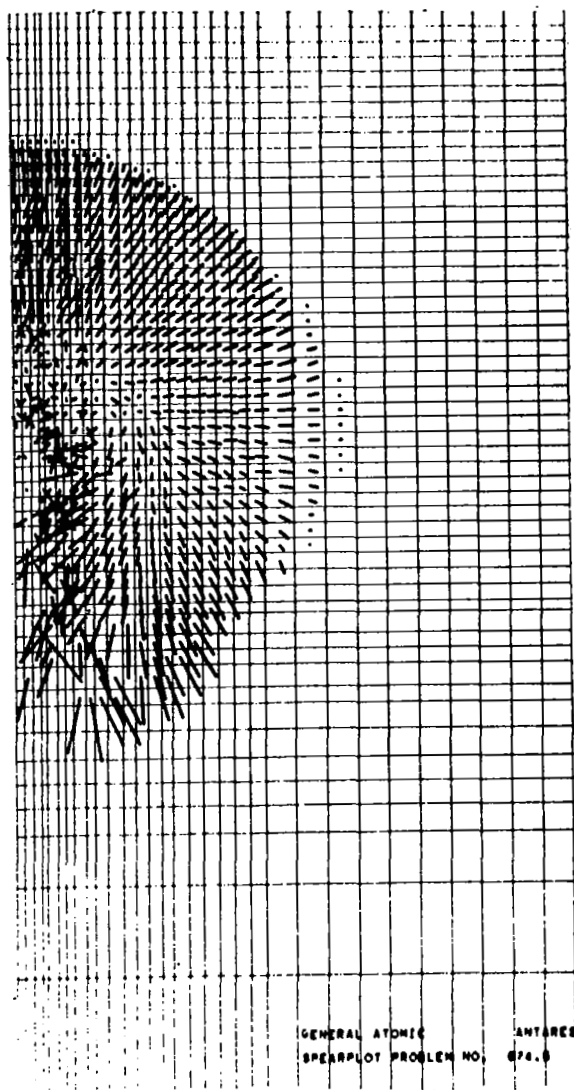


Velocity = 4×10^6 cm/sec

Figure D-1 COMPARISON OF THE LATE-TIME MASS CONFIGURATIONS FOR EQUAL-ENERGY IRON-ON-IRON IMPACTS (from Walsh and Tillotson, 1963)



Velocity = 10^7 cm/sec



Velocity = 4×10^6 cm/sec

FIGURE D-2 COMPARISON OF THE LATE-TIME VELOCITY DISTRIBUTIONS FOR EQUAL-ENERGY IRON-ON-IRON IMPACTS (from Walsh and Tillotson, 1963)

The results of the present study suggest that cases where late stage equivalence is both attained and determines the crater are likely to be at very high velocity, which agrees qualitatively with Walsh's observation. However, we have not identified a simple criterion to determine when this situation will occur. The criterion should consider all of the factors discussed above, and it is clear that the crater dimension itself enters into assessing the importance of those factors.

The results of the present study suggest that when late stage equivalence is applicable for metal targets, the thermal effects occasioned by the isolated shock are the dominant factor in determining crater size. The present results show that the thermal gradients produced in the target by this agency are very steep, and it follows that the target strength has a correspondingly steep gradient. Thus it appears likely that target strength will play a very minor role in craters determinable by late stage equivalence.

D.3 One Dimensional Late Stage Equivalence

The postulate of late stage equivalence in two dimensional hydrodynamic flow prompted the investigation of late stage equivalence in the simpler case of one dimension. The results are interesting of themselves, but unfortunately the research did not reveal any basis for connecting the results obtained in one dimension with those obtained in two or more space dimensions. Thus, there is no present means for applying the one dimensional results to an interesting hypervelocity impact problem.

The one dimensional research disclosed that late stage equivalence is attained in a variety of cases, which lends weight to the concept in multidimensions. However, the 1-D research indicated that the value of α in the similarity parameters Lu^α depends on the equation of state of the target material. This result is at odds with Walsh and Riney's late stage equivalence hypotheses, which claim that α is constant for all materials. Thus, to construct a theory which connects the 1-D to the 2-D phenomenon and supports Walsh and Riney, one must explain why α is a function of material parameters in one dimension, but not in two. As yet, it has not proved possible to construct such a theory.

Chou et al (1965) reported on a theoretical study of the occurrence of late stage equivalence for cases where thin aluminum sheets strike thick aluminum targets at various velocities. Where L is the striker plate thickness and u its velocity, Chou et al find that plates having the same value of $Lu^{1.27}$ produce the same peak shock pressure as a function of depth in the target. Equivalence in this sense is attained at a depth several times the thickness of the thickest plate considered. Allison (1965) reports experimental observations leading to this type of similarity for plates having identical values of the parameter $Lu^{1.33}$.

For the case of copper striking copper, Chou et al find equivalence is attained for the family of striker plates having the same value of $Lu^{1.70}$. For the case of an ideal gas with $\gamma = 1.4$, $Lu^{1.5}$ is the similarity parameter.

Walsh et al (1964) have demonstrated the dependence on material properties unambiguously. By theoretical means they exhibit the equivalence attained when sheets of ideal gas strike targets of ideal gas having zero internal energy. The results show that α depends on the value of γ which appears in the gas equation of state.



REFERENCES

- Alexander, W. M., McCracken, C. W., Secretan, L., and Berg, O. E., "Review of direct measurements of interplanetary dust from satellites and probes," Goddard Space Flight Center, Greenbelt, Md., X-613-62-25, 1962.
- Al'tshuler, L. V., Kormer, S. B., Bakanova, A. A., and Trunin, R. F., Soviet Physics JETP 11, 573 (1960).
- Al'tshuler, L. V., Bakanova, A. A., and Trunin, R. F., Soviet Physics, JETP 15, 65 (1962).
- Anderson, G. D., Doran, D. G., Fahrenbruch, A. L., Equation of State of Solids. Aluminum and Teflon, Air Force Weapons Laboratory Report AFWL-TR-65-147 (1965).
- Bjork, R. L. 1959, Proceedings of the Third Symposium on Hypervelocity Impact, Vol. II.
- _____ 1959a, "Effects of a Meteoroid Impact on Steel and Aluminum in Space," Proc. of Xth Int'l. Astron. Congress, London, Springer-Verlag (1959).
- _____ 1961a, "The Meteoroid Hazard to Space Vehicles," Journal of the American Rocket Society, 31 803 (June, 1961).
- _____ 1961b, Journal of Geophysical Research, 66 3379 (Oct. 1961).
- _____ 1963, "Review of Physical Processes in Hypervelocity Impact and Penetration," Proc. of the 6th Symposium on Hypervelocity Impact, August 1963.
- Bjork, R. L., Brooks, N. B., and Papetti, R., "A Numerical Technique for Solution of Multidimension Hydrodynamic Problems," RM 2628-PR, The Rand Corp., Santa Monica, Calif. (1963).
- Bjork, R. L., and Olshaker, A. E., "The Role of Melting and Vaporization in Hypervelocity Impact," RM-3490-PR, The Rand Corporation, Santa Monica, Calif. (May 1965).
- Bjork, R. L., and Rosenblatt, M., Proceedings of the Seventh Symposium on Hypervelocity Impact (1965).
- Bohn, J. L., and Fuchs, O. P., "High Velocity Impact Studies Directed Towards the Determination of the Spatial Density, Mass, and Velocity of Micrometeorites at High Altitudes," ASTIA AD 243 106.
- Brode, H. L., and Bjork, R. L., "Cratering from a Megaton Surface Burst," RM-2600, The Rand Corporation, Santa Monica, Calif. (1960).

- Chou, P. C., Sidhu, H. S., and Zajac, L. J., "The strong plane shock produced by hypervelocity impact and late stage equivalence." Proceedings of the Seventh Symposium on Hypervelocity Impact (1965).
- Elford, W. G., "Calculation of the response function of the Harvard Radio meteor project radar system," Research Report No. 8, Smiths. Ast. Obs., Cambridge, Mass. (Oct. 1964).
- Elford, W. G., and Hawkins, G. S., "Meteor Echo Rates and the Flux of Sporadic Meteors." Research Report No. 9, Smiths. Ast. Obs., Cambridge, Mass. (Nov. 1964).
- Elford, W. G., Hawkins, G. S., and Southworth, R. B., "The Distribution of Sporadic Meteor Radiants," Research Report No. 11, Smiths. Ast. Obs., Cambridge, Mass. (Dec. 1964).
- Hastings, E. C., Jr., "The Explorer XVI micrometeoroid satellite," Langley Research Center, Langley Station, Hampton, Va., NASA TMX-949, March 1964.
- Hawkins, G. S., et al, "Preliminary Analysis of Meteor Radiants and Orbits," Research Report No. 7, Smiths. Ast. Obs., Cambridge, Mass. (Aug. 1964).
- Hawkins, G. S., and Southworth, R. B., Smithsonian Contributions to Astrophysics, 2 349 (1958).
- Hawkins, G. S., and Upton, E. K. L., The Astrophysical Journal, 128 727 (November 1958).
- Jacchia, L. G., "On the Color Index of Meteors," Astronomical Journal, 62 358-362 (1957).
- Jacchia, L. G., Verniani, F., and Briggs, R. E., "An Analysis of the Atmospheric Trajectories of 413 Precisely Reduced Photographic Meteors." Smiths. Ast. Obs. Special Report No. 175 (1965).
- Herrmann, W., and Jones, A. H., Proceedings of the Fifth Symposium on Hypervelocity Impact, Vol. I, Part 2, 389 (April 1962).
- Kormer, S. B., Funtikov, A. I., Urlin, V. D., and Kolesnikova, A. N., Soviet Physics JETP 15 477 (1962).
- Kreyenhagen, K. N., Bjork, R. L., and Brooks, N. B., Proceedings of the Seventh Symposium on Hypervelocity Impact (1965).
- Latter, R., Phys. Rev. 99, 1854 (1955).
- _____ 1956, J. Chem. Phys. 24 280.
- Lundergan, C. D., and Herrmann, W., Journal of Applied Physics 34 2046 (July 1963).

- McCloskey, D. J., "An Analytic Formulation of Equation of State," RM-3095-PR, The Rand Corporation, Santa Monica, Calif. (Feb. 1964).
- McCracken, C. W., and Alexander, W. M., "The Distribution of Small Interplanetary Dust Particles in the Vicinity of the Earth," Goddard Space Flight Center, Greenbelt, Md., NASA TN D-1349 (July 1962).
- Naumann, R. J., "Pegasus Satellite Measurements of Meteoroid Penetration," NASA TMX-1192, George Marshall Space Flight Center, Huntsville, Ala. (Dec. 1965).
- Olshaker, A. E., and Bjork, R. L., Proceedings of the Fifth Symposium on Hypervelocity Impact, (1962).
- O'Neal, R. L., "The Explorer XXIII Micrometeoroid Satellite," NASA TMX-1123, Langley Research Center (August 1965).
- Riney, T. D., Proceedings of the Sixth Symposium on Hypervelocity Impact (1963).
- Riney, T. D., and Heyda, J. F., Proceedings of the Seventh Symposium on Hypervelocity Impact, Vol. II, 77 (1965).
- Stull, D. R., and Sinke, G. C., "Thermodynamic Properties of the Elements," American Chem. Soc., Washington, D. C. (1956).
- Tillotson, J. H., Metallic Equations of State for Hypervelocity Impact, General Atomic Report GA-3216 (July 1962).
- Verniani, F., "On the Luminous Efficiency of Meteors," Research in Space Science Special Report No. 145, Smiths. Ast. Obs., Cambridge, Mass. (Feb. 1964).
- _____, 1964b, "On the Density of Meteoroids. II The Density of Faint Photographic Meteors." *Nuovo Cimento*, 33 1183 (1964).
- Verniani, F., and Hawkins, G. S., "On the Ionizing Efficiency of Meteors," Research Report No. 5, Smiths. Ast. Obs., Cambridge, Mass. (Feb. 1964).
- _____, 1965, "Masses, Magnitudes, and Densities of 320 Radio Meteors," Harvard College Observatory, Smiths. Ast. Obs., Research Report No. 12 (March 1965).
- Walsh, J. M., Proceedings of the Sixth Symposium on Hypervelocity Impact (1963).
- Walsh, J. M., et al, "Summary Report on the Theory of Hypervelocity Impact," General Atomics Report GA-5119 (March 1964).

Walsh, J. M., and Johnson, W. E., Proceedings of the Seventh Symposium on Hypervelocity Impact, Vol. II (1965).

Whipple, F. L., "On Meteoroids and Penetration," Journal of Geophysical Research, Vol. 68, No. 17, 4929 (Sept. 1963).